University of Calgary

PRISM Repository **https://prism.ucalgary.ca**

The Vault Open Theses and Dissertations

2023-09-12

Impact of Homeostasis Disruption on the Structure and Function of Murine Articular Cartilage

Oliveira Masson, Anand

Oliveira Masson, A. (2023). Impact of homeostasis disruption on the structure and function of murine articular cartilage (Doctoral thesis, University of Calgary, Calgary, Canada). Retrieved from https://prism.ucalgary.ca.

https://hdl.handle.net/1880/117035

Downloaded from PRISM Repository, University of Calgary

UNIVERSITY OF CALGARY

Impact of Homeostasis Disruption on the Structure and Function of Murine Articular Cartilage

by

Anand Oliveira Masson

A THESIS

SUBMITTED TO THE FACULTY OF GRADUATE STUDIES

IN PARTIAL FULFILMENT OF THE REQUIREMENTS FOR THE

DEGREE OF DOCTOR OF PHILOSOPHY

GRADUATE PROGRAM IN BIOMEDICAL ENGINEERING

CALGARY, ALBERTA

SEPTEMBER, 2023

© Anand Oliveira Masson 2023

Abstract

Articular cartilage plays a vital role in facilitating pain-free movement and load distribution in synovial joints, such as the knee. Owing to its complex structure-functional requirements and limited regenerative capacity, articular cartilage is particularly vulnerable to deterioration triggered by intrinsic and extrinsic insults. For instance, abnormal loading, trauma and aging can disrupt cellular, anatomical, and functional homeostasis within the knee joint and/or articular cartilage microenvironment, contributing to the pathogenesis of tissue degradation and degenerative joint diseases, particularly osteoarthritis (OA). In this context, it is essential to understand how cartilage and the joint microenvironment respond to differential levels of tissue homeostatic disruption and the resulting implication on remodeling and repair outcomes. In this multifaceted study, I employed several transgenic mouse models in conjunction with histological, imaging, and mechanical testing modalities to deepen our understanding of structural and functional changes associated with degeneration and regeneration of murine articular cartilage.

My initial investigation centered on understanding the role of chondrocyte death on cartilage degeneration. Given that chondrocytes, the sole cells found in healthy cartilage, are critical in synthesizing and maintaining the extracellular matrix, the loss of these cells often correlates with tissue degeneration and disease. Yet, the cause-and-effect relationship between chondrocyte loss/death and degeneration remains disputed. To address this controversy, I induced selective depletion of chondrocytes using a genetic approach and demonstrated that a substantial reduction in cellularity through chondrocyte apoptosis did not predispose mouse cartilage to degeneration nor the development of an OA-like phenotype. Furthermore, focal areas devoid of chondrocytes did not repopulate after genetically induced cell depletion, implying an adaptative response from surviving cells.

My second study shifted focus to proteoglycan-4 (PRG4), also known as lubricin, a key player in the structural and functional integrity of articular cartilage. PRG4 deficiency in humans and mice leads to premature and irreversible joint failure. Abnormalities in cartilage thickness and bone morphology have been anecdotally reported; however, to date no study has employed a quantitative approach to empirically determine the role of *Prg4* in joint morphology (e.g., geometry). This prompted me to examine and quantify the three-dimensional shape of distal femurs from wildtype controls and *Prg4* knockout mice. I also mapped spatial differences in their articular cartilage microscale biomechanical properties to address limitations inherent to cross-sectional morphological studies and gain further insight into genotype-phenotype differences. I have shown that *Prg4*$^{-/-}$ femurs vary in size and shape compared to age-matched controls, with more dramatic abnormalities observed within condyle and trochlea regions. These results suggest that *Prg4* deficiency not only impacts tissue homeostasis but also joint morphology.

Finally, I investigated cartilage's response to injury. Despite the identification of various progenitor pools in articular cartilage and associated tissues, cartilage defects repair poorly (if at all), gradually leading to degenerative changes and joint failure. Recent lineage tracing studies have uncovered a new cohort of tissue-resident quiescent mesenchymal progenitors (MPs) in skeletal muscle, skin and heart, marked by *Hic1* expression, capable of contributing to regenerative and pathological processes in a tissue- and context-dependent manner. To investigate the role of these MPs in cartilaginous tissues, I performed lineage-tracing experiments during normal aging and in response to injury within auricular (ear) and articular (knee) cartilage. Moreover, I developed a new transgenic model to dysregulate the cell cycle machinery within these cells and investigate outcome results in endogenous cartilage regeneration post-injury. My findings show *Hic1*-progeny can assume a fibro-like phenotype leading to scarring, and intriguingly that cell cycle dysregulation in *Hic1* cells positively impacts wound closure and articular cartilage regeneration, albeit with minimal (if any) direct contribution of *Hic1*-progeny to contribute to newly formed cartilage tissue.

In summary, this thesis highlights the complexity of articular cartilage response to different stressors, leading to adaptative and maladaptive remodeling. Having employed various transgenic

mouse models and advanced investigative techniques, I have significantly contributed to advancing our understanding of cartilage biology and its intrinsic response to injury and other insults, providing valuable insights that may pave the way for the development of novel therapeutic strategies for cartilage diseases and regeneration.

Preface

This thesis is presented in a manuscript-based format and is organized into seven chapters. Portions of this thesis have resulted in peer-reviewed publications, and publications currently under review or in preparation as follows:

Chapter 1 discusses critical variables that contribute to the gradient of articular cartilage degenerative and regenerative competence seen in pre-clinical animal models, focusing on mice.

Masson AO, Krawetz RJ. (2020) *Understanding cartilage protection in OA and injury: a spectrum of possibilities.* BMC Musculoskeletal Disorders, 21, 432.

*Final version is available online at: https://doi.org/10.1186/s12891-020-03363-6

Chapter 2 expands on key concepts relevant to this doctoral study that were not discussed in Chapter 1. It provides an overview of the structure, composition and function of the articular cartilage, the health and disease perspective. It also outlines the aims.

Chapter 3 details the development and optimization of biomechanical testing, enabling the assessment of murine articular cartilage, then employed in other chapters of this thesis.

Masson AO, Besler B, Edwards WB, Krawetz RJ. (2022). *High spatial resolution analysis using automated indentation mapping differentiates biomechanical properties of normal vs. degenerated articular cartilage in mice*. Elife 11:2021.10.26.465857.

*Final version is available online at: https://doi.org/10.7554/eLife.74664

Chapter 4 discusses the use of a genetic model to target and selectively deplete chondrocytes in articular cartilage and explores the significance of chondrocyte death in the initiation of cartilage degenerative cascade.

Masson A.O, Corpuz J.M., Corpuz K., Biernaskie J., Edwards W.B., Krawetz R.J. *Induced chondrocyte depletion disrupts articular cartilage homeostasis but is not a driver of degeneration.*
* In preparation for submission.

Chapter 5 explores the implications of proteoglycan-4 (*Prg4*) loss of function on distal femur morphology and articular cartilage mechanical properties in adulthood.

Masson A.O., Devine J., Das N., Coveney C.R., Hallgrimsson B., Capellini T.D., Biernaskie J., Edwards W.B., Krawetz R.J. *Prg4 deficiency alters femur morphology.*
*In preparation for submission.

Chapter 6 focuses on cartilage tissue repair/regeneration and explores the role of recently identified *Hic1*$^{+}$ mesenchymal progenitors on homeostasis and in response to injury.

Masson AO, Corpuz J, Besler B, D., Krahn N., Underhill T.M., Biernaskie J, Edwards W.B., Krawetz R.J. *The Hic1-lineage dictates the balance between cartilage repair and regeneration.*
*In preparation for submission.

Chapter 7 aims to discuss and contextualize the main findings from the preceding chapters, followed by limitations and potential areas for further research.

Acknowledgments

I would like to express my gratitude to Dr. Roman Krawetz, my supervisor, for his consistent support and guidance throughout my academic career. It has been over a decade since our first encounter during my exchange program from Brazil to Canada, and your recognition of my potential as a summer intern back then was life changing. It opened the door to a world of possibilities and ultimately led me to move to Canada and pursue a PhD. Your passion for science and dedication to your students are admirable, and I am truly honored to have worked alongside you for the past few years. Your mentorship and encouragement have helped me navigate through the complexities of research and life, and for that I will be forever thankful.

I am also grateful for my committee members, Drs. Brent Edwards and Jeff Biernaskie. Your insights and expertise have been critical in shaping this body of research. Thank you for your guidance, kindness, and mentorship. I would also like to acknowledge my appreciation for my examining committee members, Drs. Sarah Manske, Peng Huang and James J.D. Johnston, for their scholarly and thoughtful input.

I would also like to thank my incredible lab mates, past and present, who have supported me on this journey. I will always be grateful for your help and intellectual contributions, but most of all for your friendship and for the memories we have shared over the years, the laughs, the tears, the coffee runs and bubble tea celebrations. A sincere thank you to my wonderful colleagues in the McCaig Institute and University of Calgary: Alex Olsen, Bryce Besler, Catherine Leonard, Christina Jablonski, Deepthi Rajashekar, Dragana Ponjevic, Ibukun Oni, Jaqueline Rios, Jay Devine, Jessica Corpuz, Kristian Corpuz, Leah Ferrie, Leila Larijani, Luiz Gustavo Almeida, Nabangshu Das, Needa Aljezani, Nicole Krahn, Nicoletta Ninkovic, Priyatha Premnath, Rocio

Araujo, Sarthak Sinha, Saleem Abubacker, Sophia Shah, Thiago Valentin, Wei Liu – I feel truly fortunate to have had the opportunity to befriend and collaborate with such incredible people.

I cannot express enough gratitude for my incredible family, who have been so loving, supportive, and patient with me throughout this journey. To my parents, Claudenir and Valéria, and my brother, Bruno, I am forever thankful for the love and strength you have instilled in me. Your encouragement has guided me every step of the way, *obrigada por tudo, vocês são minha vida, minha história, meu amor*! To my beloved Brazilian *família*, though we may be separated by distance, you are always in my heart. I miss you every day! To the Barisow clan, thank you for welcoming me into your family and for your love and kindness. I am blessed to have you all in my life, and I could not have achieved this without your support. Lastly, but certainly not least, to my husband Daniel, thank you for your patience and understanding during this process.

Dedication

To my loving parents.

To my beloved husband, Dan, for the joy and strength you bring into my life. You inspire me in so many ways. Te amo Vida!

Table of Contents

Abstract ... ii

Preface ... v

Acknowledgments ... vii

Dedication ... ix

Table of Contents ... x

List of Tables ... xiv

List of Figures ... xv

List of Symbols, Abbreviations and Nomenclature ... xvii

Chapter One: Understanding cartilage protection in OA and injury: a spectrum of possibilities ... 1

- 1.1. Abstract ... 2
- 1.2. Background ... 3
- 1.3. Main text – factors influencing regeneration and degeneration of cartilage ... 6
  - 1.3.1. Diversity of regenerative potential across animal models ... 6
  - 1.3.2. Effect of genetic makeup: spectrum from endogenous regeneration to spontaneous degeneration ... 8
  - 1.3.3. Aging and the regenerative potential ... 10
  - 1.3.4. Models of OA and cartilage damage ... 12
- 1.4. Conclusion ... 20
- 1.5. Acknowledgements ... 21
- 1.6. Author contributions ... 21

Chapter Two: Introduction ... 22

- 2.1. Knee joint anatomy ... 23
- 2.2. Osteoarthritis – burden of disease ... 24
- 2.3. Articular Cartilage ... 26
  - 2.3.1. Structure and Function ... 26
- 2.4. Joint-resident mesenchymal stem cells ... 30
- 2.5. Hypermethylated in Cancer 1 (*Hic1*) ... 32
- 2.6. Transgenic mouse models ... 33
  - 2.6.1. Cre/loxP system ... 33
- 2.7. Scope of Research ... 35
- 2.8. Acknowledgments ... 36

Chapter Three: High spatial resolution analysis using automated indentation mapping differentiates biomechanical properties of normal vs. degenerated articular cartilage in mice ... 37

3.1. Abstract 38
3.2. Introduction 39
3.3. Materials and Methods 42
  3.3.1. Animals 42
  3.3.2. Automated indentation mapping 42
  3.3.3. Needle probing – thickness measurement 43
  3.3.4. 3D XRM imaging 44
  3.3.5. Imaging processing 44
  3.3.6. Statistical analysis 45
3.4. Results 46
  3.4.1. Automated indentation mapping reliability 46
  3.4.2. Cartilage thickness characterization: comparison between needle probing and XRM imaging 50
  3.4.3. Altered biomechanical properties in degenerated murine articular cartilage 55
3.5. Discussion 58
3.6. Acknowledgements 62
3.7. Author Contribution 62
3.8. Supplementary Information 62
Chapter Four: Induced chondrocyte depletion disrupts articular cartilage homeostasis but is not a driver of degeneration 64
4.1. Abstract 65
4.2. Introduction 66
4.3. Methods 68
  4.3.1. Animal models 68
  4.3.2. Histology 68
  4.3.3. Immunofluorescence 69
  4.3.4. Image quantification 69
  4.3.5. Biomechanical assessment 70
  4.3.6. Statistical analysis 71
4.4. Results 72
  4.4.1. Depletion of articular cartilage chondrocytes post DTA-induction 72
  4.4.2. Preservation of cartilage structure post-chondrocyte depletion 75
  4.4.3. DTA mice display transient upregulation of ADAMTS5 in articular cartilage 78
  4.4.4. Effect of chondrocyte depletion on stiffness and thickness of articular cartilage 80
4.5. Discussion 83

4.6. Acknowledgments ... 89
4.7. Author's contributions ... 89
4.8. Supplementary information ... 90
Chapter Five: *Prg4* deficiency alters femur morphology ... 92
5.1. Abstract ... 93
5.2. Introduction ... 94
5.3. Materials and Methods ... 97
5.3.1. Animals ... 97
5.3.2. Histology ... 97
5.3.3. 3D X-ray microscopy (XRM) imaging ... 98
5.3.4. Morphology data acquisition ... 98
5.3.5. Size and shape comparisons ... 99
5.3.6. Condylar and trochlea cartilage RNA-seq data collection and analysis ... 100
5.3.7. Biomechanical assessment ... 101
5.3.8. Statistical analysis ... 102
5.4. Results ... 103
5.5. Discussion ... 114
5.6. Acknowledgements ... 116
5.7. Author’s contribution ... 116
5.8. Supplementary information ... 117
Chapter Six: The *Hic1*-lineage dictates the balance between cartilage repair and regeneration ... 119
6.1. Abstract ... 120
6.2. Introduction ... 121
6.3. Materials and Methods ... 123
6.3.1. Mouse strains ... 123
6.3.2. Lentiviral RNA analysis and RT-qPCR ... 124
6.3.3. Administration of tamoxifen ... 124
6.3.4. Ear wound and size evaluation ... 125
6.3.5. Articular cartilage defect model ... 125
6.3.6. Histology and immunofluorescence ... 125
6.3.7. In vivo EdU labeling ... 127
6.3.8. 3D X-ray microscopy (XRM) imaging ... 127
6.3.9. Biomechanical testing ... 128
6.3.10. Statistical analysis ... 128
6.4. Results ... 129

6.4.1. Cells of the Hic1 lineage reside in the ear pinna and knee joint microenvironments but do not undergo differentiation into auricular or articular cartilage tissues under homeostatic conditions 129

6.4.2. Hic1-expressing cells contribute to wound healing/closure in the ear 131

6.4.3. Perturbation of cell cycle machinery in Hic1+ve cells alters ear wound healing outcomes 132

6.4.4. Hic1^{+ve} progenitors are mobilized in response to acute articular cartilage injury 135

6.4.5. Hic1-lineage recruitment to defect site and contribution to repaired tissues....... 137

6.4.6. Cartilage biomechanical function is not restored despite improved structural morphology 140

6.5. Discussion 143

6.6. Acknowledgements 146

6.7. Author’s contribution 146

6.8. Supplementary information 147

Chapter Seven: Discussion and Future Directions 153

7.1. Overview 154

7.2. Significance 155

7.2.1. Cartilage degeneration vs. regeneration 155

7.2.2. Synovial crosstalk in health and disease........ 158

7.2.3. Structural vs. functional regeneration........ 160

7.3. Future directions........ 162

7.4. Limitations........ 163

7.5. Concluding remarks........ 165

Appendix A 166

Journal copyright permissions........ 166

Appendix B........ 168

Co-author copyright permission letters. 168

References 171

List of Tables

Table 1.1. Summary of most widely used osteoarthritis models and direct cartilage injury models with respect to their type/mode of action and most commonly employed species............... 14

Table 3.1. Mean peak force (X: N) and coefficient of variation (CV: %) from triplicate measurements for each of the 31 positions (L1-M17) of assessment over mice femoral condyles... 49

Table 3.2. Mean and standard deviation (SD) values for peak force (N) as determined by automated indentation test performed for n = 10 distal femur samples of murine articular cartilage. 50

Table 3.3. Mean and standard deviation (SD) values for cartilage thickness as determined by needle probing for distal femur samples of murine articular cartilage (n = 10). 53

Table 3.4. Mean and standard deviation (SD) values for cartilage thickness as determined by x-ray microscopy imaging for distal femur samples of murine articular cartilage (n = 10). 54

Table 6.1. Comparison between groups for mean values of structural stiffness (SS: N/mm), relaxation time (Rt: s) and residual force after 120 s relaxation (Feq: N) for uninjured and injured hindlimb trochlear groove (TG) 142

List of Figures

Figure 1.1. Factors influencing the regeneration and degeneration processes in cartilage 5
Figure 1.2. Assumed outcomes based on three different possible scenarios using an osteoarthritic model of PTOA or a FTCD cartilage injury model. 17
Figure 1.3. Comprehensive view of the effect of targeted treatments in inhibiting cartilage degeneration and enhancing cartilage regeneration.. 20
Figure 2.1. Knee joint anatomy 23
Figure 2.2. Comparative representation of a healthy and osteoarthritic knee joint...................... 25
Figure 2.3. Zonal organization and variation within articular cartilage. 28
Figure 2.4. Schematic overview of transgenic mice and assay modalities employed in Chapters 4-6. 36
Figure 3.1. Indentation mapping of murine articular cartilage. 47
Figure 3.2. Thickness mapping of murine articular cartilage. 52
Figure 3.3. Correlation graphs per testing site for the lateral (n = 135 positions) and medial (n = 167) condyles; 55
Figure 3.4. Altered biomechanical properties in degenerated murine articular cartilage............. 57
Figure S3.1. Specimen preparation and assemble to sample holder for automated indentation mapping using custom setup, allowing for repositioning of the sample and non-destructive retrieval for three-dimensional x-ray microscopy imaging (scale bars equal to 4 mm). 62
Figure S3.2. Setup for needle probing thickness measurement, using a 30G×1.4" hypodermic needle (TSK Laboratory, Japan) adapted to the 1-mm spherical indenter *(Biomomentum Inc*, Laval, QC) (scale bars equal to 4 mm). 63
Figure S3.3. XRM imaging of femoral condyles. 63
Figure 4.1. DTA-induction leads to chondrocyte depletion in mouse articular cartilage............. 74
Figure 4.2. Histopathological comparison of articular cartilage in control and Acan-CreER^{T2}; DTA mice. 77
Figure 4.3. Transient upregulation of ADAMTS5 following DTA-induced chondrocyte depletion. 80
Figure 4.4. Functional analysis of articular cartilage. 83
Figure 4.5. Summary schematic reflecting the difference in tissue response after chondrocyte depletion compared to commonly used models of post-traumatic or chemically induced mouse articular cartilage injury. 88
Figure S4.1. Immunofluorescence imaging analysis and quantification. 90

Figure S4.2. Safranin-O-stained frontal knee sections from control and *Acan*-CreER^{T2}; DTA mice 1-week and 1- to 16-weeks, respectively, post 4-OHT treatment. 91
Figure S4.3. Articular cartilage 7-months post-4-OHT treatment demonstrate chondrocyte-depleted areas are maintained. 91
Figure 5.1. *Prg4*$^{-/-}$ mice exhibit morphological changes in the distal femur and articular cartilage 104
Figure 5.2. *Prg4*$^{-/-}$ distal femur changes in size and shape. 107
Figure 5.3. Quantitative morphological analysis of individual anatomical features. 110
Figure 5.4. Abnormalities in articular cartilage structure and biomechanics of *Prg4*$^{-/-}$ mice with aging. 112
Figure S5.1. Comparison of WT and *Prg4*$^{-/-}$ mice distal femur morphology during aging. 117
Figure S5.2 Additional parameter evaluated in size and shape geometric morphometric comparisons. 118
Figure 6.1. *Hic1*-lineage contribution to physiological in vivo tissue turnover. 131
Figure 6.2. Hic1-expressing cells and their progeny participate in ear wound healing.............. 134
Figure 6.3. Articular cartilage healing after FTCD. 137
Figure 6.4. Contribution of Hic1-lineage to cartilage formation and repair post-FTCD............ 139
Figure 6.5. Evaluation of morphology and mechanical properties of repaired tissue. 141
Figure S6.1. Generation of E2F1 over-expressing transgenic mice. 147
Figure S6.2. Ear tissue immunofluorescence imaging analysis and quantification..................... 148
Figure S6.3. Knee joint immunofluorescence imaging analysis and quantification. 149
Figure S6.4. *Hic1*-lineage recruitment and contribution to ear tissue outgrowth after injury..... 150
Figure S6.5. Col2aCre; R26^{E2F1} are unable to regenerate articular cartilage after FTCD. 151
Figure S6.6. *Hic1*-lineage recruitment and response to injury after FTCD................................ 152
Figure S6.7. Characterization of αSMA expression after FTCD. 152

List of Symbols, Abbreviations and Nomenclature

3D	Three dimensional
4-OHT	4-hydroxytamoxifen
αSMA	Alpha Smooth muscle actin or Alpha-actin 2
ACAN	Aggrecan
ACI	Autologous chondrocyte implantation
ACL	Anterior cruciate ligament
ACLT	Anterior cruciate ligament transsection
ADAMTS	A Disintegrin and metalloproteinase with thrombospodin motifs
ANOVA	Analysis of variance
CACP	Camptodactyly-artropathy-coxa vara-pericarditis
cDNA	Complementary DNA
Cre	Cre recombinase
DMM	Destabilization of the medial meniscus
DTA	Diphtheria toxin fragment A
E2F1	E2F Transcription Factor 1
ECM	Extracelullar matrix
EDTA	Ethyleneglycoltetraacetic acid
Edu	5-ethynyl-2'-deoxyuridine
FTCD	Full-thickness cartilage defect
GAG	Glycosaminoglycan
HIC1	Hypermethylated in cancer 1
IAF	Intra-articular fracture
ICC	Intra-class correlation coeficient
MANOVA	Multivariate analysis of variance
MMP	Matrix metalloproteinase
MRL	Murphy Roths Large
MP	Mesenchymal progenitor cells
NBF	Neutral buffer formalin
NP	Needle probing
OA	Osteoarthritis
OARSI	Osteoarthritis Research Society International
PBS	Phosphate buffer saline

PCA	Principal component analysis
PRG4	Proteoglycan-4
PTA	Phosphotungstic acid
PTOA	Post-traumatic osteoarthritis
RNA	Ribonucleic acid
RMSE	Root mean squared error
SD	Standard deviation
tdTomato	Tanden dimer tomato fluorescent protein
XRM	X-ray microscopy

Chapter One: Understanding cartilage protection in OA and injury: a spectrum of possibilities

Masson A.O, Krawetz R.J. - Final version is available on BMC Musculoskeletal Disorders

My contributions to this work were as follows:

- *Co-conceptualized the scope of the review, synthesized the current body of literature, and wrote the manuscript.*

1.1. Abstract

Background: Osteoarthritis (OA) is a prevalent musculoskeletal disease resulting in progressive degeneration of the hyaline articular cartilage within synovial joints. Current repair treatments for OA often result in poor quality tissue that is functionally ineffective compared to the hyaline cartilage and demonstrates increased failure rates post-treatment. Complicating efforts to improve clinical outcomes, animal models used in pre-clinical research show significant heterogeneity in their regenerative and degenerative responses associated with their species, age, genetic/epigenetic traits, and context of cartilage injury or disease. These can lead to variable outcomes when testing and validating novel therapeutic approaches for OA. Furthermore, it remains unclear whether protection against OA among different model systems is driven by inhibition of cartilage degeneration, enhancement of cartilage regeneration, or any combination thereof. **Main text:** Understanding the mechanistic basis underlying this context-dependent duality is essential for the rational design of targeted cartilage repair and OA therapies. Here, we discuss some of the critical variables related to the cross-species paradigm of degenerative and regenerative abilities found in pre-clinical animal models, to highlight that a gradient of regenerative competence within cartilage may exist across species and even in the greater human population, and likely influences clinical outcomes. **Conclusions:** A more complete understanding of the endogenous regenerative potential of cartilage in a species-specific context may facilitate the development of effective therapeutic approaches for cartilage injury and/or OA.

Keywords: Chondroprotection, Regeneration, Cartilage, Animal models, Osteoarthritis

1.2. Background

As a leading cause of disability and morbidity worldwide, osteoarthritis (OA) is a degenerative joint pathology associated with significant health and economic burden to patients and society (Hunter et al., 2014; Sharif et al., 2016). The development of OA involves a series of structural changes within the joints, and it is influenced by numerous risk factors, such as aging, genetics, and injury/trauma. Despite extensive heterogeneity observed in the onset and pathogenesis of OA, the progressive degradation of the articular cartilage appears as a unifying feature, and it remains a central focus in regenerative medicine approaches to the treatment of OA.

The articular cartilage is an intricate and remarkable tissue that provides the biomechanical properties and low friction surface necessary for the proper function of synovial joints (Sophia Fox et al., 2009; Zhang et al., 2009). While articular cartilage grants pain-free mobility under physiological conditions, once damaged, it presents poor innate healing capacity. Moreover, common surgical interventions aiming to improve cartilage healing, such as microfracture and autologous chondrocyte implantation (ACI), often result in a fibrocartilage patch (i.e., repair) as opposed to restoring the native hyaline cartilage (i.e., regeneration). The differences in structure and composition combined with a lack of integration with the native tissue render fibrocartilage biomechanically incompatible with the articular cartilage. These shortcomings are thought to accelerate the fibrocartilage breakdown leading to further articular cartilage injury/degeneration over time (Rai et al., 2012; Shapiro et al., 1993).

Attempts have been made to circumvent this poor intrinsic regenerative ability of cartilage and protect it from further degradation after damage or disease, by promoting an environment that is chondroprotective (preventing cartilage breakdown) and/or chondro-inductive (restoring cartilage) (Chevalier et al., 2013). These include inhibiting catabolic-related processes (Miller et al., 2013; Wang et al., 2013), modulating inflammation (Robinson et al., 2016), favoring chondrogenesis (Hochberg et al., 2016; M. H. Li et al., 2017), and recruiting or exogenously delivering cells of various potencies (e.g., stem cells derived from various tissue sources to chondrocytes) (Leonard et al., 2015; Mak et al., 2016; McGonagle et al., 2017; Richardson et al., 2016). Despite many efforts, however, the development of effective disease-modifying therapies for injured cartilage and OA has yet to be realized.

The therapeutic potential of cell-, drug- or surgical-based interventions focused on cartilage injury and OA is commonly assessed using pre-clinical animal models. Notably, not only different species but also strains at various ages and contexts of joint damage (direct cartilage injury, post-traumatically induced or spontaneous OA) are employed. All these variables can influence the regenerative and degenerative responses, create a spectrum of outcomes (Figure 1.1) and have critical implications for validating new therapeutic strategies. For instance, spontaneous and trauma-induced cartilage injuries appear to differ in terms of molecular signatures and responses to interventions (Usmani et al., 2016), likely due to divergent mechanisms of disease pathogenesis. Also, age and genetic/epigenetic traits may influence the regenerative competence of animals, thus appearing as confounding factors in cartilage-related studies (Joutoku et al., 2019; Usmani et al., 2016).

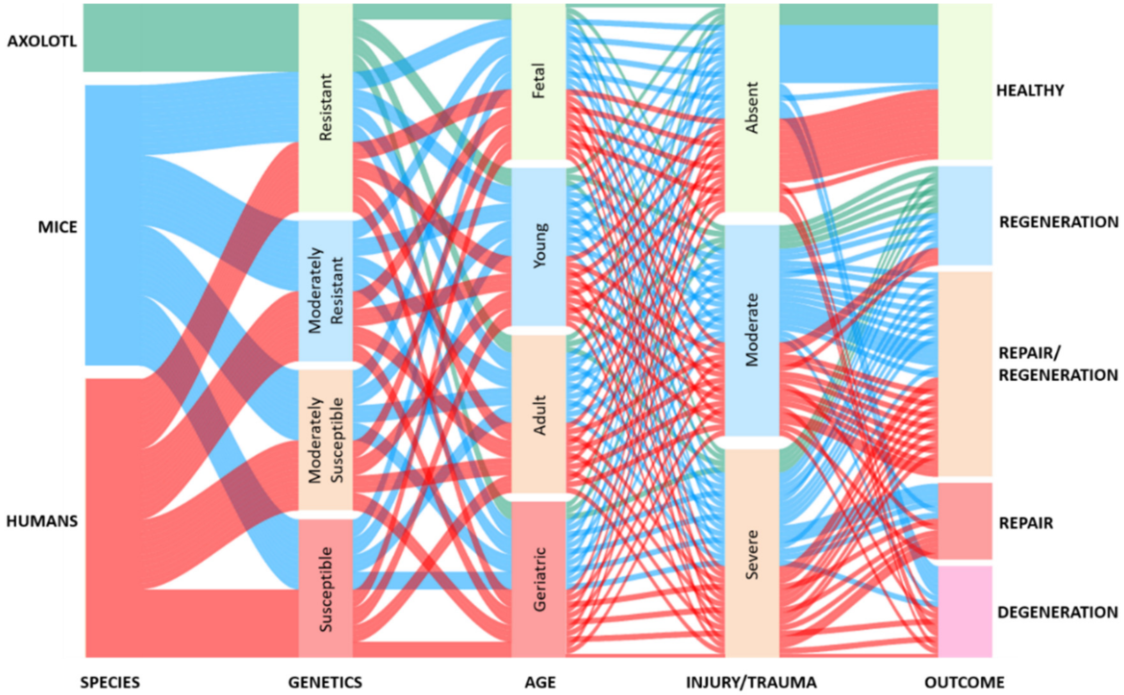
AXOLOTL
MICE
HUMANS
Resistant
Moderately Resistant
Moderately Susceptible
Susceptible
Fetal
Young
Adult
Geriatric
Absent
Moderate
Severe
HEALTHY
REGENERATION
REPAIR/ REGENERATION
REPAIR
DEGENERATION
SPECIES
GENETICS
AGE
INJURY/TRAUMA
OUTCOME

Figure 1.1. Factors influencing the regeneration and degeneration processes in cartilage. The roles of species, genetic and epigenetic traits, age, as well as the type and severity of the cartilage damage need to be considered in how this modulates the gradient of regenerative competence, homeostasis, and tissue degeneration.

Moreover, previous studies have reported that the rate of progression and severity of cartilage degeneration and OA-related changes in the joint differ among commonly used trauma-induced models (Glasson et al., 2007; Haase et al., 2019), such as destabilization of the medial meniscus (DMM) and anterior cruciate ligament transection (ACLT). In that sense, one might question whether the inability to protect against OA is driven by an overwhelmed endogenous repair response or the complete lack of any regenerative potential in the tissue. Another important consideration, often overlooked, is whether chondroprotective outcomes seen in OA pre-clinical studies are driven by inhibiting cartilage degeneration or enhancing cartilage regeneration, and if/how these factors may interrelate in the observed outcome. Despite the critical role that the balance between cartilage regeneration and degeneration plays in tissue maintenance and homeostasis, few studies (Deng et al., 2019; Jablonski et al., 2019) provide a comprehensive view of how specific treatments contribute to the prevention of cartilage degeneration, in the context of cartilage regeneration (or vice versa) within a given model system.

Therefore, in this review, we provide an overarching view of some of the key variables and their impact on cartilage tissue regeneration and degeneration. Also, we discuss how understanding the baseline of the endogenous regenerative capacity within pre-clinical models, and its modulation within a conducive environment is essential and should be integrated into the assessment of therapeutic approaches for cartilage injury and OA, in a context-specific manner.

1.3. Main text – factors influencing regeneration and degeneration of cartilage

1.3.1. Diversity of regenerative potential across animal models

While most tissues in mammals often fail to regenerate, as opposed to more primitive organisms such as amphibians, a certain inherent capacity to respond to injury is present. Regenerative competence after distal digit tip amputation, for instance, has been reported in mice (Dolan et al., 2018; Miller et al., 2019) and similarly in the fingertip of humans (Illingworth, 1974), and shown to persist to some degree into adult life (Vidal and Dickson, 1993). Yet, it remains unclear if fingertip regeneration like digit tip regeneration is mediated by blastema formation (Dolan et al., 2018), wherein mesenchymal precursors contribute to the multi-tissue regeneration. Endogenous appendage regeneration involving cartilaginous tissues has also been identified after through-and-through ear punches in different species (Clark et al., 1998; Gawriluk et al., 2016), and interestingly in the antlers of deer, which are known to regenerate periodically and naturally, as well as after injury or amputation (Price and Allen, 2004).

Various animal models have been employed in cartilage injury and OA-related studies, including mice, rats, guinea pigs, rabbits, dogs, and larger animals such as goats and horses (Chinzei et al., 2019; Chu et al., 2010; Frenkel et al., 2005; Guo et al., 2018; Matyas et al., 2004;

Teeple et al., 2013; Wayne Mcilwraith et al., 2011). Each animal model presents advantages and limitations in terms of their cost-benefit, suitability to mechanistic and molecular studies, and translational potential (i.e., relevance to human OA), all of which have been previously reviewed (Kuyinu et al., 2016; Teeple et al., 2013). However, diversity in regenerative potentials across and intra-species is also known to exist and can influence the outcome of cartilage-related studies.

Rabbits have been shown to possess robust intrinsic healing compared to humans, with previously reported wound regeneration of ear biopsy punch (Gawriluk et al., 2016; Goss and Grimes, 1972) and superior healing response to full-thickness cartilage lesions (Shapiro et al., 1993; Wei et al., 1997). Caution has also been advised on the use of mice and rats given their persisting open growth plates as adults (Chu et al., 2010), which possibly enhances the natural healing of articular cartilage. However, contradictory to such belief, age-related decline in the regenerative potential of cartilage has been demonstrated within rodents, including among different strains of mice (Eltawil et al., 2009; Matsuoka et al., 2015). Larger animals such as dogs and horses, on the other hand, seem to mimic the lack of intrinsic cartilage healing generally observed in humans, and thus are often considered as more appropriate models to evaluate the translational potential of clinical treatments for OA. Despite that, the genetic diversity within larger animals is regarded as a source of variability in cartilage repair studies (Chu et al., 2010), which possibly has wide-reaching implications on the outcomes. Therefore, unraveling the genetic/epigenetic differences that drive heterogeneity may help us understand why specific individuals are protected from OA, whereas others are more susceptible to its development.

While a comprehensive genome screening of the greater human population remains elusive, mouse studies can provide some insights into how genetic variations might be associated with OA resistance or vulnerability (Chinzei et al., 2019). Murine models are powerful tools in the investigation of specific genes related to mammalian tissue regeneration and degeneration, owing to the ease and sophistication of current genetic manipulations, abundant availability of recombinant inbred lines, and a broad-spectrum of cartilage regenerative potential among strains, from healers to non-healers (Rai and Sandell, 2014), to those displaying spontaneous cartilage degeneration (Poulet et al., 2013). Gaining a better understanding of model systems which display endogenous cartilage regeneration at the molecular/genetic level, for instance, can inform us why these processes are ineffective in non-healing model systems, often leading to the development of OA.

1.3.2. Effect of genetic makeup: spectrum from endogenous regeneration to spontaneous degeneration

Overall, few mammalian model systems demonstrate robust cartilage regeneration in vivo. In mice, it has been observed in the Murphy Roths Large (MRL/MpJ) strain, whose superior ability to regenerate cartilaginous tissue was first demonstrated in the ear pinnae after through-and-through punch wound (Clark et al., 1998) and later in the knee joint following a full-thickness cartilage defect (FTCD) (Fitzgerald et al., 2008). The Sandell group has demonstrated a strong correlation between auricular (ear) and articular (knee) cartilage regenerative abilities post-injury, as well as protection from OA (Rai et al., 2012) , such that the healing phenotype is associated with a heritable component. The parental strain LG/J, which shares 75% of MRL/MpJ genome, and the LGXSM-6 intercross, which shares 76% of LG/J genome, have also been found to exhibit similar regenerative abilities (Rai et al., 2012).

Subsequent studies showed that MRL/MpJ regenerative abilities extend to other tissues (Chadwick et al., 2007; Ueno et al., 2005), and more in-depth investigations provided insightful information regarding the mechanisms underlying its superior cartilage regeneration. Of note, disturbance of the cell cycle machinery including increased DNA damage and decreased levels of p21 protein, known as a critical cell cycle regulator, were identified in cells derived from MRL/MpJ mice. Later, the enhanced healing potential of through-and-through ear injuries was observed in *p21* knockout (*p21*$^{-/-}$) mice, suggesting the lack of *p21* is at least partially responsible for the enhanced regenerative phenotype seen in MRL/MpJ mice (Bedelbaeva et al., 2010). This has been further corroborated by recent findings implicating *p21* deletion in articular cartilage regeneration (Jablonski et al., 2021). However, the involvement of *p21* in other intricate cellular processes, such as apoptosis (Karimian et al., 2016) and inflammation (Mavers et al., 2012), in addition to its tight regulation, hinders our ability to elucidate the exact mechanisms associated with the healing phenotype seen after its deletion (Arthur and Heber-Katz, 2011). Overall, the molecular pathways controlling tissue regeneration within the abovementioned models remains unclear and of great interest in regenerative medicine.

More recently, multi-tissue regeneration has been identified in the African spiny mice (*Acomys*), including scar-free healing of auricular cartilage after ear biopsy punch (Seifert et al., 2012). Yet, no evidence of articular cartilage regeneration has been shown within this model to date. Notably, however, cell cycle regulation in progenitor cells was pinpointed as one of the key features separating regeneration after ear punches in *Acomys* from scarring in wild-type controls (Gawriluk et al., 2016). The same study revealed that a gradient of regenerative potential exists not only between species (healers and non-healers) but also within healer species, wherein ear pinna regeneration varied in closure rate and was likely influenced by factors such as sex and genetic variants (Gawriluk et al., 2016). While it is more natural to identify species that fall within the opposite ends of the healing spectrum, from fibrotic to regenerative responses, comprehending the differences that give rise to this healing continuum will greatly inform the design of targeted cartilage and OA therapies for humans.

In this context, understanding the processes leading to spontaneous OA pathogenesis and associated cartilage degeneration is just as important, since it is the most common form of OA in humans, affecting mainly elderly populations. Spontaneous cartilage degeneration has been reported in the Dunkin Hartley guinea pig (3 months old) (Jimenez et al., 1997), the commonly employed C57BL/6 mice with advanced age (> 17 months old) (Wilhelmi and Faust, 1976), and in the STR/Ort mouse (12 to 20 weeks of age) (Mason et al., 2001), which shares many similarities to the severity and progressive rate of joint deterioration that occurs in humans (Poulet, 2017). Age-dependent spontaneous degeneration has also been reported in larger species, such as dogs and horses (Kuyinu et al., 2016; Teeple et al., 2013). Despite recapitulating many of the patterns of disease progression described in human OA, spontaneous OA models present various challenges, such as longer experimental times and variable incidence and progression of OA between animals, likely owing to genetic variation. Moreover, aging brings about various changes in the molecular, cellular, and functional levels both locally in the joint tissues and systemically in the body, all of which can influence the dynamics of OA pathogenesis and may diminish the tissue's regenerative response.

1.3.3. Aging and the regenerative potential

The age of the animal is always an essential consideration, as it is generally agreed that younger animals have increased intrinsic cartilage regenerative potential compared to adults. Pre-clinical studies to date have demonstrated correlations between aging and regenerative decline within mammals (Matsuoka et al., 2015; Wei et al., 1997). Yet, the biological and molecular mechanisms responsible for enhanced regenerative competence at a younger age remains poorly understood. Joutoku *et al.* (2019) have recently studied the involvement of chemokines, namely the CCL21/CCR7 axis, in regulating cartilage regeneration at a younger age. Interestingly, juvenile mice deficient in CCR7 displayed significantly impaired cartilage healing post-injury (longitudinal full-thickness cartilage injury in the trochlear groove) compared to wild-type controls, while adult CCR7-deficient mice developed similar fibrocartilaginous tissue as controls in response to injury. Moreover, exogenous delivery of CCL21 ligand, whose transient expression had been identified at the injury site in juvenile mice, led to enhanced healing in adult rabbit after osteochondral defects

(Joutoku et al., 2019). Collectively, these findings suggest that this signaling pathway could be a promising target for the enhancement of adult tissue regeneration.

As for disease development, studies investigating correlations between spontaneous OA and aging have pinpointed the increase in senescent chondrocytes with age as an essential contributing factor to cartilage degeneration (Childs et al., 2015; Jeon et al., 2017; Zhou et al., 2004). Additionally, diminished chondrocyte activity and consequently reduced turnover of ECM components (Heinemeier et al., 2016; Rahmati et al., 2017), a diminished or dysfunctional pool of stem cells (Barry and Murphy, 2013; McGonagle et al., 2017), oxidative stress, and differential expression of pro-inflammatory cytokines and chemokines (Loeser, 2009) all seem to play a role in age-related OA. Some of these molecular features have also been shown in post-traumatically induced OA (PTOA) models (Coleman et al., 2018); however, there are few comprehensive studies exploring the synergistic effects of age and trauma, and how it influences response to treatment.

When comparing age paradigms in different strains of mice, it has been shown that OA severity in aged mice is greater than young mice following injury (Huang et al., 2017; Loeser et al., 2012; Usmani et al., 2016). Huang *et al.* (2017) described age-dependent structural changes post-trauma in the articular cartilage and subchondral bone of mice, with OA features appearing earlier and being more pronounced in the aged groups. Furthermore, Loeser *et al.* (2012) have previously reported that age also alters gene expressions in the whole joint, even in the absence of injury, highlighting this likely affects the tissue response after a traumatic event. Not surprisingly, old versus young animals have been shown to respond differently to intervention (Jeon et al., 2017; Usmani et al., 2016). For instance, selective removal of senescent cells that arise in the knee joint after traumatic-injury at 10-week old mice was shown to protect them from OA development, decrease pain and promote a pro-chondrogenic environment. In contrast, the clearance of senescent cells in aged mice (19-months old) was insufficient to overcome disease progression (Jeon et al., 2017).

Similarly, Usmani *et al.* (2016) explored the therapeutic potential of inhibiting TGFα, a growth factor previously implicated in OA pathogenesis, within the context of spontaneous and post-traumatic OA. The latter employed a DMM surgery model to induce cartilage injury in young (10-week old), as well as aged (6-month old) mice. The authors found that TGF-α deficiency did not protect mice from the development of spontaneous OA and that its effect in trauma-induced OA is age-dependent, whereby only young mice were protected from OA progression (Usmani et al., 2016). Ultimately, the etiology of human OA is highly complex, thus thoughtful consideration must be given to the species, age, and disease model chosen, including if it is spontaneous or post-traumatically induced, and how appropriate each one is for the exploration of specific human clinical subtypes.

1.3.4. Models of OA and cartilage damage

Research focusing on cartilage degeneration typically employs animal models of spontaneous or post-traumatic OA to elucidate the mechanisms of onset and progression of the disease (Table 1.1). As previously discussed, models of spontaneous cartilage degeneration primarily explore the effects of genetic traits and aging on the susceptibility to OA, whereas PTOA models typically induce cartilage degeneration by surgically producing joint instability and altering its regional distribution of loads (e.g., ACLT, DMM, meniscectomy). Although such approaches have provided valuable information on related risk factors, diagnostic biomarkers, and potential therapeutic targets, different models can promote distinct yet intertwined pathways leading to cartilage degeneration, thus influencing the study outcome. Haase *et al.* (2019) have recently compared two surgically induced PTOA models in C57BL/6 mice, specifically DMM and transection of the medial collateral ligament (MCL-MM). Mice that underwent MCL-MM demonstrated rapid and pronounced degradation of the collagen matrix component, with cartilage lesions being identified as early as 6-weeks post-surgery. By contrast, no cartilage lesions were seen for the duration of the assessment (12 weeks post-surgery) in the DMM model, which displayed slow OA progression, with proteoglycan loss over an extended period and identifiable collagen degradation by 8-weeks post-surgery (Haase et al., 2019). It is worth noting, however, that other studies have reported histological evidence of cartilage lesions after DMM surgery at earlier time-points (Fang et al., 2018; Huang et al., 2017; Liao et al., 2017; Loeser et al., 2012) than the one observed in this study, which might own to factors such as sex and age of the animals at the time of injury (Huang et al., 2017). That aside, even though mechanical destabilization serves as the initiating factor in both models, differences in the dynamics of molecular and structural changes, and associated progressive cartilage degeneration were distinct, which speaks to differential regulation of secondary mechanisms.

Of note, surgical models of PTOA are invasive, with the surgery itself inducing inflammation, and possibly degenerative changes in the joint environment, thereby diminishing our ability to understand the mechanisms underlying the disease phenotype. Therefore, non-invasive approaches mimicking PTOA have been developed, which involve mechanical overloading of the joint to induce cartilage lesions (Table 1.1). Some examples would be non-physiological cyclic compression and closed intra-articular tibial fracture (IAF) (Christiansen et al., 2012; Furman et al., 2007; Ko et al., 2013; Lockwood et al., 2014). Regardless of the initial trigger, divergences in the mechanistic aspects of progression and severity of degenerative changes have been shown in comparative studies involving surgical and non-surgical PTOA models across species and strains (Bapat et al., 2018; Hayami et al., 2006; Kamekura et al., 2005; Ko et al., 2013).

Table 1.1. Summary of most widely used osteoarthritis models and direct cartilage injury models with respect to their type/mode of action and most commonly employed species (Cope et al., 2019; Fitzgerald et al., 2008; Matsuoka et al., 2015).

CARTILAGE DEGENERATION	Osteoarthritis models			Commonly used species
	Spontaneous	Aging	Naturally occurring	Guinea Pig, Mouse, Dog
		Genetic	Genetically modified	Mouse
	Induced	Chemical	Collagenase	Mouse, Rat, Rabbit
			Sodium Monoiodoacetate (MIA)	
		Diet-induced	Obesity/Metabolic syndrome	Mouse, rat
		Post-traumatic (non-invasive)	Cyclic tibial compression	Mouse, Rabbit, Dog
			Intra-articular tibial fracture	
		Post-traumatic (invasive/surgical)	Anterior cruciate ligament transection (ACLT)	Rat, Rabbit, Dog
			Destabilization medial meniscus (DMM)	Mouse, Rat
			Meniscectomy	Mouse, Rat, Rabbit, Dog, Goat
CARTILAGE REGENERATION	Cartilage Injury Models			Commonly used species
	Induced	Longitudinal full-thickness cartilage defect (Matsuoka et al., 2015)	Osteochondral/Chondral defect - trochlear groove	Mouse, Rabbit
		Full-thickness cartilage defect (FTCD) (Fitzgerald et al., 2008)	Focal osteochondral defect - trochlear groove	Mouse, Rat, Rabbit, Dog, Horse

Other examples of induced OA models, yet non-traumatic in nature, include chemically and diet-induced models (Table 1.1). Chemically induced models rely on the injection of compounds that promote damage to cartilage components, compromising its function, whether by means of inflammation or toxicity (Bapat et al., 2018; Cope et al., 2019). Sodium monoiodoacetate (MIA) is one of the most widely used compounds as it promotes joint inflammation and chondrocyte death. While less invasive than surgically induced models, the rapid progressing degeneration induced by these compounds bares little resemblance to the pathophysiology of OA, thus they are more commonly employed for pain-related studies. Given the relevance of obesity and metabolic syndrome associated risk in the development of OA (Courties et al., 2015), efforts have been directed to understanding their effects on the incidence and pathogenesis of the disease. Diet-induced OA models, most typically performed in rodents, expose the animals to high-fat or high-fat/high-sucrose diet regimens. These models have been shown to successfully induce OA-like joint degeneration (Collins et al., 2018, 2015; Griffin et al., 2010) mainly driven by low-grade inflammation (Courties et al., 2015). In line with other studies, age has been shown as a contributing factor in diet-induced OA severity (Collins et al., 2020). It is interesting, however, that individuals from the same species have been reported to display distinct obesity phenotypes in response to diet-induced metabolic disturbance, and that their susceptibility or resistance can be associated with severity of OA-like knee damage (Collins et al., 2016; Griffin et al., 2010). However, the impact of obesity and low-grade inflammation displayed in these models on cartilage regeneration has not yet been characterized.

While it is broadly assumed that articular cartilage has little to no intrinsic repair at a population level, what if cartilage regeneration can outplace cartilage degeneration in some proportion of the population. This hypothesis is supported by results from previous clinical studies, wherein only about 50% of human patients that undergo cartilage or joint injury develop OA over time (Anderson et al., 2011; Lohmander et al., 2007). In this context, one might reasonably question whether the protection against OA in these individuals is driven by enhanced regenerative capability and/or muted degenerative response. Therefore, genetic background and the individual's baseline of endogenous regenerative capacity should be considered and controlled for when comparing outcomes post-injury. While this is inherently difficult to test in humans directly, preclinical mouse studies support this hypothesis.

Despite their genetic predisposition to the development of spontaneous OA, STR/ort mice are less prone to cartilage lesion formation after joint compressive overloading than CBA mice (Poulet et al., 2013), suggesting that inherent genetic risk of developing OA is not directly associated with susceptibility to trauma-induced cartilage damage. Interestingly, the "super-healer" MRL/MpJ mice are resistant to cartilage damage and show reduced severity of PTOA when compared to C57BL/6 mice, whether following surgical DMM (Deng et al., 2019) or non-surgical IAF (Ward et al., 2008). Similar results are seen in the LG/J strain (Chinzei et al., 2019), whereas p21$^{-/-}$ mice seem to be vulnerable to cartilage damage following DMM surgery (Hayashi et al., 2015), despite its superior regenerative potential after full-thickness cartilage injury (Jablonski et al., 2021).

Direct cartilage injury is commonly used to study the tissue regenerative potential by producing a partial or a FTCD, focally or longitudinally in the trochlear groove, that can reach into the subchondral bone (Table 1.1) (Fitzgerald et al., 2008; Joutoku et al., 2019; Roelofs et al., 2017). These models help examine the effect of genetic manipulations and exogenously delivered treatments, such as cell therapy and tissue-engineered constructs, on cartilage regeneration. Owing to the nature of their targeted site of injury, cartilage defect models allow for a straightforward revaluation of progressive tissue healing, although the relative size of injury in smaller species somewhat limits the comparison to the human condition.

As alluded to, models of direct cartilage injury and PTOA reflect the duality of cartilage regeneration and degeneration (Figure 1.2). In the context of direct cartilage injury, such as FTCD, one can investigate the mechanisms underlying the endogenous regenerative ability of a species/strain, as well as infer the efficacy of treatment of interest in enhancing cartilage regeneration. Conversely, when using an OA model, one can analyze whether the treatment of choice is capable of attenuating or preventing OA development and cartilage degeneration when compared to untreated controls.

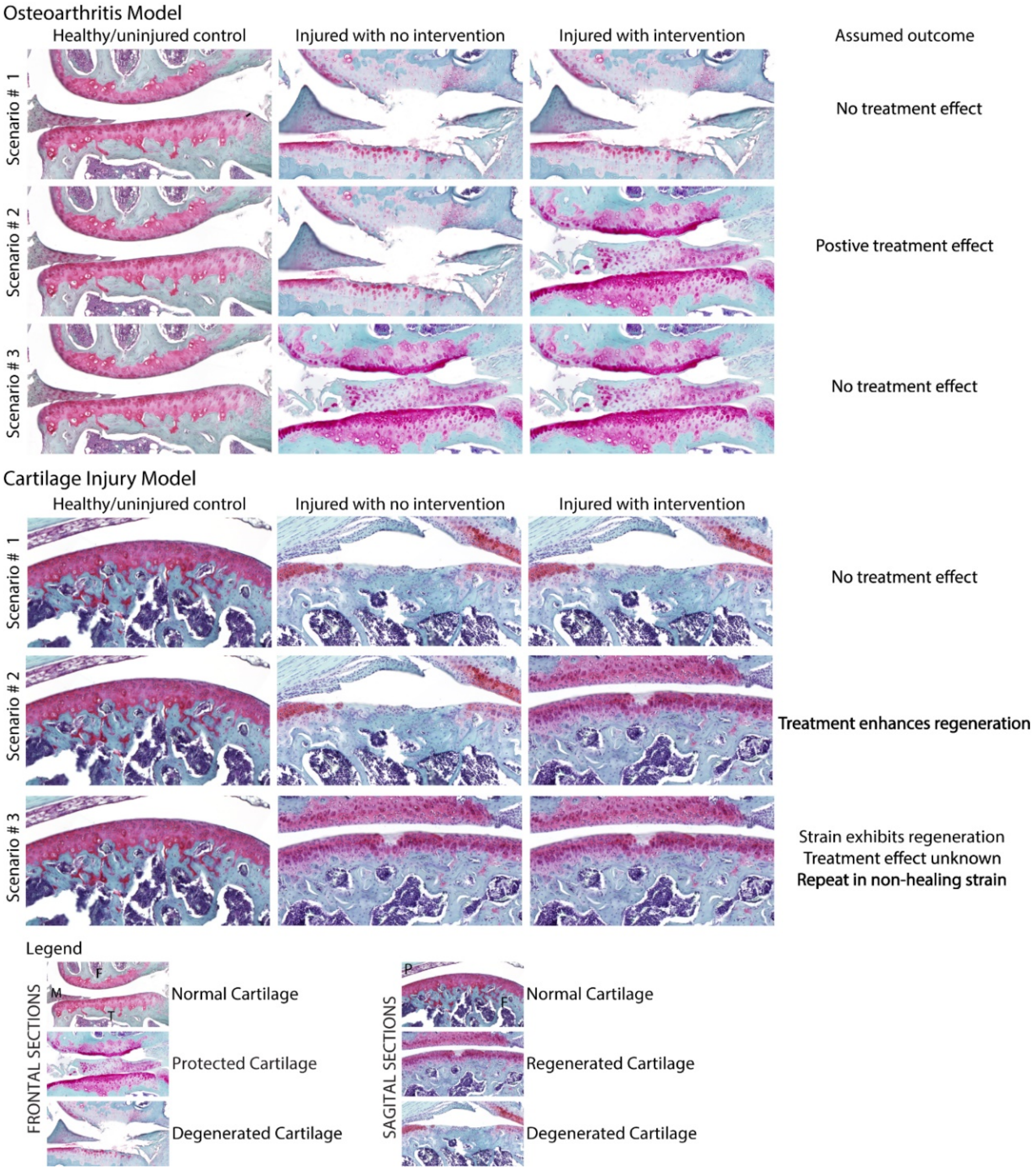
Osteoarthritis Model
Healthy/uninjured control
Injured with no intervention
Injured with intervention
Assumed outcome
Scenario # 1
No treatment effect
Scenario # 2
Postive treatment effect
Scenario # 3
No treatment effect
Cartilage Injury Model
Healthy/uninjured control
Injured with no intervention
Injured with intervention
Scenario # 1
No treatment effect
Scenario # 2
Treatment enhances regeneration
Scenario # 3
Strain exhibits regeneration
Treatment effect unknown
Repeat in non-healing strain
Legend
FRONTAL SECTIONS
F
M
T
Normal Cartilage
Protected Cartilage
Degenerated Cartilage
SAGITAL SECTIONS
P
F
Normal Cartilage
Regenerated Cartilage
Degenerated Cartilage

Figure 1.2. Assumed outcomes based on three different possible scenarios using an osteoarthritic model of PTOA or a FTCD cartilage injury model. In the context of indirect cartilage damage (OA model), one can analyze whether the treatment of choice is capable of attenuating or preventing OA development and cartilage degeneration (i.e., chondroprotection) when compared to untreated controls. However, the endogenous regenerative potential of the strain or species might interfere with the assumed outcome. Conversely, when using a direct cartilage injury model, one can investigate the mechanism underlying the endogenous regenerative ability, as well as to infer the efficacy of treatment of interest in enhancing cartilage regeneration.

However, to elucidate the biological mechanisms promoting a protective phenotype in the latter, it is necessary to understand whether the intervention inhibited degeneration and/or promoted regeneration of the cartilage. In which case, the causative role associated with an intrinsic healing potential and the chosen therapeutic intervention should also be investigated. Intra-articular injection of kartogenin, for instance, has been shown to protect mice against the development of OA following surgically-induced trauma (Johnson et al., 2012). Such outcome is likely due to a combinatory effect of enhanced regenerative response and chondroprotection, resulting from the modulation of endogenous stem cells and expression of chondrogenic factors, and the promotion of a conducive environment with decreased expression of catabolic enzymes, respectively (Cai et al., 2019; Johnson et al., 2012).

Recent studies investigating the involvement of chemokines and correlated inflammatory component in OA pathogenesis have linked the CCL2/CCR2 signaling axis, mainly known for its role in monocyte recruitment, to trauma-induced and age-associated OA phenotypes in humans and rodents (Hulin-Curtis et al., 2013; Kyostio-Moore et al., 2011; Li and Jiang, 2015). Interestingly, controversy remains regarding CCL2/CCR2 contribution to cartilage degeneration. Using a murine DMM model, Miller et al. found that while depletion of CCR2 improved pain associated outcomes, it did not protect CCR2$^{-/-}$ mice from cartilage degeneration (Miller et al., 2012). Expanding on these findings, Zarebska *et al.* (2017) reported similar outcomes due to ligand deficiency, with CCL2$^{-/-}$ mice showing decreased pain and comparable histopathological scores to CCR2$^{-/-}$ and wild-type controls after induced-PTOA. Yet, statistical significance was reached by 20- weeks following DMM in CCL2$^{-/-}$ mice, associated with less severe cartilage degeneration compared to the other mouse groups (Miotla Zarebska et al., 2017).

Likewise, *Raghu et al.* (2017) demonstrated that CCL2 deficiency was protective of cartilage degeneration, and promoted a significant decrease in macrophage infiltration, inflammation and expression of matrix-degrading molecules (Raghu et al., 2017). However, contradictory to previous findings, lack of CCR2 was also shown to mitigate mouse OA, whether through genetic inactivation of CCR2 or pharmacologic blockage of this receptor by a CCL2 antagonist (Raghu et al., 2017). Given such conflicting results, Jablonski and colleagues (2019) explored the association between the CCR2/CCL2 signaling axis and cartilage regeneration using the FTCD model of direct cartilage injury. Interestingly, the authors found that CCR2$^{-/-}$, but not CCL2$^{-/-}$ nor CCL2$^{-/-}$ CCR2$^{-/-}$ mice display enhanced cartilage regeneration following FTCD (Jablonski et al., 2019). Collectively, these results suggest that while depletion of CCL2 levels may inhibit cartilage degeneration (chondroprotective) it does not promote cartilage regeneration, whereas depletion of CCR2 is conducive of cartilage regeneration and likely associated with the controversial outcomes regarding chondroprotection post-trauma.

Overall, studies providing a comprehensive view of how specific treatments contribute to the prevention of cartilage degeneration, as well as to the enhancement of its regeneration are scarce; however, the previous examples highlight the importance that a combined analysis has in informing the outcome of targeted therapies for OA and cartilage injury (Figure 1.3).

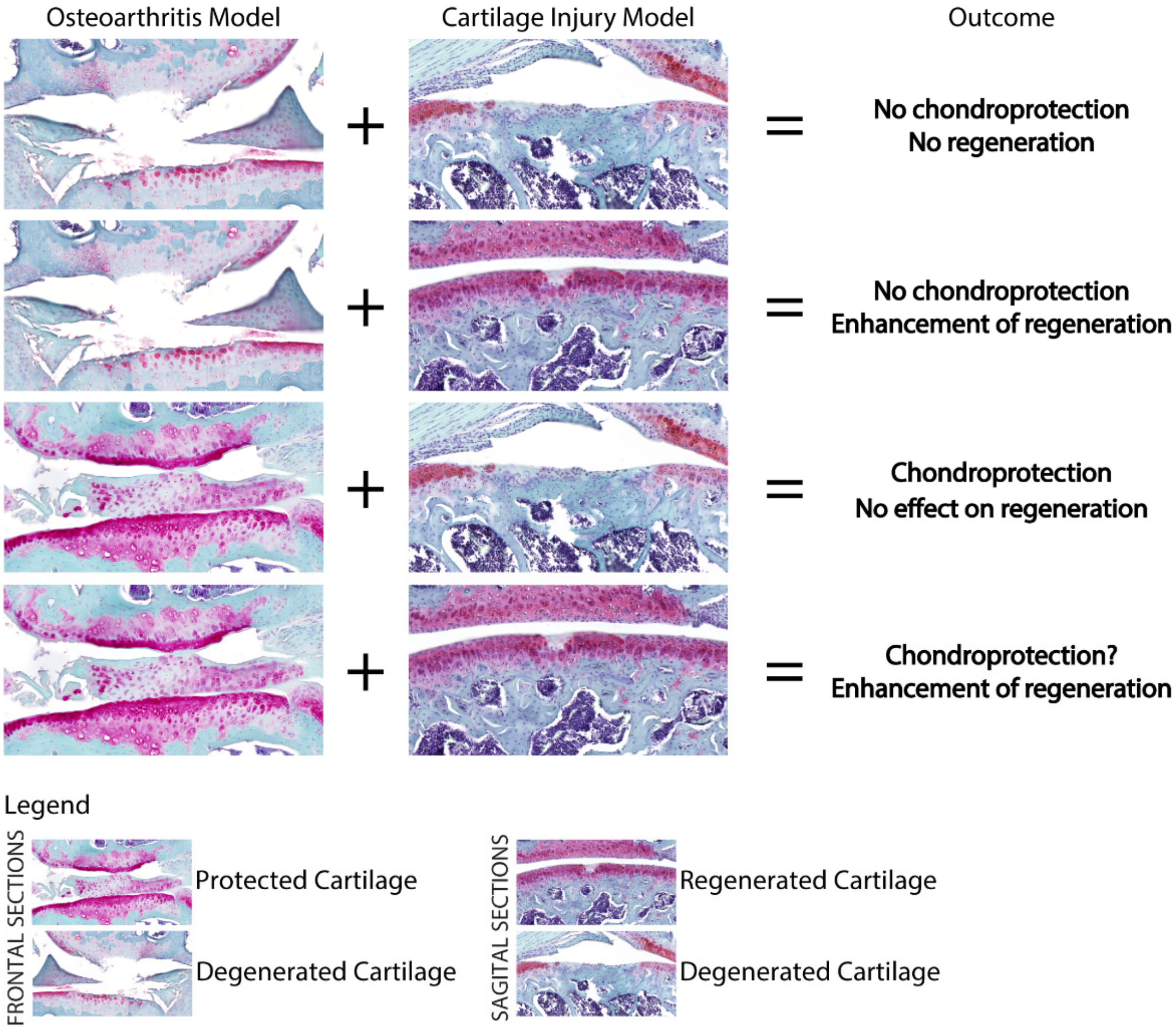
Osteoarthritis Model
Cartilage Injury Model
Outcome
+
=
No chondroprotection
No regeneration
+
=
No chondroprotection
Enhancement of regeneration
+
=
Chondroprotection
No effect on regeneration
+
=
Chondroprotection?
Enhancement of regeneration
Legend
FRONTAL SECTIONS
Protected Cartilage
Degenerated Cartilage
SAGITAL SECTIONS
Regenerated Cartilage
Degenerated Cartilage

Figure 1.3. Comprehensive view of the effect of targeted treatments in inhibiting cartilage degeneration and enhancing cartilage regeneration. The power of the combined analysis in informing the outcome of targeted therapies for OA and cartilage injury is greater than the one provided by the models isolation.

1.4. Conclusion

It is widely accepted that several risk factors can alter the progression of OA such as obesity, joint trauma, improper mechanical loading, and aging. A recent review by Mimpen and Snelling (2019) has suggested that heterogeneities in endotypes that predispose to OA onset and progression should be considered in patient selection and outcome assessment in clinical trials (Mimpen and Snelling, 2019). We suggest that the considerations highlighted in this review in terms of pre-clinical animal models may also apply to humans. There is a general belief that humans lack a regenerative response within the cartilage tissue; however, it remains unknown whether there is a gradient of regenerative competence within cartilage across the greater human population and how this might affect clinical outcomes. We are encouraged by recent findings on the topic, suggesting that the regenerative capacity of cartilage is variable and depends on where it resides in the human body, being more robust in the ankle joints (Hsueh et al., 2019). We believe it is plausible that a level of variation in endogenous regenerative response exists across patients as well, due to genetic traits or molecular mechanisms, and should also be considered in clinical studies and in the future clinical trials. In essence, a predisposition to cartilage regeneration might be present among patients that show a positive response to chondroprotective therapies. Hence, a thorough understanding of the role of treatment interventions on the dynamics of endogenous regenerative and degenerative responses may help us develop targeted and effective therapeutic approaches, wherein given a conducive environment, the regenerative stimuli can prevail among tissues and/or organs otherwise known as non-regenerative as is the case with OA.

1.5. Acknowledgements

Not applicable.

1.6. Author contributions

AOM and RJK contributed to the conception of the work; AOM drafted the work; RJK revised it critically for important intellectual content; AOM and RJK both provided final approval of the version to be published.

Chapter Two: Introduction

2.1. Knee joint anatomy

A well-functioning knee joint is critical for supporting body weight and facilitating pain-free mobility during common activities like walking, sitting, or using the stairs. The complex functional demands on this organ system are reflected in its intricate design and fulfilled by the combined effort of various structural components, including bone, cartilage, ligaments, muscles, and adjacent connective tissues (Norkin and Levangie, 2011). From an anatomical point of view, the knee joint consists of two articulating surfaces: the tibiofemoral and patellofemoral joints. The first is responsible for the articulation between the distal femoral condyles and proximal tibial plateaus (medial and lateral compartments), while the latter specifies the articulation between the patella and the femoral trochlear groove (Figure 2.1). The ends of these articulating skeletal surfaces are protected by a smooth and resilient cartilage layer, which is responsible for friction reduction and load bearing/distribution during joint motion (Buckwalter et al., 2005).

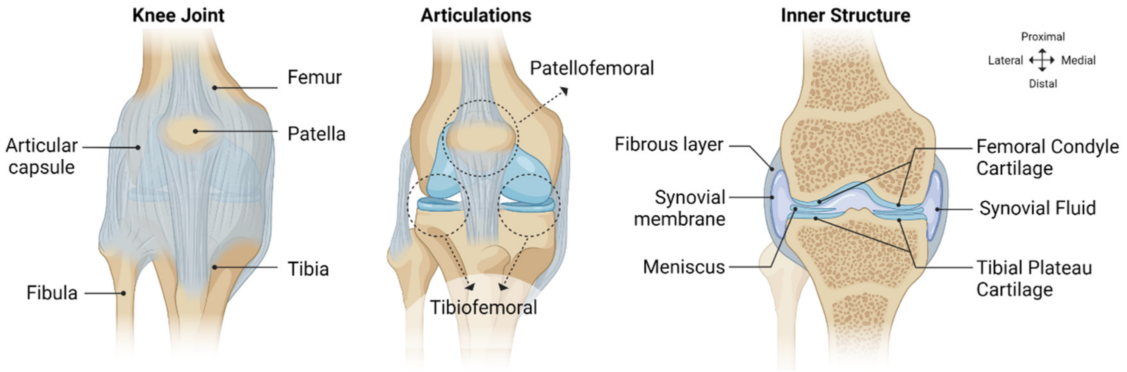
Knee Joint
Femur
Articular capsule
Patella
Tibia
Fibula
Articulations
Patellofemoral
Tibiofemoral
Inner Structure
Proximal
Lateral
Medial
Distal
Fibrous layer
Synovial membrane
Meniscus
Femoral Condyle Cartilage
Synovial Fluid
Tibial Plateau Cartilage

Figure 2.1. Knee joint anatomy. An articular capsule encloses the knee joint, which consists of two separate articulations: the patellofemoral (patella-femur) and the tibiofemoral (tibia-femur) joints. The inner surface of the articular capsule, known as the synovial membrane, secretes synovial fluid, a lubricating substance that helps reduce friction during joint movement. The medial and lateral compartments of femoral condyles and tibial plateaus face the joint cavity, and they are protected by a thin layer of articular (hyaline) cartilage, which provides a resilient, low-friction surface that plays a critical role in bearing and distributing loads across the joint during a lifetime of motion.

As a synovial joint, the knee is enclosed by an articular capsule composed of an outer fibrous layer lined by a synovial membrane, also known as synovium. Both articular cartilage and synovium surfaces face the joint cavity and are lubricated by a thin synovial fluid film, which also nourishes the avascular cartilage tissue and provides waste product removal (Levick and McDonald, 1995; Norkin and Levangie, 2011). In addition, menisci (fibrocartilaginous wedges) located over the medial and lateral tibial plateau surfaces help increase congruency with curved-shaped femoral condyles, thus improving joint stability and load distribution (Fithian et al., 1990; Masouros et al., 2010). Aside from the articulating surfaces, intra-joint and peri-joint ligaments, and other associated structures such as muscles and tendons, mainly contribute to knee joint stability, resisting forces and preventing abnormal movements.

Unfortunately, the contradictory mobility and stability requirements of the knee joint, added to the complex and interrelated nature of its structural components (Masouros et al., 2010), render it susceptible to damage and dysfunction. For instance, one or more knee tissues can become faulty or fail due to injury, improper mechanical loading, disease, and aging, having wide-ranging implications for overall joint health and function.

2.2. Osteoarthritis – burden of disease

Osteoarthritis (OA) is a musculoskeletal disorder that leads to disability and significant direct and indirect health care costs on a worldwide basis. In Canada alone, it affects over 4 million individuals aged 15 and older (Badley et al., 2021), which significantly impacts these individuals quality of life. The most affected joints by this disease are the hips, hands and knees (Hunter and Bierma-Zeinstra, 2019), and an estimated 86.7 million individuals (20 years and older) with incident knee OA worldwide in 2020 (Cui et al., 2020). OA places a huge economic strain annually, with total expenditure expected to escalate to 1.4 billion dollars in Canada by 2040 (Bombardier et al., 2011). This prediction considers healthcare system costs and indirect expenses, such as diminished productivity due to aging and associated comorbidities of the disease. OA burden is increasing exponentially, mainly due to our aging community, as well as increasing rates of obesity and joint injury. Considering this, the improvement in prevention and care strategies becomes even more relevant.

Despite the vast amount of research in OA, current treatments are unable to change the long-term outcome of this disease, promoting temporary and/or incomplete improvements in pain, function, and quality of life for patients. Important challenges in identifying solutions lie in the fact that various risk factors and structural changes have been associated with OA. The former include increasing age, sex, genetic factors, obesity, joint trauma, abnormal biomechanics, and systemic inflammation (Mahmoudian et al., 2021; Martel-Pelletier et al., 2016). Pathological changes in OA affect all joint tissues and involve structural alterations in articular cartilage, subchondral bone, and synovial membrane (Figure 2.2) (Hunter and Bierma-Zeinstra, 2019). Cells within these tissues are affected by and contribute to the initiation and/or progression of OA, but inevitably late stage OA results from progressive cartilage degeneration (Sandell and Aigner, 2001).

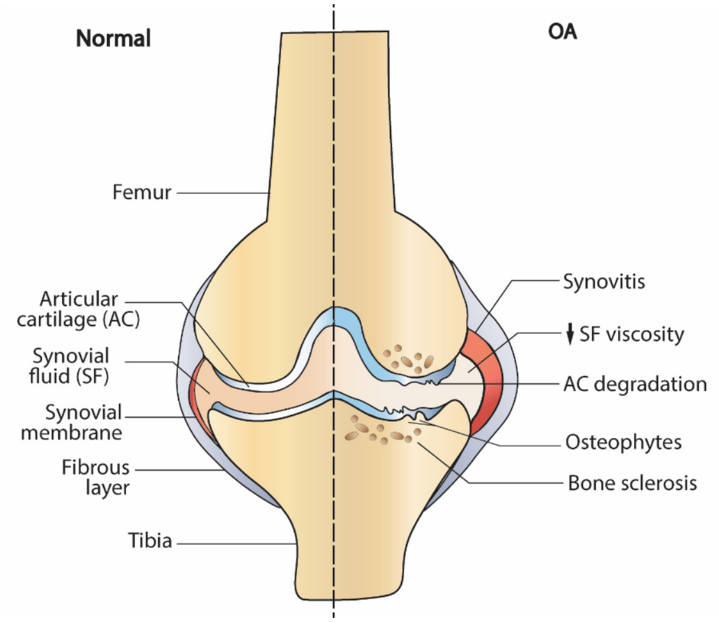
Normal
OA
Femur
Articular cartilage (AC)
Synovial fluid (SF)
Synovial membrane
Fibrous layer
Tibia
Synovitis
↓ SF viscosity
AC degradation
Osteophytes
Bone sclerosis

Figure 2.2. Comparative representation of a healthy and osteoarthritic knee joint. Structural changes include articular cartilage (AC) degradation, osteophyte formation, subchondral bone sclerosis and synovial inflammation, ultimately leading to joint failure.

Maintenance of a healthy articular cartilage is fundamental to pain-free mobility and skeletal function (Kinner et al., 2005). As discussed in Chapter 1, despite considerable advances in the field, effective and long-lasting therapeutic strategies to prevent or mitigate cartilage degeneration (chondroprotective) in connection with OA and promote native articular cartilage regeneration (chondro-inductive) remain elusive (Elhadad et al., 2022; Mimpen and Snelling, 2019; Muthu et al., 2023). These challenges relate, at least in part, to cartilage's avascular nature, low cellularity, and the complexity of its structure and composition, all of which contribute to its limited self-repair capacity. To develop novel therapeutic strategies for cartilage diseases and regeneration of this tissue, it is crucial to gain a comprehensive understanding of cartilage biology and its response to injury.

2.3. Articular Cartilage

2.3.1. Structure and Function

The structure and function of articular (hyaline) cartilage are intricately intertwined. Structurally, this specialized connective tissue has a small cellular component of chondrocytes that are dispersed in an abundant and unique ECM. The cartilage ECM has a high-water content (up to 80% of wet weight) owing to an environment rich in negatively charged proteoglycans, predominantly aggrecan (ACAN). ACAN is typically found as large aggregates non-covalently associated with a core filament of hyaluronan (HA) and contains numerous chondroitin and keratan sulphate glycosaminoglycan (GAGs) chains (Hardingham and Fosang, 1995). Fluid attraction by these negatively charged chains creates a swelling state that is restrained by the abundant network of collagen fibrils (mainly type II collagen), conferring strength and shape to the tissue and providing support and resistance to compressive, shear and tensile forces (Martel-Pelletier et al., 2008; Sophia Fox et al., 2009). As expected, a compromised collagen network and reduced proteoglycan content are two features that can alter cartilage’s ability to function and are associated with cartilage degeneration and OA (Cohen et al., 1998). The surface of articular cartilage is also comprised of non-collagenous proteins, such as proteoglycan-4 (PRG4, also known as lubricin), a mucin-like glycoprotein found within the synovial fluid and bound to articular cartilage surface (Schmidt et al., 2009). PRG4 expression in the joint is maintained by synoviocytes in the lining (intima) of the synovium and chondrocytes within the superficial layer of cartilage, providing lubrication to articulating surfaces and near frictionless joint motion (Coles et al., 2010; Jay et al., 2001). Despite the repetitive mechanical stress experienced by knee articular cartilage, the joint undergoes minimal frictional forces in physiological conditions, however, the absence of PRG4 results in an abnormal increase in frictional forces during joint motion, which increase shear stress, leading to collagen fibrillations and chondrocyte apoptosis (Jay et al., 2007; Waller et al., 2013) .

Over postnatal life, healthy articular cartilage acquires a characteristic depth-dependent zonal organization comprising the superficial, intermediate, deep, and calcified zones (Figure 2.2), which display histologic and phenotypic differences (Darling et al., 2004; Poole et al., 2001). The superficial zone is designed to resist high shear stresses, tension and facilitate frictionless gliding between juxtaposed surfaces. To facilitate this, chondrocytes in this zone produce biological lubricants HA and PRG4 (Decker et al., 2017; Jay et al., 2001), take on a flat/elongated appearance; align parallel to the surface; and are interweaved into a densely packed horizontal arrangement of collagen fibres. The intermediate zone is composed of larger and more randomly oriented collagen fibres and a high concentration of proteoglycans, mostly ACAN, which is distributed throughout the matrix and is an important mediator of cell-cell and cell-matrix cross-talk (Kiani et al., 2002). With the highest proportion in volume of uncalcified cartilage (40-60% of thickness), it provides load support, transfer and dissipation (Gahunia and Pritzker, 2020). Chondrocytes in this zone are rounder in appearance and lack an organized/patterned distributed in the matrix. As we move into the deep zone, chondrocytes become larger and organized into a columnar structure perpendicular to the surface, as is the collagen fibre network found in this zone (Darling et al., 2004). The transition from uncalcified to calcified zone is histologically delineated by a basophilic region, termed tidemark (Gahunia and Pritzker, 2020); however, knowledge regarding its developmental origin and patterning is limited (Rux et al., 2022). Lastly, the bottom calcified cartilage layer contains hypertrophic-like chondrocytes, constituting a transition area between uncalcified cartilage and underlying subchondral bone. Given the heterogeneity of composition and properties, the articular cartilage can be considered from a mechanical perspective, as a composite material (Mansour, 2013). Its molecular interaction and ultrastructural organization confer unique properties to the tissue that otherwise could not be achieved by any of its individual components.

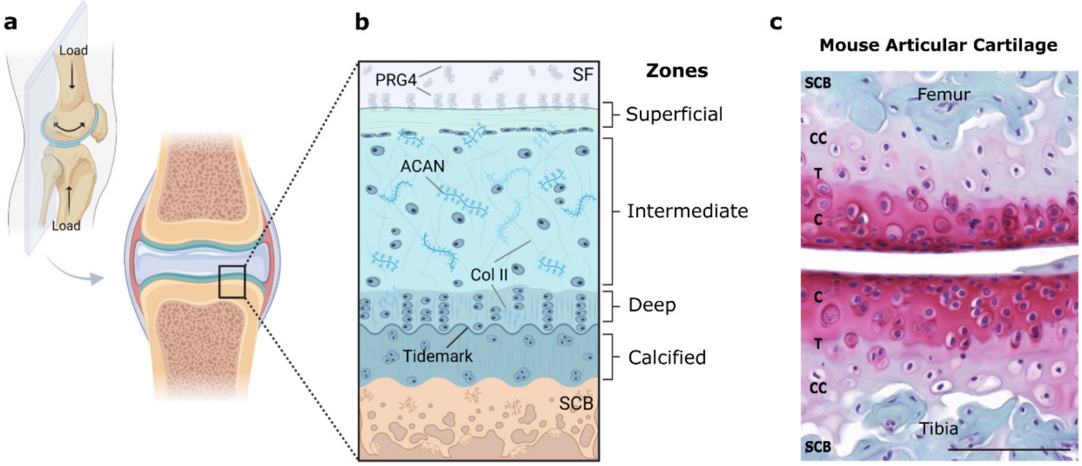

Figure 2.3. Zonal organization and variation within articular cartilage. (a) Articular cartilage is primarily subjected to compressive and shear stresses and thereby presents with a unique and specialized microarchitecture essential for proper tissue function in this mechanical environment. (b) Descriptively, articular cartilage can be subdivided into four zones (superficial, intermediate, deep, and calcified) based on cell and matrix constituents' variations throughout the tissue thickness. Note the parallel surface orientation of cells and collagen fibres in the superficial layer, contrasted with the vertical orientation and columnar cell arrangement attained at the deep layer, which is separated from calcified cartilage by the tidemark line. PRG4 - proteoglycan-4, SCB - subchondral bone, (c) Representative image of mouse articular cartilage non-calcified and calcified cartilage zones, Scale bar, 100 µm. C – uncalcified cartilage, CC - calcified cartilage, SCB - subchondral bone, T- tidemark.

While chondrocytes constitute a small percentage of tissue volume (humans about 2-5% and mice: about 20%) and display little to no proliferation, they are metabolically active and play a fundamental role in tissue maintenance and remodelling by directing the synthesis and upkeep of its matrix components

(Archer and Francis-West, 2003). These cells interact closely with the surrounding ECM, which transduces biomechanical signals to chondrocytes, consequently influencing their metabolic activity and survival (Buckwalter et al., 2005; Vincent et al., 2022). This interplay is hypothesized to be vital for tissue homeostasis; and multiple forms of insults, whether caused by intrinsic or extrinsic factors have been shown to result in tissue degeneration. This topic will be further explored on Chapter 4.

At the tissue level, mechanical stimuli play a vital role in cartilage health. Regular, moderate mechanical loading, as occurs with physical activity, enhances nutrient diffusion, and stimulates chondrocyte metabolism and matrix synthesis (Roos and Arden, 2016). Meanwhile, a lack of compressive forces acting upon the cartilage surface, due to immobilization or unloading, hinders fluid movement and nourishment to cartilage, leading to atrophy (Vincent and Wann, 2019). Conversely, abnormal loading, due to joint trauma or excessive use, can disrupt cartilage homeostasis, leading to increased matrix degradation by expression of proteases (aggrecanases - ADAMTS and metalloproteinases – MMPs) (Glasson et al., 2010; Haseeb and Haqqi, 2013; Lohmander et al., 2003; Miller et al., 2013; Morais et al., 2021), further escalating damage and consequently cartilage breakdown (Arokoski et al., 2000). This disrupts the balance of cartilage remodeling, tipping the scales towards extensive degradation of the cartilage (Sandell and Aigner, 2001). As part of this destructive cascade, chondrocytes undergo apoptosis, further impacting the production of matrix constituints and cartilage function (Sandell and Aigner, 2001; Thomas et al., 2007). This process is also observed during OA progression (Goldring and Goldring, 2016). Furthermore, systemic factors including genetics, age, and metabolism can also influence the health of articular cartilage. For example, advanced age is associated with a decline in chondrocyte function and an increased risk of cartilage degeneration (Loeser, 2009), as introduced in Chapter 1.

As previously mentioned, regeneration of articular cartilage is challenging due to the complex structural organization and composite nature of this tissue. Autologous chondrocyte implantation (ACI), osteochondral allograft transplantation (OAT), and microfracture (i.e., marrow-stimulating therapy) represent typical surgical approaches that aim to repair focal and/or full-thickness lesions, albeit with relatively poor tissue quality (Brittberg et al., 1994; Brody, 2015; Muthu et al., 2023; Zhang et al., 2009). Clinical translation of ACI and OAT approaches has proved challenging, mainly due to donor-site comorbidity (tissue is harvested from a non-load bearing region) and limited availability of donor tissue, respectively (Zhang et al., 2009). Microfracture, known as a marrow-stimulating technique, consists of the creation of holes into the subchondral bone that allows for the influx of blood and marrow stem/progenitor cells (Richardson et al., 2016). The rationale behind this approach derives from cartilage's poor healing ability being partially attributed to its avascularity, which impair the recruitment of stem/progenitor cells to the injury site (Huey et al., 2012; Richardson et al., 2016). However, the resulting repair tissue is often fibrocartilage, which does not possess the same load-bearing ability and therefore longevity. As result, in cases of extensive joint damage, joint arthroplasty is typically the most viable option for long-term relief and restoration of joint function, but is often considered a last resort because of the level of invasivness, lengthy-recovery and rehabilitation times and limited longevity of the prosthetic joint (Elhadad et al., 2022; Roos and Arden, 2016; Zhang et al., 2009).

Hence, despite functional benefits, current regenerative approaches are unable to restore the native tissue or normal function. Stem cells are unique in their ability to self-renew and to differentiate into a variety of cell/tissue types. Specifically, mesenchymal stem/progenitor cells (MPCs) can be expanded in culture and retain the potential to differentiate into bone, cartilage, and fat cells, potentially aiding in tissue regeneration. These characteristics have motivated the exploration of MPCs as an attractive alternative to cartilage regeneration, extending beyond their recruitment in microfracture technique.

2.4. Joint-resident mesenchymal stem cells

Stem cells and the idea of regenerative medicine have permeated our society in many ways, but perhaps more relevant to this thesis is the promise of disease treatment and tissue regeneration. Typically regarded as undifferentiated or unspecified cells, stem cells possess the ability to self-renew through cell division or give rise to daughter cells that can mature and differentiate into various cell types depending on the stem cell type and tissue of origin (Weissman, 2000). The functional potential of stem cells lies in their ability to generate various cell types (i.e., potency). At the highest level, known as totipotency, stem cells can give rise to an entire embryo and the necessary extraembryonic components to form a multicellular organism. However, as stem cells become more differentiated/specialized and/or lineage restricted, so do their cell progeny and tissue types that they can differentiate into (Balistreri et al., 2020). Pluripotent embryonic stem cells reside in the blastocyst (inner cell mass) and give rise to all three germ layers – ectoderm, mesoderm, and endoderm – that make up the adult organism. In contrast, adult (or somatic) stem/progenitor cells are generally multipotent, reside within many niches in adult tissues and typically present greater lineage restriction. Identified virtually in all tissues within the body, adult stem cells are generally rare populations and reside in a quiescence state. Upon an insult, for example, injury or stress signals, these cells can become activated and respond through proliferation, differentiation, and immunomodulation (Galliot et al., 2017; Wang et al., 2014; Weissman, 2000), frequently operating through transit amplifying/progenitor cells, to influence and/or directly contribute to tissue remodelling and wound healing outcomes.

MPC-resident pools have been described in various joint-associated tissues, including the bone marrow, synovial membrane and synovial fluid, and the infrapatellar fat pad (Koyama et al., 2008; Kozhemyakina et al., 2015; McGonagle et al., 2017; Roelofs et al., 2017). Nonetheless, the reasons why these progenitor populations seem to be ineffective in facilitating cartilage regeneration after an injury or in the case of OA remain elusive. Approaches using exogenous transplantation of expanded MPCs (predominantly from bone marrow), with or without scaffolds and/or growth factors, have shown promising results experimentally and in preliminary clinical trials; however, outcomes remain variable among clinical studies in patients, and evidence of long-term structural/functional restoration is limited (De Bari and Roelofs, 2018; Loebel and Burdick, 2018). Regardless of their source, the role MPCs play in regeneration and their potential benefits in cartilage healing, as well as the mechanisms involved in such processes, all remain unclear. Interestingly, results to date suggest that MPCs' contributions to cartilage repair, whether recruited or transplanted to the injury site, might be related to bystander effects, such as the release of trophic factors or immunomodulation (Wu et al., 2011), rather than actively undergoing differentiation and engrafting into the wounded tissue.

Lack of consensus within the field as to which surface antigens and/or lack thereof are necessary for characterization of MPCs has hindered their identification and isolation. Moreover, surface antigen expression varies with tissue source and can be influenced by culture conditions, thereby contributing to therapeutic outcomes variability (Kfoury and Scadden, 2015; Zhao, 2013). The basic criteria for isolation of human MPCs, as of now, encompasses plastic adherence under culture, multilineage differentiation into chondrocytes, osteocytes and adipocytes, as well as the expression of a panel of cell surface markers (CD90, CD105, CD73), while lacking expression of CD34 and lineage-specific markers, such as CD31 and CD45 (Dominici et al., 2006). In mice, MPCs are commonly marked using *Sca-1* (surface cell antigen-1) and/or *PDGRF-α* (platelet-derived growth factor-α); but, other endogenous markers have been proposed over the last few years, such as *LepR* (Leptin receptor) and *Prx1* (Paired related homeobox-1), with some overlapping of markers observed in sub-sets of these populations (Farahani and Xaymardan, 2015; Holmes and Stanford, 2007; Loder et al., 2023; Logan et al., 2002; Wilk et al., 2017; Zhou et al., 2014).

In 2019, quiescent-associated mesenchymal progenitors defined by the expression of Hypermethylated in cancer 1 (Hic1) transcription factor, were first described (Scott et al., 2019). Since then, *Hic1*$^{+}$ tissue-resident MPCs have been identified in other tissues, displaying a tissue- and context-dependent fate decision and contribution to remodeling processes.

2.5. Hypermethylated in Cancer 1 (*Hic1*)

Hypermethylated in Cancer 1 (*Hic1*) is well-recognized as a tumor suppressor, found epigenetically silenced (hypermethylated) in several human cancers (Fleuriel et al., 2009). Likewise, its genetic inactivation has been shown to enhance malignant tumor formation in mice within different tissues (Chen et al., 2004). Homozygous deletion is embryonically lethal and accompanied by developmental defects, including craniofacial and appendicular structures, underscoring the importance of *Hic1* during development (Carter et al., 2000). Its expression has been identified in mesenchyme of the sclerotomes during mouse embryonic development and in proximity to pre-cartilaginous condensation regions (Grimm et al., 1999), and it supports craniofacial and axial skeleton formation (Arostegui et al., 2023; Ray and Chang, 2020). Additionally, *Hic1*-positive cells have been found in different tissues within adult mice (Abbasi et al., 2020; Schreiner, 2010; Scott et al., 2019; Shah et al., 2022; Soliman et al., 2020). However, their role in homeostasis and outcomes after conditional deletion or injury-induced activation can vary significantly based on the tissue and environmental context, displaying both pathogenic (e.g., fibrotic scarring) and regenerative potential. Interestingly, the target genes of *Hic1*-encoded transcriptional repressors have been linked to differentiation, stress response and cell cycle regulation, including p21 and E2F1 (Dehennaut et al., 2013; Jenal et al., 2009). A previous study has demonstrated that *Hic1* expression overlaps with that of commonly used MSC markers (Sca-1, PDGFR-α, *Prx-1*) in different tissue compartments, including bone marrow (Nguyen et al., 2020; Shah et al., 2022; Soliman et al., 2020). Nonetheless, their role in cartilaginous tissue niches, and possible influence in maintenance/regeneration processes remain obscure. This will be the topic of investigation in Chapter 6.

2.6. Transgenic mouse models

Many of the studies investigating the cellular and molecular mechanisms of cartilage development, maintenance and disease employ murine models. As discussed in Chapter 1, this is partially due to the great availability of genetically modified strains (Jaisser, 2000; Saunders, 2011). Transgenic models allow us to interrogate tissue-specific cell populations, genes, and molecular pathways at different stages in life to better understand their involvement in homeostasis and pathological conditions, but also their role in tissue repair processes.

2.6.1. Cre/loxP system

The *Cre/loxP* system is a widely used technology for conditional gene deletion or expression in transgenic mice. Furthermore, it can be directed to specific tissues and temporally regulated. Essentially, Cre recombinase is an enzyme that can recognize a specific site in DNA known as *loxP* (34-bp) and in the presence of two *loxP* sites catalyzes their recombination, thereby deleting whichever DNA sequence is present in-between these sites (Deng, 2012; Kos, 2004). Likewise, this system can also be used to turn on a desired gene of interest. In this project, the construct contains a "STOP" sequence flanked by the *loxP* sites, which is placed upstream of the gene of interest (i.e., *loxP*-stop-*loxP*-gene of interest). Therefore, the gene of interest is not expressed until the stop sequence is excised by Cre activity (Deng, 2012). A cell/tissue-specific promoter can also be integrated into these constructs, meaning that the gene deletion or expression will be conditional and happen only in cells carrying the promoter, as the expression of Cre will be restricted to those specific populations (Saunders, 2011).

Temporal regulation can also be achieved in addition to tissue specificity. In this case, Cre is expressed in association with a modified estrogen receptor (ER) domain and sequestered to the cytoplasm, remaining inactive without a ligand. The enhanced ERT2 system allows for better control of Cre expression (Saunders, 2011). Upon the administration of an inducer (ER ligand), called tamoxifen (or its metabolite 4-hydroxytamoxifen), Cre can translocate to the nucleus and promote recombination, granting a conditional and inducible characteristic to the Cre/loxP system (Deng, 2012). Tamoxifen-inducible Cre recombination is advantageous because it allows one to study the function of genes in different stages in life, without adversely impacting the animal's embryonic developmental stages (Deng, 2012; Kos, 2004). In my thesis, I have utilized a number of different designs of transgenic mouse models, which enabled me to conditionally eliminate chondrocytes and globally disrupt *Prg4* gene expression, as well as label *Hic1*$^+$ cells and follow their lineage *in vivo*. Considering the existence of heterogeneous stem/progenitor cell populations within tissues, genetic techniques such as fluorescent labelling of cells constitute powerful tools as they enable lineage tracing of cells and the study of their behavior *in vivo* under diverse conditions.

2.7. Scope of Research

This thesis focuses on investigating microscale changes in the structure and function of articular cartilage in response to different insults to tissue homeostasis, which are considered to precede the initiation of OA (Figure 2.4). The goals of the data chapters of this thesis were:

1. To develop a reproducible biomechanical assay of mouse articular cartilage

2. To determine whether depletion of chondrocytes broadly within the articular cartilage compromises tissue mechanics and can initiate tissue degeneration;

   Hypothesis: *Genetically induced chondrocyte depletion by diphtheria-toxin expression will compromise the structure and function of the articular cartilage and lead to the development of osteoarthritis*

3. To investigate the spatiotemporal changes in morphology and biomechanics in the distal femur of adult *Prg4* deficient mice;

   Hypothesis: *Prg4 deficiency leads to abnormalities in distal femur morphology contributing to articular cartilage degeneration*

4. To determine the role of *Hic1*$^{+}$ mesenchymal progenitors and their progeny in the maintenance and repair of auricular and articular cartilage tissues, and whether their behavior can be biased towards a pro-regenerative outcome;

   Hypothesis: *Hic1 cells reside in both ear (auricular) and knee joint (articular) environments, contribute to scar-forming repair after injury, and E2F1 overexpression will enhance cartilage repair, promoting neo-cartilage formation with structural and mechanical properties that are comparable to the native cartilage*

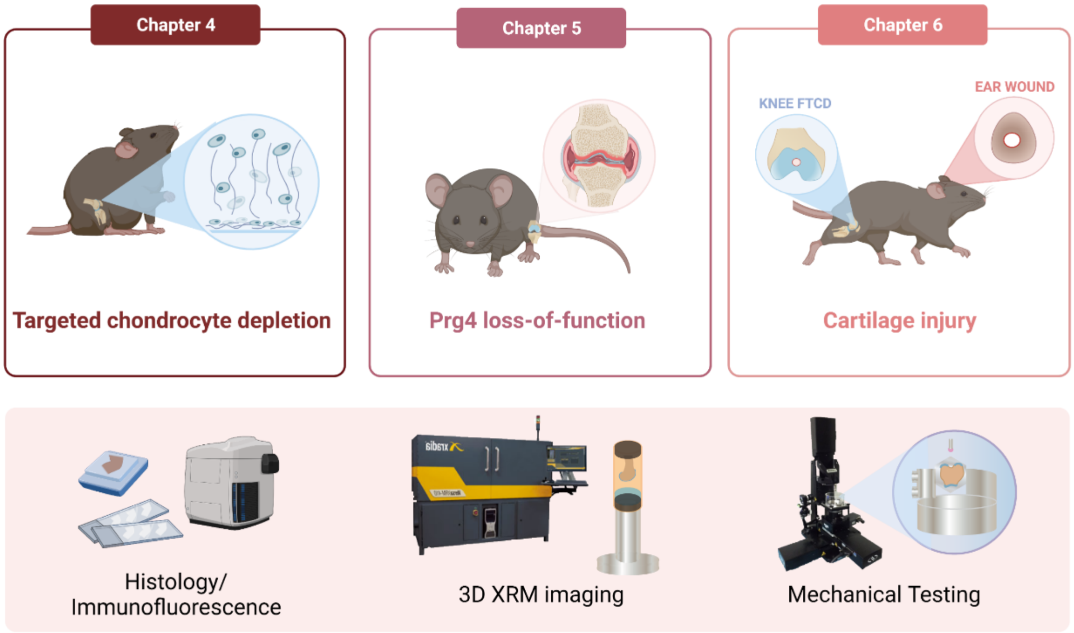
Chapter 4
Targeted chondrocyte depletion
Chapter 5
Prg4 loss-of-function
Chapter 6
KNEE FTCD
EAR WOUND
Cartilage injury
Histology/
Immunofluorescence
3D XRM imaging
Mechanical Testing

Figure 2.4. Schematic overview of transgenic mice and assay modalities employed in Chapters 4-6.

2.8. Acknowledgments

Graphical representations on Figures 2.1, 2.3 and 2.4 were created using BioRender.com.

Chapter Three: High spatial resolution analysis using automated indentation mapping differentiates biomechanical properties of normal vs. degenerated articular cartilage in mice

Masson A.O, Edwards W.B., Krawetz R.J. - Final version is available on eLife

My contributions to this work were as follows:

- *Contributed to experimental designs, performed all the experimental procedures and data analysis, except for XRM image processing (cartilage thickness).*
- *Conceptualized and created the manuscript figures and wrote the manuscript.*

3.1. Abstract

Characterizing the biomechanical properties of articular cartilage is crucial to understanding processes of tissue homeostasis vs. degeneration. In mouse models, however, limitations are imposed by their small joint size and thin cartilage surfaces. Here we present a three-dimensional (3D) automated surface mapping system and methodology that allows for mechanical characterization of mouse cartilage with high spatial resolution. We performed repeated indentation mappings, followed by cartilage thickness measurement via needle probing, at 31 predefined positions distributed over the medial and lateral femoral condyles of healthy mice. High-resolution 3D x-ray microscopy (XRM) imaging was used to validate tissue thickness measurements. The automated indentation mapping was reproducible, and needle probing yielded cartilage thicknesses comparable to XRM imaging. When comparing healthy vs. degenerated cartilage, topographical variations in biomechanics were identified, with altered thickness and stiffness (instantaneous modulus) across condyles and within anteroposterior sub-regions. This quantitative technique comprehensively characterized cartilage function in mice femoral condyle cartilage. Hence, it has the potential to improve our understanding of tissue structure-function interplay in mouse models of repair and disease.

3.2. Introduction

The articular cartilage in synovial joints has a specialized three-dimensional (3D) structure and biochemical composition that provide low-friction, wear-resistance, and load-bearing properties to the tissue. Mechanical loading is essential to tissue homeostasis and influences gene expression, chondrocyte metabolism, extracellular matrix maintenance, and associated interstitial fluid permeability (Grodzinsky et al., 2000; Vincent and Wann, 2019). Therefore, the biomechanical properties of cartilage are unique indicators of tissue homeostasis versus degeneration. Indeed, research into cartilage-related changes during the development of degenerative diseases such as osteoarthritis (OA) has demonstrated that early tissue dysfunction involves loss of proteoglycans and increased water content, resulting in reduced compressive strength and higher tissue permeability (Setton et al., 1994; Stolz et al., 2009). Disease progression leads to further structural damage and altered mechanics (Kleeman et al., 2005), ultimately resulting in tissue failure.

Mouse models are commonly used in pre-clinical studies focused on cartilage repair and pathophysiology of OA (McCoy, 2015). Mice are advantageous because of the well-established development of genetically modified strains (Helminen et al., 2002) and the availability of diverse model systems mimicking mechanisms of spontaneous and induced tissue degeneration and regeneration (Bedelbaeva et al., 2010; Christiansen et al., 2015; Kyostio-Moore et al., 2011; Murphy et al., 2020). In this regard, mouse models serve as powerful tools for the targeted assessment of cellular and molecular processes, and the discovery of novel therapeutics related to cartilage regeneration and OA. Yet, while the structural integrity and biochemical composition of murine cartilage are routinely assessed through histological and molecular approaches, the evaluation of how these features translate into mechanical function is limited. The main challenge in mechanical function assessment stems from the small joint size and thin cartilage found in mice relative to other species (Malda et al., 2013). Prior efforts to overcome these challenges include finite element modeling and optimization of small-scale indentation techniques (Berteau et al., 2016; Cao et al., 2006; Das Neves Borges et al., 2014; Stolz et al., 2009).

Mechanical indentation (including atomic force microscopy [AFM] techniques), performed using either creep or stress-relaxation protocols, is widely employed for assessing the biomechanical behavior of cartilage and OA-related changes in many species (Athanasiou et al., 1991; Hoch et al., 1983; Risch et al., 2021) and considered the gold standard for small animal joints (Lakin et al., 2017). Unlike confined and unconfined compression tests, no sectioning or subsampling of tissue (i.e. cylindrical explants) is required (Mansour, 2013). Instead, the cartilage tissue and its subchondral bone interface is kept intact, providing more physiologically relevant data. Indentation is also advantageous in that it is non-destructive and allows for repeated measures in situ (Lu and Mow, 2008). However, the natural curvature of joint articular surfaces poses a challenge to testing, as indentation must be conducted perpendicularly to the surface (Swann and Seedhom, 1989).

Recently, a novel automated indentation technique has been developed for the mechanical assessment of cartilage (Sim et al., 2017). This commercially available multi-axial apparatus (Mach-1, *Biomomentum Inc,* Laval, QC) is capable of detecting specimen surface orientation at each position of measurement and subsequently indent normal to the surface (Biomomentum, 2020; Sim et al., 2017). As such, it can map entire cartilage surfaces using a single setup with high spatial density and has been previously shown to discriminate between healthy and diseased human cartilage samples (Seidenstuecker et al., 2019; Sim et al., 2017). This apparatus has been recently employed by Woods and colleagues (Woods et al., 2021) to evaluate altered biomechanics in a mouse model of cartilage degeneration. However, the study was conducted in the non-load-bearing region of the mouse knee joint. Considering that the knee range of motion in mice is between 40 and 145° (i.e. unable to fully extend) (Jia et al., 2018), with normal gait range between 90.5 and 120° (extension-flexion) (Hu et al., 2017), the contact regions in the distal femoral condyles are located further posteriorly. Careful consideration of species-specific differences in knee joint anatomy and kinematics is imperative for proper translation of pre-clinical models (Oláh et al., 2021).

Woods and colleagues (2021) were also unable to account for site-specific cartilage thickness variations in their measurements, instead of using the mean cartilage thickness obtained via histological analysis in their assessment (Woods et al., 2021). Other studies have employed mean cartilage thickness values retrieved through histology or imaging techniques to characterize and model tissue mechanical parameters in mice (Cao et al., 2006; Das Neves Borges et al., 2014). Implicit in this approach is the underlying assumption that cartilage thickness is relatively uniform among medial and lateral compartments (e.g. femoral condyles or tibial plateaus), and along their anteroposterior or mediolateral axis. Yet, regional variations in thickness are recognized within these cartilage surfaces (Das Neves Borges et al., 2014; Li et al., 2005; Malda et al., 2013) and known to impact small-scale indentation measurements (Hayes et al., 1972; Swann and Seedhom, 1989).

Hence, the purpose of this study was to investigate the reliability of automated indentation mapping in the assessment of healthy femoral articular cartilage in mice and characterize site-specific variations in cartilage thickness. We also employed concurrent contrast-enhanced 3D x-ray microscopy (XRM) imaging to validate the cartilage thickness measurements from our optimized needle probing (NP) protocol (Jurvelin et al., 1995). Finally, this approach was used to investigate biomechanical differences in a clinically relevant mouse model of cartilage degeneration (Rhee et al., 2005). Together, we show that automated indentation is reliable and able to characterize topographic and mechanical variations across condyle cartilage locations in intact cartilage. Moreover, this technique was able to identify regional changes in cartilage thickness and stiffness in degenerated cartilage. A comprehensive and standardized biomechanical evaluation of cartilage in repair and disease can greatly contribute to our understanding of tissue structure-function interplay, thereby enhancing the clinical relevance of mouse models in this area.

3.3. Materials and Methods

3.3.1. Animals

Male C57BL/6 mice were purchased from Jackson Laboratories (Bar Harbor, ME). Animals were housed under a standard light cycle and had free access to feed (standard diet) and water. Ten mice were euthanized at 16 weeks of age, and hindlimbs (*n* =10 right and *n* = 5 left) were harvested for biomechanical testing and/or 3D XRM imaging. Age-matched PRG4 knockout mice ($Prg4^{-/-}$, *n* = 6) were generated and maintained on a C57BL/6genetic background, as previously described (Abubacker et al., 2019). Limbs were disarticulated at the hip, followed by transection of the ligaments and careful isolation of distal femurs from tibiae and menisci with the help of a dissection microscope (Leica). Femurs were preserved gently wrapped in Kimwipe soaked in phosphate-buffered saline (PBS, pH 7.4) until the time of assessment. All samples were mechanically tested no longer than 3 hr after dissection to prevent tissue degradation. Contralateral legs, not subjected to biomechanical testing were preserved in 10% neutral buffered formalin (NBF) solution for 24 hr and stored in 70% ethanol for 24hr to 48 hr before imaging.

3.3.2. Automated indentation mapping

The shafts of isolated femurs were glued into a 0.1–10 µL pipette tip (VWR, USA) using cyanoacrylate adhesive, fixed into a stainless-steel hex nut (Paulin, Model 848–216) and secured to the sample holder (Figure 3.1, Figure S3.1). This customized setup allowed for simple and proper positioning of the sample, exposing the load-bearing region of the condyles (Jia et al., 2018) for data acquisition, as well as non-destructive retrieval of samples after testing, such that subsequent XRM imaging could be carried out. A standardized mapping grid (*n* = 31 positions) was superimposed on an image of the cartilage surface, consisting of 14 and 17 measurement sites at the lateral and medial condyles, respectively (Figure 3.1A). The testing chamber was filled with PBS solution at room temperature, and the tissue was allowed to equilibrate before testing. Automated indentation mapping under stress-relaxation was then performed using the Mach-1 v500css (Biomomentum Inc, Laval, QC) device, equipped with a calibrated multiple-axis load cell (±17 N, 3.5-mN force resolution) and associated software. At each testing site (XY coordinates), height and surface orientation were identified using four surrounding contact coordinates (front, back, left, and right) in a 0.075-mm scanning grid. Then, by concurrently moving Mach-1 stages in all three-axis at different speeds, indentation can be performed along a virtual axis normal to the surface. As per manufacturer's recommendation, contact regions for surface angles ≥ 60° were considered unreliable and thus discarded. In this study, a spherical indenter (0.3 mm in diameter) was driven into the cartilage to a depth of 20 μm over 1 s followed by a 90-s hold-time. For C57BL/6, a total of three indentation mappings were performed per sample, approximately 45 min apart. Data reported consist of peak force and instantaneous modulus, as determined by fitting the Hayes et al., 1972 elastic model to the load-displacement curves at 20% strain. Assessment of how well the model fit the resulting curve per test site was done using RMSE. Since the analysis per position across specimens and genotypes reflects deviations due to anatomical positioning, calculated parameters were compared between lateral (Lat) and medial (Med) femoral condyles, as well as on four condylar sub-regions (Lateral/Anterior - Lat/Ant, Lateral/Posterior – Lat/Post, Medial/Anterior - Med/Ant, and Medial/Posterior - Med/Post), each containing at least five positions of measurement (Figure 3.1A).

3.3.3. Needle probing – thickness measurement

After indentation mapping, the spherical indenter was replaced by a 30Gx1.4" hypodermic needle (TSK Laboratory, Japan) adapted to the 1-mm spherical indenter (Biomomentum Inc, Laval, Canada) (Figure S3.2). Automated thickness mapping (Figure 3.2A) was performed on the same knee cartilage surface using the NP technique (Jurvelin et al., 1995), thickness was measured on 31 sites located adjacent to those previously identified for the indentation mapping, while keeping the relative distance between testing sites (or overall distribution grid) the same. The needle was driven vertically into the cartilage surface at a constant speed until a 0.5-N stop criteria was reached in the subchondral bone. The cartilage surface and cartilage/subchondral bone interface positions were identified in the load-displacement curves (Figure

3.2B) generated at each measurement site using the automatic mode of analysis (Biomomentum, 2020). A 0.25-N/s loading limit was defined to identify the interface position. Manual correction was employed when the algorithm failed to identify the inflection point (Biomomentum, 2020). The cartilage thickness reported corresponds to the vertical needle displacement from cartilage surface to subchondral bone multiplied by the cosine of the surface orientation angle (Figure 3.2B) as determined during automated indentation for each position. After testing, samples were preserved in 10% NBF solution for 24 hr and stored in 70% ethanol for 24hr to 48 hr before imaging.

3.3.4. 3D XRM imaging

3D XRM imaging was used for non-destructive assessment of cartilage morphology. Fixed femurs were incubated for 16–18 hr in 1% phosphotungstic acid (PTA) solution at room temperature for cartilage contrast enhancement before imaging (Das Neves Borges et al., 2014). Samples were enclosed onto a custom specimen chamber, with 1% PTA in 70% ethanol added to the chamber's bottom to minimize tissue dehydration. Zeiss Xradia 520 versa (Carl Zeiss X-Ray Microscopy, Pleasanton, CA) scans of each distal femur were obtained following previously described protocol (Jablonski et al., 2021; Richard et al., 2020). In brief, high-resolution scans of 2001 axial slices were acquired at a 4.39-µm voxel size, with low-energy (40 kVp voltage, 3 W power) x-rays.

3.3.5. Imaging processing

The contrast-enhanced cartilage surface was segmented by determining a threshold intensity, thereby delineating the femur scan into cartilage and subchondral bone voxels. For contralateral distal femurs (*n* = 5) that did not undergo biomechanical testing, a connected components filter was used to separate the medial and lateral condyles. The thickness transform was computed for each condyle, and the mean thickness was taken as the statistic of the thickness distribution (Hildebrand and Rüegsegger, 1997). For right hindlimbs, subjected to biomechanical testing, NP left a physical deformity in the articular cartilage of the right femurs visible on XRM imaging (**Figure 3.2A**), allowing for all 31 ROIs corresponding to NP to be manually landmarked. Landmarks were placed manually using the two-dimensional axial, sagittal, and coronal planes centered along the cartilage thickness and within each NP site. Cartilage segmentations were corrected manually to ensure the cartilage mask encompassed resulting volume gaps at NP positions. Then, the segmented cartilage was masked by a sphere of radius 75 µm placed on each landmark, leaving a thin disk of cartilage. The thickness transform was computed for each disk (Hildebrand and Rüegsegger, 1997) and the mean thickness values, taken as a statistic of the thickness distribution, were used to minimize variability due to morphological changes in the cartilage caused by the mechanical testing. Image processing was performed in SimpleITK (Lowekamp et al., 2013; Insight Software Consortium, v1.2.4), and morphometry was performed in Image Processing Language (IPL v5.42, SCANCO Medical AG, Brüttisellen, Switzerland).

3.3.6. Statistical analysis

Analyses were performed in GraphPad Prism software (version 9), $\alpha = 0.05$ was considered statistically significant. Continuous parameters are reported as mean values and corresponding standard deviations (SDs). Normality was assessed by Shapiro-Wilk normality test. C57BL/6 peak load and thickness data were analyzed by Student *t* test or ANOVA, with Bonferroni post hoc comparisons. To assess differences in biomechanical properties between genotypes non-parametric Mann-Whitney U test with *Bonferroni-Dunn's* correction was used. To test reliability and absolute agreement between repeated measurements, SPSS 27 (IBM, Chicago, IL) was used to obtain single-measurement, two-way mixed effect intraclass correlation coefficient estimates and respective 95% limits of agreement (Koo and Li, 2016; Müller and Büttner, 1994). When assessing cartilage thickness measurements between NP and XRM imaging techniques, *Pearson* correlation coefficient (R) was used for method-comparison and Bland-Altman analysis to assess bias between methods.

3.4. Results

3.4.1. Automated indentation mapping reliability

While previous studies have employed indentation mapping on mouse cartilage, to our knowledge none has reported on its precision and test-retest reliability. Therefore, we performed three repeated mappings of 31 predefined positions distributed over the femoral condyles of ten C57BL/6 mice (Figure 3.1A) to assess the reliability of the automated surface indentation technique. The setup was developed and optimized (Figure S3.1) to assess the load-bearing regions of the femoral condyles and achieve non-destructive retrieval of specimen post-testing for subsequent 3D XRM imaging analysis. The imposed step deformation (i.e. indentation depth) on the femoral cartilage yielded typical stress-relaxation behavior, characterized by a sharp increase in force followed by gradual relaxation over time until equilibrium (Figure 3.1B). Assessment of stress-relaxation and corresponding force-displacement curves (Figure 3.1B) demonstrated consistency among repeated measurements for single positions and visible differences in peak reaction forces between condyles. These observations were further evidenced by the spatial distribution of peak force values across condylar testing sites (Figure 3.1C, Table 3.1). A total of 930 indentation measurements were retrieved, out of which only 21 produced atypical curves (7 testing sites at specimen's periphery with higher angles yielded noisy signals, Figure 3.1C), representing a 2.26% error rate during data acquisition. High reliability and absolute agreement between repeated measures for individual testing sites were observed, with 4.7% intra-assay average coefficient of variation (Table 3.1) and intraclass correlation coefficients – ICC (lower 95%, upper 95%) – ranging from 0.974 (0.966, 0.981) for the lateral condyle to 0.971 (0.963, 0.978) for the medial condyle. Mean peak force values illustrate site-specific variations within and between condyles (Figure 3.1D). The lateral condyle values varied significantly per position ($p<0.0001$), ranging from 0.07 to 0.15 N and showed a trend for higher values at outermost positions, with a slight decrease in force posteriorly. The latter was also seen for the medial condyle, wherein heterogeneities in peak force were apparent ($p<0.0001$) and had a wider range – from 0.15 to 0.294 N. Since the analysis per testing site also reflects inherent deviations due to anatomical positioning across specimens, data was pooled for regional (between condyles) and sub-regional (between and within anteroposterior locations) comparisons.

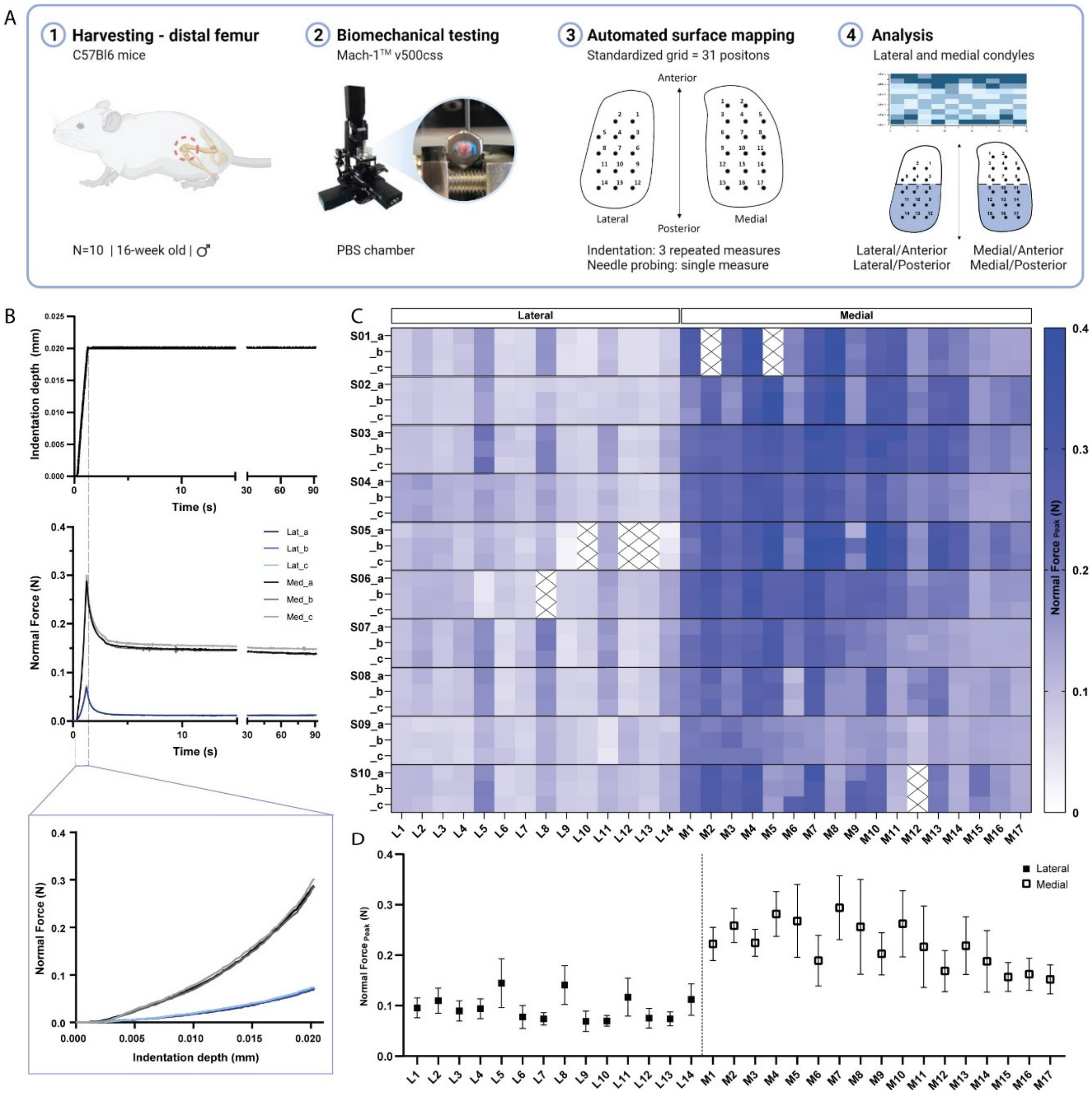

Figure 3.1. Indentation mapping of murine articular cartilage. (A) Schematic overview of experimental design employed for biomechanical testing of murine articular cartilage using Mach-1 v500css mechanical tester. (B) Step displacement used for cartilage indentation (top), with typical force-relaxation response curves obtained for three repeated measures on representative lateral and medial condyle positions (middle) and corresponding force increase with indentation depth (bottom). (C) Normal peak force recorded for all three repeated measures (A-C), considering each of the 31 testing sites, L1-L14 at lateral condyle and M1-

M17 at medial condyle, for each specimen (n=10), (S01–S10), demonstrates general agreement for intra-specimen measurements on both condyles. (D) Mean peak force values varied within and between condyle locations and higher within medial condyle testing sites. Data is presented as mean ± SD.

Table 3.1. Mean peak force ($\bar{X}$: N) and coefficient of variation (CV: %) from triplicate measurements for each of the 31 positions (L1-M17) of assessment over mice femoral condyles.

	S01		S02		S03		S04		S05		S06		S07		S08		S09		S10	
	$\bar{X}$	CV	$\bar{X}$	CV	$\bar{X}$	CV	$\bar{X}$	CV	$\bar{X}$	CV	$\bar{X}$	CV	$\bar{X}$	CV	$\bar{X}$	CV	$\bar{X}$	CV	$\bar{X}$	CV
L1	0.08	2.9	0.08	3.0	0.10	4.1	0.13	1.8	0.09	12.1	0.10	2.7	0.10	4.9	0.09	3.3	0.07	1.5	0.11	0.2
L2	0.11	1.3	0.09	2.5	0.10	2.3	0.14	6.1	0.12	8.2	0.11	4.5	0.13	4.9	0.11	6.1	0.07	13.7	0.11	5.7
L3	0.07	4.9	0.08	3.6	0.08	5.0	0.12	2.5	0.11	4.8	0.12	1.5	0.09	3.8	0.08	4.9	0.07	8.5	0.08	8.0
L4	0.10	7.2	0.07	2.8	0.10	1.3	0.11	1.6	0.08	3.6	0.11	4.7	0.13	2.2	0.09	3.0	0.06	4.8	0.09	5.5
L5	0.16	0.7	0.15	5.0	0.21	9.0	0.14	7.7	0.12	7.8	0.04	10.0	0.17	2.4	0.17	4.2	0.11	6.0	0.19	6.3
L6	0.06	9.3	0.07	7.4	0.08	13.4	0.12	4.1	0.09	5.7	0.08	2.9	0.06	9.0	0.06	6.9	0.08	6.0	0.07	5.8
L7	0.06	4.7	0.07	6.2	0.08	6.9	0.10	3.1	0.07	12.3	0.07	3.8	0.09	8.0	0.08	4.9	0.07	3.8	0.07	7.5
L8	0.16	2.2	0.09	15.9	0.19	3.2	0.14	4.9	0.11	7.9	-	-	0.20	5.8	0.17	3.1	0.12	3.5	0.12	6.5
L9	0.05	10.3	0.07	5.4	0.08	2.4	0.09	1.5	0.03	20.2	0.07	0.3	0.05	6.4	0.07	2.9	0.09	0.9	0.08	2.5
L10	0.04	4.2	0.07	6.8	0.07	3.1	0.08	4.5	-	-	0.08	3.3	0.07	3.9	0.07	5.5	0.07	1.1	0.08	3.2
L11	0.10	5.7	0.08	6.1	0.15	2.4	0.11	9.1	0.13	5.1	0.14	6.8	0.16	5.9	0.14	3.7	0.04	9.0	0.11	1.3
L12	0.05	0.9	0.08	4.6	0.07	9.4	0.07	3.6	-	-	0.09	3.1	0.06	6.2	0.06	8.8	0.11	3.6	0.10	3.3
L13	0.05	3.0	0.07	3.6	0.07	6.4	0.07	5.8	-	-	0.10	2.3	0.07	2.9	0.08	4.9	0.09	0.9	0.09	6.0
L14	0.08	5.0	0.08	5.7	0.13	4.9	0.10	4.9	0.04	19.0	0.14	1.1	0.14	3.7	0.16	1.7	0.09	12.0	0.12	1.4
M1	0.29	3.7	0.18	6.9	0.23	4.1	0.23	1.9	0.21	5.5	0.26	1.4	0.22	6.7	0.20	2.2	0.20	1.7	0.22	1.9
M2	-	-	0.25	4.6	0.25	3.2	0.26	1.0	0.28	2.3	0.29	2.1	0.27	1.5	0.24	6.3	0.20	5.4	0.29	0.9
M3	0.23	3.1	0.17	3.8	0.24	0.7	0.24	1.4	0.24	2.8	0.24	1.8	0.23	3.2	0.19	2.7	0.22	6.7	0.25	3.4
M4	0.36	5.0	0.30	6.5	0.28	0.6	0.30	2.6	0.29	3.1	0.31	2.7	0.25	5.8	0.26	3.1	0.19	4.5	0.30	2.7
M5	-	-	0.38	10.0	0.30	3.9	0.30	1.9	0.36	1.1	0.26	0.7	0.30	2.4	0.25	5.5	0.18	4.3	0.15	5.1
M6	0.19	1.7	0.17	6.3	0.25	3.4	0.23	3.8	0.19	5.6	0.26	2.3	0.21	0.7	0.11	10.9	0.16	3.9	0.20	15.1
M7	0.30	3.3	0.30	4.2	0.34	5.9	0.30	1.9	0.37	7.0	0.31	1.7	0.26	2.2	0.28	1.1	0.16	1.4	0.30	6.9
M8	0.37	3.3	0.36	6.2	0.33	2.0	0.28	5.1	0.35	5.6	0.23	2.0	0.23	6.0	0.17	3.6	0.13	1.7	0.14	4.2
M9	0.20	3.8	0.16	2.5	0.27	5.6	0.21	2.8	0.18	19.6	0.25	1.2	0.20	4.2	0.16	0.9	0.15	3.4	0.24	18.6
M10	0.26	2.8	0.30	2.0	0.33	7.1	0.28	1.2	0.39	2.2	0.25	2.4	0.19	2.5	0.25	2.0	0.16	2.4	0.24	2.7
M11	0.28	2.0	0.30	2.8	0.30	6.0	0.21	1.6	0.31	3.8	0.22	2.0	0.16	1.1	0.14	0.7	0.13	7.8	0.11	7.1
M12	0.16	1.6	0.19	5.9	0.25	1.6	0.18	0.6	0.17	2.3	0.18	6.4	0.15	6.9	0.18	5.7	0.09	7.7	-	-
M13	0.22	4.3	0.26	4.6	0.29	3.0	0.20	2.3	0.32	4.0	0.20	2.6	0.15	1.2	0.21	3.6	0.14	0.1	0.20	2.9
M14	0.19	1.6	0.27	1.2	0.25	4.2	0.17	2.6	0.27	1.2	0.20	0.8	0.14	2.9	0.13	4.1	0.12	3.2	0.12	1.8
M15	0.16	3.7	0.16	0.5	0.18	1.6	0.14	1.6	0.18	0.7	0.13	1.9	0.13	1.7	0.14	1.1	0.14	1.6	0.21	9.2
M16	0.14	1.3	0.19	1.3	0.20	0.9	0.14	2.1	0.22	1.4	0.16	2.7	0.12	0.8	0.15	1.2	0.13	1.4	0.16	1.7
M17	0.14	2.2	0.21	1.1	0.17	3.4	0.15	2.6	0.19	3.1	0.15	5.5	0.13	2.1	0.12	3.0	0.13	1.4	0.13	2.2

As Table 3.2 shows, the average peak force was significantly higher on the medial condyle and on both its anterior and posterior sub-regions when compared to lateral counterparts (Lat/Ant vs. Med/Ant and Lat/Post vs. Med/Post). Interestingly, no significant differences were observed between sub-regions of the lateral condyle (Lat/Ant vs. Lat/Post). In contrast, the mean peak force yielded at the Med/Post sub-region was 20% lower than on the Med/Ant ($p<0.01$). As cartilage thickness variations between and within condyle locations could affect peak forces measured at same indentation depth (Michalak et al., 2019), with thinner cartilage yielding higher force values, we sought to determine the cartilage thickness distribution within the same surfaces and validate this approach using XRM imaging.

Table 3.2. Mean and standard deviation (SD) values for peak force (N) as determined by automated indentation test performed for $n = 10$ distal femur samples of murine articular cartilage. Mean values compared between condyles (Lateral/Medial; unpaired, Student's t test, $\alpha=0.05$) and within sub-regions of condyles (Lat/Ant, Lat/Post, Med/Ant, Med/Post; one-way ANOVA, $p<0.05$).

Peak Force [N]				
Condyle	Mean (SD)	Condyle	Mean (SD)	Lat - Med
Lateral	0.096 (0.011)	Medial	0.219 (0.037)	$p < 0.0001$
Lat/Ant	0.107 (0.017)	*Med/Ant*	0.250 (0.037)	$p < 0.0001$
Lat/Post	0.090 (0.011)	*Med/Post*	0.199 (0.037)	$p < 0.0001$
Ant - Post	*ns*	Ant - Post	$p < 0.01$	-

ns, no significant difference; -, comparison not applicable

3.4.2. *Cartilage thickness characterization: comparison between needle probing and XRM imaging*

NP thickness mapping was performed on all 10 femoral condyles, which were subsequently scanned using contrast enhanced XRM imaging (Figure S3.2). As shown in Figure 3.2A, reconstructed 3D datasets of murine distal femurs allowed us to validate the spatial distribution of NP testing sites, whereby the corresponding region of interest (ROI) coordinates for imaging processing could be determined. Additionally, the two-dimensional slices confirmed that the needle probe pierced the full length of the cartilage, reaching the subchondral bone (Figure 3.2A). The cartilage surface and cartilage-subchondral bone interface positions were identified using the load-displacement curves from NP (Figure 3.2B), and the cartilage thickness for each position was then calculated considering the surface angle (see Methods section for details). There was a 2.58% rate of needle probe failure (8 out of 310 measurements, testing sites near the specimen's edge) during data acquisition. NP and contrast enhanced XRM imaging yielded similar cartilage thickness distributions on both condyles (Figure 3.2C), demonstrating a highly significant correlation between paired values (R=0.842, n=302, p<0.0001) (Figure 3.2D). Further method-comparison using a Bland-Altman plot (Figure 3.2E) illustrated XRM measurements were approximately 6.8 µm thicker on average than NP, representing only a 1.55 voxels difference (4.39 µm resolution - XRM). Moreover, no significant differences were found between pairwise mean thickness values (NP vs. XRM) for individual positions within the lateral condyle (Figure 3.2F). Similar results were shown for the medial condyle, wherein higher mean thickness values from XRM were only seen on M06 ($\Delta = 8.68$ µm, $p = 0.028$), M11 ($\Delta = 9.89$ µm, $p < 0.01$), and M13 ($\Delta = 9.34$ µm, $p = 0.012$) testing sites. No obvious reason for these localized differences was found, and dullness of needle was ruled out since subsequent testing sites (M14 to M17) yielded comparable cartilage thickness values between techniques.

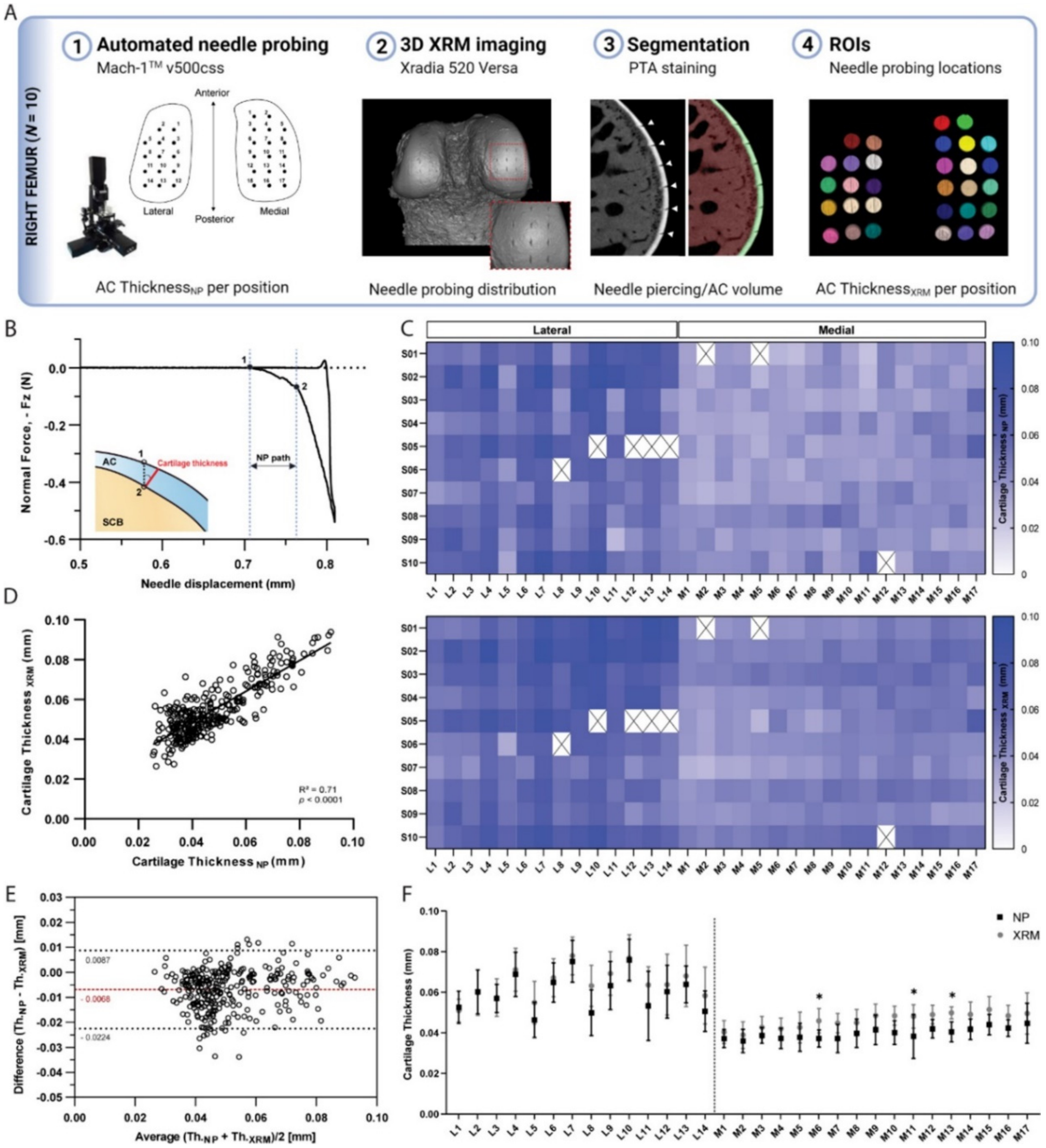

Figure 3.2. Thickness mapping of murine articular cartilage. (A) Assessment of agreement between needle probing (NP) and x-ray microscopy (XRM) imaging cartilage thickness per position of measurement within right femoral condyles (n=10). (B) Representative normal force-displacement curve obtained during NP test depicting articular cartilage (AC) surface (1) and subchondral bone interface (2) positions and cartilage thickness calculated normal to the surface (red) using the surface angle orientation. (C) Mapping distributions of cartilage thickness values per position as measured by NP and XRM. (D) Correlation graph of cartilage thickness measured by NP vs. XRM, R=0.842, n=302, $p<0.0001$, and corresponding (E) Bland-

Altman plot showing overall agreement between methods, with average difference of 6.8 µm in thickness. Dotted black lines show upper and lower 95% limit of agreement. (F) Pairwise assessment of mean cartilage thickness NP vs. XRM per position for the lateral and medial condyles (* $p<0.05$, ** $p<0.01$, *two-way* ANOVA). Symbols represent the means and error bars the standard deviation.

Unlike peak force distributions, spatial heterogeneities in cartilage thickness were apparent among individual testing sites only on the lateral condyle ($p < 0.0001$), with averaged values ranging from 46 to 76 µm; whereas thickness distributions within the medial condyle were more uniform ($p = 0.06$), ranging from 36 to 45 µm. Nevertheless, no significant differences were observed within condyles when comparing their anteroposterior sub-regions; whereas the medial condyle was significantly thinner than its lateral counterpart, both in its anterior and posterior sub-regions (Tables 3.3 and 3.4). XRM segmentation of contralateral femoral condyles ($n = 5$) not subjected to biomechanical testing (Figure S3.3) yielded mean cartilage thicknesses of 40.63 ± 3.14 µm and 56.99 ± 6.26 µm for the medial and lateral condyles, respectively. Comparison to the averaged values retrieved by site-specific NP and XRM following NP suggests repeated indentations did not compromise cartilage before NP test, whereas compromise of cartilage integrity by NP may have impacted subsequent XRM evaluation leading to overestimation of site-specific cartilage thicknesses.

Table 3.3. Mean and standard deviation (SD) values for cartilage thickness as determined by needle probing for distal femur samples of murine articular cartilage (*n* = 10). Mean values compared between condyles (Lateral/Medial; unpaired, Student's *t* test) and within sub-regions of condyles (Lat/Ant, Lat/Post, Med/Ant, Med/Post; *one-way* ANOVA, $\alpha=0.05$).

Cartilage Thickness [µm]				
Condyle	Mean (SD)	Condyle	Mean (SD)	Lat - Med
Lateral	60.3 (6.3)	Medial	39.8 (2.9)	$p < 0.0001$
Lat/Ant	57.0 (5.9)	*Med/Ant*	37.5 (3.8)	$p < 0.0001$
Lat/Post	62.3 (7.8)	*Med/Post*	41.9 (3.0)	$p < 0.0001$
Ant - Post	*ns*	Ant - Post	*ns*	-

ns, no significant difference; -, comparison not applicable

Table 3.4. Mean and standard deviation (SD) values for cartilage thickness as determined by x-ray microscopy imaging for distal femur samples of murine articular cartilage (*n* = 10). Mean values compared between condyles (Lateral/Medial; unpaired, Student's *t* test) and within sub-regions of condyles (Lat/Ant, Lat/Post, Med/Ant, Med/Post; *one-way* ANOVA). p-value reported.

Cartilage Thickness [N]				
Condyle	Mean (SD)	Condyle	Mean (SD)	Lat - Med
Lateral	64.4 (8.4)	Medial	46.5 (4.4)	$p < 0.0001$
Lat/Ant	59.0 (8.2)	*Med/Ant*	42.9 (5.1)	$p < 0.0001$
Lat/Post	67.4 (9.7)	*Med/Post*	49.5 (4.3)	$p < 0.0001$
Ant - Post	*ns*	Ant - Post	*ns*	-

ns, no significant difference; -, comparison not applicable

As expected, pairwise comparisons for individual testing sites demonstrated a significant negative correlation between peak force and thickness measurements within lateral (R = −0.554, $n = 135$, $p < 0.001$, Figure 3.3A) and medial (R = −0.463, $n = 167$, $p < 0.001$, Figure 3.3B) condyles. Knowledge of site-specific thickness variations allowed the compressive stiffness to be determined for the same mechanical strain at each testing site. Instantaneous modulus was calculated using Hayes et al. elastic model (Hayes et al., 1972) at 20% strain, wherein linear elastic behavior can be assumed, and instantaneous response is considered as flow-independent (*Poisson's* ratio, $\upsilon = 0.5$ assumed; (Armstrong, 1986). Regardless of femoral condyle, instantaneous stiffness demonstrated no significant correlation to thickness variations (Figure 3.3C–D). Notably, compressive stiffness differed significantly between condyles (Lat vs. Med, $p<0.001$), but no longer within a condyle (Lat/Ant vs Lat/Post: $p>0.99$; Med/Ant vs Med/Post: $p=0.546$), like seen for peak reaction force on the medial side. Together, cartilage thickness appears as a contributing factor but not the sole explanation to mechanical variations, which is also affected by differences in composition and morphology. Next, we assessed the potential of this indentation testing in identifying microscale biomechanical differences between healthy and degraded cartilage.

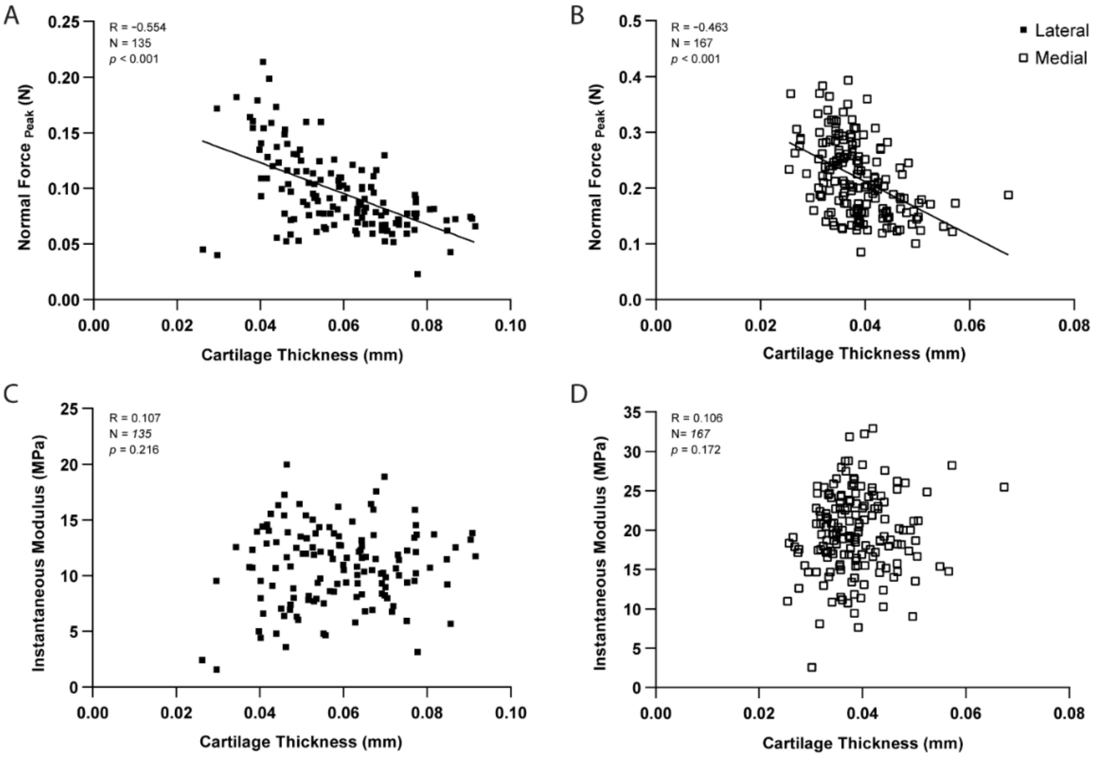

Figure 3.3. Correlation graphs per testing site for the lateral (n = 135 positions) and medial (n = 167) condyles; showing cartilage thickness (needle probing) is significantly correlated to peak indentation force at 20 um (A-B), but not to instantaneous modulus values as determined by Hayes *et al.* (1972) elastic model at 20% strain. Pearson correlation performed and *p*-values reported.

3.4.3. Altered biomechanical properties in degenerated murine articular cartilage

To assess the changes in mechanical response within the context of cartilage degeneration, we employed the same testing protocol on age-matched Proteoglycan 4 (PRG4) knockout mice (n = 6) and compared the outcomes to the C57BL/6 controls. PRG4 is a mucin-like glycoprotein highly conserved across species (Askary et al., 2016; Ikegawa et al., 2000) and functionally relevant in joint homeostasis and lubrication (Coles et al., 2010; Jay et al., 2007; Rhee et al., 2005). PRG4 loss of function, as seen in knockout mice ($Prg4^{-/-}$), leads to degenerative joint changes recapitulating the phenotype of human camptodactyly-arthropathy-coxavara-pericarditis syndrome (Marcelino et al., 1999; Rhee et al., 2005). As a spontaneous model of cartilage degeneration, $Prg4^{-/-}$ structural and morphological joint changes are expected to be more consistent across specimens and less susceptible to variability derived from models that rely on injury/intervention. Histological alterations of articular cartilage have been comprehensively described and include surface roughness, tissue thickening, and loss of collagen parallel orientation at the superficial layer, progressing to irreversible tissue damage with age (Karamchedu et al., 2016; Rhee et al., 2005).

Yet, the microscale assessment of site-specific mechanical variations, aside from friction, has not been described so far for *Prg4*$^{-/-}$ knee cartilage surfaces. Mapping of biomechanical parameters allowed site-specific differences in *Prg4*$^{-/-}$ cartilage to be visualized, and outcomes were largely reproducible across femoral specimens (Figure 3.4A–B). These findings were supported by the combined quantitative assessment between genotypes for the different condyle regions and subregions (Figure 3.4C–F). *Prg4*$^{-/-}$ mean cartilage thickness on both lateral (67.9 ± 3.5 µm, $p = 0.032$) and medial (56.3 ± 3.7 µm, $p < 0.001$) sides of the knee was higher compared to controls (Figure 3.4C). Differences in cartilage thickness between genotypes on anteroposterior sub-regions, however, were only detected on the medial condyle (Figure 3.4E). The site-specific thickness measurements enabled us to determine the instantaneous modulus at each testing site for the same mechanical strain. The utilized Hayes et al. (1972) elastic model could fit the response of mouse cartilage with great accuracy (root mean square error [RMSE] equal to 0.017 ± 0.007 MPa for controls and 0.010 ± 0.003 MPa for *Prg4*$^{-/-}$). Cartilage compressive stiffness was significantly lower on the medial condyle of *Prg4*$^{-/-}$ mice compared to controls (8.67 ± 1.79 MPa vs. 19.52 ± 2.44 MPa, respectively, $p < 0.001$). Similar patterns were seen when considering the anteroposterior subregions of the medial condyle (Figure 3.4F). No significant differences in lateral condyle cartilage stiffness were observed (10.85 ± 1.73 MPa - control vs. 8.73 ± 2.39 MPa - *Prg4*$^{-/-}$, $p = 0.187$).

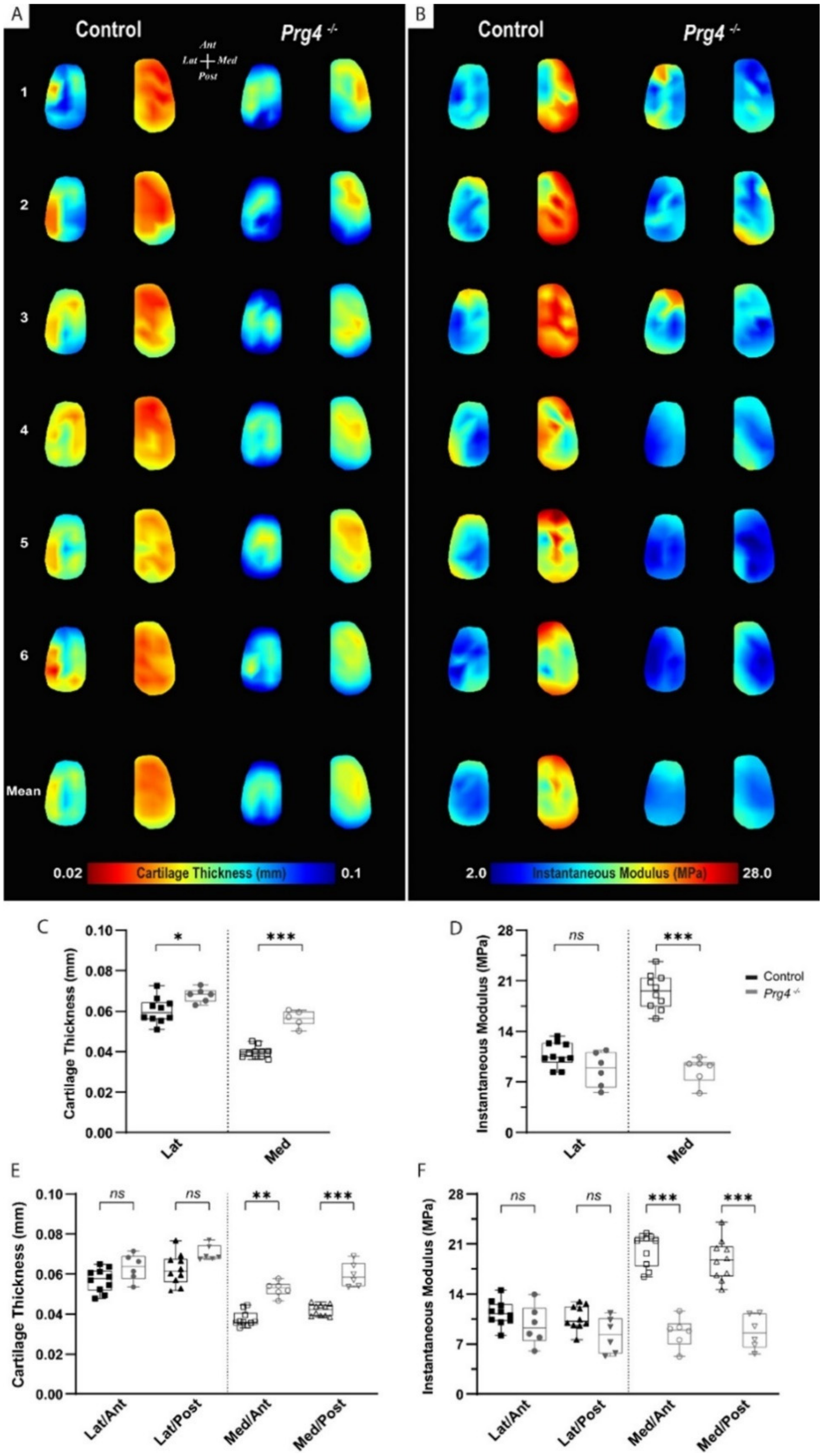

Figure 3.4. Altered biomechanical properties in degenerated murine articular cartilage. (A–B) Heat maps and corresponding boxplots comparing (C–D) regions - lateral and medial - and their (E–F) sub-regions - Lat/Ant, Lat/Post, Med/Ant, Med/Post - highlight spatial differences in biomechanical parameters on femoral cartilage surface between controls (C57Bl/6, n=10) and PRG4 knockout mice ($\text{Prg4}^{-/-}$, n=6).

Maps shown for six representative samples per genotype, as well as the corresponding averaged map of all samples. Parameters illustrated are thickness measured by needle probing (A, C, E) and instantaneous modulus as determined by Hayes et al., 1972 elastic model (B, D, F). Pairwise comparison between genotypes for mean values on the lateral and medial condyles and anteroposterior sub-regions (Mann-Whitney U with Bonferroni-Dunn correction, $^{*}p<0.05$, $^{**}p<0.01$, $^{***}p<0.001$).

3.5. Discussion

Using a novel microscale instrumented apparatus, we were able to detect and quantify spatial variations in biomechanical parameters across murine cartilage surfaces, both within healthy and degenerated femoral condyles. Compared to recent mouse studies using this commercially available apparatus (Lavoie et al., 2015; Woods et al., 2021), the optimization of sample mounting and NP protocols allowed for unprecedented quantitative mapping of the mechanical behavior and associated cartilage thickness on load-bearing regions of distal femurs with higher spatial density.

For healthy, 4-month-old C57BL/6 mice, test-retest micro-indentation measurements were reproducible at any given testing site, also indicating that the instantaneous deformation and sustained compression steps in the stress-relaxation protocol did not compromise the mechanical behavior of the freshly harvested cartilage tissue. Heterogeneity in peak forces was identified across anatomical locations. Notably, the medial condyle surface yielded approximately two times higher peak forces on average than its lateral counterpart. Moreover, both condyles displayed a shift toward lower values at posterior regions. Previous studies have shown significant variation in mechanical properties within different cartilage surfaces in healthy joints (Froimson et al., 1997; Korhonen et al., 2002), or even over a single surface (Hoch et al., 1983; Samosky et al., 2005). Considering the structural and material 3D complexities of articular cartilage, it is intuitive that reaction forces in indentation response are influenced by depth of indentation and applied strain rate (Bae et al., 2006). As thickness variations across the cartilage surfaces are unknown prior to indentation test, the relative intra-tissue strain at each testing site varied due to the fixed indentation depth imposed, thereby influencing the measured reaction forces. In general, higher peak reaction forces in intact cartilage were associated with lower thickness values. However, the effect of site-specific cartilage geometry, such as thickness, when characterizing the mechanical properties of cartilage in indentation is often overlooked ((Moshtagh et al., 2016; Sim et al., 2017).

Studies in mice commonly rely on mean thickness values from histology, requiring longer turnaround and lacking spatial specificity. The optimized NP protocol used here was able to resolve spatial thickness variations across condyle surfaces and closely localizes cartilage thickness measures to the footprint of indentation on mouse distal femurs. Moreover, 3D visualization of the femoral cartilage surfaces after XRM imaging validated the positioning and distribution of the testing grid used, allowing us to pinpoint individual testing sites and compute their thicknesses. A highly significant correlation between pairwise cartilage thickness values from NP and XRM, per measurement site, was observed. Variations seen between averaged thickness values could be explained by differences in instrument resolution capabilities (Mach-1 z-axis: 0.5 µm vs XRM: 4.39 µm voxel size) and partial volume artifacts, which may affect the accuracy of tissue detection on the XRM segmentation. It is worth noting, however, that previous research (Das Neves Borges et al., 2014) on murine cartilage thickness has been performed using greater voxel sizes. Compromise of cartilage integrity by NP likely contributes to observed differences as well, leading to higher XRM measurements, possibly due to tissue swelling. Comparable mean cartilage thickness values between NP and XRM segmentation from contralateral femurs not subjected to biomechanical testing support this conclusion. Nevertheless, mean thickness values were in line with earlier reports for mouse cartilage (Kotwal et al., 2012; Oláh et al., 2021; Poulet et al., 2013), with marked greater cartilage thicknesses measured on the lateral condyle compared to the medial counterpart (Malda et al., 2013).

Localized cartilage thickness measurements by NP enabled us to account for the effect of cartilage geometry on indentation, with implementation of aspect ratio (indenter radius-to-cartilage-thickness) corrections as per Hayes's (Hayes et al., 1972) analytical formulation when calculating compressive stiffness distributions at 20% strain (considered as physiological loading; (Simha et al., 2007). A common area of concern in in situ indentation of thin materials, such as mouse articular cartilage, is the effect of substrates on the measured mechanical properties, wherein the indentation response of articular cartilage could be somewhat influenced by the underlying rigid bone, especially on thinner areas (Julkunen et al., 2008). While we recognize this limitation when employing microindentation, we argue that knowledge of thickness variations improves the reliability of the indentation assessment and aids interpretation of results following degradation and loss. According to the present results, there was no significant variation in mean thickness of healthy cartilage over a condyle surface, therefore biomechanical parameters were compared between matched regions and sub-regions when assessing degeneration.

Compared to C57BL/6 control, the loss of *Prg4* function resulted in an increase in thickness and decrease in stiffness of the knee cartilage in 16-week-old mice. This is consistent with previous observations on hip articular cartilage of *Prg4*$^{-/-}$ mice (same age), using AFM indentation (Coles et al., 2010). Apparent modulus values in our study were about an order of magnitude larger than those reported by Coles et al., 2010 for *Prg4*$^{-/-}$ and healthy controls, a discrepancy we attribute to differences in compression rate (1 μm/s *vs* 20 μm/s) and indentation scale (micro- *vs.* nanoindentation depth), leading to differences in strain fields, and the level of structure that is probed (Bae et al., 2006). It is worth noting that anatomical locations of assessment also differed between studies. The cartilage thickness values determined by NP in our study are in a similar range to those reported by Karamchedu et al., 2016. In their micro-CT imaging study, the *Prg4*$^{-/-}$ mice displayed cartilage thickness averaging 61.0 ± 4.3 μm and 42.4 ± 2.6 μm for the load-bearing regions of the lateral and medial condyle, respectively. Furthermore, *Prg4*$^{-/-}$ cartilage was also shown to be significantly thicker than in control littermates (Karamchedu et al., 2016), even though mice were younger (10 weeks old) than in our study.

Reduction in the instantaneous compressive modulus in our study was confined to the medial compartment. We attribute that to differences in thickening in *Prg4*$^{-/-}$ femoral cartilage compared to controls, 12.6 vs 41% on lateral and medial condyles, respectively, as well as *Prg4*$^{-/-}$ compromised structural integrity (Drewniak et al., 2012; Jay et al., 2007; Rhee et al., 2005) having a bigger functional impact on the medial compartment, recognized as the main load-bearing region in most mammalian joints.

Microscale indentation characterizes the overall tissue resistance to deformation (Simha et al., 2007) and disrupted architecture, and composition can impart tissue mechanical response. Due to the rapid compression rate employed in the present protocol, normal cartilage tissue is expected to deform with minimal change in volume (Armstrong, 1986), as its low permeability restrains fluid flow; thereby localizing the strain near the surface as fluid pressure pushes against the collagen meshwork. Thus, under instantaneous (rapid) loading the ability of cartilage to resist compression is known to be affected by the collagen fibril meshwork (Julkunen et al., 2008; Laasanen et al., 2003), particularly tangentially oriented collagen fibrils on the superficial tissue layer (Korhonen et al., 2002). In *Prg4*$^{-/-}$ mice, the normal parallel organization of collagen fibrils adjacent to the surface is known to be disrupted (Jay et al., 2007), likely affecting fluid pressurization, helping explain the lower instantaneous modulus compared to controls.

Limitations of this study include evaluation of the anatomy of the distal murine femoral condyles and not the opposing articulation (i.e. proximal tibia). Also, we focused on a single timepoint of analysis; however, investigations related to aging and progressive degeneration are of interest as they are known to affect the biochemical composition and structural integrity of cartilage (Julkunen et al., 2009; Rahmati et al., 2017; Rhee et al., 2005), thereby influencing its mechanical properties. Finally, due to the biphasic/poroviscoelastic nature of cartilage, future studies should consider the use of more complex analytical models (Julkunen et al., 2009; Mow et al., 1980) that are able to capture the time-dependent viscoelastic behavior of cartilage in mice.

In this study, we have gained insights into the patterns of varying surface geometry and mechanics present within murine articular cartilage at the microscale. 3D indentation mapping was able to resolve site-specific differences in thickness and mechanical properties across knee cartilage surfaces in healthy mice. Moreover, it identified functional changes on the *Prg4*$^{-/-}$ mouse model. This technique could also prove helpful for the study of other mouse models mimicking different mechanisms of, or therapies focused on, repair and degeneration of articular cartilage, as microscale indentation with high spatial density can provide a more comprehensive characterization of cartilage's mechanical properties.

3.6. Acknowledgements

Graphical representation of experimental designs was created using BioRender.com. The authors thank Biomomentum inc. for their assistance during optimization of indentation testing protocol. AOM would like to thank the University of Calgary and Alberta Innovates for support during the period this study was conducted.

3.7. Author Contribution

A.O.M. was responsible for the study design, data collection, analysis, interpretation, and draft of the manuscript. B.B. carried out imaging processing and data analysis. W.B.E. contributed to the study design. R.K. contributed to the study design and data interpretation. B.B., W.B.E. and R.K. provided critical review, commentary, and revisions to the manuscript.

3.8. Supplementary Information

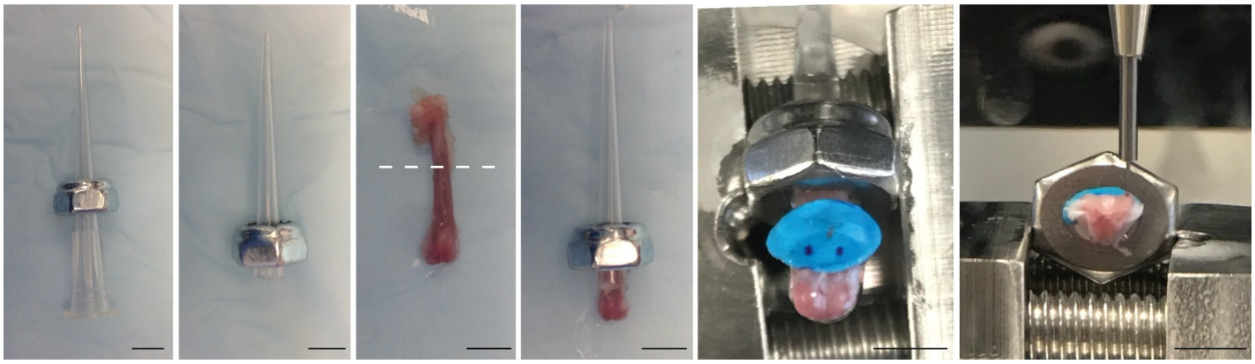

Figure S3.1. Specimen preparation and assemble to sample holder for automated indentation mapping using custom setup, allowing for repositioning of the sample and non-destructive retrieval for three-dimensional x-ray microscopy imaging (scale bars equal to 4 mm).

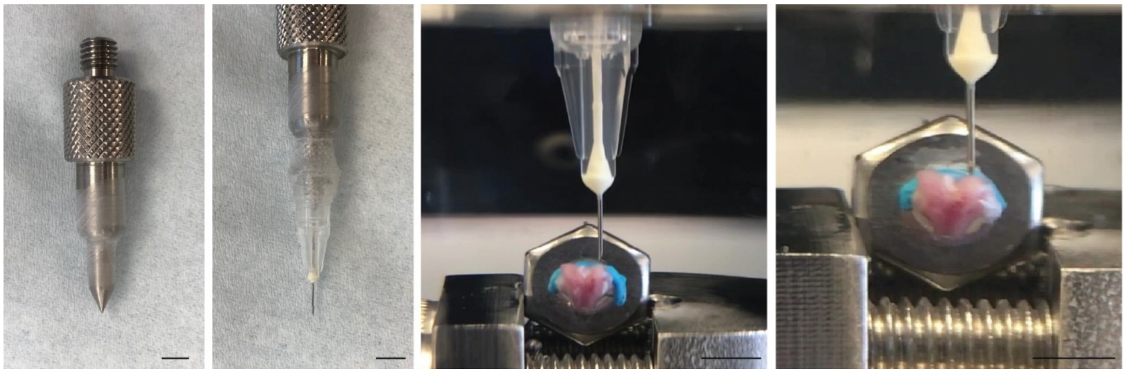

Figure S3.2. Setup for needle probing thickness measurement, using a 30G×1.4” hypodermic needle (TSK Laboratory, Japan) adapted to the 1-mm spherical indenter *(Biomomentum Inc*, Laval, QC) (scale bars equal to 4 mm).

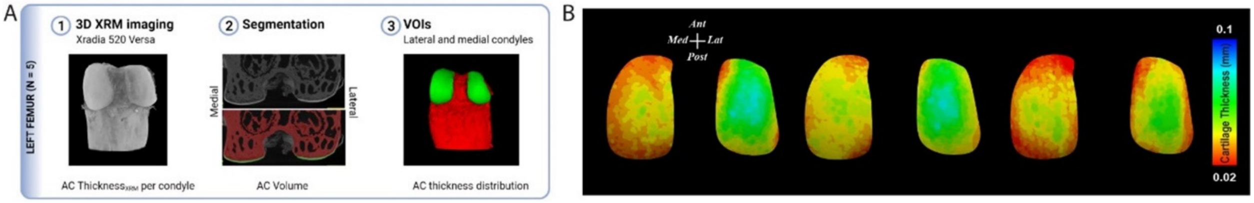
A
① 3D XRM imaging
Xradia 520 Versa
② Segmentation
③ VOIs
Lateral and medial condyles
LEFT FEMUR (N = 5)
Medial
Lateral
AC Thickness$_{XRM}$ per condyle
AC Volume
AC thickness distribution
B
Ant
Med
Lat
Post
0.1
Cartilage Thickness (mm)
0.02

Figure S3.3. XRM imaging of femoral condyles.

(A) Three-dimensional phosphotungstic acid-x-ray microscopy (PTA-XRM) imaging and segmentation protocol of contralateral femoral condyles (n = 5) that were not subjected to biomechanical testing. (B) Cartilage thickness distribution maps as measured by PTA-XRM imaging for three representative samples. AC: articular cartilage, VOIs: volumes of interest.

Chapter Four: Induced chondrocyte depletion disrupts articular cartilage homeostasis but is not a driver of degeneration

Masson A.O, Corpuz J.M., Corpuz K., Biernaskie J., Edwards W.B., Krawetz R.J.

** In preparation for submission*

My contributions to this work were as follows:

- *Contributed to experimental designs*
- *Performed experimental procedures and data analysis*
- *Conceptualized and created the manuscript figures, and wrote the manuscript*

4.1. Abstract

Chondrocytes define and maintain tissue architecture in articular cartilage and are critical in regulating the microenvironment in health and disease. Their loss/dysfunction has been associated with aging, injury, and osteoarthritis (OA), which is characterized by cartilage degradation. However, the role of chondrocyte death in cartilage degeneration remains controversial. We employed a Cre-inducible diphtheria toxin mouse model to deplete articular chondrocytes and evaluated the spatiotemporal effects on tissue structure and functional integrity. Chondrocyte-depleted mice exhibit altered proteoglycan staining, mechanical properties, and transient upregulation of proteases. Despite overt hypocellularity in aged mice, the phenotype did not progress to cartilage degeneration, nor OA. Our results suggest that murine articular cartilage has the ability, albeit limited, to compensate for the loss of chondrocytes and mitigate the consequent degree of harm. We demonstrate that chondrocyte depletion in the absence of injury, inflammation, or other insult is insufficient to initiate the OA disease cascade.

4.2. Introduction

The articular cartilage is an intricate and remarkable tissue comprised of a heterogeneous three-dimensional extracellular matrix (ECM) optimized to withstand high shear and compressive stresses over a lifetime of use. The depth-dependent arrangement of collagen fibers and distribution of water-retaining proteoglycans (mainly aggrecan) from the surface to deeper cartilage layers enables effective transfer and absorption of loads and confers resilience to the tissue (Sophia Fox et al., 2009). Additionally, lubricating molecules at its surface, such as Proteoglycan-4 (PRG4) (also known as lubricin), contribute to nearly frictionless, pain-free joint motion (Coles et al., 2010; Jay et al., 2007; Rhee et al., 2005).

It has long been appreciated that chondrocytes, the only tissue-resident cells in articular cartilage, are essential for homeostatic deposition and remodelling of its highly specialized ECM. Under normal physiological conditions, chondrocytes rarely undergo cell division, while individual cells (housed in lacunae) can survive for the lifespan of the organism in the avascular matrix (Mankin, 1968; Stockwell, 1967). The turnover rate of ECM proteins is collectively low in healthy cartilage, yet there can be a wide range of individual protein turnover times ranging from days/weeks (aggrecan) to decades (collagen) (Heinemeier et al., 2016; Hsueh et al., 2019; Maroudas et al., 1998). Moreover, protein synthesis and degradation can be influenced by signals from the microenvironment and become dramatically modified upon injury, aging, and disease (Bobacz et al., 2004; Hashimoto et al., 1998; Vincent and Wann, 2019), as chondrocytes undergo direct damage and/or phenotypic changes affecting their survival, proliferation, and metabolic activity.

Cell loss and matrix damage are frequently associated with cartilage injury and are observed in the context of aging and osteoarthritis (OA) (Bobacz et al., 2004; Hashimoto et al., 1998; Hwang and Kim, 2015; Loeser, 2009; Natoli et al., 2008; Thomas et al., 2007). However, we still lack understanding regarding the contribution of direct cellular death to cartilage damage and disease initiation and progression (Hwang and Kim, 2015). Given chondrocytes' key role in cartilage maintenance, reduced cellularity should result in impaired matrix turnover and, eventually, tissue failure. Surprisingly, previous work demonstrated the preservation of knee articular cartilage following targeted depletion of *Prg4*/lubricin-expressing superficial chondrocytes in young mice (Zhang et al., 2016). Moreover, cell depletion prior to surgically induced OA was negatively correlated to cartilage damage (Zhang et al., 2016). The findings of non-damaged, albeit structurally altered, articular cartilage seems paradoxical to the chondrocyte's role in tissue maintenance/function. However, they could have been impacted by the young age at which chondrocyte depletion was induced when the articular cartilage is still undergoing growth and maturation (Decker et al., 2017) and presents with the ability to undergo repair (Matsuoka et al., 2015). Another factor to consider is the observation that superficial cells exhibit a progenitor-like phenotype compared to chondrocytes in the other cartilage layers (Decker et al., 2017; Li et al., 2017). Hence, it remains controversial whether reduced tissue cellularity reflects cause or outcome of the onset and progression of tissue demise.

Hence, in the current study, we examined the spatiotemporal effects of widespread chondrocyte depletion on articular cartilage maintenance and degeneration in adult mice. To accomplish this, we adopted a Cre-inducible diphtheria toxin A (DTA) model (Voehringer et al., 2008), generally used for cell depletion (Englund et al., 2020; He et al., 2021; Wilk et al., 2017; Zhang et al., 2016). DTA inhibits protein synthesis leading to subsequent cell death (Strauss and Hendee, 1959). By breeding Rosa-DTA mice with a cartilage-specific *Aggrecan*-CreER^{T2} mouse line (Henry et al., 2009), we generated heterozygous Cre-inducible DTA mice under the control of the *aggrecan* (*Acan*) promoter. Aggrecan presents a more robust gene expression than type II collagen, cartilage's principal fibrillar component, and *Acan*-CreER^{T2} mice display articular cartilage recombination postnatally within the whole depth of non-calcified cartilage (Henry et al., 2009; Liao et al., 2017), even when recombination is induced in aged mice (1-year old) (Henry et al., 2009). We found that DTA-induced chondrocyte depletion resulted in partially altered cartilage structure and function, as well as transient upregulation of proteolytic enzymes, without predisposing aging mice to cartilage degeneration nor the development of an OA-like phenotype.

4.3. Methods

4.3.1. Animal models

All animal-related experiments were conducted in accordance with the guidelines of the Canadian Council of Animal Care and received prior approval from the University of Calgary Animal Care Committee (protocols AC16-0043 and AC20-0042). Mice were housed under standard light cycle conditions and provided food and water *ad libitum.* All mice used in this study were purchased from The Jackson Laboratory (Bar Harbor, Maine) and bred in-house at the University of Calgary. For recombination efficiency studies, Cre-inducible tdTomato mice under the control of the aggrecan promoter (referred to as *Acan*-CreER^{T2};tdT) were generated by breeding *Acan*-CreER^{T2} mice (Henry et al., 2009) to R26R^{tdTomato} reporter (stock no. 019148 and 007914, respectively). For experiments involving conditional depletion of chondrocytes, *Acan*-CreER^{T2} mice were bred to R26R^{DTA} mice (Voehringer et al., 2008) (stock no. 009669). Both the $Acan^{+/CreERT2}$; $DTA^{+/-}$ heterozygous offspring (referred to as *Acan*-CreER^{T2}; DTA) and the $Acan^{+/+}$; $DTA^{+/-}$ littermates, which served as control, were used. To induce Cre recombination, 8–9-week-old mice were injected intraperitoneally with 4-hydroxytamoxifen (4-OHT, Sigma H6278) diluted in 10% ethanol in sunflower oil for five consecutive days (1 mg/day). *Acan*-CreER^{T2}; tdT mice ($n = 4$) were sacrificed 1-week after 4-OHT injections (Figure 4.1A). To assess the spatiotemporal changes in articular cartilage after targeted chondrocyte depletion, *Acan*-CreER^{T2}; DTA and control mice (n = 5/group) were euthanized at various endpoints (1-, 5-, 9-, 12-, 16- weeks) after DTA-induction and hindlimbs were harvested for analysis (Figure 4.1F).

4.3.2. Histology

Left hindlimbs were dissected free of skin, fixed in 10% phosphate-buffered formalin (*VWR*), and decalcified in 10% EDTA solution (pH 7.4) at room temperature for up to 18 days on a shaker. Samples were embedded in paraffin, and ten-micron thick coronal sections of flexed tibiofemoral joints were stained with Safranin-O/fast-green. OARSI scoring (Glasson et al., 2010) was used to evaluate the degree of knee joint degeneration. The assessed area consisted of the articular cartilage in the mid-to-posterior load-bearing regions of the knee, limited by anterior and posterior cruciate ligament insertion. Three sections at approximately 180 µm intervals were scored for each animal, and the sum of histopathological scores obtained per knee joint was reported.

4.3.3. Immunofluorescence

Serial sections were used for immunofluorescence staining. Slides were deparaffinized and rehydrated in serial dilutions of ethanol to distilled water. Then, samples were incubated for 1 hour in 10mM sodium citrate solution (pH 6) for antigen retrieval, followed by blocking in 5% bovine serum albumin (BSA; Sigma) for 2 hours. Enhancement of tdTomato signalling was performed using anti-tdTomato (#AB8181-200, Origene). Detection of apoptotic cells was performed using anti-cleaved caspase-3 (#PA5-23921, Thermo Fisher), while anti-MMP3 (#ab53015, Abcam) and anti-ADAMTS5 (#E-AB-15506, Elabscience) antibodies were used as catabolic markers. For ADAMTS5, an added step of antigen retrieval prior to serum blocking was performed using 0.25% hyaluronidase/PBS (#H6254, Sigma) for 60 min at 37°C. Slides were incubated overnight at 4°C with primary antibody, washed twice in PBST and once in PBS before being incubated in secondary antibody NothernLights 557 (#NL001, R&D), Alexa Fluor 568 (#A11011, Thermo Fisher) or Alexa Fluor 647 (#406414, BioLegend) for 1 hour at room temperature. After washing, slides were mounted using EverBrite Hardset mounting medium containing DAPI (#23004, Biotium) and imaged with AxioScan.Z1 (Zeiss) slide scanner.

4.3.4. Image quantification

Quantitative immunofluorescence staining analysis was performed using TissueQuest v.7 (TissueGnostics) software. On each section evaluated, regions of interest were manually delineated to encapsulate the articular cartilage from medial and lateral femoral condyles and tibial plateaus (Figure S4.1). Automatic segmentation via a threshold classifier was used to define and quantify DAPI nuclei-stained cells. The efficiency of recombination and percentage of chondrocyte death were determined, respectively, according to colocalization of DAPI-positive cells to tdTomato-positive (*n* = 4 mice/group, three sections per mouse) and cleaved capase3-positive (*n* = 5 mice/group, two to three sections per mouse) staining, upon gating selection (Supplementary Fig.1). To determine chondrocyte cell density in control and *Acan*-CreER^{T2}*;* DTA, the area and the total number of DAPI-positive cells were acquired for each of the delineated tibiofemoral regions (*n* = 5 mice/group, three to six sections per mouse). The percent of ADAMTS-s5-positive and MMP3-positive cells was calculated per hundred DAPI stained chondrocytes at 1-,5-,9-,12- and 16-weeks (*n* = 5 mice/group, two to three sections per mouse) post-4-OHT treatment.

4.3.5. Biomechanical assessment

At the time of sacrifice, right hindlimbs were dissected free of skin and muscle tissue, and femurs were isolated for biomechanical testing, as previously described (Masson et al., 2022). In brief, the femur was inserted into a 10µL pipette tip filled with cyanoacrylate glue and tightly mounted into a hex nut by the shaft, with condyles facing up. Then, the nut was clamped on the sample holder and secured onto the testing chamber of Mach-1 v500csst (Biomomentum Inc.) multiaxial mechanical tester. The chamber was filled with PBS, and articular cartilage was allowed to equilibrate before automated indentation mapping. Testing was performed at 31 predefined measuring sites across the medial and lateral femoral condyles (17 and 14 positions, respectively) using a 0.3 mm diameter spherical indenter and a 70N multiaxial load cell calibrated before each use. Following automated indentation, the indenter was retrofitted by a 30G x 1/4" needle (TSK Laboratory), and thickness mapping via needle probing was performed on the same femoral surfaces at adjacent locations to indentation mapping sites while keeping the same distribution grid. Cartilage surface and cartilage-subchondral bone interface positions could be identified through the load-displacement curves. The cartilage thickness was calculated according to the surface angle for each position, as previously described (Masson et al., 2022). The load–displacement curve, limited to the indentation depth of 0.02 mm, was evaluated by applying the Hayes model (Hayes et al., 1972), with Poisson's ratio set to 0.5. Then, the instantaneous elastic modulus, limited to a nominal deformation of 20% strain, was determined by using the calculated articular cartilage thickness.

4.3.6. Statistical analysis

Statistical analysis was performed using GraphPad Prism v.8 (GraphPad Software). Values are expressed as mean ± standard deviation (SD). Differences between groups (*Acan-Cre*ER^{T2}*;* tdT lateral vs. medial; control vs. *Acan-Cre*ER^{T2}*;* DTA) were assessed by unpaired Student's t-tests when data were distributed normally. Statistical significance between OARSI scorings was determined by Mann-Whitney U non-parametric test. *p*-values ≤ 0.05 were considered statistically significant.

4.4. Results

4.4.1. Depletion of articular cartilage chondrocytes post DTA-induction

To evaluate the recombination efficiency in articular cartilage, 2-month-old *Acan*-CreER^{T2}*;* tdTomato (tdT) mice were treated with 4-OHT intraperitoneally for five consecutive days, and tdT fluorescence was analyzed after 1-week (Figure 4.1A). As illustrated on Figure 4.1B, successful recombination was achieved in the knee joint. Closer examination of magnified images revealed a similar pattern of tdT expression throughout the non-calcified articular cartilage in the medial (Figure 4.1C) and lateral (Figure 4.1D) tibiofemoral regions, representing 70.6 ± 0.73% vs. 73.2 ± 2.21% of all chondrocytes (DAPI labelled nuclei within the articular cartilage region) (Figure 4.1E, Figure S4.1). tdT-positive cells were also observed in the patellofemoral cartilage, growth plate, and meniscus, and to a lesser degree in ligaments (Figure 4.1B). Previous studies using *Acan*-CreER^{T2} reported similar joint-tissue specificity (Henry et al., 2009; Liao et al., 2017). For chondrocyte depletion experiments, the offspring of heterozygous *Acan*-CreER^{T2} and Rosa-DTA mice were treated with the same 4-OHT regiment to activate diphtheria toxin expression in *aggrecan*-expressing cells (Figure 4.1F). Mice lacking the Cre allele in the offspring, and thus unable to drive Cre recombination, served as littermate controls. Whole joints were evaluated since distinct responses between medial and lateral compartments have been previously reported in other models (Dumond et al., 2004; Mason et al., 2001). One week after the last 4-OHT injection, immunodetection of apoptotic cells (cleaved caspase-3 positive) was identified within the middle to upper cartilage zones of the femoral condyles and tibial plateau in DTA mice (Figure 4.1G), representing a 5-fold increase in cell death across the lateral and medial compartments compared to controls (Figure 4.1H, Figure S4.1). In DTA mice, cell loss appeared to be diffuse throughout the cartilage at earlier time points, markedly increasing in the central areas of articular cartilage over time (Figure 4.1I). Reduced cellularity was observed irrespective of knee compartment (Figure 4.1J-K). At 1-week post-induction, chondrocyte density decreased by approximately 16% (lateral) and 19% (medial). In subsequent time points, chondrocyte numbers progressively reduced compared to age-matched controls, nearing an overall 50% reduction in cellularity 16 weeks post-DTA-induced chondrocyte depletion relative to control knee joints (Figure 4.1L). Together, these data show that DTA-induced recombination leads to overt chondrocyte depletion in mouse articular cartilage, with increasing cell loss observed after the 4-OHT has been cleared.

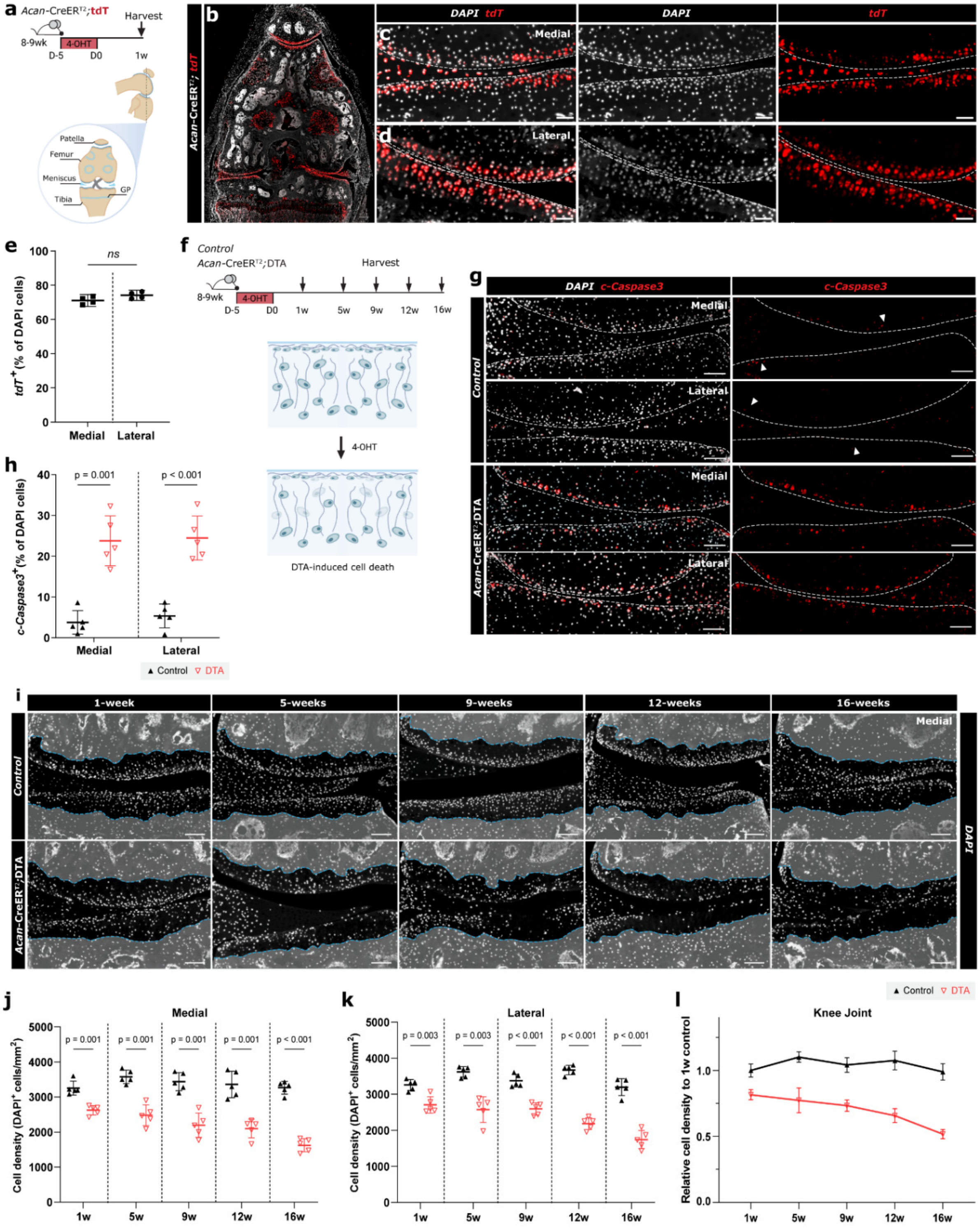
a
Acan-CreER^T2;tdT
Harvest
8-9wk
4-OHT
D-5
D0
1w
Patella
Femur
Meniscus
GP
Tibia
b
Acan-CreER^T2; tdT
DAPI tdT
DAPI
tdT
c
Medial
d
Lateral
e
ns
tdT+ (% of DAPI cells)
100
80
60
40
20
0
Medial
Lateral
f
Control
Acan-CreER^T2;DTA
Harvest
8-9wk
4-OHT
D-5
D0
1w
5w
9w
12w
16w
4-OHT
DTA-induced cell death
g
DAPI c-Caspase3
c-Caspase3
Control
Acan-CreER^T2;DTA
Medial
Lateral
h
p = 0.001
p < 0.001
c-Caspase3+ (% of DAPI cells)
40
30
20
10
0
Medial
Lateral
▲ Control ▽ DTA
i
1-week
5-weeks
9-weeks
12-weeks
16-weeks
Control
Acan-CreER^T2;DTA
Medial
DAPI
j
Medial
Cell density (DAPI+ cells/mm²)
5000
4000
3000
2000
1000
0
p = 0.001
p = 0.001
p = 0.001
p = 0.001
p < 0.001
1w
5w
9w
12w
16w
k
Lateral
Cell density (DAPI+ cells/mm²)
5000
4000
3000
2000
1000
0
p = 0.003
p = 0.003
p < 0.001
p < 0.001
p < 0.001
1w
5w
9w
12w
16w
l
▲ Control ▽ DTA
Knee Joint
Relative cell density to 1w control
1.0
0.5
0.0
1w
5w
9w
12w
16w

Figure 4.1. DTA-induction leads to chondrocyte depletion in mouse articular cartilage. (A) Scheme demonstrating time of 4-OHT treatment and knee harvest for Acan-CreER^{T2}; tdTomato (tdT) reporter mice (B) Immunofluorescence of knee sections (frontal) 1-week post-induction displayed abundant tdT-positive cells in the articular cartilage, growth plate (GP) and meniscus. Tibiofemoral cartilage displayed similar

tdT expression across the (C) medial and (D) lateral compartments, (E) totalling over 70% of cells (DAPI positive) (*n* = 4 mice, 3 sections/mouse). (F) Strategy to achieve diphtheria toxin (DTA) mediated chondrocyte depletion in 8-9w old Acan-CreER^{T2}; DTA mice and endpoints of assessment. One week after 4-OHT treatment, articular cartilage was probed with (G) anti-cleaved caspase 3 antibody, demonstrating increased staining in DTA mice compared to controls (white arrows indicate stained c-caspase-3 cells). (H) Corresponding counts showed that the number of c-caspase-3 immunoreactive cells was significantly increased in both the medial and lateral cartilage regions (*n* = 5 mice/group, 3 sections/mouse). (I) Representative images of the medial tibiofemoral compartment from control and DTA mice show chondrocyte depletion and hypocellularity over time (1- to 16-weeks post-4-OHT). (J-K) Cell density (cell number/mm2) in tibiofemoral cartilage (*n* = 5 mice/group, 3-6 sections/mouse) differed significantly between groups by 1-week post-4-OHT in both the medial and lateral compartments of cartilage. (L) Acan-CreER^{T2}; DTA knee joint averaged cell numbers progressively decreased relative to the 1-week controls. Average cell counts ± SD from each genotype/treatment group are shown. Statistical significance was determined by Student's t-test ($\alpha = 0.05$), p-value reported. The dashed blue line demarcates the osteochondral junction. Scale bars represent 100 µm.

4.4.2. Preservation of cartilage structure post-chondrocyte depletion

Histological analysis was undertaken to determine if chondrocyte depletion negatively impacted homeostasis and led to cartilage degeneration. Compared with age-matched controls, there were noticeable histological differences in the articular cartilage of DTA mice beyond cell loss; however, spontaneous cartilage degeneration was not observed (Figure 4.2A-B). By 5-weeks post DTA-induction, diminished safranin-O staining suggestive of proteoglycan loss was observed within areas of hypocellularity, explicitly at mid-portions of femoral condyles and tibial plateau, extending from the superficial cartilage to the tidemark. Yet, the remaining chondrocytes often displayed intense pericellular safranin-O staining. This proteoglycan phenotype was partially recovered at subsequent time points, although heterogeneity in the proteoglycan staining throughout the articular cartilage was noticeable at all time points examined. However, despite alternations in proteoglycan staining, the cartilage surface retained a smooth appearance with minor evidence of fibrillation, suggesting limited to no damage to the collagenous portion of the ECM.

This was confirmed by the maintenance of joint tissue morphology at 7-months post-DTA-induction (Figure 4.2C). At closer inspection, morphological differences observed within the articular cartilage at earlier time points in the DTA mice were still visible, including reduced cellularity (empty lacunae) and heterogeneous safranin-O staining (Figures 4.2C, S4.3A). Yet, further decrease in cell density was not observed (Figure S4.3B) It is also important to note that although aggrecan (and by extension *Acan*-CreER^{T2}) is expressed in other joint tissues such as the synovium, no abnormal phenotypes were observed in aged DTA mice (Figure 4.2C), and there was no evidence of synovitis (Figure S4.2). OARSI histological scoring in DTA mice was significant ($p = 0.047$) compared to controls at 5 and 9 weeks after DTA-induction (Figure 4.2D), mainly driven by reduced safranin-O-stained matrix. However, no significant difference, rather a tendency of joint preservation, was observed in DTA mice with aging. Taken together, these data show that chondrocyte death alone is insufficient to induce cartilage degeneration and highlight an underlying ability of mouse articular cartilage to retain its integrity despite chondrocyte loss.

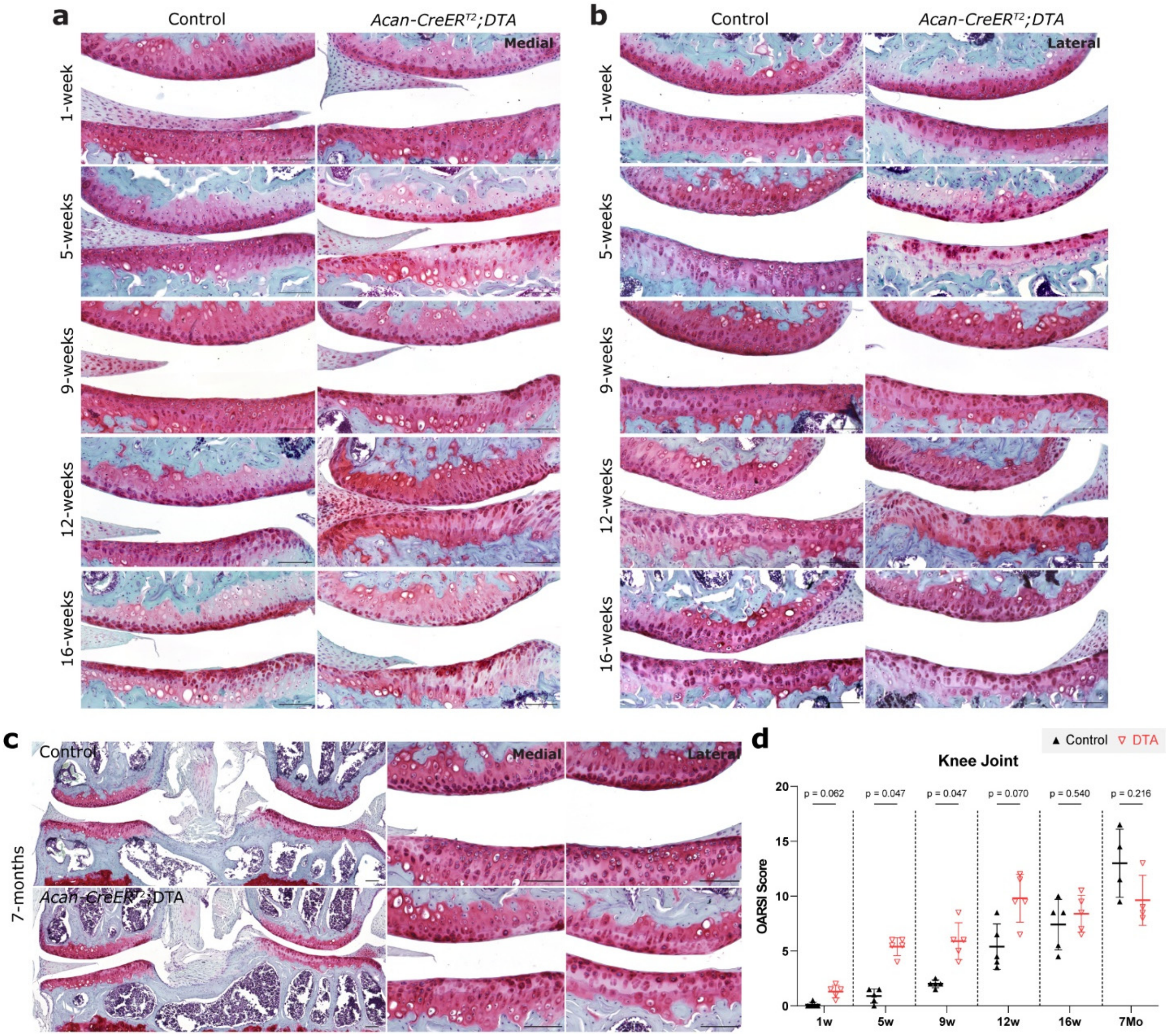
a
Control
Acan-CreER^{T2};DTA
Medial
1-week
5-weeks
9-weeks
12-weeks
16-weeks
b
Control
Acan-CreER^{T2};DTA
Lateral
1-week
5-weeks
9-weeks
12-weeks
16-weeks
c
Control
Acan-CreER^{T2};DTA
7-months
Medial
Lateral
d
▲ Control ▽ DTA
Knee Joint
p = 0.062
p = 0.047
p = 0.047
p = 0.070
p = 0.540
p = 0.216
OARSI Score
20
15
10
5
0
1w
5w
9w
12w
16w
7Mo

Figure 4.2. Histopathological comparison of articular cartilage in control and Acan-CreER^{T2}; DTA mice. Representative safranin-O stained sections of (A) medial and (B) lateral tibiofemoral compartments up to 16-weeks post-4-OHT treatment demonstrate structural changes in articular cartilage after DTA-induced chondrocyte depletion, but no progression of cartilage damage was observed. Of note are focal areas where hypocellularity is associated with diminished proteoglycan (lighter pink) staining and nearby chondrocytes where intense pericellular proteoglycan (deep red) staining is observed. (C) No apparent deleterious effects were observed on knee joint surfaces, even 7-months following DTA-induced chondrocyte depletion. (D) Pathological changes quantified by OARSI scoring did not demonstrate progression to an OA-like phenotype. Data represent means ± SD (*n* = 5 mice/group, sum of compartment scores). Mann-Whitney U non-parametric test control vs. DTA mice for individual endpoints ($\alpha \leq 0.05$). *p*-value reported. Scale bars represent 100 μm.

4.4.3. DTA mice display transient upregulation of ADAMTS5 in articular cartilage

Upregulation of catabolic enzymes has been widely implicated in the degeneration of the cartilage ECM (Glasson et al., 2005). Therefore, the cartilage of controls and *Acan*-CreER^{T2}; DTA mice were evaluated for expression of ADAMTS5 and MMP3. Interestingly, ADAMTS5 expression was increased in the central load-bearing regions of DTA mice articular cartilage by 9-weeks post-induction (Figure 4.3A, C-D), particularly in the medial compartment. However, by 12-weeks, expression was diminished and comparable to controls. MMP3 expression in DTA mice was more varied, peaking at 9-weeks, but still comparable to controls at all time points (Figure 4.3B, E-F). These findings suggest that while an increase in protease expression is induced post-depletion, the articular cartilage has an intrinsic regulatory capacity that halts catabolic activity before it can proceed to a chronic phenotype, contrasting with what is observed in surgically induced models of OA.

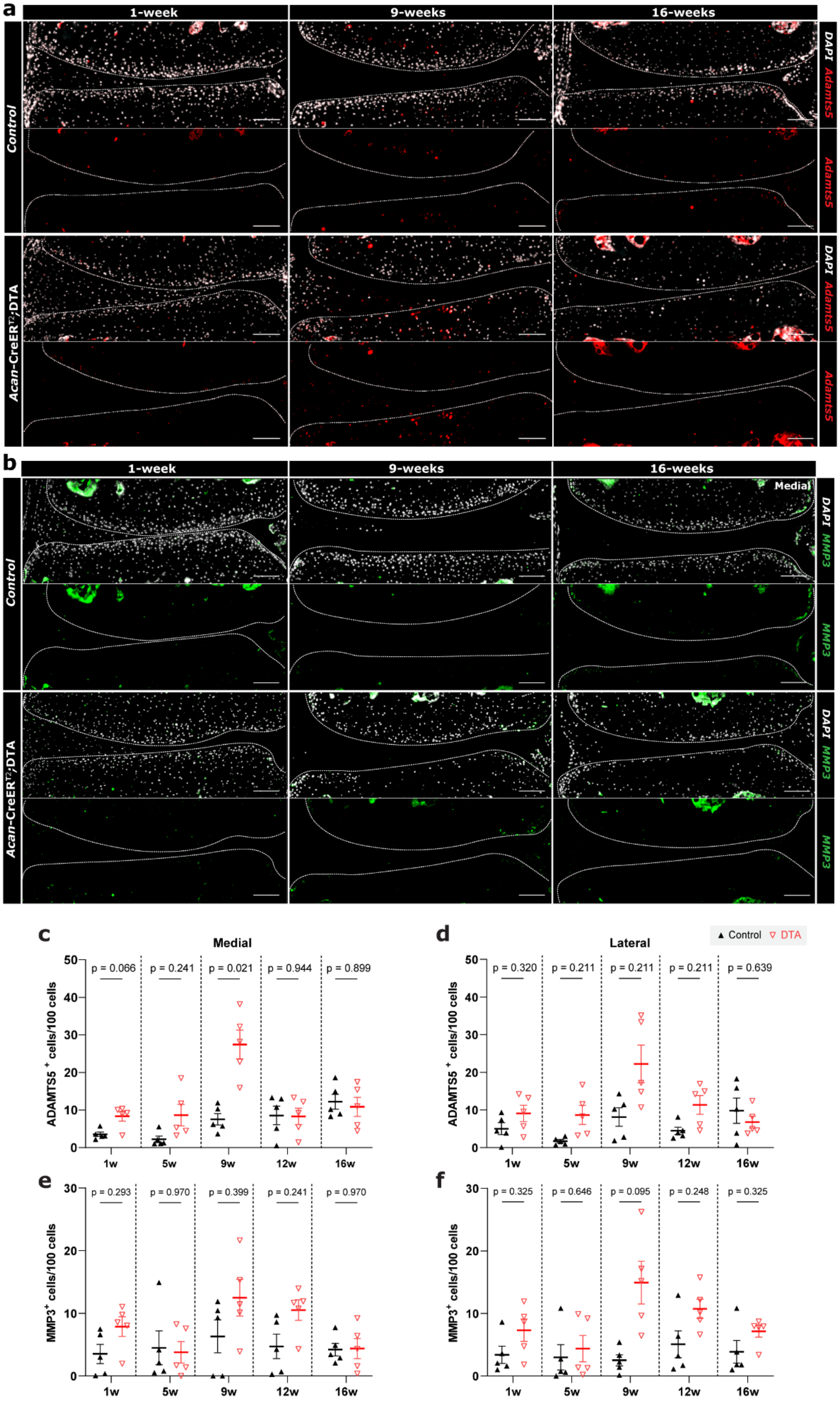
a
1-week
9-weeks
16-weeks
Control
Acan-CreERT2;DTA
DAPI Adamts5
Adamts5
b
1-week
9-weeks
16-weeks
Medial
Control
Acan-CreERT2;DTA
DAPI MMP3
MMP3
c
Medial
ADAMTS5+ cells/100 cells
p = 0.066
p = 0.241
p = 0.021
p = 0.944
p = 0.899
1w
5w
9w
12w
16w
d
Lateral
▲ Control ▽ DTA
ADAMTS5+ cells/100 cells
p = 0.320
p = 0.211
p = 0.211
p = 0.211
p = 0.639
1w
5w
9w
12w
16w
e
MMP3+ cells/100 cells
p = 0.293
p = 0.970
p = 0.399
p = 0.241
p = 0.970
1w
5w
9w
12w
16w
f
MMP3+ cells/100 cells
p = 0.325
p = 0.646
p = 0.095
p = 0.248
p = 0.325
1w
5w
9w
12w
16w

Figure 4.3. Transient upregulation of ADAMTS5 following DTA-induced chondrocyte depletion. Immunofluorescence analysis and corresponding quantification showed weak expression of (A, C-D) ADAMTS5 and (B, E-F) MMP3 in *Acan*-CreER^{T2}; DTA mice articular cartilage up to 5-weeks after DTA-induced chondrocyte depletion, which was comparable to controls. However, expression of ADAMTS5 was increased by 9-weeks, particularly in the tibial plateau, and extended further from the surface of central cartilage regions. MMP3 immunostaining was variable and increased by 9-weeks, although still comparable to controls. Average cell counts ± SD ($n = 5$ mice/group, 3 sections/mouse) are shown. Student's *t-test* of control vs. DTA mice for individual endpoints ($\alpha \leq 0.05$). p-value reported. Scale bars represent 100 µm.

4.4.4. Effect of chondrocyte depletion on stiffness and thickness of articular cartilage

While the articular cartilage maintained its morphology post-depletion, we investigated if and how chondrocyte depletion impacted the tissue biomechanically. Alterations to the structure and composition of the ECM can influence the mechanical behaviour of articular cartilage and precede histological evidence of disease (Doyran et al., 2017). Recently, we validated a testing protocol for microscale mechanical characterization of mouse femoral cartilage *in situ*, wherein indentation mapping captured spatial differences in the mechanical properties of healthy vs. degenerated articular cartilage (Masson et al., 2022). Therefore, we performed indentation test at 31 predefined positions distributed across the lateral and medial femoral condyles of fresh murine cartilage samples, followed by needle probing thickness measurements in adjacent locations (Figure 4.4A). We analyzed five samples per genotype per timepoint and compared the spatial distribution of thickness and instantaneous modulus from DTA mice to age-matched controls. Macroscopically, no gross visible lesions or areas of cartilage erosion were observed in mouse femoral condyles post-depletion (Figure 4.4B). Mappings of the thickness (Figure 4.4C) and instantaneous modulus (Figure 4.4D) for the femoral condyles allowed us to visually discern variations in the spatial distribution of these parameters across timepoints, within and between genotypes. Overall, we did not observe any overt differences in the DTA cartilage thickness patterns compared to controls (Figure 4.4C, E-F), except for a slight increase in tissue thickness at 5-weeks - albeit non-significant (Figure 4.4E-F) it also correlated with a low stiffness region in the medial condyle (Figure 4.4D). DTA mouse cartilage displayed a stiffening trend at the mid-to-peripheral regions on the medial and lateral condyles with aging, up to 12-weeks (Figure 4.4D), which was also reflected numerically (Figure 4.4G-H). Effects of aging on mechanical properties cannot be ruled out, as a similar pattern of compressive instantaneous modulus was seen in age-matched controls (Figure 4.4D). Many biochemical and architectural features influence cartilage's mechanical behavior (Mansour, 2013), and site-specific differences are reported within and between articular cartilage surfaces. At a high physiological strain rate, used in the current study, the instantaneous stiffness response is mainly influenced by the high fluid pressurization and collagen fibril network of the articular cartilage matrix (Julkunen et al., 2008). Therefore, an increase in cartilage thickness despite diminished proteoglycan staining at 5-weeks, coupled with increased stiffness at later stages, suggests that variations in water content and/or collagen fibril network, secondary to proteoglycan loss, may have occurred. Nevertheless, consistent with microscopic assessment and histological findings, little to no differences in cartilage function were observed between controls vs. chondrocyte-depleted mice.

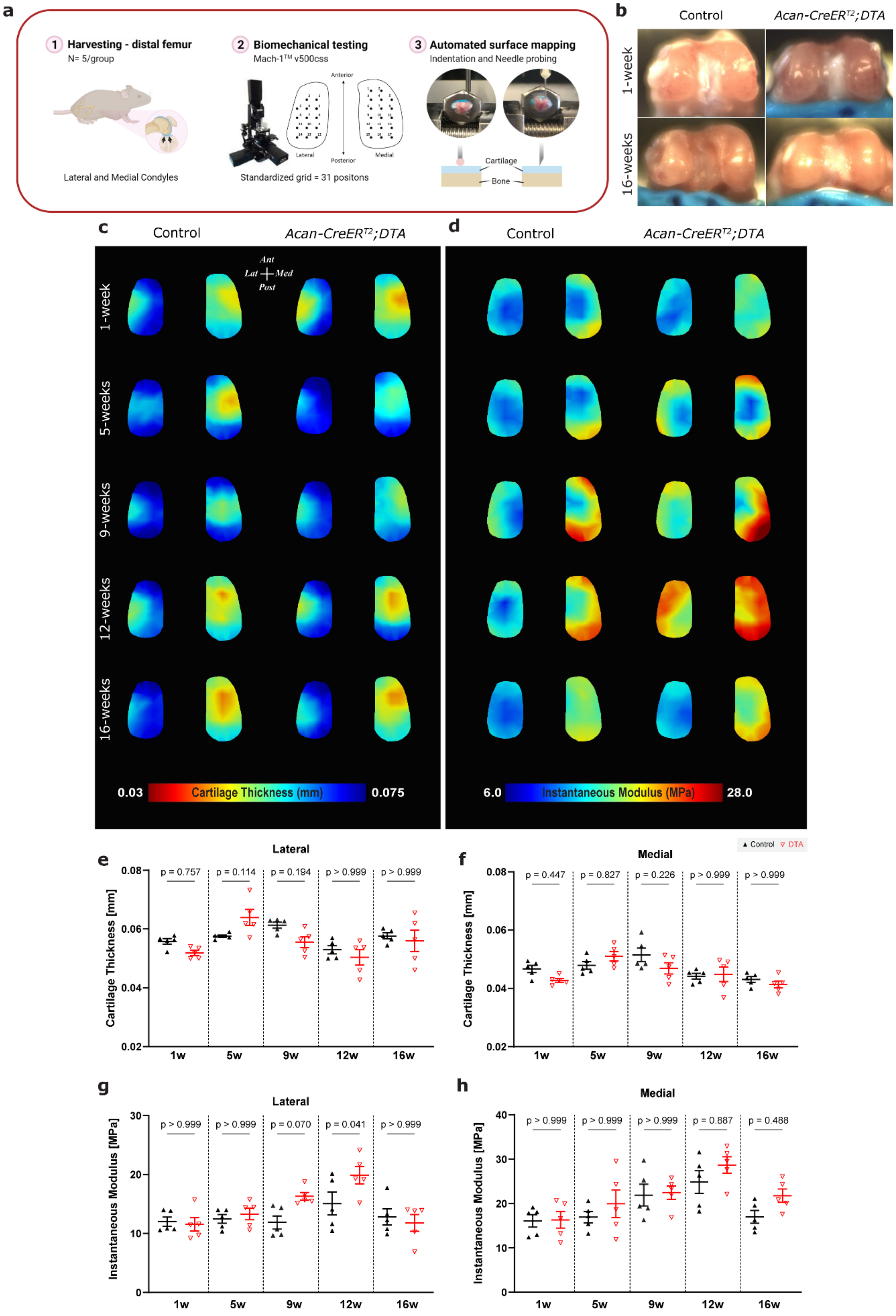
a
1 Harvesting - distal femur
N= 5/group
Lateral and Medial Condyles
2 Biomechanical testing
Mach-1™ v500css
Anterior
Lateral
Posterior
Medial
Standardized grid = 31 positons
3 Automated surface mapping
Indentation and Needle probing
Cartilage
Bone
b
Control
Acan-CreER^T2;DTA
1-week
16-weeks
c
Control
Acan-CreER^T2;DTA
Ant
Lat
Med
Post
1-week
5-weeks
9-weeks
12-weeks
16-weeks
0.03
Cartilage Thickness (mm)
0.075
d
Control
Acan-CreER^T2;DTA
6.0
Instantaneous Modulus (MPa)
28.0
▲ Control ▽ DTA
e
Lateral
Cartilage Thickness [mm]
0.08
0.06
0.04
0.02
p = 0.757
p = 0.114
p = 0.194
p > 0.999
p > 0.999
1w
5w
9w
12w
16w
f
Medial
Cartilage Thickness [mm]
0.08
0.06
0.04
0.02
p = 0.447
p = 0.827
p = 0.226
p > 0.999
p > 0.999
1w
5w
9w
12w
16w
g
Lateral
Instantaneous Modulus [MPa]
30
20
10
0
p > 0.999
p > 0.999
p = 0.070
p = 0.041
p > 0.999
1w
5w
9w
12w
16w
h
Medial
Instantaneous Modulus [MPa]
40
30
20
10
0
p > 0.999
p > 0.999
p > 0.999
p = 0.887
p = 0.488
1w
5w
9w
12w
16w

Figure 4.4. Functional analysis of articular cartilage. (A) Schematic overview of experimental design employed for biomechanical testing of murine articular cartilage using the Mach-1^{TM} v500css mechanical tester (B) No visible macroscopic changes were present in the articular cartilage of femoral condyles by 16-weeks post DTA-induction. Colour maps of averaged values and corresponding site-specific distributions comparing lateral and medial condyle cartilage thickness (C, E-F) and instantaneous modulus (D, G-H), as determined by Hayes et al. (1972) elastic model at 20% strain. Data highlights slight differences between cartilage thickness distributions across time points between genotypes, albeit with no significant differences in averaged thickness for either condyle observed. Similarly, the instantaneous modulus mapping points to areas of cartilage matrix stiffening at 9- and 12-weeks, which happen to a lesser extent in the control samples, mainly within the mid-to-peripheral regions of the condyles, returning to comparable values by 16-weeks. This trend was also shown quantitatively, albeit with borderline significance only displayed at the lateral condyle at 12-weeks. Averaged thickness or instantaneous modulus ± SEM (n = 5 mice/group, average of 27-31 positions/mouse) are shown. Student's t-test control *vs*. DTA mice for individual endpoints ($\alpha < 0.05$). p-values reported.

4.5. Discussion

This study investigated the impact of *in vivo* targeted chondrocyte depletion on articular cartilage homeostasis in adult mice and whether the resulting tissue response post-depletion was biased towards cartilage degeneration and phenotypic changes associated with OA. In mature cartilage, chondrocytes rarely proliferate, and through a balance between anabolism and catabolism, these cells continuously affect tissue properties by modulating ECM composition. While chondrocyte-mediated matrix remodelling is considered essential in homeostasis and disease, our findings demonstrate that DTA-induced chondrocyte death is insufficient to drive phenotypic changes associated with OA, nor cartilage failure. Our results are consistent with Zhang *et al.* (Zhang et al., 2016), who conditionally depleted the surface layer chondrocytes using a *Prg4*-CreER^{T2}; DTA approach in young mice. A recent follow-up study by the same group reported similar findings after targeted chondrocyte depletion at the temporomandibular joint (He et al., 2021). Both studies also reported that genetic-depleted chondrocyte areas were not repopulated over time, and we observed the same effect over seven months in the current study. As we were able to independently phenocopy the main findings of *Zhang et al.* (Zhang et al., 2016)*,* this shows that murine articular cartilage is able to tolerate a significant loss of chondrocytes and compensate for the perturbed micro-environment in the absence of chondrocyte replenishment. Furthermore, regardless of the mechanism(s) involved in the depletion of chondrocytes (e.g., *Prg4*$^{+ve}$ vs. *Acan*$^{+\mathrm{ve}}$ cells), progression to a degenerative phenotype is not observed.

While achieving effective 4-OHT recombination in mature articular cartilage can be challenging because of the avascular nature of the tissue, when using the tdT reporter mouse, we demonstrated Cre-recombination in >65% of DAPI-labelled articular chondrocytes. Yet, cell depletion in *Acan*-CreER$^{\mathrm{T2}}$; DTA mice 1-week post-4-OHT treatment was lower than anticipated (<20% chondrocyte depletion). This variability may be explained by differences in the design of the two transgene constructs and the promoter driving expression for the tdT reporter vs. DTA strain. Notably, the tdT reporter mice contain a strong exogenous promoter (CAG). CAG-driven transgene expression has been previously shown to yield 8-10-fold higher expression levels than the endogenous ROSA26 promoter (Chen et al., 2011; Tchorz et al., 2012). Also, the lag between DTA induction and cell death (Brockschnieder et al., 2004); and the time required for the DNA to no longer be DAPI reactive also need to be considered. The marked increase in apoptotic cells 1-week post-4-OHT injections suggests that the effect of Cre-recombination on chondrocyte viability was higher than captured initially by nuclei count, and the further decline in cell density by 5-weeks likely resulted from that initial DTA-induced death.

Overall, we have demonstrated that cartilage structural heterogeneity arises post-DTA mediated chondrocyte depletion. Yet, the subsequent tissue response leads to an adaptive rather than a pathological remodelling outcome, contrasting with what is routinely observed after surgical or chemical insults that lead to chondrocyte death (Figure 4.5). Marked alterations in cartilage proteoglycan staining by 5-weeks in both the medial and lateral compartments are consistent with the relatively rapid turnover of aggrecan (Heinemeier et al., 2016; Maroudas et al., 1998). Furthermore, DTA inhibition of chondrocyte protein synthesis and a subsequent net loss of cellular density at early stages clearly impacted the degree of matrix deposition in the cartilage. The restoration of proteoglycan staining by 9-weeks and maintenance thereon, coupled with the observation of enriched safranin-O staining at surrounding areas of surviving chondrocytes (starting at 5-weeks), provide evidence of enhanced proteoglycan synthesis in the remaining cells and potential compensatory anabolic responses. Similar outcomes have been observed in animal studies of joint unloading followed by remobilization (Säämänen et al., 1990; Setton et al., 1994; Vanwanseele et al., 2002), whereby the implementation of physiological loading is able to ameliorate catabolic phenotypes and revert proteoglycan synthesis and content, all of which were negatively impacted by the absence of mechanical stimuli. Our findings support the view that acute proteoglycan loss alone is not a determinant of pathological progression of cartilage degeneration (Bay-Jensen et al., 2010; Little et al., 2009).

Chondrocyte depletion induced in 2-month old *Acan*-CreER^{T2}; DTA mice did not lead to progressive articular cartilage loss or apparent surface damage up to 7-months later. Simon *et al.* (Simon and Green, 1971) showed similar results for rabbit cartilage after localized freezing, whereby cryoprobe-driven chondrocyte depletion resulted in focal reduction in proteoglycan staining, yet the tissue maintained structural appearance six months post-insult. Another approach used to explore the relationship between chondrocyte death and cartilage degeneration *in vivo* utilizes intra-articular injections of monosodium iodoacetate (MIA), an inhibitor of cellular glycolysis which leads to cell death. When used in rodents, the severity of joint degeneration is dose-dependent (Guingamp et al., 1997; Udo et al., 2016), with MIA-injected joints typically showing rapid progression of pathology, including cartilage fibrillation and erosion, loss of proteoglycan staining, synovial inflammation, subchondral bone sclerosis and pain (Guingamp et al., 1997; Guzman et al., 2003; Mohan et al., 2011; Udo et al., 2016). The divergence in outcomes between MIA and DTA cell depletion models might be due to the induction of inflammation in the MIA model, which is absent following DTA expression in our study, as well as in Zhang *et al.* (2016). Collectively, these results suggest that chondrocyte depletion in isolation is not a critical injury to the cartilage since it does not result in a degenerative joint phenotype (Figure 4.5). Yet, it would be of interest to induce joint/synovial inflammation in the DTA-induced model to determine how this affects the phenotypic outcome.

One aspect that merits discussion is the ongoing loss of chondrocytes from weeks 1-16 post-DTA induction. Our experimental procedure was not developed to address the mechanisms resulting in DTA-independent cell loss at later time points. Still, it is reasonable to speculate that several factors acted in concert. Having said that, we did notice that post-DTA population decline was preferentially localized at central load-bearing regions of femoral condyles and tibial plateaus over time. This might suggest an excessive biomechanical burden on the residual population, thus predisposing cells in areas of higher mechanical demand to phenotypic instability and/or direct injury.

There is a general consensus that chondrocytes can alter their metabolic phenotype in response to mechanical and biochemical stresses (Vincent and Wann, 2019; Zheng et al., 2021), consequently influencing matrix adaptation. Yet, the threshold for irreversible tissue disruption and shift into a pathological phenotype remains unclear. Studies involving deficiency or suppression of proteolytic enzymes in mice (Clements et al., 2003; Glasson et al., 2005; Hoshi et al., 2017; Little et al., 2009) highlight the critical role alterations in metabolic homeostasis play in cartilage ECM breakdown and OA onset and progression. For example, in ADAMTS5 knockout mice, the absence of this aggrecanase protects the articular cartilage from degeneration after surgically induced OA (Glasson et al., 2005). Furthermore, mice deficient in MMP13 collagenase activity are also protected against cartilage erosion in a surgical OA model but not aggrecan depletion (Little et al., 2009), demonstrating the importance of collagen degradation in the progression of OA. In contrast, MMP3-knockout mice display accelerated cartilage degeneration when subjected to surgically induced OA (Clements et al., 2003), pointing to a potential beneficial role of MMP3 during tissue injury response. Here, we observed upregulation of ADAMTS5 and MMP3 with a peak at 9-weeks post-DTA induction; however, the expression of these proteases returned to baseline levels three weeks later. Furthermore, the transient upregulation was not associated with structural damage to the articular cartilage. This suggests that even when catabolic responses are activated in the cartilage, depending on the insult, they can be endogenously resolved without initiating a cascade of degenerative processes leading to OA.

Regarding the differences observed in the biomechanical properties of the cartilage post-DTA cell depletion, Stolz *et al.* (Stolz et al., 2009) previously reported an age-dependent increase in nanostiffness, but not microstiffness in healthy mouse articular cartilage. It is important to note that focal indentation induces both tensile and compressive stresses, and collagen architecture affects tensile behaviour. Therefore, it is reasonable to assume that regional variations in collagen architecture would result in corresponding differences in measured mechanical stiffness. Furthermore, short-term exposure of cartilage constructs to chondroitinase ABC promotes transient proteoglycan depletion with a concomitant increase in dynamic compression modulus (Bian et al., 2009). A recent study by Merrild *et al.,* (2022) reported that enzymatic proteoglycan depletion improved endogenous repair of articular cartilage defects in the absence of chondrocytes through intrinsic collagen fibril formation. Together, these results, including our own, suggest that the transient loss of proteoglycan may actually be beneficial to the collagen-based ECM, whereby stiffening may protect cartilage from excessive strain. Yet, the critical threshold between maintenance vs. degeneration is potentially temporal in nature. An experimental design focused on temporally controlling aggrecan expression in the cartilage may address this hypothesis. Additional metrics of tissue biochemistry may also help explain site-specific differences in stiffness.

As mentioned earlier, it would be interesting to assess how the cartilage response changes in these cell depletion models within the context of an altered microenvironment induced by surgical or traumatic injury, and whether chondrocyte depletion reduces susceptibility to cartilage degeneration, as shown by Zhang *et al.*(Zhang et al., 2016). Given the role of mechanical stimulus on chondrocyte metabolism/gene expression and ECM remodelling (Gilbert et al., 2021; Vincent and Wann, 2019), further exploration on the effects of exercise and joint unloading following cell depletion would also be of interest. Furthermore, characterization of cellular/molecular level changes following DTA-induced cell depletion and assessment of cartilage relaxation properties (i.e., equilibrium modulus) over time would help us gain key insights into the spatial heterogeneity in cell death and the mechanisms involved in cartilage preservation.

In summary, we have shown that *Acan*-CreER^{T2}; DTA model can induce a significant level of hypocellularity in the mature articular cartilage, but even with this level of insult, cartilage can maintain structural and functional competency. Many have suggested a chicken vs. egg scenario in chondrocyte death vs. cartilage degeneration, and we can clearly say that chondrocyte death is not analogous to the chicken in this scenario… or wait, is it the egg?

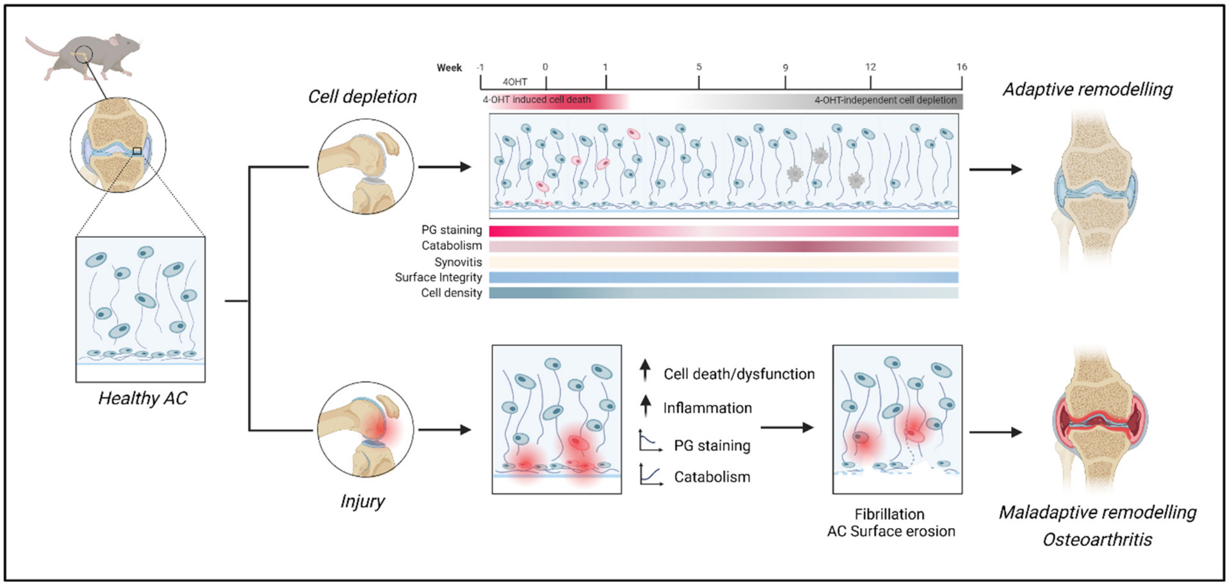
Week
-1
0
1
5
9
12
16
4OHT
4-OHT induced cell death
4-OHT-independent cell depletion
Cell depletion
Adaptive remodelling
PG staining
Catabolism
Synovitis
Surface Integrity
Cell density
Healthy AC
Injury
Cell death/dysfunction
Inflammation
PG staining
Catabolism
Fibrillation
AC Surface erosion
Maladaptive remodelling
Osteoarthritis

Figure 4.5. Summary schematic reflecting the difference in tissue response after chondrocyte depletion compared to commonly used models of post-traumatic or chemically induced mouse articular cartilage injury. Cartilage-specific chondrocyte depletion after 4-OHT-induced DTA expression leads to adaptive but non-pathological tissue remodelling in the articular cartilage. In contrast, a progressive pathophysiological phenotype is typically displayed after chemical or trauma-induced tissue disruption. AC: articular cartilage, PG: proteoglycan.

4.6. Acknowledgments

This work was supported by grants from Natural Sciences and Engineering Research Council (NSERC) of Canada RGPIN-2014-04586; Canada Foundation for Innovation; the Calgary Foundation, Grace Glaum Professorship. A.O.M. was funded by the University of Calgary and Alberta Innovates' graduate scholarships and R.K was supported by the Canada Research Chairs program. The funders had no role in study design, data collection and analysis, decision to publish, or preparation of the manuscript. The authors would like to thank the Cumming School of Medicine ARC staff for assistance with animal husbandry. Figure 4.5 and some graphics used in Figures 4.1 and 4.4 were created with biorender.com.

4.7. Author's contributions

A.O.M. and R.K. conceived, designed, and oversaw experiments with scientific assistance from J.B. and W.B.E. A.O.M. performed all experiments, analyzed data, and wrote the manuscript. J.M.C. and K.C. assisted with data collection. R.K., assisted with data interpretation. All authors were involved in editing the manuscript.

4.8. Supplementary information

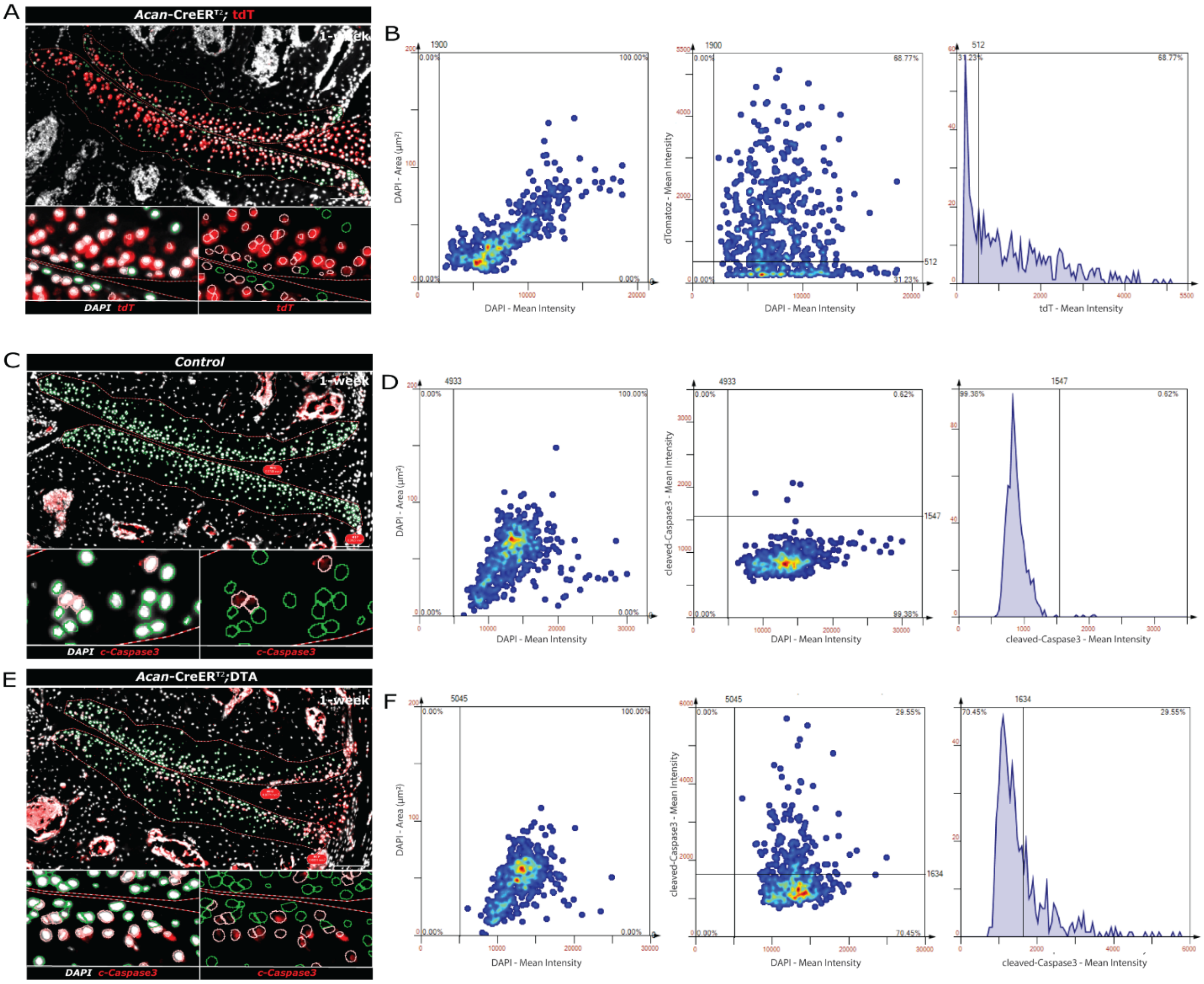
A
Acan-CreER^{T2}; tdT
1-week
DAPI tdT
tdT
B
1900
DAPI - Area (µm²)
DAPI - Mean Intensity
0.00%
100.00%
dTomatoz - Mean Intensity
68.77%
31.23%
512
tdT - Mean Intensity
C
Control
1-week
DAPI c-Caspase3
c-Caspase3
D
4933
0.62%
99.38%
1547
cleaved-Caspase3 - Mean Intensity
E
Acan-CreER^{T2};DTA
1-week
DAPI c-Caspase3
c-Caspase3
F
5045
29.55%
70.45%
1634
cleaved-Caspase3 - Mean Intensity

Figure S4.1. Immunofluorescence imaging analysis and quantification. Representative images of tibiofemoral cartilage showing contouring of regions of interest and corresponding gating strategy, wherein detected DAPI-positive nuclei are outlined in green and cells co-expressing fluorescence marker of interest are outlined in light pink for (A-B) tdtomato expression in *Acan*-CreER^{T2};tdT mice and cleaved caspase-3 expression in (C-D) control mice and (E-F) *Acan*-CreER^{T2};DTA mice 1-week after 4-OHT treatment.

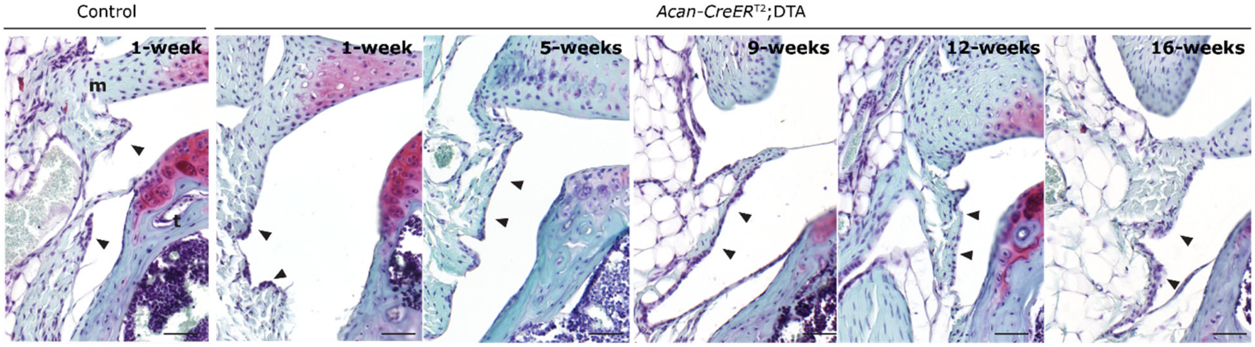

Figure S4.2. Safranin-O-stained frontal knee sections from control and *Acan*-CreER^{T2}; DTA mice 1-week and 1- to 16-weeks, respectively, post 4-OHT treatment. Tibia (t), meniscus (m) and synovium (arrowheads) are indicated. Note synovium does not appear to differ significantly between control and DTA mice, with a slight thickening of lining by 9-weeks post DTA-induced chondrocyte depletion. Scale bars represent 100 µm.

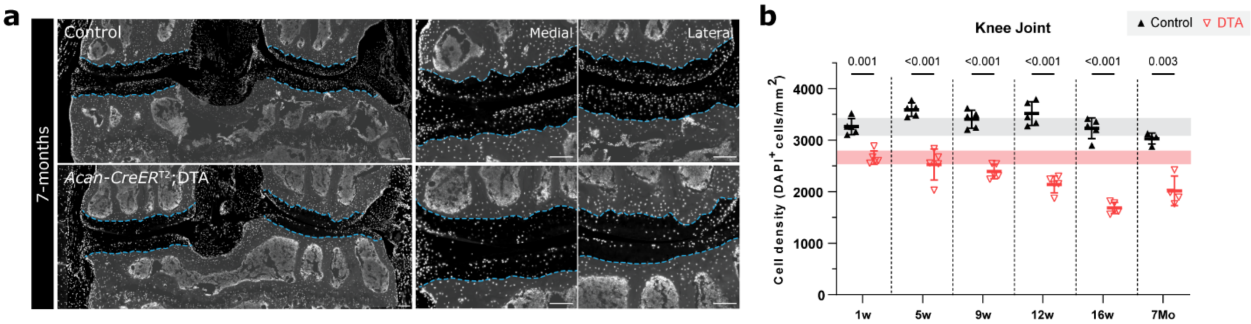

Figure S4.3. Articular cartilage 7-months post-4-OHT treatment demonstrate chondrocyte-depleted areas are maintained. (A) Representative images of knee joint and close ups of medial and lateral tibiofemoral compartment from control and DTA mice show chondrocyte depletion and hypocellularity are maintained with aging (7-months post-4-OHT). The dashed blue line delineates the osteochondral junction. Scale bars represent 100 µm. (B) Cell density (cell number/mm^2) in tibiofemoral cartilage (n = 4-5 mice/group, 3-6 sections/mouse) differed significantly between groups for all timepoints of assessment. Average cell counts ± SD from each genotype/treatment group are shown, and light-colored horizontal lines represent cell density range at 1-week post-4-OHT for control (light grey) and DTA mice (light red). Statistical significance was determined by Student's t-test ($\alpha = 0.05$), p-value reported.

Chapter Five: *Prg4* deficiency alters femur morphology

Anand O. Masson, Jay Devine, Nabangshu Das, Clarissa R. Coveney, Benedikt Hallgrimsson, Terence D. Capellini, Jeff Biernaskie, W. Brent Edwards, and Roman J Krawetz

My contributions to this work were as follows:

- *Contributed to study design*
- *Data acquisition and data analysis, except image processing and geometric morphometrics*
- *Conceptualized the manuscript figures and wrote the manuscript.*

5.1. Abstract

Many studies have reported on the role of Proteoglycan-4 (PRG4, aka lubricin) in the reduction of friction between cartilage surfaces with a specific focus on chondroprotection within the joint. Disruption of the *Prg4* gene in humans and mice leads to premature joint failure, hallmarked by synovial hyperplasia and premature articular cartilage fibrillation. Our lab has published extensively using *Prg4* knockout mice (*Prg4*$^{-/-}$) and have consistently noticed variable distal femoral morphology in these animals when compared to *Prg4*$^{+/+}$ wild-types (WT). This prompted me to undertake a quantitative study examining joint element size and shape to elucidate if this phenotype was consistent in a larger sample size. High-resolution X-ray microscopy (XRM) imaging was obtained from WT and *Prg4*$^{-/-}$ mice between 8- and 36-weeks of age. We then employed geometric morphometrics to characterize mouse femora shape changes, which were correlated to cross-sectional histological findings. We have shown that *Prg4*$^{-/-}$ femora vary in size and shape compared to WT controls. Distal femurs in *Prg4*$^{-/-}$ mice are enlarged, extended (anteroposterior) and narrower (mediolateral), with the largest regional deviations being traced to trochlear groove, epicondyles, and medial condyle. Additionally, quantifiable changes in condylar articular cartilage thickness were associated with abnormal compressive biomechanical properties. Collectively, this data suggests the consequence of PRG4 loss extends beyond joint homeostasis and critically impacts joint morphology.

5.2. Introduction

The knee joint is an inherently complex anatomical structure. Its geometry to the varied properties and structural requirements of its constituent tissues are of critical importance for locomotion and daily activities. The distal femur comprises two distinct articulating surfaces, namely patellofemoral (PF) and tibiofemoral (TF) articulations, and their morphological features greatly impact the biomechanical properties and stability of the knee joint (Masouros et al., 2010). Knee joint formation initiates during embryonic development and relies on a series of coordinated cellular and molecular events coupled with mechanical signals for proper patterning and specification of individual joint structures. However, the mature morphological features of each knee joint element (e.g., compartments) are determined postnatally. Likewise, the articular cartilage acquires its specialized internal structure and mature shape through postnatal remodelling (Decker et al., 2017; P. Julkunen et al., 2009). Yet, the precise regulatory mechanisms driving morphogenesis of the knee joint and articular cartilage, as well as postnatal growth and maturation, remain elusive.

Mutations in genes responsible for synthesizing, assembling, and modifying cartilage extracellular matrix components have been implicated throughout the gradient of known skeletal abnormalities. Disruptions in these developmental and remodelling processes can lead to structural and functional issues in multiple tissues within synovial joints, from bones to cartilage, ligaments, and menisci, resulting in non-physiological loading of the knee joint, increasing the risk of injury and degenerative conditions like osteoarthritis (OA). One gene of interest is PRG4 (Proteoglycan-4), a mucin-like glycoprotein mostly known as a lubricating and chondroprotective molecule in synovial joints. *In situ* hybridization and genetic lineage tracing studies have established that *Prg4*-expression is upregulated during the later stages of mouse embryogenesis (~E17.5) and is enriched within the newly forming synovial membrane and articular cartilage (Decker et al., 2017; Koyama et al., 2008; Rhee et al., 2005). Its expression is retained in the synovium and articular cartilage surfaces of adult joints, and *Prg4* protein products are found at high levels in the synovial fluid and bound to the surface of the articular cartilage and synovium where it is believed to be essential for joint tissue homeostasis and functionality (Flannery et al., 1999; Rhee et al., 2005; Schmidt et al., 2007). Not surprisingly, it has been demonstrated that loss-of-function mutations in this gene have been implicated in joint pathology in mice and humans.

In humans, *PRG4* mutations have been linked to camptodactyly-arthropathy-coxa vara-pericarditis (CACP) syndrome (Bahabri et al., 1998; Marcelino et al., 1999), a rare genetic condition with various joint-related clinical features. Disease manifestation includes congenital or early childhood-onset flexion deformity of phalangeal joints (camptodactyly) and arthropathy of larger joints, such as the knee, associated with swelling, restricted range of motion, non-inflammatory synovial hyperplasia and articular cartilage degeneration (Mannurita et al., 2014; Marcelino et al., 1999). Moreover, decreased levels of PRG4 have been observed in the synovial fluid in patients with OA or rheumatoid arthritis (RA) degenerative joint diseases (Kosinska et al., 2015). In mice, *Prg4*-null (*Prg4*$^{-/-}$) mutations recapitulate many of the phenotypic changes identified in CACP patients, including synovial hyperplasia, abnormal cartilage surface, restricted range of motion and joint failure (Rhee et al., 2005).

Given the onset expression of Prg4 during embryonic development, it is surprising that knee joints have been reported to look phenotypically normal at birth (Abubacker et al., 2019; Rhee et al., 2005). Yet, previous investigations during early post-natal development have demonstrated microstructural changes in subchondral bone and articular cartilage, including increased bone porosity, disrupted collagen structure and arrangement in articular cartilage, which is also thickened (Abubacker et al., 2019; Coles et al., 2010; Jay et al., 2007; Maenohara et al., 2021). Prg4 expression has also been proposed to regulate bone skeletogenesis in mice (Novince et al., 2013, 2012). However, to date, no study has employed a quantitative approach to empirically determine the impact of Prg4 in overall femoral morphology.

Building upon anecdotal evidence gained from multiple investigations on *Prg4*$^{-/-}$ mice, we employed histological cross-sectional evaluation and landmark-based geometric morphometrics to identify, quantify and characterize variations in the distal femoral morphology of *Prg4*$^{-/-}$ mice in adulthood compared to age-matched controls. Since the geometry and anatomy of articular surfaces relate to their function, we also examined regional differences in condyle cartilage thickness and indentation biomechanics. Although the published literature recognizes that loss of Prg4 does not impede developmental knee joint formation, its role in tissue patterning and joint structure/geometry/anatomy remains obscure and could have implications on proper maintenance and function of these elements.

5.3. Materials and Methods

5.3.1. Animals

All animal procedures were performed in accordance with the Canadian Council of Animal Care guidelines and approved by the University of Calgary Animal Care Committee (protocols AC16-0043 and AC20-0042). *Prg4*$^{-/-}$ mice (*Prg4*$^{\text{tm1Mawa/J}}$, stock # 025737), whose generation has been described previously (Rhee et al., 2005), and wild-type (WT) mice (C57BL/6J, stock #000664) were obtained from The Jackson Laboratory and maintained in-house at the University of Calgary. *Prg4*$^{-/-}$ mice were backcrossed to C57BL/6J for ten generations and genotyping from ear biopsies was carried out to confirm homozygous *Prg4*$^{-/-}$ status. Age-matched C57BL/6J (backcrossing colony littermates, referred to as WT) mice were used as controls. All animals were housed under a standard light cycle and had access to food and water *ad libitum*. Mice were euthanized at postnatal weeks 8, 12, 16, 20, 25, and 36. Hindlimb specimens from at least four animals per group were used to ensure reproducibility in histological, morphometrical and biomechanical analyses.

5.3.2. Histology

Hindlimbs were fixed in 10% neutral formalin buffer (NBF) solution (Fisher Scientific), decalcified using 10 w/v EDTA (pH 7.4) for 2.5 weeks with solution changes every other day. During paraffin embedding, specimens were oriented such that the typical knee joint flexion was preserved, and the tibia was kept parallel to the sectioning surface. Serial sections (10 μm) were mounted onto Superfrost Plus glass slides (Fisher Scientific) for further analysis. To examine the gross joint morphology and degree of cartilage degeneration, slides were stained in Safranin-O/Fast-green and scored using the Osteoarthritis Research Society International (OARSI) mouse histopathological scoring system (Glasson et al., 2010). Articular cartilage in the mid-to-posterior load-bearing regions of the knee, identified by the presence of cruciate ligaments were scored in each animal, and the sum of the maximum histopathological score of two independent scorers (one blinded), per knee joint femoral compartment was reported.

5.3.3. *3D X-ray microscopy (XRM) imaging*

To obtain a three-dimensional representation of the complex femoral shape and determine the effect of *Prg4* loss-of-function on morphology and associated age-related changes, right murine distal femurs (*n* = 4-5 per genotype) were scanned at a 4.4 µm isotropic voxel resolution using X-ray microscopy (XRM) imaging system (Versa 520, Carl Zeiss X-ray Microscopy, USA). Specimens were fixed in 10% NBF for 24 hours and preserved in 70% ethanol until the day before scanning (no more than three days), when they were incubated in 1% phosphotungstic acid (PTA) solution for 18-24h prior to scanning for optimal contrast enhancement (Das Neves Borges et al., 2014; Masson et al., 2022). Specimens were enclosed in a Kapton straw chamber (5 mm diameter, GoodFellow Cambridge) vertically (Figure 5.1a) with PTA solution on the bottom of the chamber to minimize specimen desiccation. Scan parameters were: 40kVp voltage, 3W power, 2001 projections. Image projections were reconstructed with the ZEISS XMReconstructor software.

5.3.4. *Morphology data acquisition*

To quantify phenotypic changes related to *Prg4* loss-of-function, we adapted a registration-based approach (Devine et al., 2020; Percival et al., 2019) to the femur to collect anatomical landmarks and segmentations for morphometric analysis. Since the femora were stained and thus susceptible to differential staining artifacts, we corrected for intensity non-uniformity using the N4 algorithm (Tustison et al., 2010) and normalized the intensities. Then, a subsample (*n* = 25) of the femur scans was funneled through a computer-automated workflow to generate a study-specific atlas or anatomical average. The atlas was labelled with 43 anatomical landmarks that provided sparse yet comprehensive coverage of distal femoral shape (Figure 5.2a). Also, atlas segmentation of cartilage, bone (including marrow space), and growth plate were carried out for volume measurements (Figure S5.2). Next, each specimen was non-linearly registered to the atlas. While the affine alignment was computed with a multi-resolution framework (Lerch et al., 2011), the subsequent non-linear alignment was performed with the SyN (Symmetric Normalization) algorithm (Avants et al., 2011). Afterwards, the affine and non-linear transformations were concatenated and inverted to propagate the atlas labels to each individual image. All image processing was performed on the ARC compute cluster at the University of Calgary using the open-source MINC (Medical Imaging NetCDF) software (https://github.com/BIC-MNI/minc-toolkit-v2).

5.3.5. Size and shape comparisons

To understand how genotype and age influence size variation across the femur, centroid size of each landmark configuration and volume of each segmented compartment were computed, to understand how genotype and age influence size variation across the femur. Centroid size was calculated as the square root of the sum of squared distances of all landmarks from their centroid (Rohlf and Slice, 1990). For shape comparisons, all landmark configurations were superimposed into a common shape space via Generalized Procrustes Analysis (GPA) (Gower, 1975; Rohlf and Slice, 1990). A series of geometric morphometric (GM) tests were then undertaken on the Procrustes shape data to examine the effects of genotype and age on femoral morphology. To account for confounders, femoral shape was regressed on sex to acquire sex-adjusted Procrustes shape variables. Group differences were evaluated using Procrustes analysis of variance (ANOVA) (Collyer and Adams, 2019) and further visualized using principal component analysis (PCA) and distance heatmaps. While the PCA visualizations involved deforming the mesh of the mean shape to the extremes od each PC via thin-plate spline, the heatmap visualizations involved deforming the mesh of the WT mean to the *Prg4*$^{-/-}$ via thin-plate spline (Bookstein, 1989). Then, the magnitude and direction of shape deviations at each point in the deformation were quantified. Comparison between WT and *Prg4*$^{-/-}$ mean femoral shape was carried out for each age (Figure 5.2d) and comparisons within each genotype across timepoints was carried out relative to their respective baseline 8-week-old (Figure S5.2e,f). Geometric morphometric analyses were performed in R with the geomorph (Adams et al., 2016), RRRP (Collyer and Adams, 2019, 2018) and Morpho packages (Schlager, 2017). Additional morphometric analyses (linear distance/angle) were carried out between WT and *Prg4*$^{-/}$ regarding specific traits of interest: trochlear groove depth (TD) and sulcus angle (SA), anteroposterior distance (length) of medial (M_{AP}) and lateral (L_{AP}) compartments, bicondylar width (BCW), intercondylar notch width (IN), condylar width (medial – MCW, lateral - LCW).

5.3.6. Condylar and trochlea cartilage RNA-seq data collection and analysis

The articular cartilage from the trochlea and condyles of C57BL6 mice was dissected under a light microscope in PBS on ice and collected in 2mL tubes containing 200 µl of TRIzol and a 5 mm stainless steel bead. Samples were obtained at postnatal stages P0, P30 and 1 year age (*n* = 4/group*)*. Right and left sides of each specimen were pooled and sample processing was carried out as previously described (Young et al., 2022). In brief, each sample underwent a homogenization process at 50 Hz frequency for 2 min. After a brief cooling period (1 min), samples were subjected to a final homogenization at the same frequency for an additional 2 min. Samples were stored at -80°C until RNA extraction. A phenol-chloroform reaction was initially employed for RNA extraction; thus, each sample was transferred into a new microcentrifuge Eppendorf tube with 200 µl of chloroform for every 1 ml of TRIzol present in the sample. After being thoroughly vortexed and incubated at room temperature for 2 min before being centrifuged at 4°C, 12,000g force for 5 minutes. Post centrifugation, the aqueous layer was carefully separated and moved into a new Eppendorf tube. Final RNA extraction was performed using the Zymo Direct-zol RNA MicroPrep kit according to the manufacturer's instructions, and the final RNA sample was eluted in 15 µl of nuclease-free water. The resultant RNA was quantified using a Qubit per the manufacturer's protocols. Samples were also nano-dropped to determine 260/230 and 260/280 values and stored at −80°C. Aliquots were also run on a TapeStation to determine their RNA integrity number (RIN) value, and only samples with RIN scores of 7 or higher were used for subsequent steps. Samples were normalized to a single concentration for cDNA library generation and sequencing, and libraries were prepared using KAPA mRNA Directional Library Preparation methods following the manufacturer's protocols. Twenty libraries were then run as quality control on a TapeStation. Then, a quantitative polymerase chain reaction (PCR) was performed on the library pool before sequencing the library on NextSeq High 2 × 38. The library was sequenced repeatedly using paired-end sequencing on three lanes to obtain a minimum of 10 million reads for each sample, with some samples requiring only one or two lanes. Computational analysis of RNA-seq data began with running

Fast QC on each Fastq file to determine the per-base sequence quality, GC content, etc., to ensure that all files met our standards. Because the samples had each been run on three lanes to achieve the desired number of reads, the reads for each sample were concatenated into a single file for R1 and a second file for R2. STAR version 2.6.0 was then used to map reads to the mouse genome, GRCm39. DESeq2 was then used to quantify differential *Prg4* expression and downstream comparisons.

5.3.7. Biomechanical assessment

Femurs (*n* = 5/group) were isolated under a dissection microscope (*Leica*). With condyles facing up, the femur bone shaft was placed into a pipette tip filled with cyanoacrylate glue. The construct was secured to a customized sample holder and affixed to the Mach-1 (v500csst Biomomentum) mechanical tester within a plexiglass chamber that contained PBS. Thirty-one measurements were performed across the medial and lateral femoral condyles by fast (0.02 mm/s) indentation of articular cartilage with a 0.3 mm diameter indenter probe to a displacement of 0.02 mm (Masson et al., 2022). Indentation tests were performed under stress-relaxation, after which a 30G needle replaced the indenter probe, and thickness was determined at immediately adjacent locations by needle probing technique, as previously described (Masson et al., 2022; Shepherd and Seedhom, 1999). Measurement points were performed in the same chronological order for all samples. Load-displacement curves were recorded for indentation and needle probing assessments and used for instantaneous modulus and cartilage thickness determination. Analysis was performed on Automated Indentation and Thickness Batch Analysis software (v.2.0.2 Biomomentum) to obtain cartilage thickness and instantaneous moduli (Poisson's ratio ν = 0.5), which was determined by fitting the Hayes model (Hayes et al., 1972) to the force/displacement curves. Heatmaps for data display were generated using Analysis-MAP software (v 1.0.0.2).

5.3.8. Statistical analysis

Statistical analyses aside from geometric morphometrics were performed using GraphPad Prism v.8. Unless stated otherwise, results are presented as mean ± standard error of the mean (SEM). For multiple comparisons, Holm-Šidák or Bonferroni correction was applied after performing Mann-Whitney non-parametric test or ANOVA. Statistical tests are noted in figure legend. A *p*-value less than 0.05 was regarded as statistically significant.

5.4. Results

5.4.1 Phenotypic abnormalities in Prg4$^{-/-}$ distal femur

Gross morphological differences in distal femurs were obvious at 8 weeks of age in *Prg4*$^{-/-}$ mice (Figures 5.1a, S5.1). At the macroscopic level, clear differences were observed including misshaped trochlear grooves with a deepened center sulcus (anterior view) and outward projection of its medial and lateral facets (medial side view and distal views). An enlarged general appearance was also visible compared to age-matched wild-type (WT) femurs (distal view). The posterior view demonstrated no noticeable morphological differences in femoral condyle shape (Figure 5.1a). With aging, some of the described morphological traits appeared to change. For instance, posterior extension of medial condyle (medial side view) and flattening of trochlear groove proximal center sulcus (anterior and distal views) were qualitatively observed in aged (36-week-old) femurs. To further characterize these spatiotemporal phenotypic changes, we isolated femurs at various postnatal ages and carried out histopathological and X-ray microscopy (XRM) imaging (Figure 5.1b). Femurs were stained with the contrast agent phosphotungstic acid (PTA) before being imaged to differentiate murine soft tissues from bone structures (Das Neves Borges et al., 2014; Masson et al., 2022). Tissue contrast was readily apparent in the sagittal plane, highlighting visibly enlarged articular cartilage in the trochlear region and, to a lesser extent, on the condyles of *Prg4*$^{-/-}$ mice (Figure 5.1c, arrowheads). Closer examination of comparative XRM and histological transverse cross-sections confirmed an overall dysmorphic femur in *Prg4*$^{-/-}$ mice, with abnormalities in both soft and hard tissues compared to WT controls across all time points. In line with previous reports, an osteopenic phenotype was observed in *Prg4*$^{-/-}$ mice (Novince et al., 2012; Rhee et al., 2005), with visible reduction of subchondral trabecular bone by 36w age (Figure 5.1c). Together, this data indicated that postnatal femoral morphology is impacted in the *Prg4* loss-of-function mice.

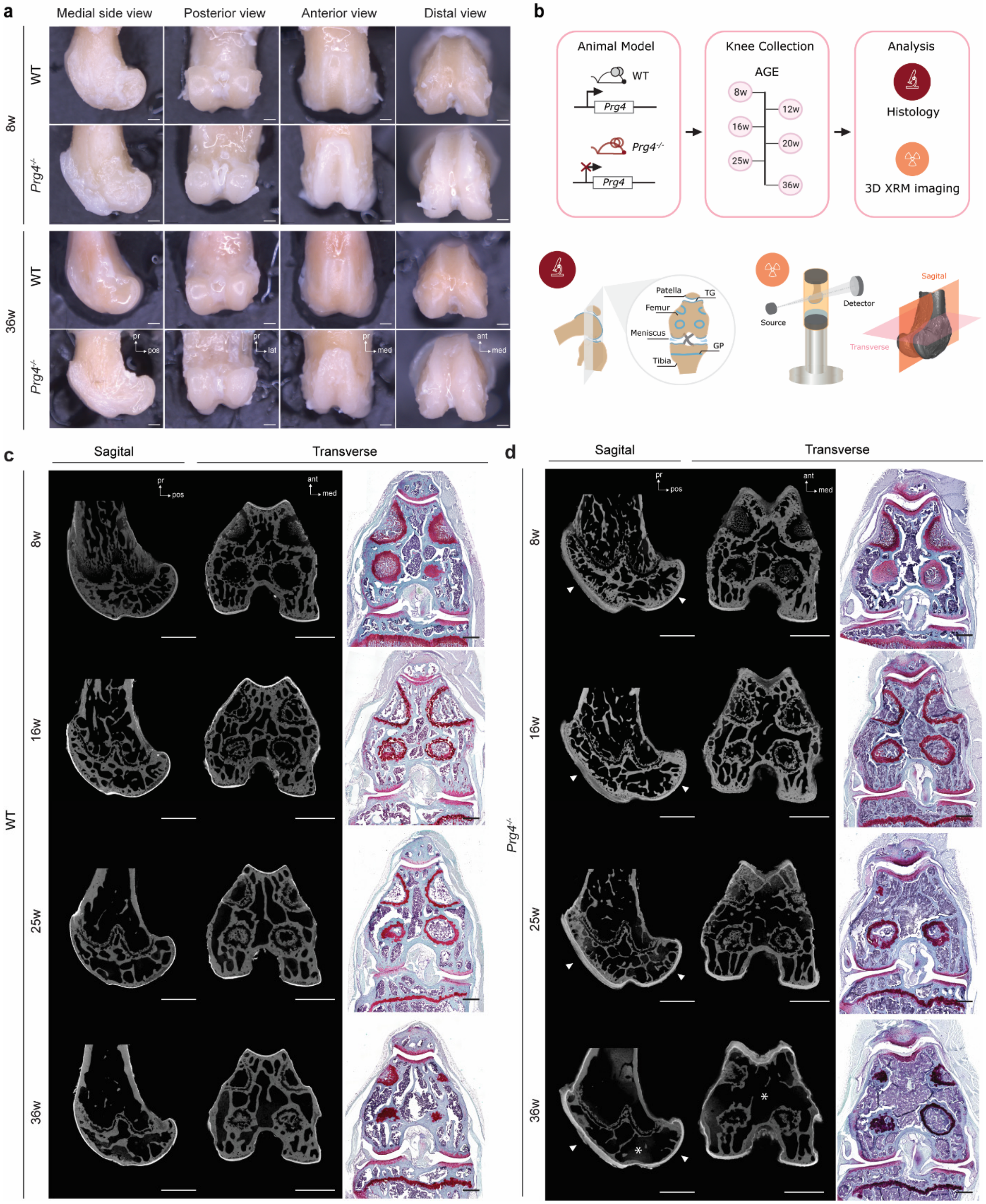
a
Medial side view
Posterior view
Anterior view
Distal view
8w
WT
Prg4-/-
36w
WT
Prg4-/-
pr
pos
pr
lat
pr
med
ant
med
b
Animal Model
WT
Prg4
Prg4-/-
Prg4
Knee Collection
AGE
8w
12w
16w
20w
25w
36w
Analysis
Histology
3D XRM imaging
Patella
TG
Femur
Meniscus
GP
Tibia
Source
Detector
Sagital
Transverse
c
Sagital
Transverse
pr
pos
ant
med
8w
16w
WT
25w
36w
d
Sagital
Transverse
pr
pos
ant
med
8w
16w
Prg4-/-
25w
36w
*
*

Figure 5.1. *Prg4*$^{-/-}$ mice exhibit morphological changes in the distal femur and articular cartilage. (a) General appearance of distal femora at 8w and 36w of age in WT and *Prg4*$^{-/-}$ mice. Note the abnormal shape of the trochlear groove at 8w, with protrusion of trochlear ridges and deepening of the trochlear groove, still identifiable by 36w of age, wherein the medial condyle appeared to extend posteriorly. Scale bars, 500

µm. (b) Schematic of sample collection timeline and further characterization through histology and 3D X-ray microscopy (XRM) imaging. (c) Representative images showing sagittal and transverse cross-sections of PTA-stained femurs and comparative knee joint safranin-O histology across ages for both genotypes, highlighting notable morphological alterations in trochlear and condylar cartilage thickness (arrowheads) in *Prg4*$^{-/-}$ mice, as well as epiphyseal osteopenia (asterisk) at 36w age. Scale bars = 1000 µm (XRM); 400 µm (safranin-O). Ant - anterior, lat - lateral, med - medial, pos - posterior, pr - proximal, TG - trochlear groove, GP - growth plate.

5.4.2 Distal femur size and shape are altered in Prg4$^{-/-}$ ***mice***

Next, morphometric analyses were employed to quantitatively assess the phenotypic femoral abnormalities related to *Prg4* loss-of-function. Landmark-based geometric morphometrics is commonly employed in studying anatomical variation between natural populations or experimental groups due to its ability to capture and quantify subtle and complex shape alterations (Percival et al., 2019; Zelditch et al., 2012). Here, a study-specific atlas (reference average volume) was generated and labelled with a standardized set of 43 anatomical landmarks to comprehensively represent the distal femur geometry (Figure 5.2a). The morphological displacement of the landmark configuration of each specimen was assessed to understand the effects of genotype and age on femoral size and shape. A landmark-based centroid size comparison was carried out since *Prg4*$^{-/-}$ mouse femurs appeared visually larger. On average, *Prg4*$^{-/-}$ femurs exhibited a 6.8% increase in centroid size compared to WT femurs (WT: 9.47 ± 0.153 mm *vs.* *Prg4*$^{-/-}$:10.11 ± 0.162 mm; $p < 0.001$), holding sex and age constant. Of note, sex differences did not significantly contribute to variations in femur size ($p = 0.627$). We also investigated differences in the size of specific tissues between mouse strains and found that *Prg4*$^{-/-}$ mice displayed substantially more cartilage, bone (with marrow space) and growth plate volume (Figure S5.2a-d), yielding, 20%, 13.4% and 22.1% respective increases on average compared with the WT group.

To visualize the major sources of femoral shape variation among genotypes and ages, PCA was performed on sex-adjusted shape variables (Figure 5.2.b). The first principal component (PC1) accounted for 40% of the total variation in femoral shape. Moreover, distinct clusters between genotypes could be observed along PC1, with *Prg4*$^{-/-}$ femurs scoring more positively and WT femurs scoring negatively. Shape morphs along the extremes of PC1 (i.e., PC1 min: WT femur and PC1 max: *Prg4*$^{-/-}$ femur) (Figure 5.2.b) helped visualize significant sources of shape variation between genotypes, including mediolateral narrowing and proximodistal/anteroposterior elongation. Notably, many of these changes were recapitulated in distance heatmaps comparing the WT and *Prg4*$^{-/-}$ femoral mean shapes (i.e., how far the mean WT femur shape needs to be displaced to match the mean *Prg4*$^{-/-}$ femur shape) for each timepoint (Figure 5.2c). Regions of outward expansion (red) were mainly traced back to the medial condyle and proximal region of the trochlear groove, and to a lesser extent, the lateral condyle and outer ridges of the trochlear groove. Conversely, areas of inward contraction (blue) were of greater magnitude at the central sulcus of the trochlear groove and lateral/medial epicondyles.

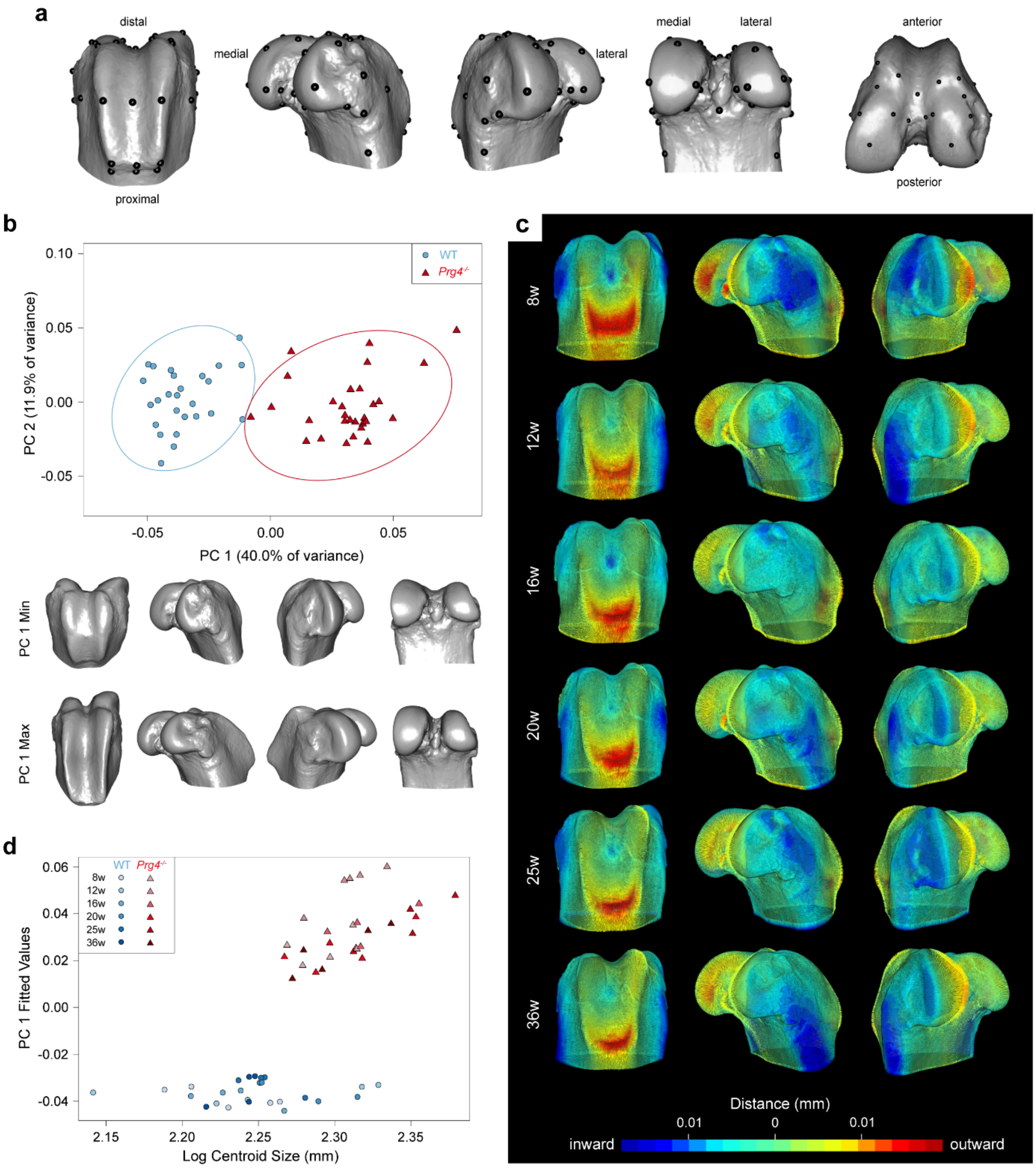

Figure 5.2. *Prg4*$^{-/-}$ distal femur changes in size and shape. (a) Representation of distal femur global reference atlas and the forty-three anatomical landmarks configuration used for geometric morphometrics analyses. (b) Scatter plots of the first two principal component analysis (PCA) of Procrustes shape variables show how WT and *Prg4*$^{-/-}$ femurs exhibit distinct shapes along the major axis of variation (PC1), as represented by respective morphs (bottom) along the extremes of PC1 (exaggerated by a factor of 2). PC1 min: WT femur; PC1 max: *Prg4*$^{-/-}$ femur. (c) 3D distance heatmaps represent the mean shape deviations

between genotypes for each time point and indicate how far inward (blue) or outward (red) the mean WT femur shape needs to be displaced to match the mean *Prg4*$^{-/-}$ femur shape at each respective age of assessment. (d) Scatter plot showing the relationship between fitted PC1 scores (i.e., shape scores predicted by regression of shape on size) and centroid size (log) for each experimental group.

One essential aspect of shape variation that PC1 often captures is the allometric effect of size (Klingenberg, 2016). Allometry refers to the correlation between size and shape, and despite being a ubiquitous phenomenon in nature, its importance in biomedical studies of morphology is underappreciated (Hallgrímsson et al., 2019; Klingenberg, 2016). To investigate how shape correlates with size, fitted PC1 scores (i.e., predicted shape score by regression of shape on size) were compared to centroid size (log-transformed) for each experimental group (Figure 5.2.d). At any given centroid size, *Prg4*$^{-/-}$ femurs scored more positively in predicted shape and deviated from the allometric pattern expected based on WT femurs. Collectively, these results demonstrate that *Prg4* deficiency impacts both the size and shape of distal femurs, leading to larger femurs on average, which are not simply geometrically scaled versions of WT femurs, but also display distinct shapes (narrower, extended, etc), and these effects covary.

5.4.3 Changes in individual anatomical features

Next, individual anatomical features of interest and clinical relevance, such as the intercondylar notch width (IN) and trochlear groove sulcus angle (SA) (Charles et al., 2013; Richard et al., 2020; Sonnery-Cottet et al., 2011) were quantified (Figure 5.3.a-j). At 8-weeks of age, *Prg4*$^{-/-}$ mouse femurs had a deeper trochlear groove associated with lower values of sulcus angle, indicating a steeper and more pronounced groove compared to the WT group. As the mice aged, *Prg4*$^{-/-}$samples gradually approximated the trochlear morphology of WT femurs (Figure 5.3b,c) by becoming shallower and flatter. This phenomenon was associated with abnormal soft and hard tissue remodelling, as seen histologically (Figure 5.3j). In contrast, the WT group demonstrated relatively stable trochlear features. In addition to the differences in trochlear groove, *Prg4*$^{-/-}$ mice displayed a distinct and consistently narrower bicondylar width (Figure 5.3.c). Interestingly, as the WT mice aged, they showed an increase in intercondylar width while simultaneously experiencing a decrease in both medial and lateral condyle widths, resulting in minimal changes in the bicondylar width (Figure 5.3d-g). Linear distance measurements also demonstrated a anteroposterior elongation in *Prg4*$^{-/-}$ mice compared to WT in both the medial and lateral compartments (Figure 5.3h,i), being more prominent on the former. Histological examination suggests that this elongation may be influenced by micro-environmental constraints (Figure 5.3k), and likely associated with synovial hyperplasia and contracture phenotypes observed and previously described for *Prg4*$^{-/-}$ mice (Rhee et al., 2005).

The obvert phenotype observed between trochlea and condyle cartilage prompted me to investigate the transcript levels of *Prg4* through RNAseq at different postnatal stages (P0, P30, P1 year). The analysis revealed increased *Prg4* expression in condyles over time, in contrast to higher expression levels at P0 for trochlear cartilage. These findings suggest that *Prg4* loss-of-function may have compartment-specific effects which are also age-dependent, impacting trochlear morphogenesis to a higher degree than condylar cartilage, but important for maintenance of condylar cartilage with aging. In this regard, mean shape deviations were visually apparent at the trochlear groove ridges and medial condyle and to a lesser extent on lateral condyle for the *Prg4*$^{-/-}$ mice with aging (36w compared to 8w) (Figure 5.3n, Figure S5.2f). The presence of areas of contraction in these specific regions could be associated with biomechanical stress and imbalances in the joint, possibly contributing to the degradation of the articular cartilage over time in the *Prg4*$^{-/-}$ mice, which has been extensively described in the literature (Coles et al., 2010; Jay et al., 2007; Rhee et al., 2005).

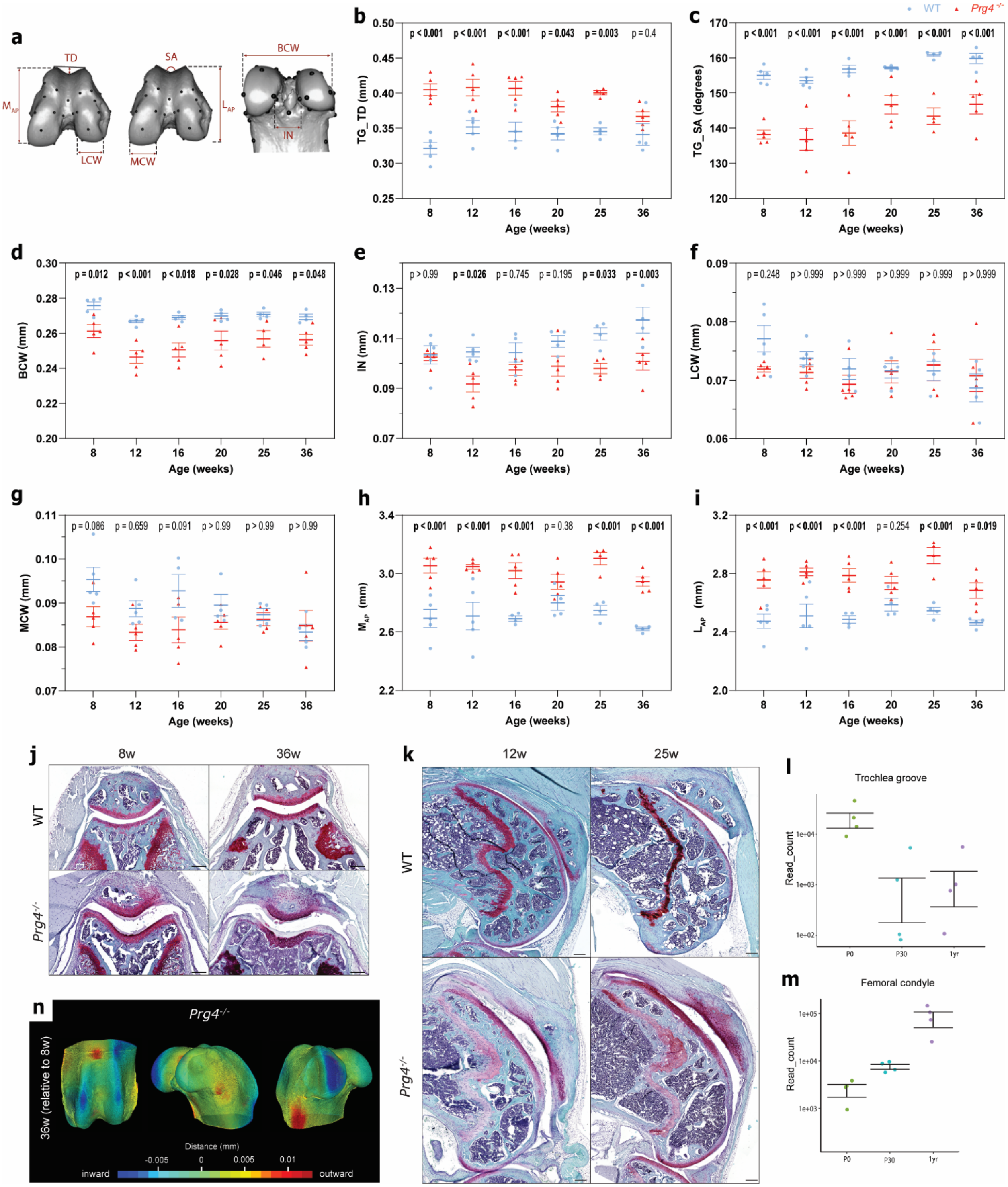

Figure 5.3. Quantitative morphological analysis of individual anatomical features. (a) XRM measurements of femoral anatomical features in WT and *Prg4*$^{-/-}$ mice (*n* = 4-5 mice/group) of interest included (b) trochlear groove depth (TD) and (c) sulcus angle (SA), (d) bicondylar width (BCW), (e) intercondylar notch width (IN) and the (f,h) width and height of the lateral condyle (LCW and L_{AP}) and

(g,i) medial condyle (MCW and M_{AP}). Data presented as mean ± SEM (n = 4-5 mice/group). Analysis of variance ANOVA control vs. *Prg4*$^{-/-}$ mice for individual endpoints with Bonferroni correction for pair-wise comparison. p-values reported. (j,k) Representative histology demonstrating changes in trochlear groove and anteroposterior extension of the femur in *Prg4*$^{-/-}$ *vs* WT mice. Transcript expression of *Prg4* (by RNAseq) varies with age in the (l) trochlea and (m) condyle articular cartilage in WT mice. (n) Heatmaps represent the mean shape deviations for the *Prg4*$^{-/-}$ mice at 36w age relative to its respective 8w old femur. Note the inward contraction regions at the trochlear groove ridges and medial condyle (dark blue), and to a lesser extent on lateral condyle.

5.4.4 Prg4$^{-/-}$ *morphological changes associate with condyle articular cartilage degeneration*

Since articular cartilage in *Prg4*$^{-/-}$ mice has been previously characterized as being thicker and mechanically inferior (Coles et al., 2010; Karamchedu et al., 2016; Masson et al., 2022), we wanted to test the hypothesis that the localized shape changes with advanced aged seen at *Prg4*$^{-/-}$ condyle regions would correlate with spatial changes in thickness and mechanical properties. We employed a previously validated protocol for indentation and cartilage thickness mapping of murine articular cartilage (Masson et al., 2022). The data demonstrated regional differences between genotypes, with consistently thicker articular cartilage in *Prg4*$^{-/-}$ condyles, associated with lower modulus, irrespective of age (Figure 5.4a,b). However, with aging, thinning of *Prg4*$^{-/-}$ cartilage was observed in the mid-outer portion of the condyles, particularly prominent in the medial side, despite no corresponding apparent increase in instantaneous modulus (Figure 5.4a,b arrowhead). These findings were also observed histologically, wherein in where areas of cartilage fibrillation and erosion primarily localized to the mid-to-outer portions of the medial condyle in *Prg4*$^{-/-}$ mice (Figure 5.4c, arrowheads) and worsen with aging (Figure 5.4c,h,i). Site-specific measurements in the mid-outer regions of both lateral (Figure 5.4d,f) and medial condyles (Figure 5.4e,g) highlighted differences in thickness and instantaneous modulus. These findings provide valuable insights into the biomechanical alterations and histological changes associated with the absence of *Prg4* in the femoral condyles.

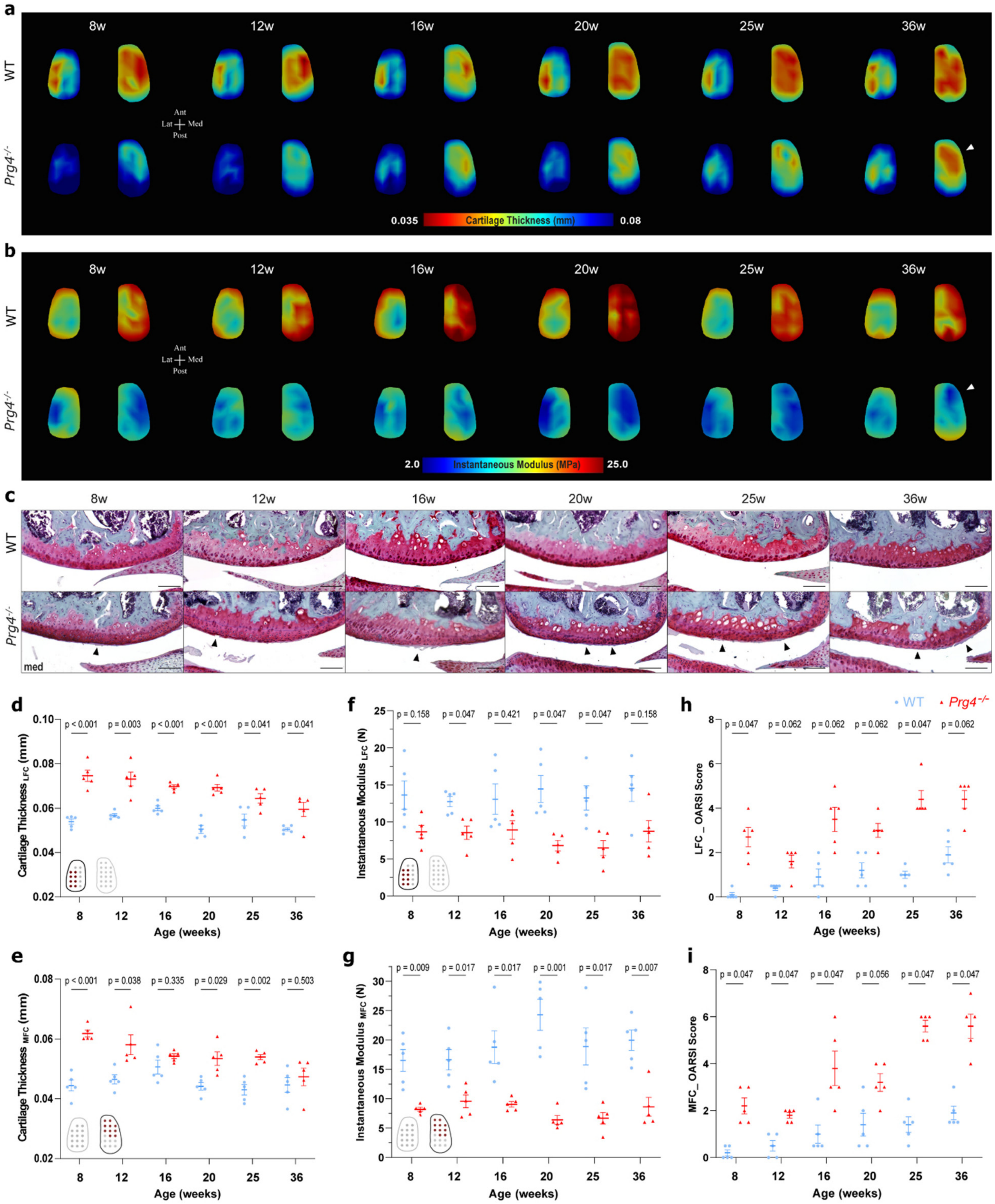

Figure 5.4. Abnormalities in articular cartilage structure and biomechanics of *Prg4*$^{-/-}$ mice with aging. Colour maps of averaged values for lateral and medial condyle cartilage thickness (a) and instantaneous modulus (b) as determined by Hayes et al. (1972) elastic model at 20% strain. Data highlights regional

differences between genotypes for both parameters, with articular cartilage being consistently thicker in *Prg4*$^{-/-}$ condyles, and of lower stiffness, irrespective of age. Note, however, thinning of *Prg4*$^{-/-}$ cartilage at mid-outer portion of condyles with aging, being more prominent in the medial side (arrowhead) and corresponding to an increase in stiffness. In contrast, condyle cartilage surfaces in WT mice demonstrated little variation in thickness with aging, albeit matrix stiffening with peak at mid-age (16w and 20w). and corresponding (c) Representative images of safranin-O/fast-green staining of articular cartilage of the medial femoral condyles of WT (top) and *Prg4*$^{-/-}$ mice (bottom) from 8- to 36-weeks of age, highlight areas of cartilage fibrillation and erosion (arrowhead) in *Prg4*$^{-/-}$ mice primarily on mid-to-outer portions of condyles. Scale bars, 100 µm. Site-specific measurements for mid-outer regions (schematic bottom corner) wherein differences in thickness and instantaneous modulus were identified during mapping for medial (d,f) lateral and (e,g) medial condyles. Thickness and instantaneous modulus presented as mean ± SEM (*n* = 5 mice/group, 8-10 positions/mouse) are shown. Student's t-test control vs. *Prg4*$^{-/}$ mice for individual endpoints with Holm-Šidák correction. *p*-values reported. OARSI histopathological scoring of (h) lateral and (i) medial condyles cartilage damage. Data represented as mean ± SEM (*n* = 5 mice/group), Mann-Whitney tests with Holm-Šidák correction. *p*-values reported. MFC- medial femoral condyle, LFC - lateral femoral condyle

5.5. Discussion

This study investigated phenotypic abnormalities in adult joint tissues associated with *Prg4* loss-of-function, specifically the impact on distal femur shape, size, and articular cartilage degeneration with aging. The data presented here provide empirical evidence that the loss of Prg4 profoundly impacts distal femur geometry and the anatomy of its structural components. At the tissue level, changes in size and shape within *Prg4*$^{-/-}$ femurs are directly associated with corresponding changes in bone and cartilage tissues (bulk and internal structure/composition), resulting in distal femur enlargement, increased anteroposterior extension and reduced mediolateral width and misshaped trochlear groove when compared to WT controls.

Changes in condylar articular cartilage thickness associated with inferior compressive biomechanical properties in young mice (up to 16w of age) are in keeping with previous reports (Coles et al., 2010; Masson et al., 2022). Here, we add to the body of knowledge by demonstrating that with aging, the disruption in cartilage biomechanical properties and joint lubrication due *Prg4* loss is associated with cartilage thinning predominantly in the medial condyle and in its mid-anterior aspect, which is noticeable at the histological level as well. This suggests that mechanical and joint loading factors are at play within the progressive degenerative phenotype that spontaneously occurs within these *Prg4*$^{-/-}$ mice. Of note, loss of Prg4 has been shown to alter ankle range of motion and mice develop an abnormal hopping gait (Novince et al., 2012; Rhee et al., 2005), strengthening the link between joint geometry and function within these mice. Notably, this regional variation could also be captured in distance heatmaps generated via landmark-based geometric morphometrics analysis, highlighting the ability of this technique in quantifying size and shape phenotypes in even relatively small-scale investigations (Devine et al., 2020; Percival et al., 2019).

In vivo studies in *Prg4*$^{-/-}$ mice have underscored the importance of this molecule as a boundary lubricant and inhibitor of cell adhesion. These lubrication and chondroprotection properties are crucial for maintaining tissue homeostasis within the adult joint and preventing spontaneous degenerative cartilage changes (Drewniak et al., 2012; Waller et al., 2013). However, the implications of the absence of Prg4 on joint formation and patterning, given the onset expression of Prg4 occurs during embryonic development

(Rhee et al., 2005) are less understood. While Prg4 deficiency does not prevent knee joint formation, it appears to influences the morphology and structural components of the joint during early postnatal development (Abubacker et al., 2013; Karamchedu et al., 2016; Maenohara et al., 2021).

The early postnatal period is a crucial time for the growth and maturation of joint tissues, including bone and cartilage, which attains its characteristic zonal structure (Decker et al., 2017, 2015). It is possible that the lack of proper lubrication due to Prg4 deficiency can hinder smooth sliding and increase adhesion and shear between opposing cartilage surfaces, thereby creating abnormal stresses and strains in both the developing and maturing joint tissues – particularly in areas of cartilage-cartilage contact. This disruption in normal movement and mechanical signaling during critical growth and maturation phases could result in abnormal chondrocyte activity, matrix organization, and overall joint structure seen in *Prg4*$^{-/-}$ mice, ultimately manifesting into the dysmorphology observed at 8 weeks of age. Further research during developmental and early postnatal stages may provide further insights on underlying mechanisms and its implications for joint morphology.

The complexity of joint development arises from the interplay of genetic factors, mechanical loading, and biochemical signaling that influences growth and remodeling. Furthermore, beyond its well-known lubricating function, over the past decade Prg4 has been implicated in various biological processes, such as regulation of inflammation (Alquraini et al., 2015; Iqbal et al., 2016), adhesion-dependent proliferation (Rhee et al., 2005), fibrosis (Qadri et al., 2020), angiogenesis and wound healing (Krawetz et al., 2022), and bone homeostasis (Abubacker et al., 2019; Novince et al., 2012). Many of these processes are involved in limb development and could be simultaneously affected thus, dissecting out specific contributions, particularly when using global deletion models is challenging, and will require further investigation.

A limitation of this study was the small number of specimens, although it should be noted that results demonstrated predictable shape variation patterns despite limited sample size. The morphometric and biomechanical analysis presented here was restricted to the distal femur; thus, in future studies, it would be interesting to quantify these parameters within opposing patella and tibial plateau surfaces, to gain insight into the extent of dysmorphologies in *Prg4*$^{-/-}$ mouse and infer possible effects on joint kinematics and contact mechanics. An inherent limitation of *Prg4*$^{-/-}$ mouse studies is that this mouse model has global gene deletion of *Prg4*. Since *Prg4* expression has been shown in other musculoskeletal tissues, like bone and tendons (Ikegawa et al., 2000; Rees et al., 2002), as well as in other tissues like liver, possible local and systemic confounding factors cannot be excluded.

In summary, this study provides new insights into the intricate role of *Prg4* loss-of-function on overall joint morphology and articular cartilage health and function in adulthood. Our findings shed light on the intricate relationship between joint geometry and function, reinforcing the importance of *Prg4* in maintaining joint homeostasis, but also at potential implications of *Prg4* deficiency during early postnatal development, where disrupted lubrication may affect joint maturation and morphology.

5.6. Acknowledgements

A.O.M. was supported by University of Calgary and Alberta Innovates' graduate scholarships. This work was funded by the Natural Sciences and Engineering Research Council (NSERC) of Canada. The funders had no role in study design, data collection and analysis, or manuscript preparation. We wish to thank Wei Liu at the Hallgrimsson Lab at the University of Calgary for his technical expertise and help with the initial set up for 3D XRM imaging.

5.7. Author's contribution

A.O.M, R.K. conceived, designed, and oversaw experiments with suggestions from J.B. and W.B.E. A.O.M., performed data collection and analysis, data visualization and wrote original manuscript. J.D. performed geometric morphometrics analysis and data visualization, N.D. and J.C. assisted on data collection, C.C. and T.C. performed RNA data collection and analysis.

5.8. Supplementary information

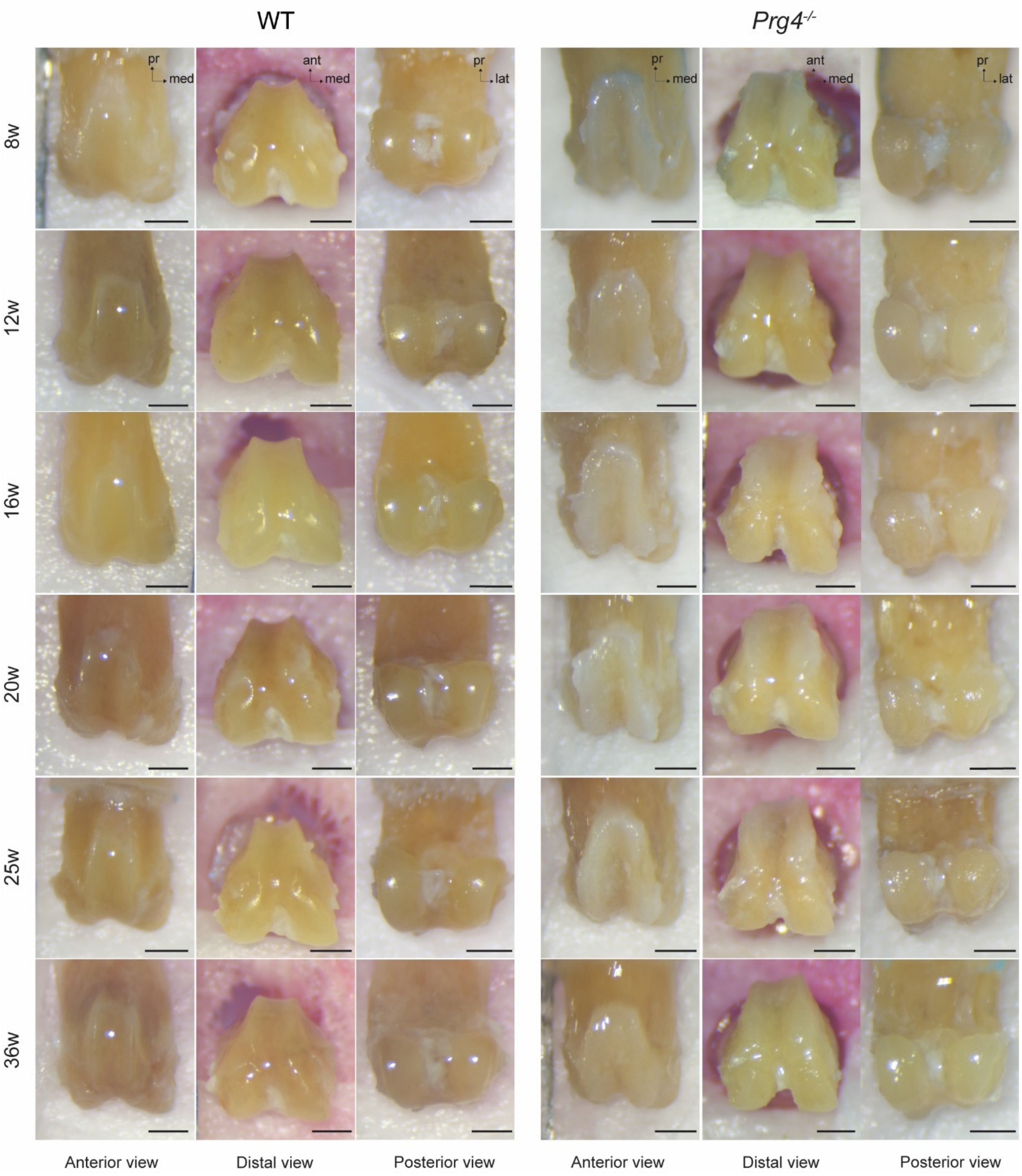
WT
Prg4-/-
pr
med
ant
med
pr
lat
pr
med
ant
med
pr
lat
8w
12w
16w
20w
25w
36w
Anterior view
Distal view
Posterior view
Anterior view
Distal view
Posterior view

Figure S5.1. Comparison of WT and *Prg4$^{-/-}$* mice distal femur morphology during aging. Representative images from various angles of the distal femur (anterior femur, femoral notch and posterior femur). Scale bars, 1000 µm.

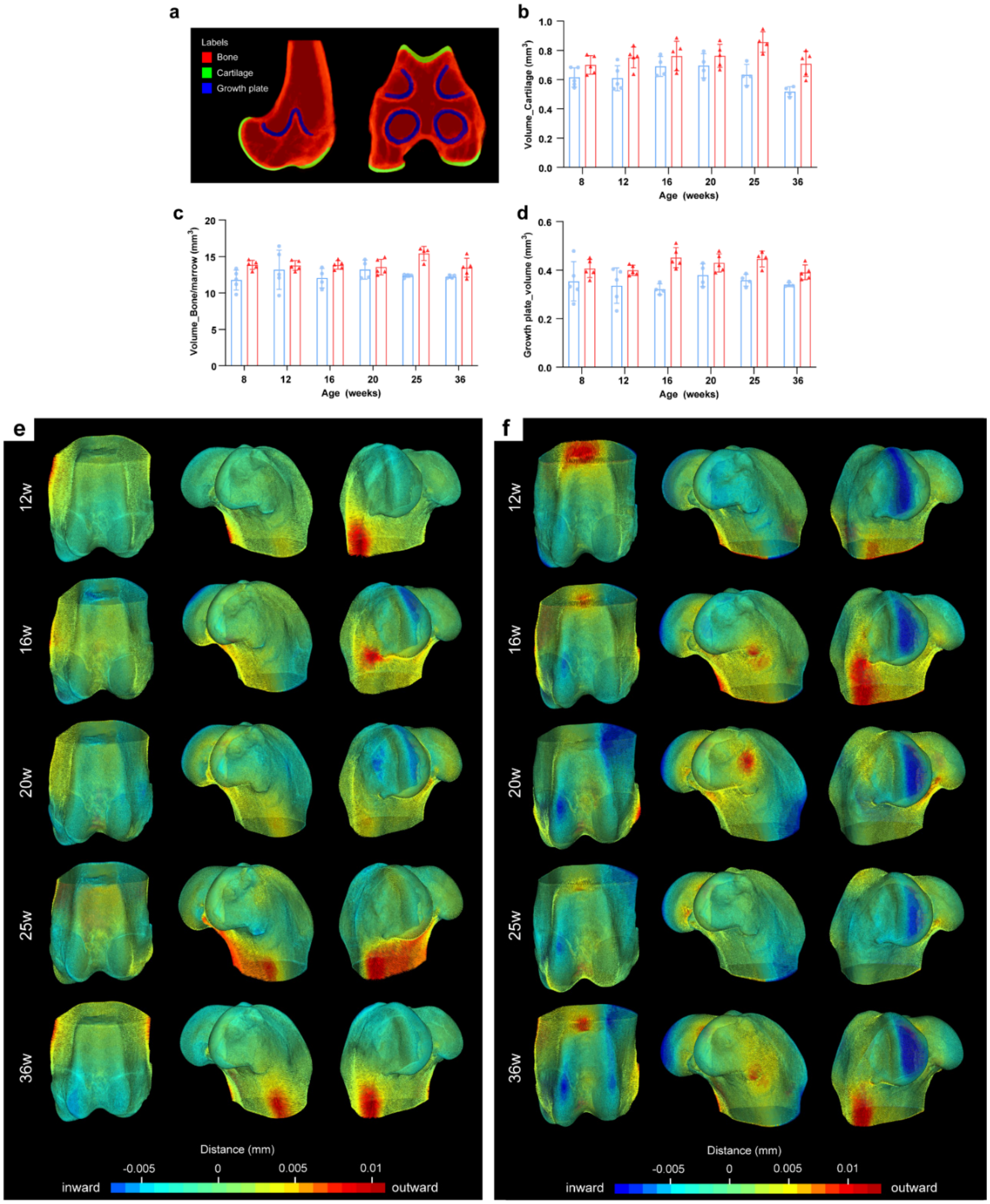

Figure S5.2 Additional parameter evaluated in size and shape geometric morphometric comparisons. (a) Study-specific atlas was segmented into cartilage, bone (with marrow space), and growth plate. Calculated volume per segmentation label (b) cartilage, (c) bone and (d) growth plate for WT and *Prg4*$^{-/-}$ mice across age. Heatmaps represent the mean shape deviations within genotypes across timepoints, relative to their respective 8w old femur shape, for (e) WT and (f) *Prg4*$^{-/-}$ mice. Note the inward contraction regions at the trochlear groove ridges and mid-outer medial condyle area (blue), consistent with area of cartilage thinning in histological findings and needle probing mapping.

Chapter Six: The *Hic1*-lineage dictates the balance between cartilage repair and regeneration

Anand O. Masson, Jessica Corpuz, Bryce Besler, Nicole Krahn, T. Michael Underhill, Jeff Biernaskie, W. Brent Edwards, and Roman J Krawetz

My contributions to this work were as follows:

- *Contributed to experimental designs*
- *Performed experimental procedures, data acquisition and analysis, except imaging processing*
- *Conceptualized and created the manuscript figures and wrote the manuscript*

6.1. Abstract

Emerging evidence suggests that Hypermethylated in cancer 1 (*Hic1*) is a marker for quiescent mesenchymal progenitors (MPs). These cells are found within multiple tissues in adult mice and present with varying lineage potential and regenerative capacities, depending on their tissue of residence, environmental niche and injury/wound context. Little is known, however, about the functional significance of these MPs, if any, regarding adult cartilaginous tissue. Therefore, this study was undertaken to investigate the functional role of *Hic1*-expressing progenitors in the maintenance and repair of typically regenerative-incompetent cartilaginous tissues present within the ear (auricular) pinnae and knee joint (articular) microenvironments. we have shown that *Hic1*$^{+ve}$ cells reside within both tissue compartments in adult mice, but do not contribute to the physiological turnover of cartilaginous tissues. Moreover, a minor perturbation of the *Hic1*-lineage led to a measurable impact on the healing response phenotype and resulting tissue morphology post-ear wound and osteochondral knee injury. Taken together, these results indicate that the *Hic1*-lineage are able to modulate healing within both microenvironments, through indirect and/or direct contributions to remodelled tissue. This raises the possibility of this cell lineage being exploited as a therapeutic target.

6.2. Introduction

Tissue regeneration is a fundamental biological process that allows organisms to repair and/or restore function to damaged tissues. Adult mammalian tissues harbour resident-progenitor cells known to contribute to tissue maintenance and repair (Pellettieri and Alvarado, 2007; Rennert et al., 2012). While the existence of an endogenous progenitor pool in adult cartilage remains controversial; mesenchymal stem/progenitor cells have been identified in several joint-associated niches, including synovium, synovial fluid, and infrapatellar fat pad, as well as bone marrow (McGonagle et al., 2017). Regardless, cartilage displays suboptimal intrinsic repair following injury indicating that tissue-resident and progenitor cell pools within the joint are unable to mount an effective regenerative response, whereby the native mechanisms are insufficient or likely overwhelmed (Rennert et al., 2012). In this context, the possibility of endogenously guiding articular cartilage healing towards a regenerative phenotype is quite compelling.

Interestingly, recent findings suggest the transcription factor Hypermethylated in cancer 1 (*Hic1*) identifies a unique cohort of quiescent mesenchymal progenitors (MPs) (Scott et al., 2019) that serve as tissue-resident postnatal reservoirs and critically support homeostasis, regeneration and repair (i.e. scar formation) processes in various tissues (Abbasi et al., 2020; Scott et al., 2019; Shah et al., 2022; Soliman et al., 2020). As the name indicates, *Hic1* gene is frequently found deleted or silenced by promoter hypermethylation in several human cancers (Chen et al., 2004; Fleuriel et al., 2009). Since previous efforts have been mainly focused on understanding its tumour-suppressive function (Jenal et al., 2009; Zheng et al., 2012), knowledge of the role of *Hic1*$^+$ MPs and their progeny in health and disease across cartilage-related tissues remains limited.

Constitutive gene ablation of *Hic1* results in embryonic lethality with significant developmental defects, including craniofacial and limb/digit deformities (Carter et al., 2000). Meanwhile, ubiquitous deletion of *Hic1* in adult mice results in exit of MPs from quiescence and expansion of this cell pool (Scott et al., 2019). Similarly, *Hic1*$^+$ MPs identified in skeletal muscle, heart and skin tissues (Abbasi et al., 2020; Scott et al., 2019; Soliman et al., 2020) are shown to respond to acute injury. However, their behavior and regenerative potential appear to be tissue-specific and modulated by niche-associated factors (Abbasi et al., 2020; Kim and Braun, 2020).

Here, we interrogated the role and fate of *Hic1*$^+$ MPs in two distinct injury models, ear biopsy punch and knee full-thickness cartilage defect (FTCD), both involving typically regenerative-incompetent tissues comprised of cartilage. The limited success in treating cartilage-related conditions is attributed, in part, to the lack of a comprehensive understanding of why articular cartilage fails to naturally regenerate (Muthu et al., 2023). Hence, new insights into cell types and molecular pathways influencing or driving normal healing processes in cartilaginous tissues might help uncover potential therapeutic targets that could be manipulated to enhance tissue repair in the future.

6.3. Materials and Methods

6.3.1. Mouse strains

Hic1^{CreERT2};R26^{tdTomato} mice (Scott et al., 2019) were provided by Dr. T. Michael Underhill (University of British Columbia, Canada). To generate a mouse that can conditionally overexpress *E2f1*, the complete murine *E2f1* open reading frame (ORF) was acquired from Origene (CAT#: MC208010) and it was validated through sequencing. It was then subcloned into the ROSAiZEG vector (iZEG plasmid with ROSA26 homology arms) to create the ROSAiZEG-*E2f1* vector. Specifically, a *lox*P-geo-STOP-*loxP* cassette was placed between the CAG promoter and E2F1 ORF. Downstream of the E2F1 ORF, an IRES, eGFP and poly A sequences were inserted, in that order. To target the ROSA26 locus, we employed a zinc finger nuclease obtained from Sigma-Aldrich (CompoZrTM Custom Zinc Finger Nucleases target Rosa26). Nucleofection (Lonza, Nucleofector II with the Mouse ES Cell Nucleofector® Kit) was used to transfect 10 ug of superhelical plasmid DNA expressing Rosa26 ZFN-pair and 10 ug of superhelical ROSAiZEG-*E2f1* plasmid DNA into C57BL/6 ES cells. Neo-resistant colonies were picked and expanded under standard ES conditions, and PCR was performed on the 5' and 3' junctions to confirm location and direction of the transgene. A total of 36 ES clones had the insert in the correct location and direction, and 6 out of these had over 95% normal karyotype. One of these clones was used for micro-injection into 8-cell stage B6(Cg)-Tyr c-2J /J (C57BL/6 albino) mice. Chimeric mice were obtained and bred to C57BL/6 albino mice to determine which ES cell injections contributed to the germline. Mice that had germline contributions from the injected ES cells were then crossed to C57BL/6J mice to obtain the R26$^{\text{CAG-E2f1}}$strain used in the current study (Figure S6.1). Ear punch samples were taken from mice (3-8 weeks of age) for genotyping by PCR to confirm homozygote (Figure S6.1b,c). *Hic1*^{CreERT2};R26^{tdTomato} were crossed to R26$^{\text{CAG-E2F1}}$ to generate *Hic1*^{CreERT2};R26^{tdTomato};*R26*^{E2F1} mice. R26$^{\text{CAG-E2F1}}$ mice was also bred to *Col2a*^{Cre}, (Ovchinnikov et al., 2000) (B6;SJL-Tg(Col2a1-cre)1Bhr/J, stock # 003554, The Jackson Laboratory) to generate *Col2a*^{Cre};*R26*^{E2F1}mice . Three to five animals per genotype/group were used for each experiment to ensure reproducibility. Animal experiments were approved by the Animal Care Committee (protocols AC16-0043 and AC20-0042) at the University of Calgary and followed the Canadian Council of Animal Care guidelines. All animals were housed under a standard light cycle and had access to food and water *ad libitum*.

6.3.2. Lentiviral RNA analysis and RT-qPCR

To induce and quantify E2f1 expression *in vitro*, cells derived from synovium and bone marrow of *Hic1*^{CreERT2};R26^{tdTomato}, *Hic1*^{CreERT2};R26^{tdTomato};*R26*^{E2F1} and R26$^{\text{CAG-E2F1}}$ mice were transduced at passage 2 with high-titre lentiviral Cre vector in the presence of polybrene, and incubated at 37°C in 5% CO_2 for 48 hours. RNA isolation from cultured cells was carried out using TRIzol reagent (Invitrogen) and cDNA with the high capacity cDNA reverse transcriptase (Applied Biosciences) according to the manufacturer's instructions. Quantitative real-time PCR (RT-qPCR) was carried out using TaqMan® Gene Expression Master Mix (4324018, Applied Biosystems) with a mouse specific E2f1 TaqMan® probe (Mm00432939_m1, Applied Biosystems).

6.3.3. Administration of tamoxifen

Eight-to-nine-week-old mice received intraperitoneal injections for 5-consecutive days (0.1 mL/day) of 4-Hydroxytamoxifen (4OHT, H6278 Sigma) suspended in sunflower oil (10 µg/mL). *In vivo,* Cre-driven tdTomato labelling and fate-mapping of *Hic1*-lineage cells in the absence of injury were assessed at 1-, 16- and 32 weeks post-4-OHT induction (Figure 6.1a). Injuries to ear or knee cartilage were performed one week after 4OHT administration (week 0), and mice were euthanized at the endpoints of 1-, 2-, 4- and 8-weeks post-injury (wpi) to evaluate *Hic1*-lineage response to injury and contribution to tissue remodelling (Figures 6.2a, 6.3a). To avoid any confounding variables due to 4-OHT that could influence experimental results, *Col2a*^{Cre};R26$^{\text{E2F1}}$ mice were also injected with 4-OHT using the same dosing strategy above.

6.3.4. Ear wound and size evaluation

A through-and-trough standardized hole (2-mm diameter) in the center of the ear pinna was created using a sterile biopsy punch (33-31 Integra) (Figure 6.2a). To assess wound closure, ears were photographed with a ruler in the image plane. Quantitative measurement of the ear wound area was performed using ImageJ software. Ear pinna regeneration was assessed histologically at 1-, 2-, 4- and 8-wpi.

6.3.5. Articular cartilage defect model

Full-thickness cartilage defect (FTCD) was inflicted in the trochlear groove of the right femur using a 26G needle, as previously described (Jablonski et al., 2021; Rai et al., 2012). Briefly, animals were placed under isoflurane anesthesia, and a small incision was made on the medial parapatellar region aided by a dissection microscope (Leica). The patella was then gently dislocated laterally, and a round defect reaching the subchondral bone was created on the exposed trochlear groove. Knee extension/flexion was sufficient to move the patella back into place, after which the skin incision was closed with staples. Contralateral hindlimbs served as uninjured controls. To understand articular cartilage healing comprehensively, 2D histological/immunofluorescence assessment and 3D imaging were carried out at all endpoints. Moreover, functional evaluation of the newly formed tissue was carried out at 8-wpi by biomechanical testing.

6.3.6. Histology and immunofluorescence

Ear and hindlimb samples were fixed in 10% neutral formalin buffer (NBF) solution (Fisher) for 2 and 7 days, respectively. Ear tissue samples were then washed and prepared for paraffin embedding. Hindlimbs underwent an extra decalcification step in 10 w/v EDTA solution (Ph 7.4) for 18 days before paraffin embedding. All tissues were sectioned at 10 µm thickness and mounted onto Superfrost Plus (Fisher) glass slides for further analysis. Safranin-O/Fast green staining was used to evaluate healthy and injured tissues' overall morphology and composition. Mid-injury sections were graded on a 14-point scale for articular cartilage healing, as previously described (Fitzgerald et al., 2008). Briefly, the parameters under evaluation and their respective scoring range were cell morphology (0-4), matrix staining (0-3), surface regularity (0-3), cartilage thickness (0-2) and integration with native cartilage (0-2). Thus, an overall score of 0 is attributed to a newly created FTCD, whereas the maximum score of 14 characterizes uninjured healthy cartilage.

For immunofluorescence analysis, slides were deparaffinized and antigen retrieval was performed. Sections were blocked in 5%BSA in 0.1%Triton-X PBS for 1 hr at room temperature and then incubated with primary antibodies overnight at 4ºC in a humidified chamber. The primary antibodies used in this study were: mouse monoclonal anti-alpha-Smooth muscle actin (614852 Biolegend), mouse monoclonal anti-collagen II (II-II6B3-c DSHB), monoclonal rat anti-Ki67-660 (50-5698-82 Invitrogen), polyclonal goat tdTomato (AB8181-200 Cedarlane). Sections were washed in PBST and PBS buffers and incubated with secondary antibody for 1 hr at room temperature before mounting and nuclear counterstaining with EverBrite Hardset Mounting Medium containing DAPI (Biotium). The secondary antibodies used were donkey anti-rat AlexaFluor647 (A48272 Invitrogen), donkey anti-mouse AlexaFluor647 (A31571 Invitrogen), anti-goat NL557 (NL001 Northern Lights). Slides were imaged with the Axio Scan Z1 microscope (Carl Zeiss). Image analysis and cell counting were performed using TissueQuest v.7 (TissueGnostics) software. For quantification, 3-4 biological replicates were used. For injured ears, quantification was performed on the front edge of the excision plane from both sides of the ear, encompassing epidermis and non-epidermis regions (Figure S6.2). For uninjured ears a standardized area size was used. Quantification of synovium was restricted to areas juxtaposed to the trochlea, located superiorly and inferiorly to the patella, while the bone marrow region quantified was limited to the epiphyseal subchondral bone. For uninjured and injured knees, quantification was performed in similar areas of synovium and within a standardized area size encompassing the defect site (Figure S6.3).

6.3.7. In vivo EdU labeling

Click-IT^{TM} EdU (A10044 Invitrogen) was injected in mice for 12 days, starting at the day of injury (FTCD) (Roelofs et al., 2017). Mice were sacrificed at 8-wpi, and knee joints were harvested and prepared for histological assessment as described above. To detect the incorporated EdU, we used the Click-It EdU cell proliferation imaging kit, Alexa Fluor 647 (C10340 Invitrogen), as per the manufacturer's instructions.

6.3.8. 3D X-ray microscopy (XRM) imaging

Hindlimbs were disarticulated at the hip, and distal femurs were carefully isolated from tibiae and menisci under a dissection microscope (Leica). Specimens ($n = 5$ per group) were fixed in 10% NBF for 24 hours and preserved in 70% ethanol for a maximum of three days before scanning. For micron-level visualization of cartilaginous soft tissue, samples were contrast-enhanced using 1% phosphotungstic acid (PTA) solution for 18-24 hours prior to scans. Specimens were enclosed in a Kapton straw chamber (5 mm diameter, GoodFellow Cambridge) containing a small amount of PTA solution on the bottom to prevent dehydration, secured to the device holder, and scanned using ZEISS Xradia (Versa 520, Carl Zeiss X-ray Microscopy, USA). Scans were performed at low-energy (40kVp voltage, 3W power) and high-resolution (4.4 µm nominal isotropic voxel), with imaging acquisition through 360º. Volume renderings and cross-sections (Figure 6.5a) were created using 3D Slicer (v.5.0.3) (Kikinis et al., 2014). After reconstruction, a landmark was placed in the center of the defect or corresponding location for uninjured legs, and a volume of interest was cropped to a cube of edge length 1.0 mm. This reduced the image size and allowed it to be processed on commercial hardware. The cartilage was segmented by thresholding with a per-scan user-defined threshold, followed by manual correction by the same operator. Next, the cartilage segmentation was cropped by a spherical filter of diameter 0.53 mm, focusing the analysis on the defect and corresponding uninjured area in the contralateral legs (Jablonski et al., 2021). The mean cartilage thickness (Hildebrand and Rüegsegger, 1997) Cg.Th [mm]; volume, Cg.V [mm^3]; and surface area, Cg.S [mm^2], were computed for each specimen. The cartilage surface-to-volume ratio (Cg.S/Cg.V [mm^{-1}]) was derived from the previous outputs. Processing was performed in SimpleITK (Lowekamp et al., 2013) (v2.0.2, Insight Software Consortium) and morphometry in Image Processing Language (IPL v5.42, SCANCO Medical, Brüttisellen, Switzerland).

6.3.9. Biomechanical testing

Eight-weeks after FTCD, bilateral mouse femurs (right-injured, left–uninjured control) were isolated for biomechanical testing (*n* = 5 per group). Sample preparation was carried out as previously described (Masson et al., 2022). In brief, femurs were inserted into a pipette tip containing cyanoacrylate glue, which surrounded the long bone shaft, securing the specimen in place. With trochlea facing up, the construct was mounted onto a modified sample holder (Masson et al., 2022) and attached to the Mach-1 (v500csst Biomomentum) testing chamber. Specimens were maintained in a bath of PBS for the duration of testing. Automated indentation was carried out normal to the surface at the area of injury (and equivalent uninjured area in control femurs) across nine pre-defined positions, using a 0.3 mm diameter indenter tip and a 70-N multiaxial load cell, calibrated before each use. Data analysis of mechanical parameters, including structural stiffness (N/mm), relaxation time (s) and residual force after 120s of relaxation (equilibrium) was performed using Mach-1 Automated Indentation and Thickness Batch Analysis software (v.2.0.2 Biomomentum).

6.3.10. Statistical analysis

Data statistical analysis and graphic representation were performed using GraphPad Prism software (v8.0). Data is expressed as mean ± standard deviation (SD) unless stated otherwise, and statistical tests are noted in figure legends. For comparison between genotypes over time, ANOVA with a Bonferroni *post-hoc* test was used for ear wound closure, and unpaired Student *t* test for all other analysis. For comparisons with more than two groups, *one-way* ANOVA with Bonferroni correction was used. A *p*-value less than 0.05 was considered statistically significant.

6.4. Results

6.4.1. Cells of the Hic1 lineage reside in the ear pinna and knee joint microenvironments but do not undergo differentiation into auricular or articular cartilage tissues under homeostatic conditions

To investigate the presence and *in vivo* differentiation capacity of *Hic1* lineage cells in adult mice under homeostatic conditions, we administered 4OHT to eight-week-old $Hic1^{CreERT2}$; $R26^{tdTomato}$ mice carrying the tdTomato (tdT) fluorescent reporter and examined the distribution of tdT-expressing cells in the ear pinnae and knee joint after short (week 1) and long-term (weeks 16 and 32) follow up periods (Figure 6.1a). During these experimental timeframes, *Hic1*-expressing cells and their progeny, collectively defined as *Hic*1-lineage cells, were identified in various non-cartilaginous tissues but were absent in both auricular and articular cartilage. One week after 4OHT administration, tdT expression was observed in multiple tissues of the mouse ear pinna, with marked expression in the dermis and the membranes lining the auricular cartilage, anatomically coinciding with the perichondrium (Figure 6.1b). However, cells of the *Hic1*-lineage were not observed in the auricular cartilage or the epidermis. Furthermore, the patterns of tdT expression remained largely unchanged with aging, and there was minimal expansion in the percentage number of tdT^{+ve} cells over time (Figure 6.1c). In adult knee joints, *Hic1*-lineage traced cells were identified in the synovium, fat pad, and entheses, as well as throughout the subchondral bone marrow (Figure 6.1d), most of which have been previously identified as skeletal stem/progenitor cell niches (McGonagle et al., 2017). However, no contribution to cartilaginous tissues was observed, as demonstrated by the absence of tdT^{+ve} cells on the growth plate and articular cartilage in all follow-up periods (Figure 6.1e). Positive tdT staining in the synovium persisted at later time points (Figure 6.1e,f). Of note, while there was a slight percentage increase in *Hic1*-lineage cells within the subchondral bone marrow by 8-months of age (week 32 post-induction) (Figure 6.1g), this was due to age-associated cell density decrease and related adipose accumulation in the bone marrow cavity rather than an increase in the number of tdT^{+ve} cells (Figure 6.1d). Collectively, these findings suggest that $Hic1^{+ve}$ cells are localized to specific tissues in the ear pinna and knee joint microenvironments, display low tissue turnover with aging, and under homeostatic conditions, do not contribute to auricular or articular cartilage tissues found in these niches. However, since the *Hic1*-

labelled cells were persistent in adult tissues and demonstrated mesenchymal lineage potential, in keeping with previous studies (Arostegui et al., 2022; Scott et al., 2019; Soliman et al., 2020), we tested the hypothesis that these cells might play a role in the wound healing process.

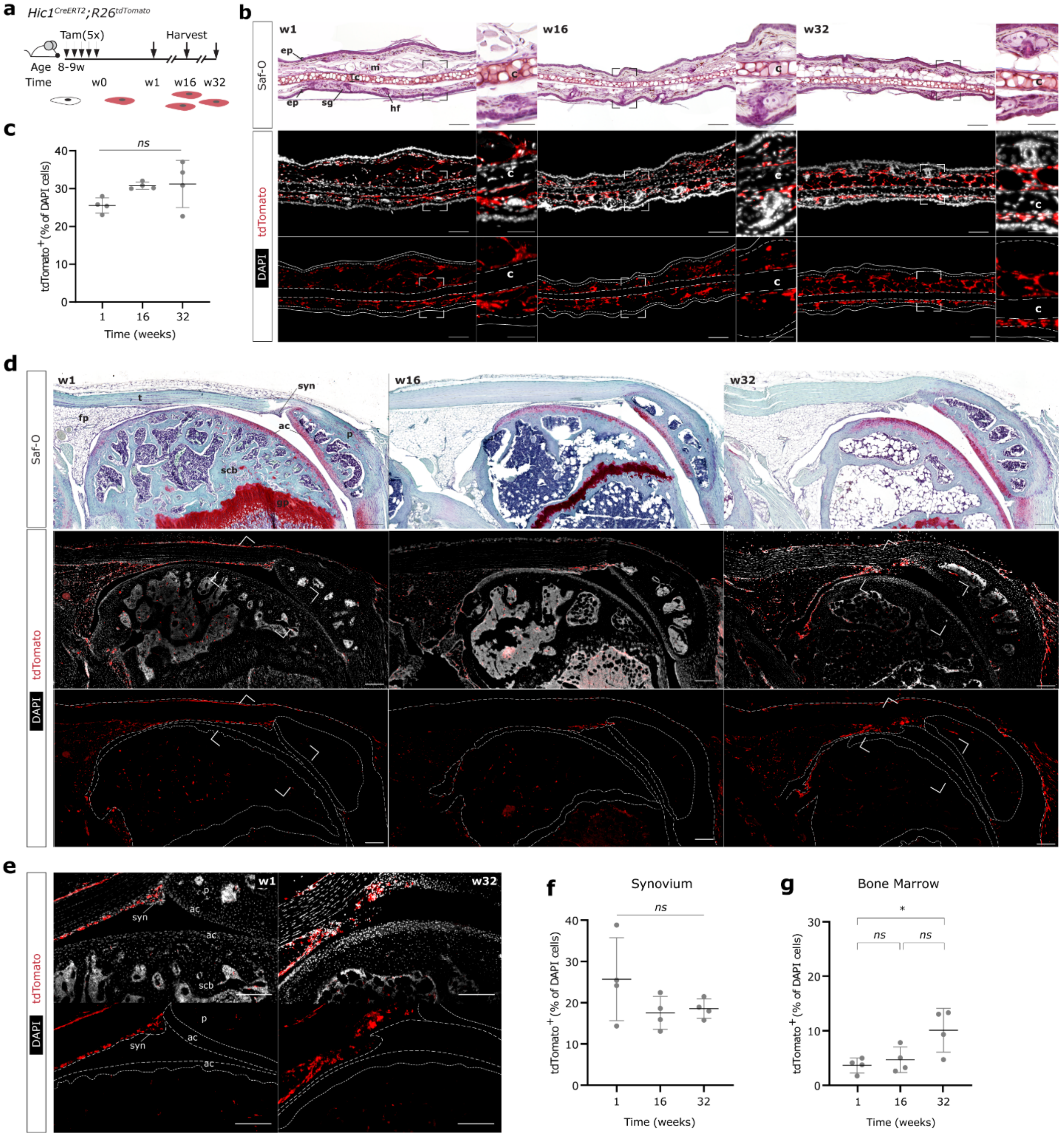
a
Hic1CreERT2;R26tdTomato
Tam(5x)
Harvest
Age 8-9w
Time
w0
w1
w16
w32
b
w1
w16
w32
Saf-O
ep
m
c
sg
hf
tdTomato
DAPI
c
tdTomato+ (% of DAPI cells)
ns
40
30
20
10
0
1
16
32
Time (weeks)
d
w1
w16
w32
syn
t
fp
ac
p
scb
gp
Saf-O
tdTomato
DAPI
e
w1
w32
syn
ac
p
scb
f
Synovium
g
Bone Marrow
*
ns
ns
ns
tdTomato+ (% of DAPI cells)
1
16
32
Time (weeks)

Figure 6.1. *Hic1*-lineage contribution to physiological in vivo tissue turnover. (a) Schematic timeline of 4OHT(Tam)-inducible Cre-recombination to label *Hic1*-expressing cells with tdTomato (tdT) (red) reporter and subsequent fate-mapping assessments at short-term (w1) and long-term (w16 and w32) follow-up times. (b) *Hic1*-lineage contributed to various tissues in the ear pinna, but no representation was observed in the cartilage or epidermis. Scale bars, 100 µm, and 50 µm on close-ups. (c) Corresponding quantification of tdT^{+ve} cells per DAPI counted nuclei demonstrated with aging ($n = 4$/group, 2 sections/animal, $p = 0.119$). (d, e) Similarly to lineage-tracing at the ear pinna, tdT^{+ve} cells were absent from knee articular cartilage and growth plate compartments but identified in joint-associated tissues, such as the synovium, fat pad and subchondral bone marrow. Scale bars, 200 µm. Quantification ($n = 4$/group, 2 sections/animal) of tdT^{+ve} DAPI nuclei in (f) synovium ($p = 0.198$) and (g) bone marrow tissues ($p = 0.021$; 1 vs 16 $p = 0.865$; 1 vs 32 $p = 0.024$ and 16 vs 32 $p = 0.055$). Data are presented as mean ± SD, and the statistical significance was determined by ANOVA ($\alpha = 0.05$) and multiple comparison with Bonferroni correction (* $p < 0.05$). Nuclei counterstained with DAPI in all immunofluorescence images. Ac – articular cartilage, c – cartilage, ep – epidermis, fp – fat pad, gp – growth plate, hf – hair follicle, m – muscle, p – patella, scb – subchondral bone, sg – sebaceous gland, syn – synovium, t – tendon.

6.4.2. Hic1-expressing cells contribute to wound healing/closure in the ear

We generated a through-and-through 2-mm biopsy punch at the centre of the mouse ear pinna to investigate the responsiveness of *Hic1*-expressing MPs to acute injury and their contribution to ear wound healing (Figure 6.2a). The ear pinna offers an interesting system for studying regeneration in mammals because it involves the coordinated remodelling of tissues from different germ layers, including the epidermis, dermis, nerves, skeletal muscle, blood vessels and cartilage (Maden and Varholick, 2020). While the outer ear shares similarities with skin tissue, wherein the contribution of *Hic1*-expressing MPs to neo-dermis and hair follicle formation has been characterized post-injury (Abbasi et al., 2020), the presence of cartilage in the ear introduces an extra layer of complexity not found in skin. As expected, $Hic1^{CreERT2}$; $\mathrm{R26}^{\mathrm{tdTomato}}$ (Hic1) mice displayed limited repair following traumatic injury to the ear pinnae. The ear hole reached maximal closure at 3-wpi, followed by a slight increase in hole area to 1.7 ± 0.63 mm^2 by 8-wpi (Figure 6.2b). Histological analysis revealed re-epithelization of wound edge by 1-wpi, but minimal restoration of tissue architecture beyond the original excision plane at later time points, despite the habitual formation of small cartilage condensations beyond the native cartilage (Figure 6.2c). *Hic1* lineage-traced progeny was visualized throughout the area of cell expansion (blastema-like area) ahead of the excision plane but beneath the wound edge epidermis (Figures 6.2d,e; S6.4a). This pattern was shown to persist at later time points and importantly, tdT^{+ve} cells rarely contributed to cartilaginous elements (Figure 6.2f,g). Proliferative cells (Ki67^{+ve}) were scarce and mainly restricted proximally to the wound epidermis at 1-wpi, with no proliferating cells being observed beneath the epidermal layer at later stages (Figure 6.2d, S6.4c). Conversely, widespread alpha-smooth muscle actin (αSMA) expression was identified towards the leading edge of the wound encompassing dermal and epidermal tissues at early time points (Figure 6.2e). This phenotype evolved over time, and by 8-wpi, αSMA expression was notably increased in the epidermis (Figures 6.2e, S6.4d), indicative of fibrotic healing. These findings indicate that *Hic1*-lineage participate in ear wound tissue repair and reinforce their regionalised expression in the ear pinna tissue.

6.4.3. Perturbation of cell cycle machinery in Hic1+ve cells alters ear wound healing outcomes

Since *Hic1* is a regulator of quiescent phenotype in adult mice (Scott et al., 2019), we hypothesized that dysregulation of the cell cycle within these quiescent progenitors prior to injury could impact their response and may predispose them to tissue regeneration *vs.* repair. Cell cycle regulators, such as cyclin D1 and E2F1, are among previously identified HIC1 target genes, which demonstrate a mechanistic relationship between these *Hic1*-lineage traced cells and cell cycle regulation (Rood and Leprince, 2013). To direct the expression of E2F1 to *Hic1*$^{+ve}$ cells, we generated a transgenic mouse for conditional overexpression of E2F1 (Figure S6.1) and bred it to *Hic1*^{CreERT2}*;* R26^{tdTomato} mice. qPCR-based detection of the transgenic allele and relative E2f1 mRNA production in Hic1- and Hic1^{E2F1}-derived cells post *in vitro* or *in vivo* induced recombination are included in Figure S6.1. An approximate 1.49-fold increase in *E2f1* expression was observed after lentiviral Cre recombination, while synovium- and bone marrow-derived cells from 4OHT induced Hic1^{E2F1} mice demonstrated approximately 1.7- and 1.46-fold increases, respectively. Injuries (2 mm) in Hic1^{E2F1} mice demonstrated a faster rate of healing compared to Hic1 mice, and resulted in a smaller residual wound area (Figure 6.2b,c). By 1-wpi, the mean wound area in Hic1^{E2F1} ears was comparable to the maximum wound closure observed in the Hic1 group (Figure 6.2b). The mean wound area was over two times smaller compared to the Hic1 mice by 3-wpi and remained unchanged at later stages. After re-epithelization in Hic1^{E2F1} mice, a thickening of the distal epidermis was noted that subsided over time. Furthermore, the presence of blastema-like cell condensations and noticeable chondrogenesis was observed at 4- and 8-wpi (Figure 6.2c). Immunofluorescence imaging was used to locate *Hic1*-lineage cells across time points and assess the contribution of proliferation and fibrosis to the enhanced ear wound healing observed in Hic1^{E2F1} mice. Analogous to Hic1 mice, tdT expression in Hic1^{E2F1} uninjured ears was found underlying the epithelium and lining the auricular cartilage, and an accumulation of tdT^{+ve} cells was observed in wounded ears at the front edge of the excision plane (Figures 6.2d,e, S6.4a). Interestingly, at 1-wpi widespread proliferation (Ki67^{+ve}) was identified within and underlying the distal epithelium in Hic1^{E2F1} mice. Proliferation was reduced at later time-points, approximating patterns seen in uninjured ears (Figures 6.2d, S6.4c). Moreover, amplification of αSMA expression observed in Hic1^{E2F1} ear up to 2-wpi notably reduced in subsequent time points (Figure 6.2e, S6.4d-e). It is important to recognize that *Hic1*-lineage demonstrated minimal contribution to newly formed cartilage tissue, whether in the typical healing process showcased by Hic1 mice (Figure 6.2.g) or in the context of accelerated and superior chondrogenic regeneration seen in Hic1^{E2F1} ear (Figure 6.2h).

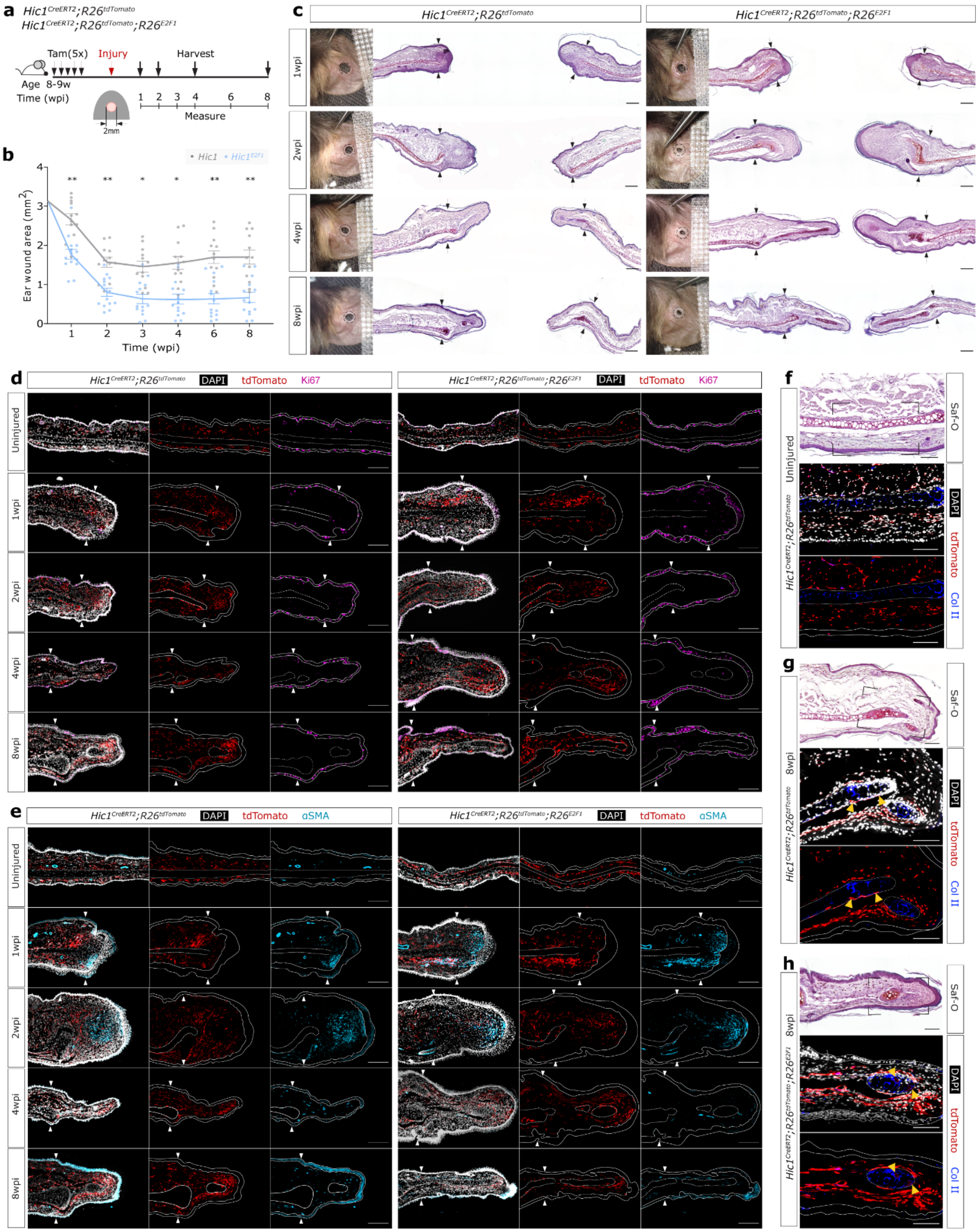
a
Hic1^{CreERT2};R26^{tdTomato}
Hic1^{CreERT2};R26^{tdTomato};R26^{E2F1}
Tam(5x)
Injury
Harvest
Age 8-9w
Time (wpi)
1 2 3 4 6 8
2mm
Measure
b
Hic1
Hic1^{E2F1}
Ear wound area (mm^2)
Time (wpi)
** ** * * ** **
c
Hic1^{CreERT2};R26^{tdTomato}
Hic1^{CreERT2};R26^{tdTomato};R26^{E2F1}
1wpi
2wpi
4wpi
8wpi
d
DAPI tdTomato Ki67
Uninjured
e
DAPI tdTomato αSMA
f
Saf-O
DAPI tdTomato Col II
g
h

Figure 6.2. Hic1-expressing cells and their progeny participate in ear wound healing. (a) Experimental timeline for tdT labelling of *Hic1* progenitors in adult mice and subsequent lineage-tracing and healing assessment after 2-mm ear wound injury (b) Quantification of ear hole closure over time between

$Hic1^{CreERT2}$;R26^{tdTomato} (Hic1) and $Hic1^{CreERT2}$;R26^{tdTomato};R26$^{\text{E2F1}}$ (Hic1$^{\text{E2F1}}$) mice. Data represent mean ± SEM ($n = 12$ Hic1, $n = 14$ Hic1$^{\text{E2F1}}$), ANOVA with Bonferroni *post hoc*, $*p < 0.01$, $**p < 0.001$ (c) Images of ears are from a single specimen representative of the average ear wound closure progression observed in Hic1 and Hic1$^{\text{E2F1}}$ mice, wherein dashed circle demarcates initial wound size (2-mm in diameter). Histological examination of mid-injury section using Safranin-O/Fast-green staining demonstrate that accelerated wound closure in Hic1$^{\text{E2F1}}$ mice was also associated with improved tissue remodelling and neo-cartilage formation. Scale bars, 200 µm. Arrows indicate the excision planes. Representative image of uninjured and unilateral mid-injury region for (d) Ki67 and I alpha-smooth muscle actin (αSMA). Considering the area ahead of the excision plane (arrowheads), proliferating cells (Ki67$^{+\text{ve}}$) were predominantly confined to the epidermis (region between solid lines) in both Hic1 and Hic1$^{\text{E2F1}}$ groups, with apparent transient increase in the dermis of Hic1$^{\text{E2F1}}$ at 1wpi. Conversely, αSMA expression was identified in both epidermis and underlying blastema-like structure in all groups at early timepoints and was shown to persist in the epidermis of Hic1 mice by 8-wpi, indicative of scarring. Scale bars, 200 µm. (d-e) Lineage-tracing at different healing stages demonstrate mobilization of $Hic1^{+}$ MPs to leading edge of injury in both strains, however, overlap with chondrogenic marker (type II Collagen – Col II), which is absent in (f) uninjured ear auricular cartilage, is rarely observed in (g-h) new cartilage condensations at 8-wpi (yellow arrowheads). Scale bars 100 µm. Nuclei counterstained with DAPI in all immunofluorescence panels.

6.4.4. Hic1^{+ve} progenitors are mobilized in response to acute articular cartilage injury

Enhanced regenerative abilities can extend to other tissues, as shown in genetically modified or naturally occurring organisms (Chadwick et al., 2007; Fitzgerald, 2017; Maden and Varholick, 2020; Seifert et al., 2012). Moreover, a strong genetic component has been observed between auricular and articular cartilage regenerative phenotypes, or lack thereof (Rai et al., 2012). Given the enhanced auricular cartilage regenerative capacity observed in Hic1$^{\text{E2F1}}$ mice, we speculated that their articular cartilage healing response could also be impacted. To test this, a full-thickness cartilage defect (FTCD) was generated in the trochlear groove of mice (Fitzgerald et al., 2008; Jablonski et al., 2021; Mak et al., 2016) 1-week after 4OHT injection (week 0), and monitored the injury repair up to 8-wpi (Figure 6.3a). A significant difference in cartilage healing score and remodelled tissue at the site of injury was observed between strains (Figure

6.3b,c). Hic1 mice demonstrated modest healing, illustrated by the formation of a thin layer of fibro-like cartilage tissue at 8-wpi, with absence of proteoglycan (safranin-O) and type II collagen matrix staining at defect site (Figure 6.3b,d). In contrast, injury repair qualitatively improved over time in Hic1^{E2F1} mice, displaying increased proteoglycan staining also associated with ECM-appropriate type II collagen expression (Figure 6.3b,e) resembling the pattern seen in adjacent intact tissue, as well as in uninjured native articular cartilage, wherein uniform type II collagen staining was observed in both Hic1 and Hic1^{E2F1} mice (Figure 6.3d,e). Of note, the abnormal subchondral bone remodelling observed in Hic1^{E2F1} was not fibrotic in nature, displaying minimal αSMA^{+ve} cells (Figure 6.3f). Importantly, inducing E2F1 overexpression in chondrocytes does not replicate the enhanced regenerative outcome post-FTCD observed in Hic1^{E2F1} mice (Figure S6.5). Taken together, these findings suggest a role for *Hic1*-lineage in shaping different healing abilities in knee cartilage and further support the idea of a common genetic basis of ear wound healing and articular cartilage regeneration.

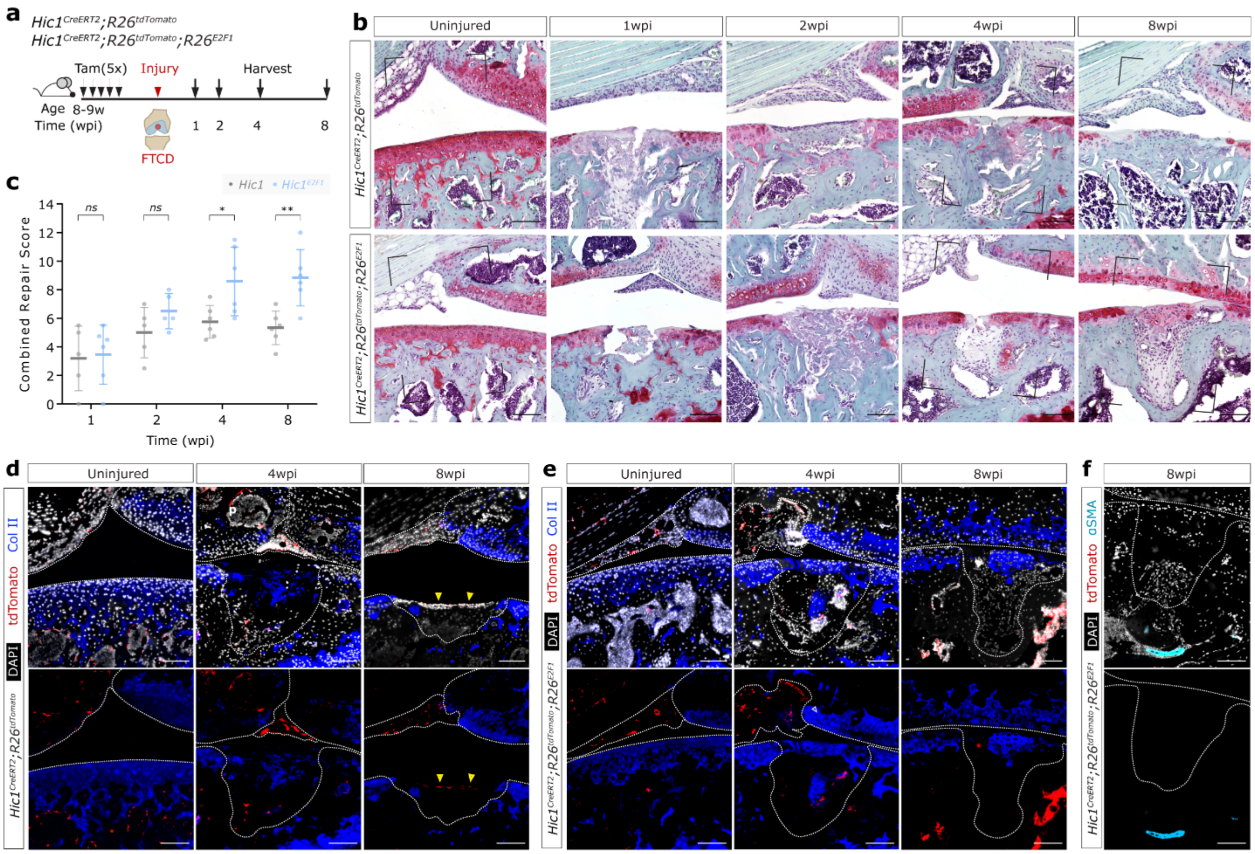
a
Hic1CreERT2;R26tdTomato
Hic1CreERT2;R26tdTomato;R26E2F1
Tam(5x)
Injury
Harvest
Age 8-9w
Time (wpi)
1
2
4
8
FTCD
c
Hic1
Hic1E2F1
Combined Repair Score
0
2
4
6
8
10
12
14
ns
ns
*
**
1
2
4
8
Time (wpi)
b
Uninjured
1wpi
2wpi
4wpi
8wpi
Hic1CreERT2;R26tdTomato
Hic1CreERT2;R26tdTomato;R26E2F1
d
Uninjured
4wpi
8wpi
Col II
tdTomato
DAPI
p
Hic1CreERT2;R26tdTomato
e
Uninjured
4wpi
8wpi
Col II
tdTomato
DAPI
Hic1CreERT2;R26tdTomato;R26E2F1
f
8wpi
αSMA
tdTomato
DAPI
Hic1CreERT2;R26tdTomato;R26E2F1

Figure 6.3. Articular cartilage healing after FTCD. (a) Experimental timeline of 4OHT administration, full-thickness cartilage defect (FTCD) in the femoral trochlear groove 1-week after 4OHT (week 0) and assessment of healing response at four different endpoints post-FTCD. (b) Safranin-O/fast-green staining at defect site across time points demonstrating differences in quality of resulting repaired tissue between strains. Area between brackets corresponding to section on images (d) and I. Scale bars, 100 µm. **(**c) Enhanced regeneration in Hic1^{E2F1} articular cartilage was also reflected on cartilage healing scores for 4-wpi and 8-wpi. Data represented as mean ± SD (n = 5/group), Student t test with Bonferroni *post hoc*, *p < 0.05, ** p < 0.01. Articular cartilage ECM collagen type II staining in (d) Hic1 and Hic1^{E2F1}mice was homogeneous and comparable in uninjured trochlea; and co-localized with enhanced safranin-O staining seen at 4-wpi and 8-wpi in Hic1^{E2F1} repaired tissue, while absent from fibro-like cartilage tissue formed at Hic1 mouse injury site, with tdT^{+ve} cells (yellow arrowheads), Scale bars, 100 µm. (f) Subchondral bone remodelling observed in Hic1^{E2F1} was not associated with αSMA^{+ve} fibrotic expression. Scale bars,100 µm. Nuclei counterstained with DAPI in all immunofluorescence images.

6.4.5. Hic1-lineage recruitment to defect site and contribution to repaired tissues

In both mouse strains, tdT^{+ve} cells were observed within bone marrow cavity and synovium post-FTCD and although their relative abundancy appear to change across timepoints, particularly in the synovium (Figure S6.6a), the overall localization of the cells within the knee joint compartment does not (Figures 6.3a, 6.4a,c). Also, a similar distribution pattern post-FTCD was observed compared to uninjured knee joints. Interestingly, by 8-wpi, a limited number of *Hic1*-lineage cells were present adjacent to or within the fibrocartilage-like tissue formed at the trochlea defect in Hic1 mice (Figures 6.3d, 6.4c, S6.6a), furthermore, the progeny of this lineage was not observed in the cartilage-like tissue formed in Hic1^{E2F1} mice (Figures 6.3e, 6.4c). Activation and expansion of *Hic1*$^{+ve}$ MPs and other cells in general in response to injury is a hallmark of healing processes, therefore we carried out immunofluorescence staining for Ki67 and EdU incorporation to assess the cell proliferation within and surrounding the defect site. At early time points both mouse strains demonstrated little actively proliferating cells (Ki67^{+ve}) at or adjacent to the defect site, with positive cells primarily observed within the bone marrow (Figure 6.4a). EdU^{+ve} cells were observed in both strains by 8-wpi and were found to be enriched in the synovium of Hic1^{E2F1} mice, which also contained label-retaining cells within the defect site (Figures 6.4b, S6.6b-c). At 1-wpi, there was no discernible difference in αSMA expression between uninjured knee joints of Hic1 or Hic1^{E2F1} mice (Figure S6.7), therefore this marker was not examined in further detail. Taken together, these results show that the overexpression of E2F1 in the *Hic1*-lineage cells act on other (e.g., *Hic1*$^{-ve}$ lineages) to influence repair, and only appear to take on a fibro-like phenotype within the knee joint microenvironment.

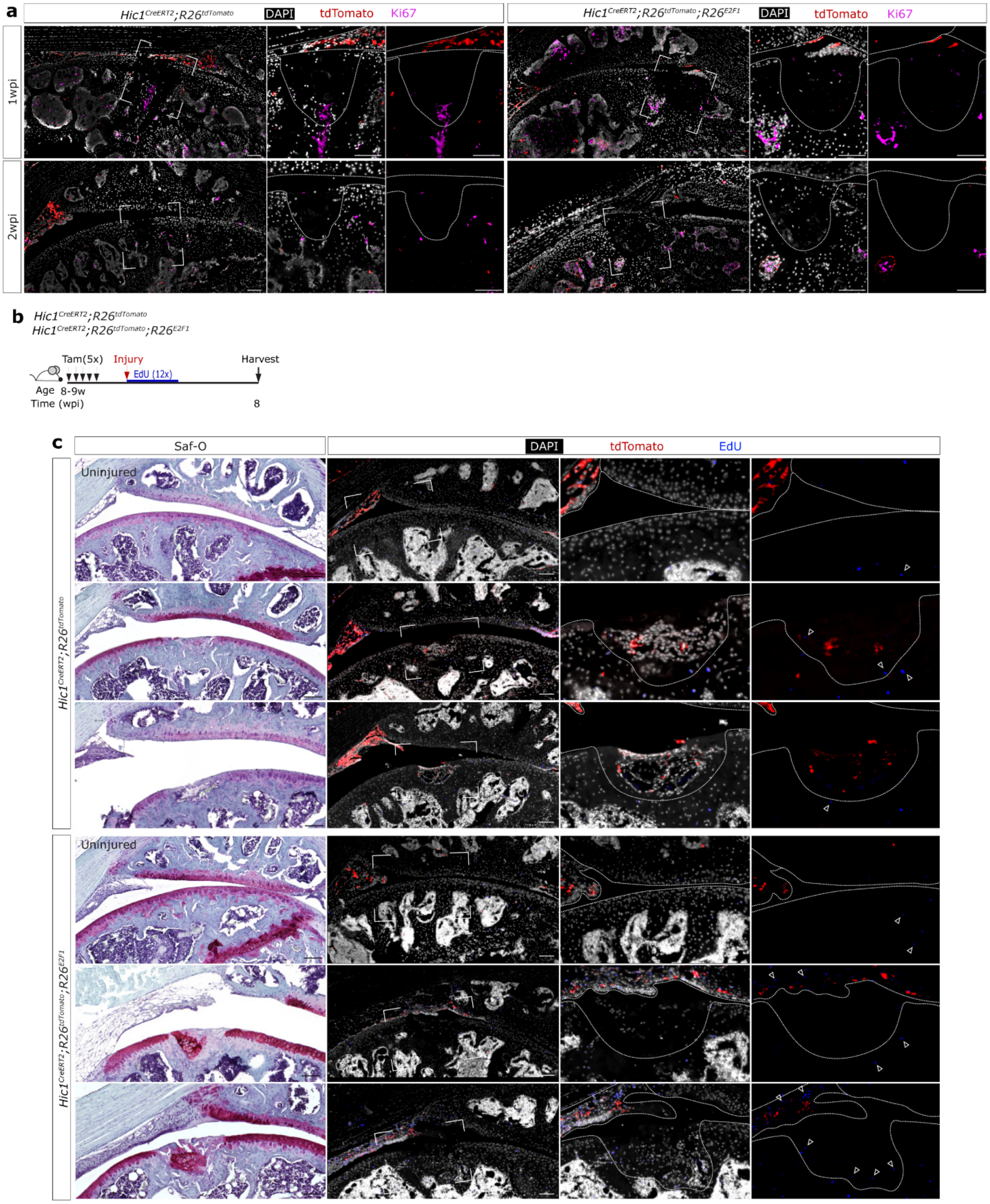
a
Hic1CreERT2;R26tdTomato
DAPI
tdTomato
Ki67
Hic1CreERT2;R26tdTomato;R26E2F1
DAPI
tdTomato
Ki67
1wpi
2wpi
b
Hic1CreERT2;R26tdTomato
Hic1CreERT2;R26tdTomato;R26E2F1
Tam(5x)
Injury
Harvest
EdU (12x)
Age 8-9w
Time (wpi)
8
c
Saf-O
DAPI
tdTomato
EdU
Uninjured
Hic1CreERT2;R26tdTomato
Uninjured
Hic1CreERT2;R26tdTomato;R26E2F1

Figure 6.4. Contribution of Hic1-lineage to cartilage formation and repair post-FTCD. (a) Immunofluorescence staining with Ki67 at Hic1 and Hic1^{E2F1} uninjured knee joint and 1- and 2-wpi (FTCD = brackets, close-ups) (b) Schematic of experimental design for data in (c) displaying representative

safranin-O and corresponding immunofluorescence for tdT and EdU (proliferation marker) in uninjured and injured knee joints for Hic1 (top panel) and Hic1^{E2F1} (bottom panel) mice at 8-wpi. Scale bars, 100 µm (*n* = 4/group). Arrowheads identify some of the EdU^{+ve} cells. Nuclei counterstained with DAPI in all immunofluorescence images.

6.4.6. Cartilage biomechanical function is not restored despite improved structural morphology

To gain topographical information injured and uninjured (contralateral) femurs were scanned using 3D X-ray microscopy (XRM) and structural properties were quantified at the injury site (or corresponding area in uninjured trochlea) within a standardized region of interest (Figure 6.5a-c). Representative cartilage thickness heat maps highlight the homogenous distribution of cartilage thickness within uninjured trochlea (Figure 6.5a), with a low surface-area-to-volume-ratio on average (Figure 6.5.c) indicative of surface regularity and comparable mean thickness between strains being observed (Figure 6.5b). As expected, through the course of healing variations in the morphology of the soft tissue being formed at the defect site contributed to further decrease on average thickness and a corresponding increase in tissue irregularity in the region of interest for up to 4-wpi. However, by 8-wpi, the repaired tissue observed within the defect site differed structurally between Hic1 and Hic1^{E2F1} mice. Thinner cartilage in Hic1 mice conferred a larger ratio of surface area-to-volume (Figure 6.5b,c). These results support our histological findings (Figure 6.3b) suggesting enhanced articular cartilage repair in Hic1^{E2F1} mice compared to controls. To determine to which extent the superior structural/compositional repair translate into proper function, comparative biomechanical assessment of the repaired tissue area in Hic1 and Hic1^{E2F1} mice was assayed via indentation (Figure 6.5d). Mapping of biomechanical parameters allowed regional differences between mid-injury and peripheral area to be visualized (Figure 6.5e). At 8-wpi, the mid-injury area in Hic1 mice repaired tissue was stiffer (red), requiring longer times to relax and residual forces remained high at equilibrium compared to uninjured trochlea and/or undamaged tissue surrounding the FTCD. In contrast, Hic1^{E2F1} displayed reduced structural stiffness and load at equilibrium (shades of blue). Quantitatively, only mid-injury mean structural stiffness significantly differed between Hic1 and Hic1^{E2F1} mice, being stiffer for the former;

however, compared to uninjured trochlea cartilage, repaired tissue yielded inferior compressive stiffness in both strains post-injury (Table 6.1).

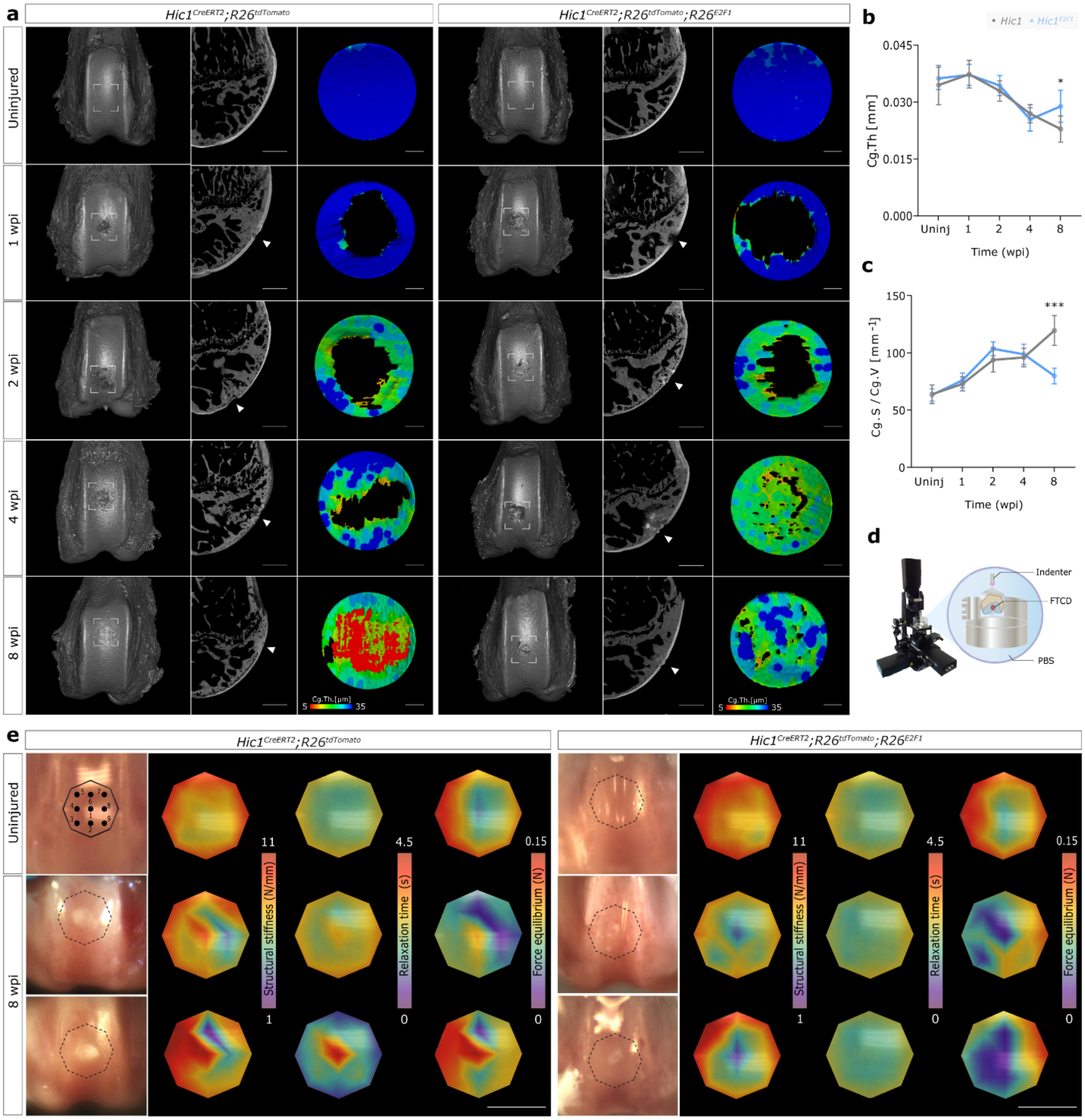
a
Hic1CreERT2;R26tdTomato
Hic1CreERT2;R26tdTomato;R26E2F1
Uninjured
1 wpi
2 wpi
4 wpi
8 wpi
Cg.Th.[µm]
5
35
b
Hic1
Hic1E2F1
Cg.Th [mm]
0.045
0.030
0.015
0.000
Uninj
1
2
4
8
Time (wpi)
*
c
Cg.S / Cg.V [mm -1]
150
100
50
0
***
d
Indenter
FTCD
PBS
e
11
1
Structural stiffness (N/mm)
4.5
0
Relaxation time (s)
0.15
0
Force equilibrium (N)

Figure 6.5. Evaluation of morphology and mechanical properties of repaired tissue. (a) Representative XRM images of uninjured and injured trochlear grooves, including 3D volume renderings and respective mid-injury cross-sections (2D), as well as corresponding representative cartilage thickness heat maps. FTCD location within brackets (3D) or indicated by arrowhead (2D). Scale bars, 500 µm; 100 µm. Quantification of (b) cartilage thickness (Cg. Th) and (c) surface area to volume ratio (Cg.S/Cg.V), *n* =

5/group, * $p < 0.05$,*** $p < 0.001$. (d,e) Biomechanical function was measured by microscale indentation at 20 µm depth from nine positions in the trochlear groove. (d) Schematic shows testing chamber filled with PBS where samples were affixed to a custom sample holder for testing, having the first position of measurement centred at the defect site. Representative uninjured and injured trochlea at 8-wpi and respective mapping obtained for structural stiffness (N/mm), relaxation time (s) and residual force at equilibrium (N). Scale bars, 50 µm.

Table 6.1. Comparison between groups for mean values of structural stiffness (SS: N/mm), relaxation time (Rt: s) and residual force after 120 s relaxation (Feq: N) for uninjured and injured hindlimb trochlear groove (TG) (*n* = 5/group; ANOVA with Bonferroni correction, $^{\lambda}$ $^{\gamma}p < 0.05$). Pairwise comparison between genotypes for trochlea groove region, and mid-injury and periphery sub-regions (*n* = 5/group; Student *t* test with Bonferroni correction, $^{\varphi}$ $p < 0.05$).

	Hic1			**Hic1^{E2F1}**		
Region	**SS (N/mm)**	**Rt (s)**	**Feq (N)**	**SS (N/mm)**	**Rt (s)**	**Feq (N)**
TG Uninj.	8.4 ± 1.50 $^{\lambda}$	1.9 ± 0.04	0.06 ± 0.021	8.7 ± 1.1 $^{\gamma}$	2.0 ± 0.12	0.07 ± 0.02
TG Inj.	6.2 ± 0.98 $^{\lambda}$	2.2 ± 0.42	0.06 ± 0.019	6.1 ± 0.60 $^{\gamma}$	2.0 ± 0.27	0.05 ± 0.011
Mid-injury	9.1 ± 2.42 $^{\varphi}$	4.1 ± 3.69	0.11 ± 0.060	4.43 ± 2.71 $^{\varphi}$	2.8 ± 2.21	0.04 ± 0.041
Periphery	6.0 ± 0.80	2.0 ± 0.16	0.05 ± 0.016	6.3 ± 0.69	1.9 ± 0.03	0.06 ± 0.013

6.5. Discussion

Tissue regeneration is a complex trait, and the inability of adult mammals to endogenously regenerate cartilage presents considerable clinical challenges (Muthu et al., 2023). Leveraging off previous studies (Abbasi et al., 2020; Arostegui et al., 2022; Scott et al., 2019; Soliman et al., 2020) demonstrating that *Hic1* expression marks a unique cohort of progenitor cells in embryonic and adult tissues with mesenchymal lineage potential, we explored the role of these cells in the maintenance and repair/healing processes of cartilaginous tissues. I have demonstrated that even though *Hic1*$^{+ve}$ cells do not reside in auricular or articular cartilage in adult mice, cells of the *Hic1*-lineage can influence healing outcomes following injury of these typically regenerative-incompetent tissues.

Within the ear, *Hic1*$^{+ve}$ lineage-traced cells were primarily observed within the dermis and lining the auricular cartilage in the ear pinnae. The limited ear wound closure in Hic1 mice aligns with previous findings in non-regenerative strains, in which it has been suggested that a short-lived regenerative response and tissue outgrowth leads to the formation of a few cartilage condensations distal to the injury site (Gawriluk et al., 2016; Rajnoch et al., 2003). Despite changes in the relative abundancy of *Hic1*-lineage in response to injury and accompanying the transient tissue outgrowth, these cells rarely contributed to cartilage condensations formed in Hic1 ear wound healing and this finding will be discussed in more detail below.

Interestingly, E2F1 overexpression in the *Hic1* lineage resulted in accelerated closure rate and improved ear wound healing. These results are in keeping with previous research involving dermal tissue (skin), wherein wound-activated *Hic1*$^{+ve}$ MPs have the potential to enhance dermal regeneration (Abbasi et al., 2020). Although Hic1^{E2F1} wound healing led to superior chondrogenic regeneration, *Hic1*-lineage demonstrated minimal contribution to newly formed cartilage, as seen in Hic1 mice. Yet, *Hic1*-progeny was abundantly present at the leading edge of the ear wound, migrating under the new epithelium and encircling cartilaginous condensations. Although intriguing, this phenomenon is reminiscent of *Hic1*-lineage behaviour recently described in embryonic appendicular development (Arostegui et al., 2022).

Lineage-tracing experiment utilizing the same *Hic1*-tdtomato reporter strain employed here denoted the migratory ability of *Hic1* cells during limb bud outgrowth, showing tdT^{+ve} cells localize to the mesenchyme underlying the epithelium, delineating but not directly contributing to chondrogenic anlagen. Thus, *Hic1*-lineage appears to create a conducive environment to promote cartilage induction and/or regeneration. This does beg the question, however, of what cells are responsible for the newly regenerated cartilage tissue. Unfortunately, there is no definitive evidence of any particular cell population being responsible for endogenous cartilage regeneration.

The presence of blastema-like characteristics in the process of ear hole closure in healer mouse strains, such as MRL/MpJ and Spiny mouse (*Acomys*) (Clark et al., 1998; Seifert et al., 2012), suggests that there are common mechanisms and cellular processes at play in both limb regeneration in amphibians and tissue repair in mammals (Zhang et al., 2015). During limb development, reciprocal interaction between apical ectodermal ridge (AER) and underlying undifferentiated mesenchyme signaling centers is believed to contribute to outgrowth and patterning of the limb (Globus et al., 1980). This phenomenon has been proposed to create a conducive environment for maintenance of a blastem-like structure, a mass of undifferentiated progenitor cells distal to the excision plane, which favours tissue regeneration (Rajnoch et al., 2003; Seifert et al., 2012). Hic1^{E2F1} mice ear wound healing process mirrored that of healer strains, such as MRL/MpJ, characterized by a rapid process of re-epithelialisation associated with increased proliferation and thickening of epidermis (Clark et al., 1998; Rajnoch et al., 2003).

In the knee joint, under homeostatic conditions, *Hic1*$^{+ve}$ cells and their progeny were observed in the synovium, fat pad and subchondral bone marrow. Following FTCD, apparent activation and expansion was observed in the synovium in both Hic1 and Hic1^{E2F1} mice, but notably a direct contribution was only observed in the fibro-like cartilage formed in regenerative-incompetent Hic1 mice. Experimental studies and clinical practice suggest that fibro-like cartilage, formed in response to osteochondral injuries or through microfracture (marrow-stimulating) surgical interventions, originates from bone-marrow derived cells. However, to the best of my knowledge, the precise lineage of these fibro-cartilage producing cells remains unknown. My data would suggest that at least a sub-population of the cells contributing to fibro-like cartilage are derived from the *Hic1*-lineage; however, any of the tissues harbouring *Hic1*$^{+ve}$ cells could be providing the fibro-cartilage generating cells. For instance, migration from synovial cells to injury site have been previously described (Hunziker and Rosenberg, 1996), and it is plausible that the release of signaling factors made possible by penetrating the subchondral bone prompts migration and contribution to the healing process. Without markers to identify tissue-specific MP subpopulations, it becomes challenging to pinpoint the specific source of these cells.

Another point to consider is the enhanced repair of articular cartilage in Hic1^{E2F1}, albeit with limited functional restoration (biomechanical properties), likely correlated with the altered subchondral bone formation observed. Given the absence of *Hic1*-lineage cells on the neo-formed cartilage, it could be argued that the most likely candidates are chondrocytes themselves; however, if this was the case then we would have expected to see more cartilage regeneration when E2F1 was overexpressed in the Col2^{Cre} mice. One hypothesis would be synovial crosstalk, whereby FTCD triggers a response from synovial progenitor cells that in turn influence the repair process and fate decisions (Chau et al., 2022). Notably, synovial hyperplasia is a hallmark of injury response (Roelofs et al., 2017) and the role of synovial cells in regulating the joint microenvironment in injury and disease, or as a pool for mesenchymal progenitors has garnered significant attention in recent years (Chau et al., 2022; Collins et al., 2023).

The intriguing regenerative effect of E2F1 expression in *Hic1*$^{+ve}$ cells raises the question about the mechanism of this activity. Apart from its crucial involvement in cell cycle (G1/S transition), E2F1 has also been implicated in apoptosis and differentiation processes (Chen et al., 2009; Ertosun et al., 2016; Shats et al., 2017). In addition to the direct influence of E2F1 on expression and activation of HIC1 (Jenal et al., 2009), there is a feedback regulatory loop with HIC1 (Van Rechem et al., 2010). Further research is required to elucidate the molecular mechanism by which inducing E2F1 expression solely in *Hic1* cells is able to drive a superior healing phenotype within these tissues and whether there are tissue-specific differences.

Furthermore, our fundamental lack of understanding of what cells contribute to wound healing processes in cartilaginous tissues (Muthu et al., 2023) emphasizes the importance of understanding the role of *Hic1*-lineage cells in the intricate process of tissue repair and regeneration, and notably their contribution to fibro-like phenotype in articular cartilage.

6.6. Acknowledgements

A.O.M. was supported by University of Calgary and Alberta Innovates' graduate scholarships. The funders had no role in study design, data collection and analysis, or manuscript preparation. This research was funded by operating grants from the Canadian Institute of Health Research (CIHR).

6.7. Author's contribution

A.O.M, R.K. conceived, designed, and oversaw experiments with suggestions from J.B. and W.B.E. A.O.M., performed all experiments, analyzed data, and wrote the manuscript. B.B. J.C. and N.K. assisted on data collection. R.K., assisted with data interpretation.

6.8. Supplementary information

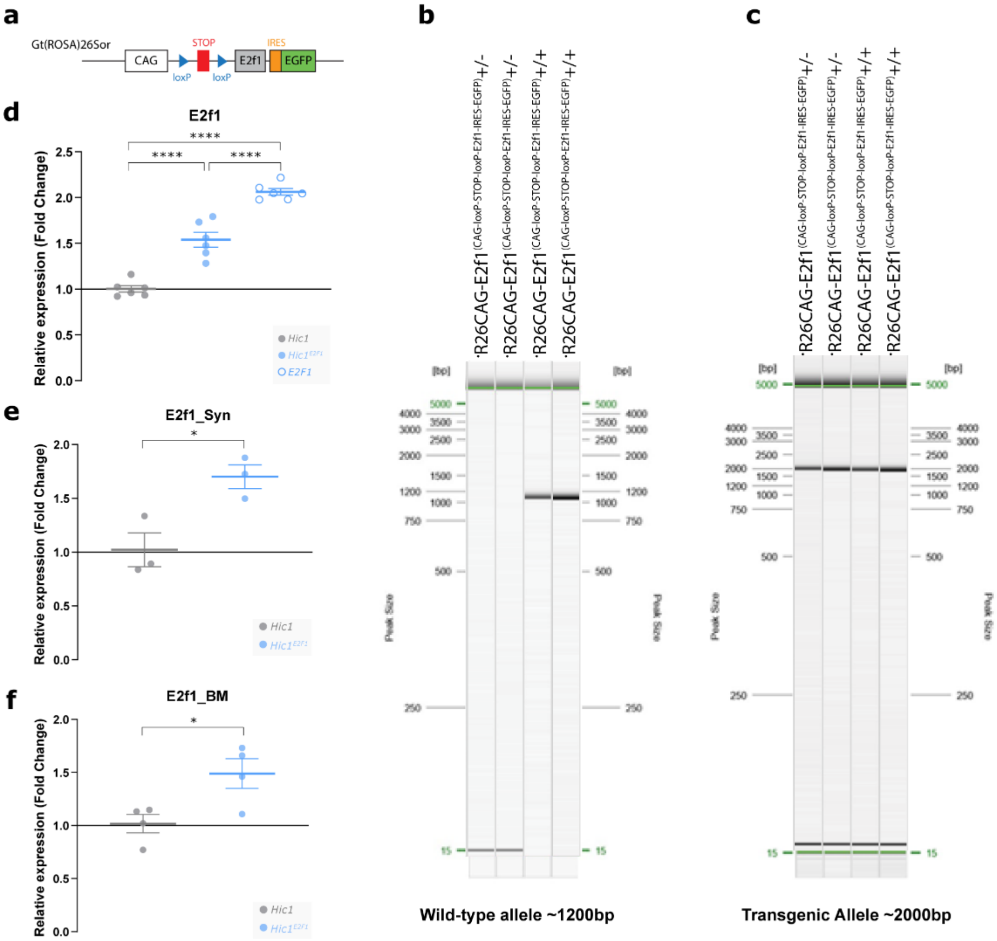

Figure S6.1. Generation of E2F1 over-expressing transgenic mice. (a) Overview of the Rosa26$^{\text{CAG-E2f1}}$ knock-in allele (b,c) Genotyping performed to confirm mice were homozygous for transgenic allele (d) Relative *E2f1* mRNA levels in expanded bone marrow cells derived from *Hic1*$^{\textit{CreERT2}}$;R26$^{\textit{tdTomato}}$ (Hic1), *Hic1*$^{\textit{CreERT2}}$;R26$^{\textit{tdTomato}}$;R26$^{\text{E2F1}}$ (Hic1$^{\text{E2F1}}$), and R26$^{\text{CAG-E2f1}}$ (E2F1) mice after *in vitro* Cre lentiviral transduction (n = 6/group). Statistical significance was determined by ANOVA with Bonferroni *post-hoc*, **** $p < 0.0001$. Relative mRNA *E2f1* increase were also similar in cells derived from (e) bone marrow (n = 4/group) and (f) synovium tissues (n = 3/group) after *in vivo* 4OHT-induced recombination. Comparison between genotypes in (e) and (f) was performed using Student's t-test, * $p < 0.05$.

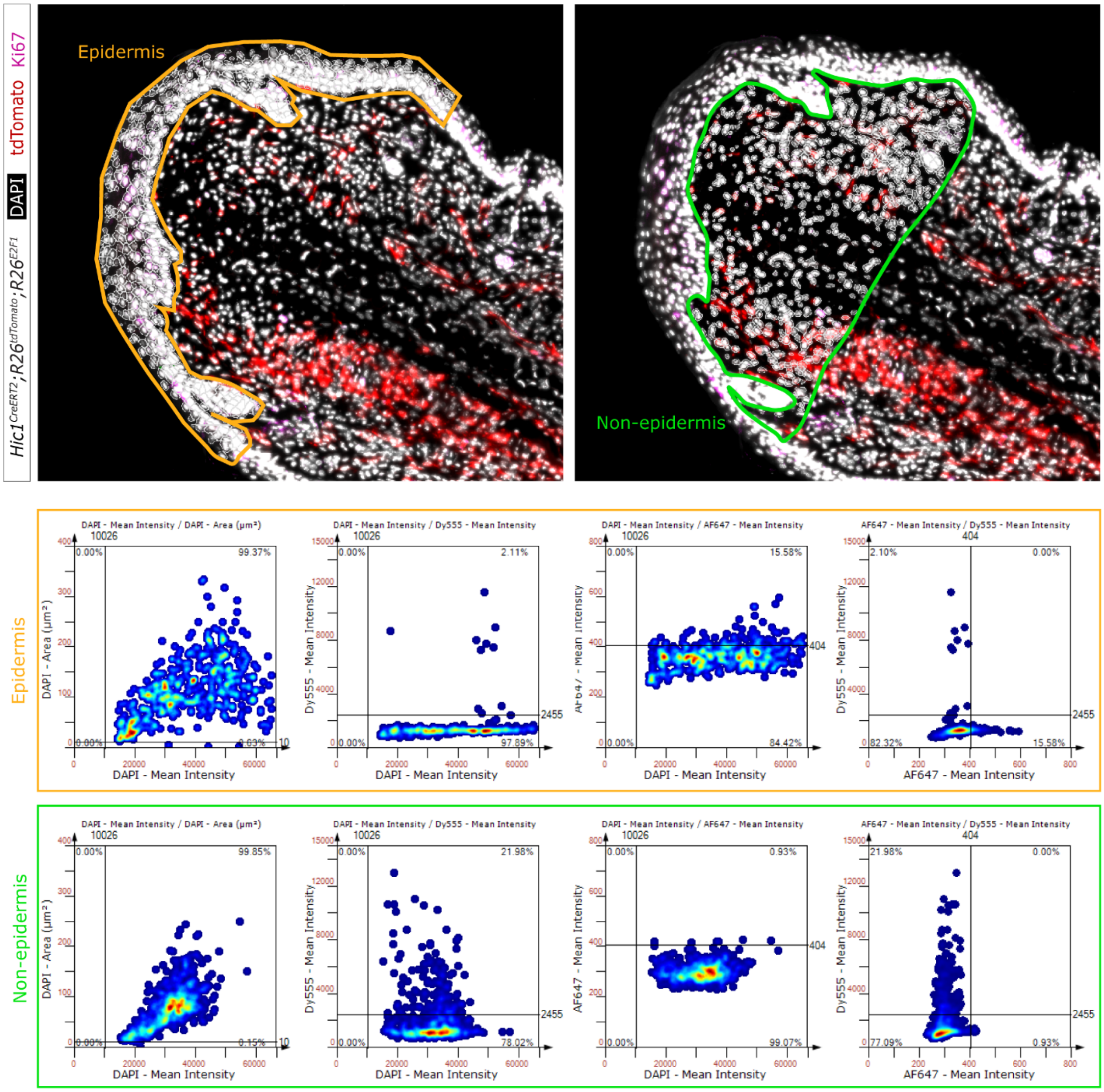
Hic1CreERT2;R26tdTomato;R26E2F1
DAPI
tdTomato
Ki67
Epidermis
Non-epidermis
Epidermis
DAPI - Mean Intensity / DAPI - Area (µm²)
10026
0.00%
99.37%
0.00%
0.63%
10
DAPI - Area (µm²)
DAPI - Mean Intensity
DAPI - Mean Intensity / Dy555 - Mean Intensity
10026
0.00%
2.11%
0.00%
97.89%
2455
Dy555 - Mean Intensity
DAPI - Mean Intensity
DAPI - Mean Intensity / AF647 - Mean Intensity
10026
0.00%
15.58%
0.00%
84.42%
404
AF647 - Mean Intensity
DAPI - Mean Intensity
AF647 - Mean Intensity / Dy555 - Mean Intensity
404
2.10%
0.00%
82.32%
15.58%
2455
Dy555 - Mean Intensity
AF647 - Mean Intensity
Non-epidermis
DAPI - Mean Intensity / DAPI - Area (µm²)
10026
0.00%
99.85%
0.00%
0.15%
10
DAPI - Area (µm²)
DAPI - Mean Intensity
DAPI - Mean Intensity / Dy555 - Mean Intensity
10026
0.00%
21.98%
0.00%
78.02%
2455
Dy555 - Mean Intensity
DAPI - Mean Intensity
DAPI - Mean Intensity / AF647 - Mean Intensity
10026
0.00%
0.93%
0.00%
99.07%
404
AF647 - Mean Intensity
DAPI - Mean Intensity
AF647 - Mean Intensity / Dy555 - Mean Intensity
404
21.98%
0.00%
77.09%
0.93%
2455
Dy555 - Mean Intensity
AF647 - Mean Intensity

Figure S6.2. Ear tissue immunofluorescence imaging analysis and quantification. Representative images of immunofluorescence imaging of injured ear 1-wpi (Hic1^{E2F1}) with contouring of front edge of injury – epidermis (yellow) and non-epidermis (green) regions of interest - and corresponding gating strategy, wherein detected DAPI-positive nuclei and cells co-expressing fluorescence markers of interest were quantified for tdtomato (Dy555) and Ki67 (AF647).

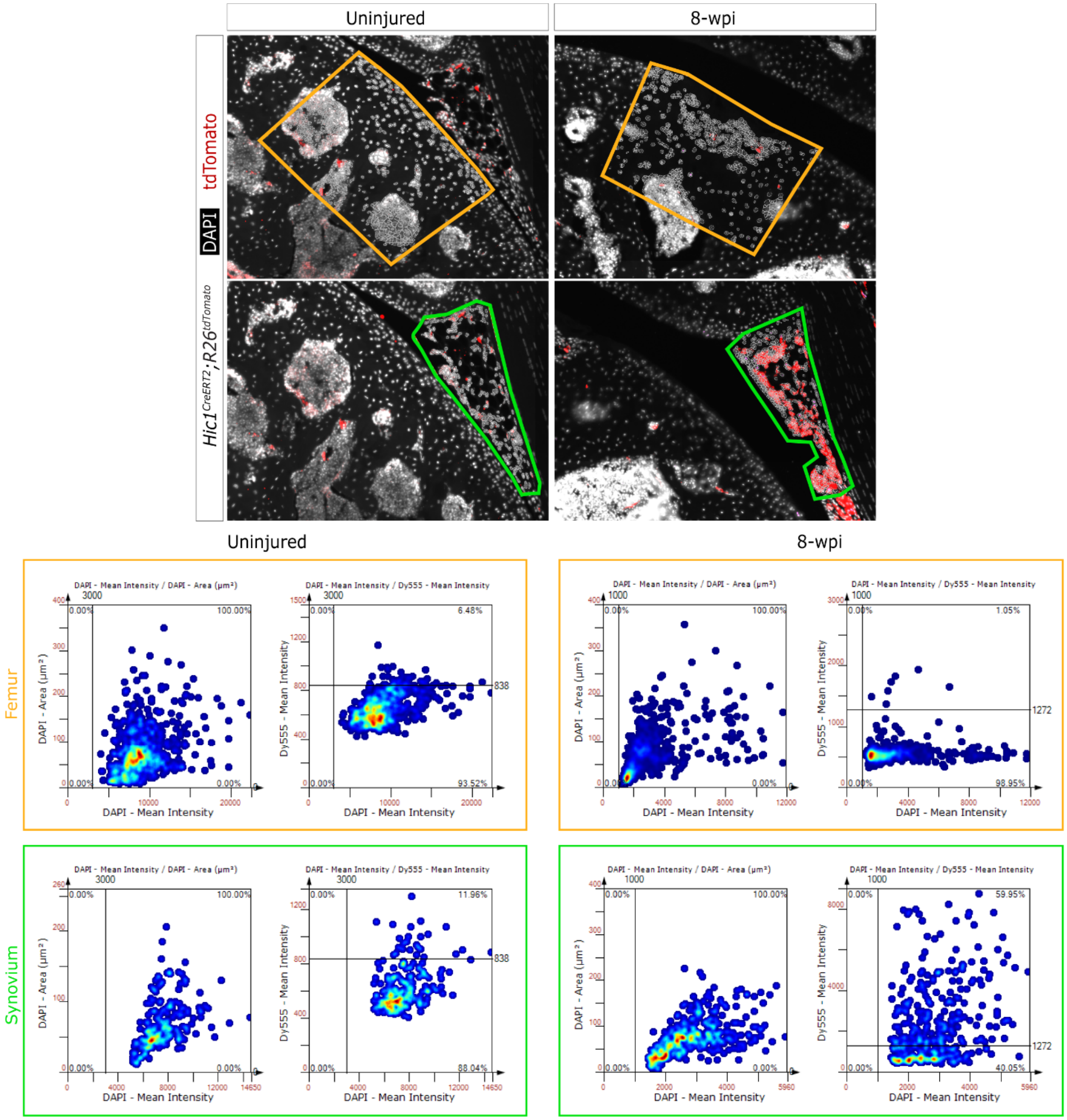

Figure S6.3. Knee joint immunofluorescence imaging analysis and quantification. Representative images of immunofluorescence imaging of uninjured knee joint and injured trochlea groove at 8-wpi (FTCD), with contouring of femur/defect site (yellow) and synovium (green) regions of interest - and their corresponding gating strategy, wherein detected DAPI-positive nuclei and cells co-expressing fluorescence markers of interest were quantified, as exemplified here for tdTomato (Dy555).

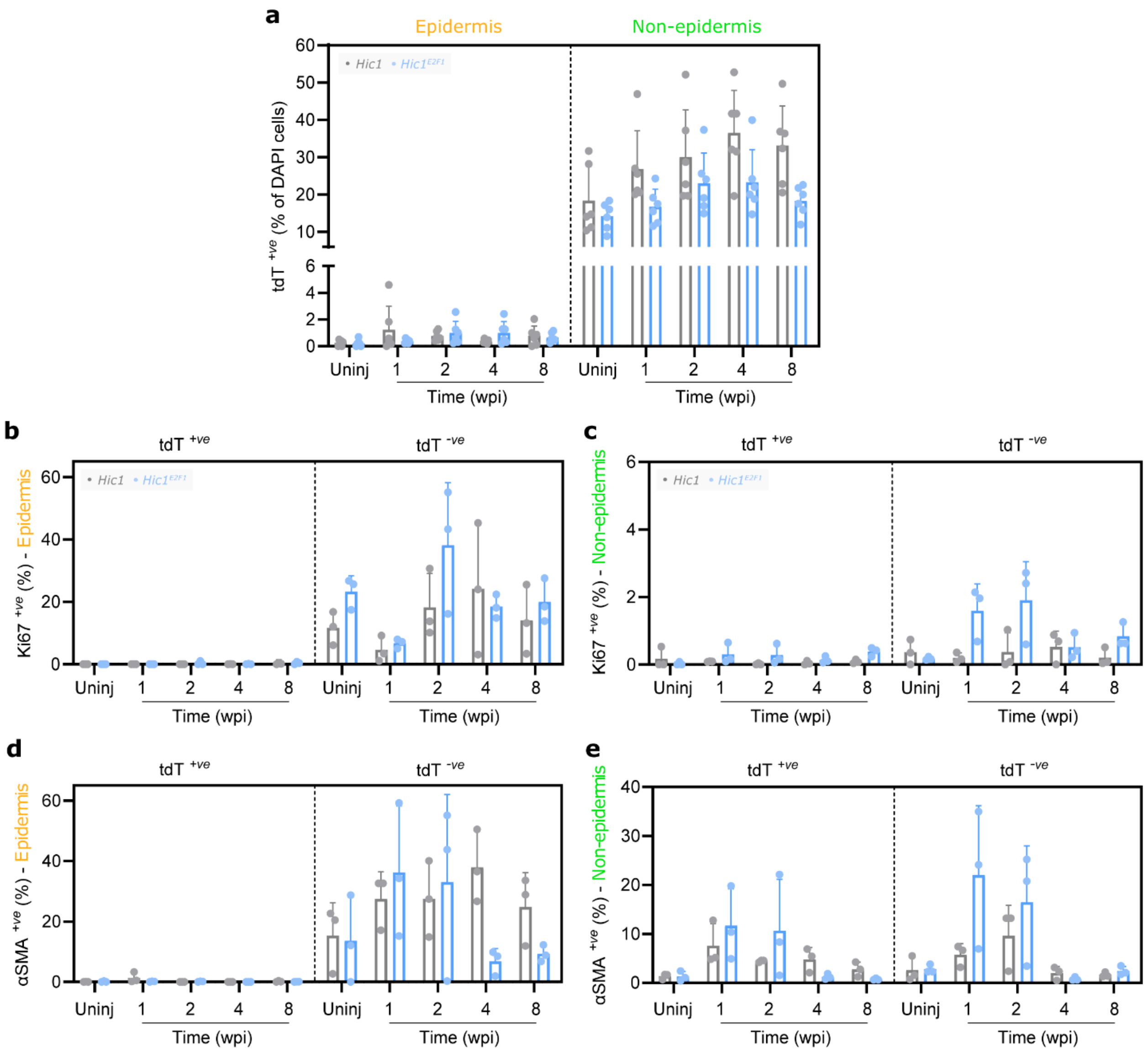

Figure S6.4. *Hic1*-lineage recruitment and contribution to ear tissue outgrowth after injury. (a) Immunofluorescence quantification in uninjured and injured ear pinnae demonstrate *Hic1*-lineage (tdT^{+ve}) is enriched in non-epidermis in both Hic1 and Hic1^{E2F1} mice, with few to no *Hic1*-derived progeny identified on epidermal tissue. Proliferative cells (Ki67^{+ve}) were confined to the (b) epidermis and (c) slight increase seen in Hic1^{E2F1}outgrowing non-epidermal tissue within 1- to 2-wpi was not associated to an expansion of the *Hic1*-lineage (tdT^{+ve}). Interestingly, Hic1^{E2F1} mice displayed a transient increase in αSMA expression in both (d) epidermal and (e) non-epidermal tissues, while Hic1 mouse injured ears kept an elevated αSMA expression in its epidermis. Average percentage (%) of DAPI^{+ve}-cells ± SD (*n* = 3-6 mice/group, 2-3 sections/mouse).

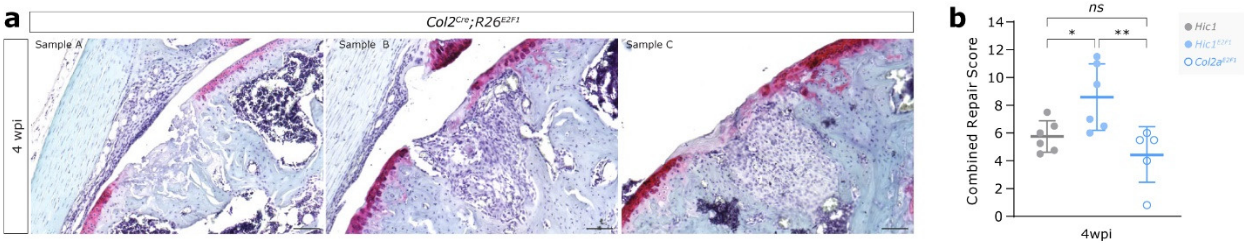
a
Col2Cre;R26E2F1
Sample A
Sample B
Sample C
4 wpi
b
ns
*
**
Combined Repair Score
14
12
10
8
6
4
2
0
Hic1
Hic1E2F1
Col2aE2F1
4wpi

Figure S6.5. Col2aCre; R26^{E2F1} are unable to regenerate articular cartilage after FTCD. Unlike *Hic1*-lineage cells, E2F1 overexpression in *Col2a*-expressing cells (*n* = 5) did not improve healing outcomes, as demonstrated by (a) Safranin-O/Fast-green staining and (b) cartilage healing scores (Fitzgerald et al., 2008) obtained 4-weeks post-FTCD. Despite not being a tamoxifen-inducible transgenic, *Col2a*^{Cre}; R26^{E2F1} was subjected to the same 4OHT protocol as Hic1 and Hic1^{E2F1} mice prior to injury to avoid any estrogen-related effects that could cofound healing outcomes. Scale bars, 100 µm. Comparison between genotypes in was performed using *one-way* ANOVA, * $p < 0.05$ ** $p < 0.01$.

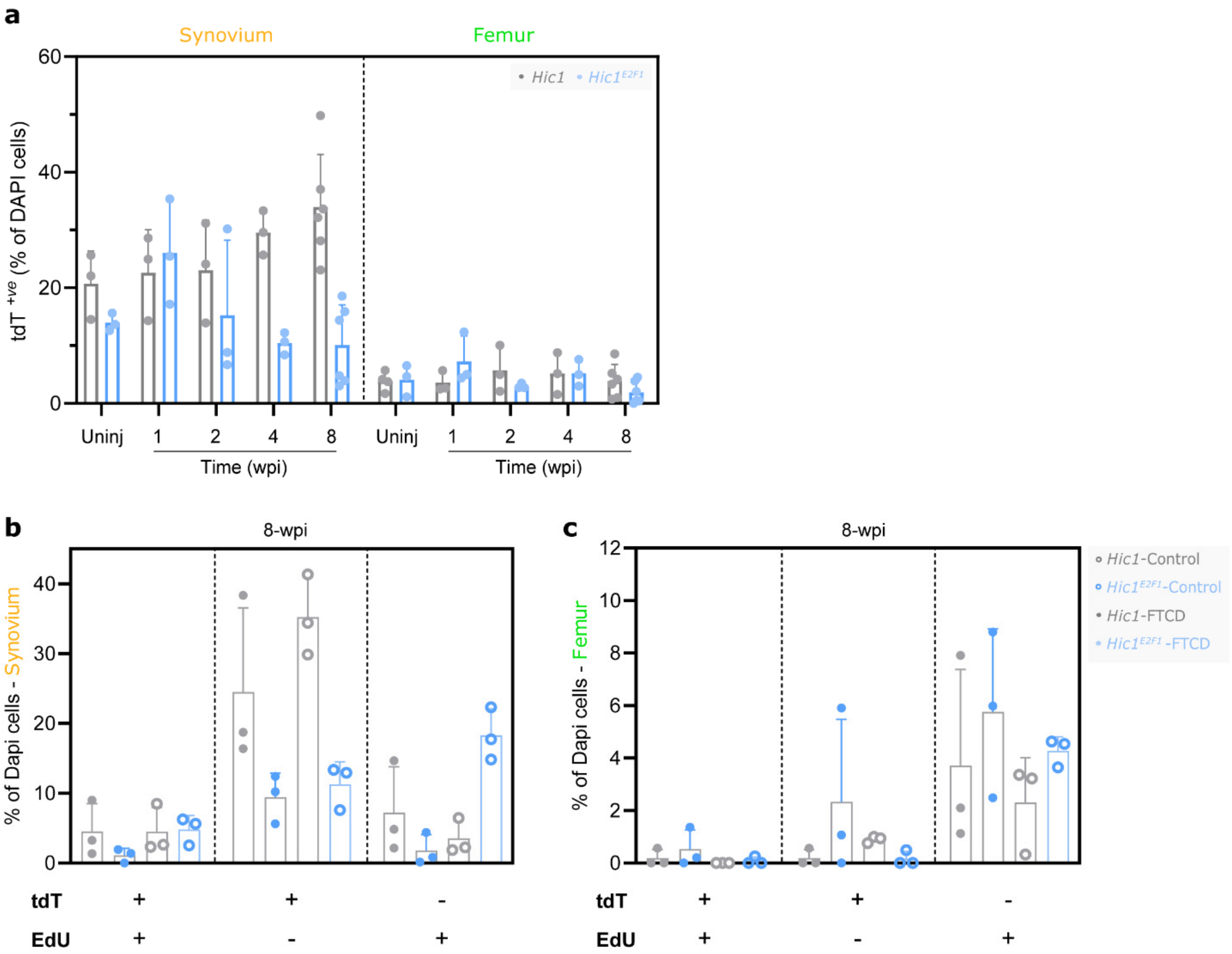

Figure S6.6. *Hic1*-lineage recruitment and response to injury after FTCD. (a) Immunofluorescence quantification demonstrate *Hic1*-lineage (tdT^{+ve}) is enriched in the synovium of both Hic1 and Hic1^{E2F1} uninjured trochlea groove, with *Hic1*-derived progeny being sustained in Hic1 synovium and decreasing in Hic1^{E2F1} by 8-wpi. (b-c) EdU-labelling showing retention of dye in injured Hic1^{E2F1} synovium at 8-wpi, particularly in the synovium region. Average percentage (%) of DAPI^{+ve} cells ± SD (*n* = 3-6 mice/group, 2-3 sections/mouse).

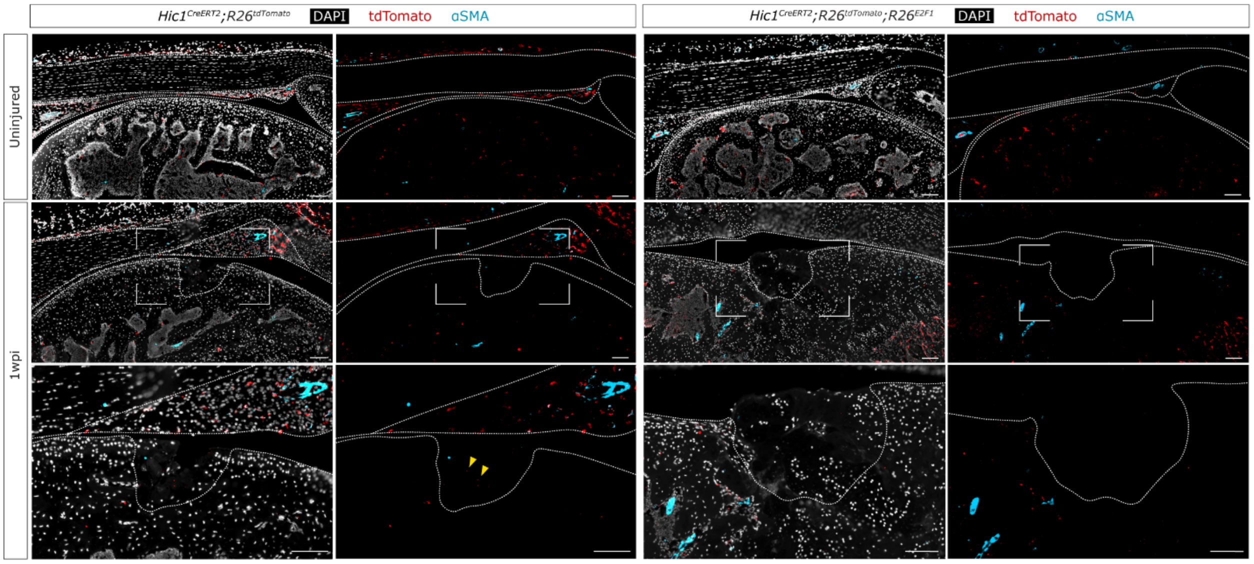
Hic1^{CreERT2};R26^{tdTomato} DAPI tdTomato αSMA
Hic1^{CreERT2};R26^{tdTomato};R26^{E2F1} DAPI tdTomato αSMA
Uninjured
1wpi

Figure S6.7. Characterization of αSMA expression after FTCD. Immunofluorescence staining with αSMA on uninjured and 1-wpi knee joints for Hic1 and Hic1^{E2F1} mice. FTCD area identified between brackets, tdT^{+ve} cells (yellow arrowheads). Scale bars, 100 µm.

Chapter Seven: Discussion and Future Directions

7.1. Overview

The knee joint comprises living structural tissues which can, to a certain extent, adapt their form and composition to meet functional demands. Failure to adapt or overuse, however, can lead to irreversible injury/degeneration and, consequently, joint failure. Using various murine models, the work presented in this dissertation explored how cartilage tissue homeostasis and function are maintained in health and changed in response to different stressors, as well as the contribution of a recently preconized MP lineage to tissue repair in cartilaginous tissues, providing new insights into adaptative and maladaptive (pathological) remodelling.

In Chapter 4, we developed a novel mouse model of non-surgically induced chondrocyte depletion, wherein mice expressing Cre recombinase under the aggrecan gene promoter (*Acan*Cre$^{\mathrm{ERT2}}$) drove inducible expression of diphtheria toxin (DTA), to understand the role of chondrocyte death on cartilage maintenance and degeneration. Despite the importance of chondrocytes in maintaining cartilage health, this work demonstrated that acute chondrocyte death in adult cartilage disrupts tissue homeostasis, without visible compromise of cartilage surface integrity or the development of OA-like symptoms. Moreover, focal areas devoid of chondrocytes did not repopulate after genetically induced cell depletion, suggesting an adaptive but non-regenerative response from surviving cells.

In Chapter 5, we focused on investigating the impact of *Prg4* loss-of function on joint morphology and cartilage health in the distal femur. While landmark-based geometric morphometrics is a well stablished approach for the study of shape variation in evolutionary biology, its intersection with biomechanics in this study, to describe and quantitatively capture structural deformations in a meaningful way, is unique. The 2D (histological) and 3D (XRM imaging) joint abnormalities and micro-environmental constraints observed in *Prg4*$^{-/-}$ mice joint likely contribute to altered mechanical loading in addition to abnormal biomechanical properties, contributing to degradation of articular cartilage over time. Overall, this study provides new insights on the intricate relationship between *Prg4* loss-of-function, joint morphology, cartilage health and function.

In Chapter 6, we utilized a lineage-tracing approach to investigate the role of *Hic1*$^{+ve}$ cells, a new cohort of tissue-resident quiescent mesenchymal progenitors, in the maintenance and healing processes of two distinct cartilaginous tissues (ear and knee) with similar regenerative limitations. The findings from this study indicate *Hic1*-progeny can assume a fibro-like phenotype leading to scarring, and intriguingly that the manipulation of E2F1 expression in *Hic1* cells and progeny positively impacts wound closure and articular cartilage regeneration, albeit with minimal (if any) direct contribution of *Hic1*-progeny to neo-chondrogenesis. Collectively, this suggests that *Hic1*-lineage cells might influence repair in other cell populations (e.g., *Hic1*-lineages) to promote healing. On the other hand, these Hic1-lineage cells may play a role in the failure of natural regeneration in cartilage. This study provided valuable insights and may hold promising implications for advancing therapeutic targets to enhance cartilage tissue repair.

7.2. Significance

7.2.1. Cartilage degeneration vs. regeneration

The ECM serves as a crucial microenvironment that guides and influences tissue repair and remodelling. Mechanotransduction, a process by which cells sense and respond to mechanical cues from their surrounding ECM, has significant implications for chondrocyte phenotype and viability. Under normal physiological conditions and in disease states, cellular responses influence ECM remodelling dynamics and the ECM, in turn, drives changes in cell behaviour (reviewed in Gilbert et al., 2021). In cartilage, a delicate balance exists between the synthesis and degradation of matrix proteins, such as ACAN and type II collagen, and this is key to maintaining cartilage's mechanical properties and function. Interestingly, even under physiological conditions, the turnover rate of ECM constituents is quite distinct. For example, ACAN turnover rates (weeks/months) are orders of magnitude greater than type II collagen (years/decades) (Heinemeier et al., 2016; Maroudas et al., 1998). Therefore, increased degradation or reduced synthesis of ACAN can disrupt tissue balance and impair the load-bearing capabilities of this composite tissue, leading to further compromise of the matrix. However, it also offers a higher likelihood of restoration of expression/function after damage through an anabolic response (Karsdal et al., 2008). In contrast, type II collagen turnover is limited in healthy cartilage and osteoarthritic joints (Heinemeier et al., 2016). While the former likely contributes to the long-term stability of the tissue, it also implies that damaged or degraded collagen is not easily replaced. Considering the mechanically demanding environment of synovial joints, this phenomenon likely contributes to poor tissue regeneration.

In Chapter 4, the loss of chondrocytes due to induced expression of DTA triggers an adaptative remodelling process that preserves collagen structure and does not lead to a degenerative phenotype. This remodelling involved transient upregulation of catabolic enzymes, changes in biomechanical stiffness distribution in femoral condyles, and reduced proteoglycan (safranin-O staining) at earlier stages, followed by compensatory, albeit incomplete recovery at later time points. In this context, increased expression of ADAMTS5 (main proteoglycan protease) may not be associated with a degenerative phenotype, but rather, it is part of the tissue response to non-homeostatic conditions which may lead to tissue damage in the case of sustained expression (Li and Xu, 2015). Therefore, the dual role of ADAMTS5 (remodelling vs. degeneration) is context-dependent and likely influenced by the microenvironment through synovial inflammation (Sanchez-Lopez et al., 2022). In *Prg4*$^{-/-}$ mice, cartilage structure and composition changes, as highlighted in Chapter 5 and in published literature (Coles et al., 2010; Karamchedu et al., 2016). These changes lead to a maladaptive remodelling predisposing the cartilage in these mice to pathological degeneration. For example, chondrocyte apoptosis in *Prg4*$^{-/-}$ cartilage increases due to excessive deformation and shear stress (Waller et al., 2013). It is plausible that the changes in anatomy and geometry revealed in my thesis also impact load distribution in the knee joint, further impacting chondrocyte metabolism and synthesis and ultimately contributing to tissue degeneration. Within the context of tissue repair (Chapter 6), the differences in healing outcomes between strains in both the ear and knee joint could have also been influenced by ECM deposition and remodelling. During ear wound healing, the deposition of collagens and other ECM components differs between regenerating and non-regenerating (scar-forming) species (Gawriluk et al., 2016). Additionally, ECM can act as a physical cue for cell migration, while its stiffness can alter cellular behaviour and fate, including MPCs differentiation and chondrogenic potential (Van Helvert et al., 2018; Zhou et al., 2022). In the context of ear wound healing, *Hic1*-lineage cells were shown to play a role in promoting wound closure and cartilage regeneration despite limited direct contribution to the formation of new cartilage tissue. Perhaps the *Hic1*-lineage plays an active role in ECM deposition, influencing cell migration and tissue remodelling, and E2F1 could have prolonged activation of *Hic1* cells, promoting tissue outgrowth and the structural foundation/microenvironment favouring chondrogenesis vs. scar. In the context of the osteochondral injury, altered bone remodelling in Hic1^{E2F1} mice underlying the FTCD might have also biased cell differentiation towards enhanced chondrogenesis by providing a different basement matrix composition and stiffness.

As stated before, chondrocytes are the primary mediators of ECM deposition and remodelling in articular cartilage. Despite the essential role of chondrocytes in tissue maintenance and homeostatic remodelling, Chapter 4 demonstrates that a 50% depletion in their numbers within mouse articular cartilage is not a driver of spontaneous tissue degeneration (e.g., in the absence of traumatic injury) within an otherwise permissive environment. However, the generalisability of these results is also subject to species-specific variations. Mature articular cartilage in humans and mice has a similar composition and overall structural arrangement but differs significantly regarding thickness and cellularity. Human knee articular cartilage is approximately 2 mm thick (Hunziker et al., 2002), making the characteristic zonal distribution easily discernible. By contrast, mouse knee articular cartilage is thinner, ranging from 30-90 µm on average, depending on anatomical location (Malda et al., 2013; Oláh et al., 2021). For instance, regional differences between medial and lateral condyles are demonstrated in Chapter 3. Chondrocytes occupy about 20% of the total tissue volume in murine articular cartilage, whereas human cartilage is sparsely populated (2-5%) (Poole et al., 2001). It is therefore plausible that mouse articular cartilage possesses a certain level of cellular redundancy that allows for greater tolerance to cell depletion compared to human articular cartilage. Nonetheless, considering that some chondrocytes are inevitably lost during aging, we would speculate that all cartilage can withstand a certain degree of cell loss and that the levels of chondrocyte death typically observed in post-traumatic joint injury or with aging is not the primary driver of OA.

Another aspect known to influence regenerative and degenerative response is the microenvironment. Although this thesis primarily focuses on articular cartilage, as stated in the introductory Chapters 1 and 2, OA is considered to be a whole-joint disease (Mimpen and Snelling, 2019) affecting structures other than cartilage. Degeneration and injury to menisci has well known associations with knee OA (Englund et al., 2012; Hunter et al., 2006). On Chapter 4, *Acan*-expressing cells could also be identified on menisci by tdTomato expression 1-week after 4-OHT induced recombination. Although we did not conduct formal quantification, it is probable that there was a reduction in the meniscal cell population, potentially resulting in tissue-specific biochemical and functional alterations. Notably, the notable expression of ADAMTS5 in the menisci of DTA-mice at 9 weeks (as depicted in Figure 4.3) suggests a certain degree of tissue disruption. However, similar to what was observed in the articular cartilage, this disturbance appeared to be temporary. Another structure known to play a critical role in joint and articular cartilage health and disease is the synovial membrane (Bartok and Firestein, 2010; Levick and McDonald, 1995; Sellam and Berenbaum, 2010; Smith, 2011). It would be, perhaps, narrowminded to believe that the synovium did not participate to some extent in phenotypes and remodelling outcomes observed in the studies presented in Chapter 4-6.

7.2.2. Synovial crosstalk in health and disease

As presented in Chapter 2, the synovial membrane (i.e., synovium) forms the inner surface of the knee joint capsule, facing the joint space. The synovial membrane comprises two layers – lining/intima and sub-lining/subintima (Smith, 2011). In the intima layer, fibroblast-like synoviocytes (type B) and macrophage-like synoviocytes (type A) coexist and are mainly responsible for the synthesis of synovial fluid, including HA and PRG4 lubricating molecules and removal of waste/debris from the joint cavity. In contrast, the sub-lining contains various cell types including immune cells and blood and lymphatic vessels that facilitate the transport of nutrients/waste products in and out of the joint (Bartok and Firestein, 2010).

The synovium continuously replenishes the synovial fluid, which is essential for joint lubrication, but also supports nourishment of the avascular articular cartilage, transporting nutrients to and from the tissue (Norkin and Levangie, 2011; Smith, 2011). Hence, synovial hyperplasia, characterized by an abnormal increase in the number of synoviocytes, can significantly impact the health and function of the synovial joint, even in the absence of inflammation, as seen in Chapter 5. *Prg4* loss of function has multi-faceted repercussions in the knee joint environment, including non-inflammatory synovial membrane thickening as previously described (Marcelino et al., 1999; Rhee et al., 2005). The proliferation of synoviocytes disrupts the balance of synovial fluid production in CACP patients, contributing to joint swelling and causing discomfort and impaired mobility. Within the context of joint morphology, synovial hyperplasia also imposes physical constraints altering joint alignment and function, consequently influencing load distribution and these clinical observations provide strong rationale that the altered shape observed in the *Prg4*$^{-/-}$ femurs may be in part dictated by changes in the size/shape/stiffness of the joint synovium/capsule.

Synoviocytes also secrete cytokines and growth factors that can influence chondrocyte behavior and ECM metabolism. In pathological conditions such as OA, synoviocytes can undergo phenotypic changes similar to a myo-fibroblast-like behaviour and produce pro-inflammatory mediators contributing to joint inflammation and cartilage degradation (Chou et al., 2020; Sanchez-Lopez et al., 2022). Similarly, it has been recently proposed that the synovial microenvironment can modulate superficial articular cartilage phenotype and inhibit hypertrophic differentiation (Chau et al., 2022). The intricate interplay between synoviocytes and chondrocytes within the articular microenvironment and its effect on joint homeostasis and pathophysiology is an expanding field of research. This enrichment of *Hic1*-lineage cells in the synovium, both in a homeostatic/quiescent state and in response to injury, suggests they are involved in tissue repair and regeneration processes. Further investigation into the specific phenotypic profile of *Hic1*-

lineage in these processes may provide valuable insights for understanding the diverging healing outcomes seen in Chapter 6.

7.2.3. Structural vs. functional regeneration

The overarching goal within the field of regenerative medicine is to stimulate the body's natural healing mechanisms and encourage tissue regeneration. However, there is often a disconnect between pre-clinical and clinical results and even desired outcomes in regenerative medicine. Here, the concepts of structural and functional regeneration might be relevant. In pre-clinical studies, researchers often focus on assessing structural regeneration, which involves restoring the anatomical components and organization of the damaged tissue. These studies may show promising outcomes in terms of tissue repair, cellular proliferation, and matrix formation; however, achieving structural regeneration alone may not guarantee functional restoration of the tissue. While structural regeneration is crucial for tissue integrity, functional regeneration is equally important to ensure the tissue can fulfill its intended biological functions. The significance of distinguishing between these was highlighted in Chapter 6, wherein improvement of articular cartilage's physical structure did not ensure its normal mechanical properties and load-bearing capacity. While structural regeneration alone may visually appear to heal a tissue, it does not guarantee that the tissue will perform its intended functions optimally. Functional assessment, either directly (biomechanical testing) or indirectly (gait, stance), becomes critical in such cases to ensure the regenerated cartilage can withstand mechanical stresses and function properly.

However, the ability to measure improvements in the quality and function of cartilage tissue in pre-clinical models, whether within the context of chondroprotection (pre-clinical models of OA) or regeneration (following cartilage injury) (summarized in Chapter 1) can only be as successful as the tools employed for evaluation. The optimized microscale biomechanical assessment devised in this thesis and its capability of providing relevant information on cartilage degeneration and regeneration reinforces the importance of functional assessment in future studies. Perhaps another consideration here is the scale and type of testing. Atomic force microscopy (AFM), which is becoming more commonly employed, offers high spatial resolution at a smaller scale. It has been shown useful in detecting early degenerative tissue changes, occurring even before visible histological abnormalities being observed (Stolz et al., 2009). Yet, considering the structural regeneration of cartilage following injury in Hic1^{E2F1}, it is possible AFM localized level evaluation would suggest a better functional restoration than evidenced by the larger scale indentation performed here. Given that osteochondral integration and integration with native cartilage are paramount for structural and functional regeneration, microscale indentation remains vital for understanding tissue behavior over loading conditions. As a field, we currently have a much better idea of what constitutes a good structural cartilage regeneration and how to determine it than we do functional regeneration. Overall, addressing both aspects of regeneration (structural and functional) enhances our understanding of tissue healing outcomes in pre-clinical models and the potential for successful clinical translation.

Combining different assay modalities is also advantageous in this scenario. Two-dimensional histopathological assessment is a staple of cartilage biology research and an invaluable tool because it allows for the characterization of changes in tissue structure and composition. However, histopathological assessment is limited by its cross-sectional and qualitative nature, unable to comprehensively capture the extent of structural changes and functional outcome per se. Aside from biomechanical testing, quantitative characterizations like 3D imaging employed throughout my work largely complement histology by providing relevant spatial information. In Chapter 6, it enabled a better understanding of the extent of cartilage regeneration regarding the volume and distribution of the newly formed cartilage. In Chapter 5, 3D imaging volume renderings played a crucial role in visualizing and quantifying morphological changes, such as cartilage thickness, femur shape, and overall geometry. Moreover, the demonstrated correlation between imaging and regions of biomechanical degeneration in *Prg4*$^{-/-}$ mice suggests volume renderings can aid in the assessment of structural/functional regeneration.

7.3. Future directions

Through the synthesis of this thesis a number of interesting questions have arisen. In regards to Chapter 4: (1) Is there a threshold of chondrocyte loss required to initiate an irreversible degenerative cascade? (2) How would an immediate 50% acute cell depletion compare to the gradual decline in cell numbers to 50% loss observed at later time points in our study? (3) Would repetitive insults (e.g., repeated tamoxifen treatments) amplify catabolic responses? These questions could be addressed by modulating the dose or frequency of tamoxifen injections to increase yield and control the timing of Cre-recombination. Furthermore, the applicability of this model system to explore the interaction of dysfunctional cells and environmental factors in degenerative processes and OA onset and progression is intriguing. If cartilage demise and OA development are driven by cell dysfunction, is cell depletion sufficient to effectively halt tissue degradation and disrupt the detrimental interplay between cell-mediated catabolism and inflammatory processes? Investigating chondrocyte depletion pre- and post-intervention (surgically or non-surgically induced OA) in murine models would significantly advance our comprehension of the underlying mechanisms driving tissue dysfunction.

During my PhD studies we have established a valuable collaboration with Dr Terence D. Capellini (Harvard University), an expert in the field of evolutionary biology. Preliminary RNA sequencing analysis of the articular cartilage from the trochlea and condyles of C57BL6 mice obtained at postnatal stages P0, P30 and 1 year age revealed regional and temporal changes in *Prg4* expression, suggesting a potential role in the observed differential phenotypic changes on trochlear groove *vs.* condyles. Further exploration during early postnatal stages, focused on dissecting the progressive changes in the different knee joint structures might help pinpoint the main drivers of abnormal joint morphology.

Aside from quantification of immunofluorescence and colocalization of phenotypic markers, a logical next step in the project presented in Chapter 6 would be to gain a better understanding of molecular events and population heterogeneities related to Hic1^{E2F1} wound healing and enhanced articular cartilage regenerative competence compared to scar-forming, or fibrocartilage response in *Hic1*-lineage from regenerative incompetent Hic1 mouse. Single- cell RNA sequencing of *Hic1*-lineage isolated from ear and knee joint tissues (synovium, bone marrow) would help characterize the nature of their transcriptome at different time points post-injury, but also compare profiles pre-injury. By analyzing the cellular responses at the single-cell level, we can identify key molecular signatures associated with regenerative competence and better understand how *Hic1* influences these processes. Furthermore, conditional deletion of *Hic1* as employed in previous studies, might provide some insights on the impact of *Hic1* MPs on ear and knee joint homeostasis and regeneration.

7.4. Limitations

While it is true that every scientific study will have its limitations, it is essential to recognize these and understand how these could impact the findings of the experiments and overall conclusions. First, wewould like to recognize a few technical limitations in this study. In terms of FTCD size and depth, the reproducibility of trochlea injury is difficult to quantify, and this in itself could introduce variation that could have impacted the semi-quantitative healing scores. To offset some of this variability, all surgical procedures were performed by the same operator and our lab has demonstrated good reproducibility when the protocol is followed (Mak et al., 2015). Regarding grading systems, it is also important to note that cumulative scores were reported for both OARSI histopathology (cartilage degeneration) and FTCD healing (cartilage repair/regeneration). Although examining individual scores from each weighted category could have provided a deeper understanding of the nuanced differences between mouse strains regenerative/degenerative outcomes in our studies, the relatively small sample size hindered comparison of individual factors reliably. Nonetheless, the sample size of $n \geq 4$ independent animals used for each data point collected for the various studies and experimental procedures here meets the threshold of most research studies and was selected based on feasibility and the three R's of animal experimentation (eBioMedicine, 2022). While these sample sizes are not optimal for pairwise comparisons during the geometric morphometric evaluations, restricting me to multiple comparisons for single linear measurements, morphometric analyses were still able to capture significant variations in shape and size between genotypes, highlighting differences in morphology.

Regarding transgenic mice, since the *Prg4*$^{-/-}$ mouse we employed presents with global deletion of the gene and complete loss of the protein, we were unable to separate the independent effects of *Prg4* loss-of-function on individual cellular cohorts and their contributions to the morphological phenotype we observed. Future studies employing conditional gene deletion in individual joint-associated tissues, would help shed light on their functional significance to the overall phenotype and determine which populations are acting in cell autonomous vs. non-cell autonomous fashions. Additionally, while the inducible Cre-LoxP system enabled me to permanently label *Hic1*-expressing cells and follow their progeny throughout aging and post-injury, or selectively target depletion of *Acan*-expressing cells, it is important to consider that the efficiency of promoter driven Cre recombination is not 100%. This means we likely did not capture the whole *Hic1* population and, as the data revealed in Chapter 4, we were unable to ablate 100% of *Acan*-expressing chondrocytes.

Another limitation is that the analysis of articular cartilage mechanical properties is focused explicitly on femoral surfaces, whether examining the mediolateral condyles (Chapters 3-5) or the trochlear groove region (Chapter 6). In the case of the trochlear FTCD outcomes, assessment of a single surface (in and around the injury site) is warranted. However, since synovial joints involve articulations, having information about the biomechanics of the opposing tibial plateau cartilage surfaces and even the menisci would help us better comprehend the dynamics of the entire joint following a disruption in homeostasis. Chapter 4 demonstrates the presence of *Acan*-expressing cells in various joint-related compartments, indicating other tissues susceptibility to DTA-mediated effects. Similarly, the loss of function in *Prg4* and resulting phenotype do not occur in isolation within the femur. Mapping the mechanical properties of femoral cartilage is challenging due to its angled geometry – the reason why our efforts focused on optimizing a protocol using the unique features of Mach-1 automated tester capabilities. This protocol now serves as a foundation for future studies in our laboratory where we aim to adapt and expand it to analyze other articular cartilage surfaces and investigate species-specific differences and similarities. Lastly, while indentation testing enabled me to comparatively evaluate changes in biomechanical patterns of articular cartilage tissue relative to a baseline control (healthy wild-type – Chapters 3-5; contralateral uninjured cartilage – Chapter 6), the single-phase constitutive modelling used assumes linear-elasticity, homogeneity, and isotropy, thereby not capturing the time-dependent (viscoelastic) behavior of the tissue and limiting the prediction or association to constituent-specific (i.e., proteoglycan, collagen fibrils) cartilage damage and degeneration. Future studies could characterize the experimental indentation measurements obtained here, using more advanced constitutive models, such as fibril-reinforced poroelastic (FRPE) model combined with finite element methods, as recently published for rat knee joints (Orozco et al., 2022).

7.5. Concluding remarks

With a growing and aging population affected by cartilage-related disorders, such as OA, there is a critical need to explore innovative strategies for successfully promoting tissue regeneration or preventing its troublesome degeneration. To address these challenges, it is important to understand underlying factors that shape and maintain cartilage structural and functional competence at the pre- and postnatal stages. Collectively, the work presented here showcases that the response of articular cartilage to homeostasis disruption and its potential for remodelling (adaptative and maladaptive/degenerative) depends on intrinsic and local factors. Moreover, the multimodality nature of the work presented here, combining histological, 3D imaging, and biomechanical approaches, underscores the importance of a comprehensive investigation to identify and respect the differences between structural and functional regeneration, or even quantify morphological changes in ultrastructure. There are still considerable gaps in our understanding of cartilage degeneration and regeneration, and we hope the work presented here may stimulate further explorations.

Appendix A

Journal copyright permissions

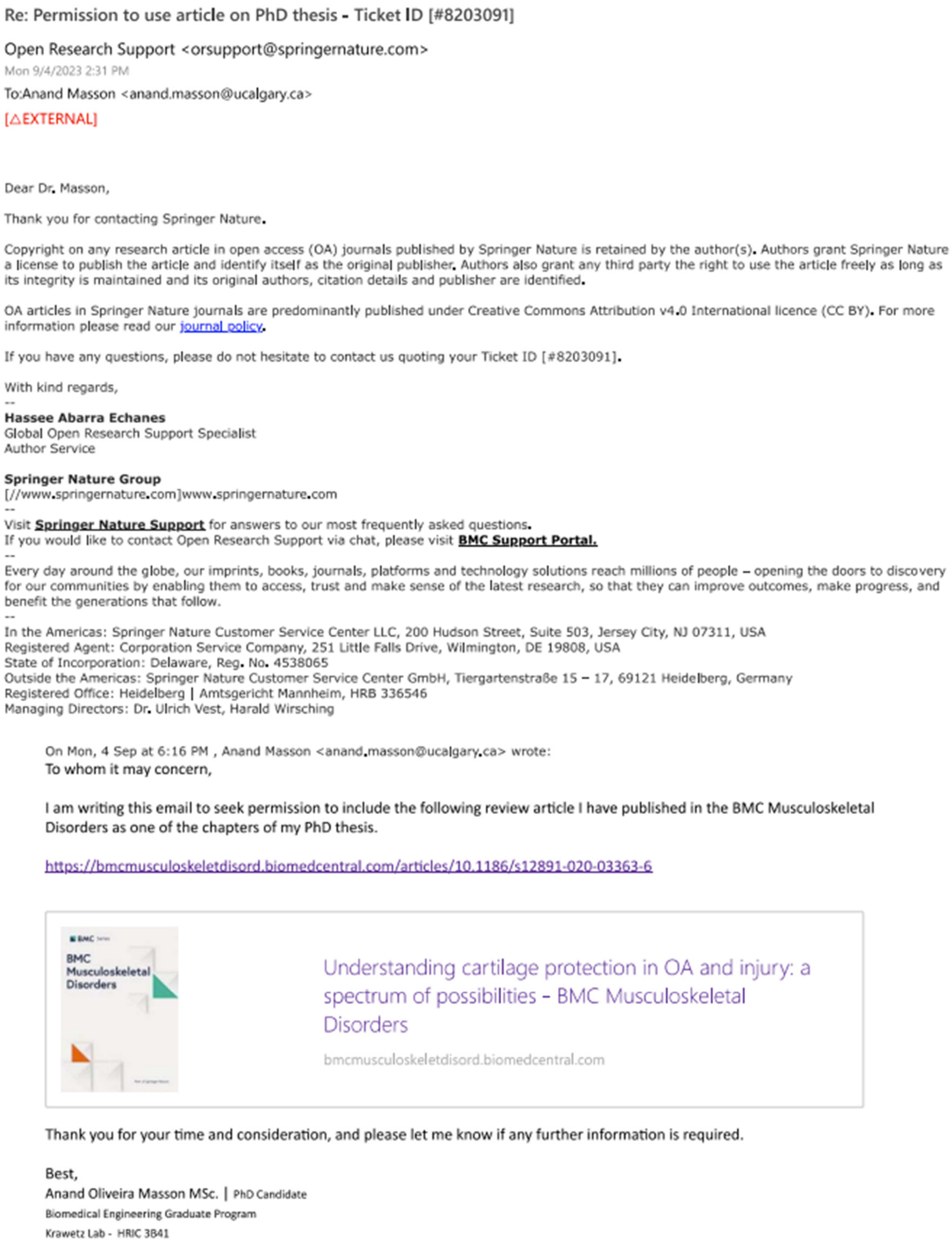

Re: Permission to use article on PhD thesis - Ticket ID [#8203091]

Open Research Support <orsupport@springernature.com>
Mon 9/4/2023 2:31 PM
To:Anand Masson <anand.masson@ucalgary.ca>
[△EXTERNAL]

Dear Dr. Masson,

Thank you for contacting Springer Nature.

Copyright on any research article in open access (OA) journals published by Springer Nature is retained by the author(s). Authors grant Springer Nature a license to publish the article and identify itself as the original publisher. Authors also grant any third party the right to use the article freely as long as its integrity is maintained and its original authors, citation details and publisher are identified.

OA articles in Springer Nature journals are predominantly published under Creative Commons Attribution v4.0 International licence (CC BY). For more information please read our journal policy.

If you have any questions, please do not hesitate to contact us quoting your Ticket ID [#8203091].

With kind regards,
--
Hassee Abarra Echanes
Global Open Research Support Specialist
Author Service

Springer Nature Group
[//www.springernature.com]www.springernature.com
--
Visit **Springer Nature Support** for answers to our most frequently asked questions.
If you would like to contact Open Research Support via chat, please visit **BMC Support Portal.**
--
Every day around the globe, our imprints, books, journals, platforms and technology solutions reach millions of people – opening the doors to discovery for our communities by enabling them to access, trust and make sense of the latest research, so that they can improve outcomes, make progress, and benefit the generations that follow.
--
In the Americas: Springer Nature Customer Service Center LLC, 200 Hudson Street, Suite 503, Jersey City, NJ 07311, USA
Registered Agent: Corporation Service Company, 251 Little Falls Drive, Wilmington, DE 19808, USA
State of Incorporation: Delaware, Reg. No. 4538065
Outside the Americas: Springer Nature Customer Service Center GmbH, Tiergartenstraße 15 – 17, 69121 Heidelberg, Germany
Registered Office: Heidelberg | Amtsgericht Mannheim, HRB 336546
Managing Directors: Dr. Ulrich Vest, Harald Wirsching

> On Mon, 4 Sep at 6:16 PM , Anand Masson <anand.masson@ucalgary.ca> wrote:
> To whom it may concern,
>
> I am writing this email to seek permission to include the following review article I have published in the BMC Musculoskeletal Disorders as one of the chapters of my PhD thesis.
>
> https://bmcmusculoskeletdisord.biomedcentral.com/articles/10.1186/s12891-020-03363-6
>
> Understanding cartilage protection in OA and injury: a spectrum of possibilities - BMC Musculoskeletal Disorders
> bmcmusculoskeletdisord.biomedcentral.com
>
> Thank you for your time and consideration, and please let me know if any further information is required.
>
> Best,
> Anand Oliveira Masson MSc. | PhD Candidate
> Biomedical Engineering Graduate Program
> Krawetz Lab - HRIC 3B41

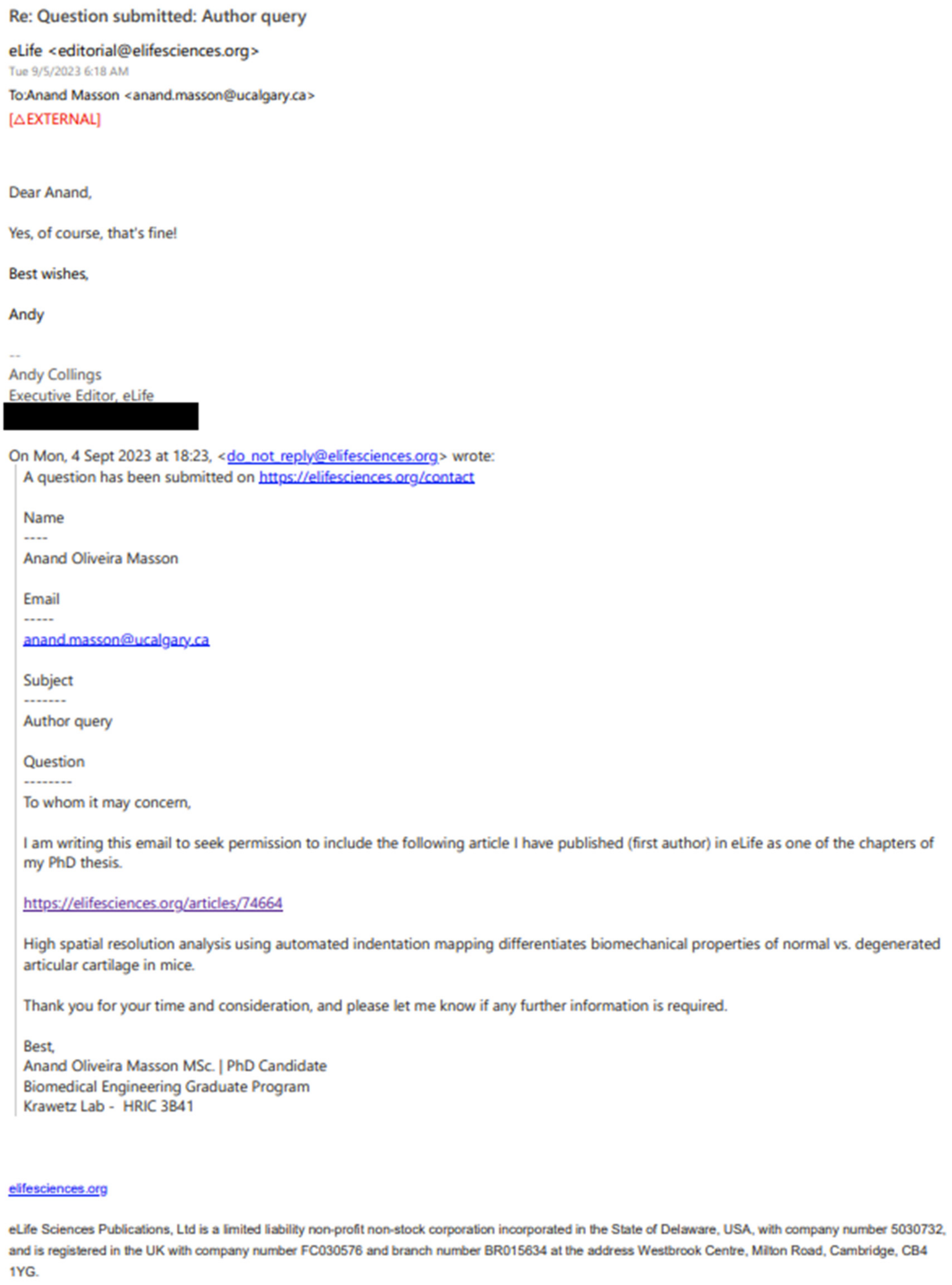

Re: Question submitted: Author query

eLife <editorial@elifesciences.org>
Tue 9/5/2023 6:18 AM
To:Anand Masson <anand.masson@ucalgary.ca>
[△EXTERNAL]

Dear Anand,

Yes, of course, that's fine!

Best wishes,

Andy

--
Andy Collings
Executive Editor, eLife
[redacted]

On Mon, 4 Sept 2023 at 18:23, <do_not_reply@elifesciences.org> wrote:

> A question has been submitted on https://elifesciences.org/contact
>
> Name
> ----
> Anand Oliveira Masson
>
> Email
> -----
> anand.masson@ucalgary.ca
>
> Subject
> -------
> Author query
>
> Question
> --------
> To whom it may concern,
>
> I am writing this email to seek permission to include the following article I have published (first author) in eLife as one of the chapters of my PhD thesis.
>
> https://elifesciences.org/articles/74664
>
> High spatial resolution analysis using automated indentation mapping differentiates biomechanical properties of normal vs. degenerated articular cartilage in mice.
>
> Thank you for your time and consideration, and please let me know if any further information is required.
>
> Best,
> Anand Oliveira Masson MSc. | PhD Candidate
> Biomedical Engineering Graduate Program
> Krawetz Lab - HRIC 3B41

elifesciences.org

eLife Sciences Publications, Ltd is a limited liability non-profit non-stock corporation incorporated in the State of Delaware, USA, with company number 5030732, and is registered in the UK with company number FC030576 and branch number BR015634 at the address Westbrook Centre, Milton Road, Cambridge, CB4 1YG.

Appendix B

Co-author copyright permission letters.

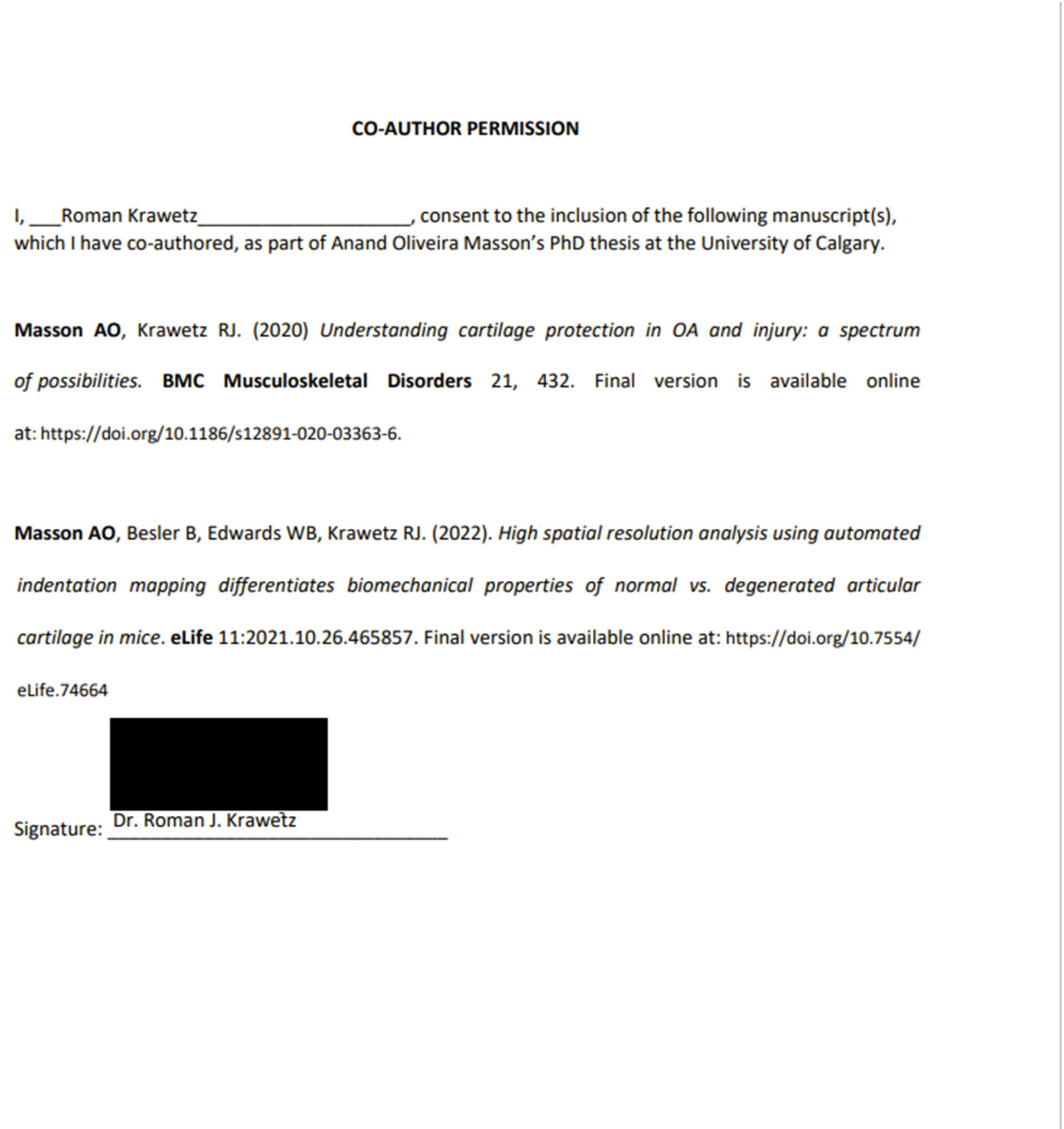

CO-AUTHOR PERMISSION

I, ___Roman Krawetz_____________________, consent to the inclusion of the following manuscript(s), which I have co-authored, as part of Anand Oliveira Masson's PhD thesis at the University of Calgary.

Masson AO, Krawetz RJ. (2020) *Understanding cartilage protection in OA and injury: a spectrum of possibilities.* **BMC Musculoskeletal Disorders** 21, 432. Final version is available online at: https://doi.org/10.1186/s12891-020-03363-6.

Masson AO, Besler B, Edwards WB, Krawetz RJ. (2022). *High spatial resolution analysis using automated indentation mapping differentiates biomechanical properties of normal vs. degenerated articular cartilage in mice*. **eLife** 11:2021.10.26.465857. Final version is available online at: https://doi.org/10.7554/eLife.74664

[redacted]

Signature: Dr. Roman J. Krawetz

CO-AUTHOR PERMISSION

I, W. Brent Edwards________________________________, consent to the inclusion of the following manuscript(s), which I have co-authored, as part of Anand Oliveira Masson's PhD thesis at the University of Calgary.

Masson AO, Besler B, Edwards WB, Krawetz RJ. (2022). *High spatial resolution analysis using automated indentation mapping differentiates biomechanical properties of normal vs. degenerated articular cartilage in mice*. **eLife** 11:2021.10.26.465857. Final version is available online at: https://doi.org/10.7554/eLife.74664

Signature: [redacted]___

Dr. William Brent Edwards

CO-AUTHOR PERMISSION

I, Bryce Besler, consent to the inclusion of the following manuscript(s), which I have co-authored, as part of Anand Oliveira Masson's PhD thesis at the University of Calgary.

Masson AO, Besler B, Edwards WB, Krawetz RJ. (2022). *High spatial resolution analysis using automated indentation mapping differentiates biomechanical properties of normal vs. degenerated articular cartilage in mice*. **eLife** 11:2021.10.26.465857. Final version is available online at: https://doi.org/10.7554/eLife.74664

Signature: [redacted]

Dr. Bryce Besler

References

Abbasi S, Sinha S, Labit E, Rosin NL, Yoon G, Rahmani W, Jaffer A, Sharma N, Hagner A, Shah P, Arora R, Yoon J, Islam A, Uchida A, Chang CK, Stratton JA, Scott RW, Rossi FMV, Underhill TM, Biernaskie J. 2020. Distinct Regulatory Programs Control the Latent Regenerative Potential of Dermal Fibroblasts during Wound Healing. *Cell Stem Cell* **27**:396-412.e6. doi:10.1016/j.stem.2020.07.008

Abubacker S, Ham HO, Messersmith PB, Schmidt TA. 2013. Cartilage boundary lubricating ability of aldehyde modified proteoglycan 4 (PRG4-CHO). *Osteoarthr Cartil* **21**:186–189. doi:10.1016/j.joca.2012.09.016

Abubacker S, Premnath P, Shonak A, Leonard C, Shah S, Zhu Y, Jay GD, Schmidt TA, Boyd S, Krawetz R. 2019. Absence of Proteoglycan 4 (Prg4) Leads to Increased Subchondral Bone Porosity Which Can Be Mitigated Through Intra-Articular Injection of PRG4. *J Orthop Res* **37**:2077–2088. doi:10.1002/jor.24378

Adams DC, Collyer M, Kaliontzopoulou A, Sherratt E. 2016. geomorph: Software for geometric morphometric analyses.

Alquraini A, Garguilo S, D'Souza G, Zhang LX, Schmidt TA, Jay GD, Elsaid KA. 2015. The interaction of lubricin/proteoglycan 4 (PRG4) with toll-like receptors 2 and 4: an anti-inflammatory role of PRG4 in synovial fluid. *Arthritis Res Ther* **17**:353. doi:10.1186/s13075-015-0877-x

Anderson DD, Chubinskaya S, Guilak F, Martin JA, Oegema TR, Olson SA, Buckwalter JA. 2011. Post-traumatic osteoarthritis: Improved understanding and opportunities for early intervention. *J Orthop Res* **29**:802–809. doi:10.1002/jor.21359

Archer CW, Francis-West P. 2003. The chondrocyte. *Int J Biochem Cell Biol* **35**:401–404. doi:10.1016/S1357-2725(02)00301-1

Armstrong CG. 1986. An analysis of the stresses in a thin layer of articular cartilage in a synovial joint. *Eng Med* 55–61.

Arokoski JPA, Jurvelin JS, Väätäinen U, Helminen HJ. 2000. Normal and pathological adaptations of articular cartilage to joint loading. *Scand J Med Sci Sport* **10**:186–198. doi:10.1034/j.1600-0838.2000.010004186.x

Arostegui M, Scott RW, Underhill TM. 2023. Hic1 identifies a specialized mesenchymal progenitor population in the embryonic limb responsible for bone superstructure formation. *Cell Rep* **42**:112325. doi:10.1016/j.celrep.2023.112325

Arostegui M, Wilder Scott R, Böse K, Michael Underhill T. 2022. Cellular taxonomy of Hic1+ mesenchymal progenitor derivatives in the limb: from embryo to adult. *Nat Commun* **13**. doi:10.1038/s41467-022-32695-1

Arthur LM, Heber-Katz E. 2011. The role of p21 in regulating mammalian regeneration. *Stem Cell Res Ther* **2**:30. doi:10.1186/scrt71

Askary A, Smeeton J, Paul S, Schindler S, Braasch I, Ellis NA, Postlethwait J, Miller CT, Crump JG. 2016. Ancient origin of lubricated joints in bony vertebrates. *Elife* **5**:1–13. doi:10.7554/eLife.16415

Athanasiou KA, Rosenwasser MP, Buckwalter JA, Malinin TI, Mow VC. 1991. Interspecies comparisons of in situ intrinsic mechanical properties of distal femoral cartilage. *J Orthop Res* **9**:330–340. doi:10.1002/jor.1100090304

Avants BB, Tustison NJ, Song G, Cook PA, Klein A, Gee JC. 2011. A reproducible evaluation of ANTs similarity metric performance in brain image registration. *Neuroimage* **54**:2033–2044. doi:10.1016/j.neuroimage.2010.09.025

Badley E, Wilfong J, Zahid S, Perruccio A. 2021. Special Report: The Burden of Osteoarthritis in Canada.

Bae WC, Lewis CW, Levenston ME, Sah RL. 2006. Indentation testing of human articular cartilage : Effects of probe tip geometry and indentation depth on intra-tissue strain **39**:1039–1047. doi:10.1016/j.jbiomech.2005.02.018

Bahabri SA, Suwairi WM, Laxer RM, Polinkovsky A, Dalaan AA, Warman ML. 1998. The camptodactyly-arthropathy-coxa vara-pericarditis syndrome: Clinical features and genetic mapping to human chromosome 1. *Arthritis Rheum* **41**:730–735. doi:10.1002/1529-0131(199804)41:4<730::AID-ART22>3.0.CO;2-Y

Balistreri CR, De Falco E, Bordin A, Maslova O, Koliada A, Vaiserman A. 2020. Stem cell therapy: old challenges and new solutions. *Mol Biol Rep* **47**:3117–3131. doi:10.1007/s11033-020-05353-2

Bapat S, Hubbard D, Munjal A, Hunter M, Fulzele S. 2018. Pros and cons of mouse models for studying osteoarthritis. *Clin Transl Med*. doi:10.1186/s40169-018-0215-4

Barry F, Murphy M. 2013. Mesenchymal stem cells in joint disease and repair. *Nat Rev Rheumatol* **9**:584–594. doi:10.1038/nrrheum.2013.109

Bartok B, Firestein GS. 2010. Fibroblast-like synoviocytes: key effector cells in rheumatoid arthritis. *Immunol Rev* **233**:233–255. doi:10.1111/j.0105-2896.2009.00859.x

Bay-Jensen AC, Hoegh-Madsen S, Dam E, Henriksen K, Sondergaard BC, Pastoureau P, Qvist P, Karsdal MA. 2010. Which elements are involved in reversible and irreversible cartilage degradation in osteoarthritis? *Rheumatol Int* **30**:435–442. doi:10.1007/s00296-009-1183-1

Bedelbaeva K, Snyder A, Gourevitch D, Clark L, Zhang X-M, Leferovich J, Cheverud JM, Lieberman P, Heber-Katz E. 2010. Lack of p21 expression links cell cycle control and appendage regeneration in mice. *Proc Natl Acad Sci U S A* **107**:5845–50. doi:10.1073/pnas.1000830107

Berteau JP, Oyen M, Shefelbine SJ. 2016. Permeability and shear modulus of articular cartilage in growing mice. *Biomech Model Mechanobiol* **15**:205–212. doi:10.1007/s10237-015-0671-3

Bian L, Crivello KM, Ng KW, Xu D, Williams DY, Ateshian GA, Hung CT. 2009. Influence of temporary chondroitinase ABC-induced glycosaminoglycan suppression on maturation of tissue-engineered cartilage. *Tissue Eng - Part A* **15**:2065–2072. doi:10.1089/ten.tea.2008.0495

Biomomentum. 2020. Mach-1 Analysis User Manual v6.4. Laval, QC.

Bobacz K, Erlacher L, Smolen J, Soleiman A, Graninger WB. 2004. Chondrocyte number and proteoglycan synthesis in the aging and osteoarthritic human articular cartilage. *Ann Rheum Dis* **63**:1618–1622. doi:10.1136/ard.2002.002162

Bombardier C, Hawker G, Mosher D. 2011. The Impact of Arthritis in Canada : Today and Over the Next 30 Years, Arthritis Alliance of Canada.

Bookstein FL. 1989. Principal Warps: Thin-Plate Splines and the Decomposition of Deformations. *IEEE Trans Pattern Anal Mach Intell*. doi:10.1109/34.24792

Brittberg M, Lindahl A, Nilsson A, Ohlsson C, Isaksson O, Peterson L. 1994. Treatment of Deep Cartilage Defects in the Knee with Autologous Chondrocyte Transplantation. *N Engl J Med*

331:889–895. doi:10.1056/NEJM199410063311401

Brockschnieder D, Lappe-Siefke C, Goebbels S, Boesl MR, Nave K-A, Riethmacher D. 2004. Cell Depletion Due to Diphtheria Toxin Fragment A after Cre-Mediated Recombination. *Mol Cell Biol* **24**:7636–7642. doi:10.1128/mcb.24.17.7636-7642.2004

Brody LT. 2015. Knee osteoarthritis: Clinical connections to articular cartilage structure and function. *Phys Ther Sport* **16**:301–316. doi:10.1016/j.ptsp.2014.12.001

Buckwalter JA, Mankin HJ, Grodzinsky AJ. 2005. Articular cartilage and osteoarthritis. *Instr Course Lect* **54**:465–480.

Cai G, Liu W, He Y, Huang J, Duan L, Xiong J, Liu L, Wang D. 2019. Recent advances in kartogenin for cartilage regeneration. *J Drug Target* **27**:28–32. doi:10.1080/1061186X.2018.1464011

Cao L, Youn I, Guilak F, Setton LA. 2006. Compressive Properties of Mouse Articular Cartilage Determined in a Novel Micro-Indentation Test Method and Biphasic Finite Element Model. *J Biomech Eng* **128**:766–771. doi:10.1115/1.2246237

Carter MG, Johns M a, Zeng X, Zhou L, Zink MC, Mankowski JL, Donovan DM, Baylin SB. 2000. Mice deficient in the candidate tumor suppressor gene Hic1 exhibit developmental defects of structures affected in the Miller-Dieker syndrome. *Hum Mol Genet* **9**:413–9. doi:ddd047 [pii]

Chadwick RB, Bu L, Yu H, Hu Y, Wergedal JE, Mohan S, Baylink DJ. 2007. Digit tip regrowth and differential gene expression in MRL/Mpj, DBA/2, and C57BL/6 mice. *Wound Repair Regen* **15**:275–284. doi:10.1111/j.1524-475X.2007.00216.x

Charles MD, Haloman S, Chen L, Ward SR, Fithian D, Afra R. 2013. Magnetic resonance imaging-based topographical differences between control and recurrent patellofemoral instability patients. *Am J Sports Med* **41**:374–384. doi:10.1177/0363546512472441

Chau M, Dou Z, Baroncelli M, Landman EB, Bendre A, Kanekiyo M, Gkourogianni A, Barnes K, Ottosson L, Nilsson O. 2022. The synovial microenvironment suppresses chondrocyte hypertrophy and promotes articular chondrocyte differentiation. *npj Regen Med* **7**. doi:10.1038/s41536-022-00247-2

Chen C, Krohn J, Bhattacharya S, Davies B. 2011. A Comparison of Exogenous Promoter Activity at the ROSA26 Locus Using a PhiC31 Integrase Mediated Cassette Exchange Approach in Mouse ES Cells **6**:6–13. doi:10.1371/journal.pone.0023376

Chen H-Z, Tsai S-Y, Leone G. 2009. Emerging roles of E2Fs in cancer: an exit from cell cycle control. *Nat Rev Cancer* **9**:785–797. doi:10.1038/nrc2696

Chen WY, Cooper TK, Zahnow CA, Overholtzer M, Zhao Z, Ladanyi M, Karp JE, Gokgoz N, Wunder JS, Andrulis IL, Levine AJ, Mankowski JL, Baylin SB. 2004. Epigenetic and genetic loss of Hic1 function accentuates the role of p53 in tumorigenesis. *Cancer Cell* **6**:387–398. doi:10.1016/j.ccr.2004.08.030

Chevalier X, Eymard F, Richette P. 2013. Biologic agents in osteoarthritis: hopes and disappointments. *Nat Rev Rheumatol* **9**:400–410. doi:10.1038/nrrheum.2013.44

Childs BG, Durik M, Baker DJ, Deursen JM Van. 2015. Cellular senescence in aging and age-related disease : from mechanisms to therapy **21**:1424–1435. doi:10.1038/nm.4000

Chinzei N, Rai MF, Hashimoto S, Schmidt EJ, Takebe K, Cheverud JM, Sandell LJ. 2019. Evidence for Genetic Contribution to Variation in Posttraumatic Osteoarthritis in Mice. *Arthritis Rheumatol*

71:370–381. doi:10.1002/art.40730

Chou CH, Jain V, Gibson J, Attarian DE, Haraden CA, Yohn CB, Laberge RM, Gregory S, Kraus VB. 2020. Synovial cell cross-talk with cartilage plays a major role in the pathogenesis of osteoarthritis. *Sci Rep* **10**:1–14. doi:10.1038/s41598-020-67730-y

Christiansen BA, Anderson MJ, Lee CA, Williams JC, Yik JHN, Haudenschild DR. 2012. Musculoskeletal changes following non-invasive knee injury using a novel mouse model of post-traumatic osteoarthritis. *Osteoarthr Cartil* **20**:773–782. doi:10.1016/j.joca.2012.04.014

Christiansen BA, Guilak F, Lockwood KA, Olson SA, Pitsillides AA, Sandell LJ, Silva MJ, van der Meulen MCH, Haudenschild DR. 2015. Non-invasive mouse models of post-traumatic osteoarthritis. *Osteoarthr Cartil* **23**:1627–1638. doi:10.1016/j.joca.2015.05.009

Chu CR, Szczodry M, Bruno S. 2010. Animal Models for Cartilage Regeneration and Repair. *Tissue Eng Part B Rev* **16**:105–115. doi:10.1089/ten.teb.2009.0452

Clark LD, Clark RK, Heber-Katz E. 1998. A New Murine Model for Mammalian Wound Repair and Regeneration. *Clin Immunol Immunopathol* **88**:35–45. doi:10.1006/clin.1998.4519

Clements KM, Price JS, Chambers MG, Visco DM, Poole AR, Mason RM. 2003. Gene Deletion of Either Interleukin-1β, Interleukin-1β -Converting Enzyme, Inducible Nitric Oxide Synthase, or Stromelysin 1 Accelerates the Development of Knee Osteoarthritis in Mice after Surgical Transection of the Medial Collateral Ligament and Partia. *Arthritis Rheum* **48**:3452–3463. doi:10.1002/art.11355

Cohen NP, Foster RJ, Mow VC. 1998. Composition and dynamics of articular cartilage: Structure, function, and maintaining healthy state. *J Orthop Sports Phys Ther* **28**:203–215. doi:10.2519/jospt.1998.28.4.203

Coleman MC, Goetz JE, Brouillette MJ, Seol D, Willey MC, Petersen EB, Anderson HD, Hendrickson NR, Compton J, Khorsand B, Morris AS, Salem AK, Fredericks DC, McKinley TO, Martin JA. 2018. Targeting mitochondrial responses to intra-articular fracture to prevent posttraumatic osteoarthritis. *Sci Transl Med* **10**:1–15. doi:10.1126/scitranslmed.aan5372

Coles JM, Zhang L, Blum JJ, Warman ML, Jay GD, Guilak F, Zauscher S. 2010. Loss of cartilage structure, stiffness, and frictional properties in mice lacking PRG4. *Arthritis Rheum* **62**:1666–1674. doi:10.1002/art.27436

Collins FL, Roelofs AJ, Symons RA, Kania K, Campbell E, Collie-Duguid ESR, Riemen AHK, Clark SM, De Bari C. 2023. Taxonomy of fibroblasts and progenitors in the synovial joint at single-cell resolution. *Ann Rheum Dis* **82**:428–437. doi:10.1136/ard-2021-221682

Collins KH, Hart DA, Reimer RA, Seerattan RA, Herzog W. 2016. Response to diet-induced obesity produces time-dependent induction and progression of metabolic osteoarthritis in rat knees. *J Orthop Res* **34**:1010–1018. doi:10.1002/jor.23103

Collins KH, Hart DA, Seerattan RA, Reimer RA, Herzog W. 2018. High-fat/high-sucrose diet-induced obesity results in joint-specific development of osteoarthritis-like degeneration in a rat model. *Bone Joint Res* **7**:274–281. doi:10.1302/2046-3758.74.BJR-2017-0201.R2

Collins KH, MacDonald GZ, Hart DA, Seerattan RA, Rios JL, Reimer RA, Herzog W. 2020. Impact of age on host responses to diet-induced obesity: Development of joint damage and metabolic set points. *J Sport Heal Sci* **9**:132–139. doi:10.1016/j.jshs.2019.06.004

Collins KH, Paul HA, Reimer RA, Seerattan RA, Hart DA, Herzog W. 2015. Relationship between inflammation, the gut microbiota, and metabolic osteoarthritis development: studies in a rat model. *Osteoarthr Cartil* **23**:1989–1998. doi:10.1016/j.joca.2015.03.014

Collyer ML, Adams DC. 2019. RRPP: linear model evaluation with randomized residuals in a permutation procedure. *R Packag version 04 0*.

Collyer ML, Adams DC. 2018. RRPP: An R package for fitting linear models to high-dimensional data using residual randomization. *Methods Ecol Evol* **9**:1772–1779. doi:10.1111/2041-210X.13029

Cope PJ, Ourradi K, Li Y, Sharif M. 2019. Models of osteoarthritis : the good , the bad and the promising **27**:230–239. doi:10.1016/j.joca.2018.09.016

Courties A, Gualillo O, Berenbaum F, Sellam J. 2015. Metabolic stress-induced joint in fl ammation and osteoarthritis. *Osteoarthr Cartil* **23**:1955–1965. doi:10.1016/j.joca.2015.05.016

Cui A, Li H, Wang D, Zhong J, Chen Y, Lu H. 2020. Global, regional prevalence, incidence and risk factors of knee osteoarthritis in population-based studies. *EClinicalMedicine* **29–30**:100587. doi:10.1016/j.eclinm.2020.100587

Darling EM, Hu JCY, Athanasiou KA. 2004. Zonal and topographical differences in articular cartilage gene expression. *J Orthop Res* **22**:1182–1187. doi:10.1016/j.orthres.2004.03.001

Das Neves Borges P, Forte AE, Vincent TL, Dini D, Marenzana M. 2014. Rapid, automated imaging of mouse articular cartilage by microCT for early detection of osteoarthritis and finite element modelling of joint mechanics. *Osteoarthr Cartil* **22**:1419–1428. doi:10.1016/j.joca.2014.07.014

De Bari C, Roelofs AJ. 2018. Stem cell-based therapeutic strategies for cartilage defects and osteoarthritis. *Curr Opin Pharmacol* **40**:74–80. doi:10.1016/j.coph.2018.03.009

Decker RS, Koyama E, Pacifici M. 2015. Articular Cartilage: Structural and Developmental Intricacies and Questions. *Curr Osteoporos Rep*. doi:10.1007/s11914-015-0290-z

Decker RS, Um H Bin, Dyment NA, Cottingham N, Usami Y, Enomoto-Iwamoto M, Kronenberg MS, Maye P, Rowe DW, Koyama E, Pacifici M. 2017. Cell origin, volume and arrangement are drivers of articular cartilage formation, morphogenesis and response to injury in mouse limbs. *Dev Biol* **426**:56–68. doi:10.1016/j.ydbio.2017.04.006

Dehennaut V, Loison I, Boulay G, Van Rechem C, Leprince D. 2013. Identification of p21 (CIP1/WAF1) as a direct target gene of HIC1 (Hypermethylated In Cancer 1). *Biochem Biophys Res Commun* **430**:49–53. doi:10.1016/j.bbrc.2012.11.045

Deng C-X. 2012. The Use of Cre–loxP Technology and Inducible Systems to Generate Mouse Models of CancerGenetically Engineered Mice for Cancer Research. New York, NY: Springer New York. pp. 17–36. doi:10.1007/978-0-387-69805-2_2

Deng Z, Gao X, Sun X, Amra S, Lu A, Cui Y, Eltzschig HK, Lei G, Huard J. 2019. Characterization of articular cartilage homeostasis and the mechanism of superior cartilage regeneration of MRL/MpJ mice. *FASEB J* **33**:8809–8821. doi:10.1096/fj.201802132rr

Devine J, Aponte JD, Katz DC, Liu W, Vercio LDL, Forkert ND, Marcucio R, Percival CJ, Hallgrímsson B. 2020. A Registration and Deep Learning Approach to Automated Landmark Detection for Geometric Morphometrics. *Evol Biol* **47**:246–259. doi:10.1007/s11692-020-09508-8

Dolan CP, Dawson LA, Muneoka K. 2018. Digit Tip Regeneration: Merging Regeneration Biology with Regenerative Medicine. *Stem Cells Transl Med* **7**:262–270. doi:10.1002/sctm.17-0236

Dominici M, Le Blanc K, Mueller I, Slaper-Cortenbach I, Marini FC, Krause DS, Deans RJ, Keating A, Prockop DJ, Horwitz EM. 2006. Minimal criteria for defining multipotent mesenchymal stromal cells. The International Society for Cellular Therapy position statement. *Cytotherapy* **8**:315–317. doi:10.1080/14653240600855905

Doyran B, Tong W, Li Q, Jia H, Zhang X, Chen C, Enomoto-Iwamoto M, Lu XL, Qin L, Han L. 2017. Nanoindentation modulus of murine cartilage: a sensitive indicator of the initiation and progression of post-traumatic osteoarthritis. *Osteoarthr Cartil* **25**:108–117. doi:10.1016/j.joca.2016.08.008

Drewniak EI, Jay GD, Fleming BC, Zhang L, Warman ML, Crisco JJ. 2012. Cyclic loading increases friction and changes cartilage surface integrity in lubricin-mutant mouse knees. *Arthritis Rheum* **64**:465–473. doi:10.1002/art.33337

Dumond H, Presle N, Pottie P, Pacquelet S, Terlain B, Netter P, Gepstein A, Livne E, Jouzeau JY. 2004. Site specific changes in gene expression and cartilage metabolism during early experimental osteoarthritis. *Osteoarthr Cartil* **12**:284–295. doi:10.1016/j.joca.2003.11.008

eBioMedicine. 2022. The 3Rs of Animal Research. *eBioMedicine* **76**:103900. doi:10.1016/j.ebiom.2022.103900

Elhadad AA, Alcudia A, Begines B, Pérez-Soriano EM, Torres Y. 2022. A multidisciplinary perspective on the latest trends in artificial cartilage fabrication to mimic real tissue. *Appl Mater Today* **29**:101603. doi:10.1016/j.apmt.2022.101603

Eltawil NM, De Bari C, Achan P, Pitzalis C, Dell'Accio F. 2009. A novel in vivo murine model of cartilage regeneration. Age and strain-dependent outcome after joint surface injury. *Osteoarthr Cartil* **17**:695–704. doi:10.1016/j.joca.2008.11.003

Englund DA, Murach KA, Dungan CM, Figueiredo VC, Vechetti IJ, Dupont-Versteegden EE, McCarthy JJ, Peterson CA. 2020. Depletion of resident muscle stem cells negatively impacts running volume, physical function, and muscle fiber hypertrophy in response to lifelong physical activity. *Am J Physiol - Cell Physiol* **318**:C1178–C1188. doi:10.1152/ajpcell.00090.2020

Englund M, Roemer FW, Hayashi D, Crema MD, Guermazi A. 2012. Meniscus pathology, osteoarthritis and the treatment controversy. *Nat Rev Rheumatol* **8**:412–419. doi:10.1038/nrrheum.2012.69

Ertosun MG, Hapil FZ, Osman Nidai O. 2016. E2F1 transcription factor and its impact on growth factor and cytokine signaling. *Cytokine Growth Factor Rev* **31**:17–25. doi:https://doi.org/10.1016/j.cytogfr.2016.02.001

Fang H, Huang L, Welch I, Norley C, Holdsworth DW, Beier F, Cai D. 2018. Early Changes of Articular Cartilage and Subchondral Bone in The DMM Mouse Model of Osteoarthritis. *Sci Rep* **8**:1–9. doi:10.1038/s41598-018-21184-5

Farahani RM, Xaymardan M. 2015. Platelet-Derived Growth Factor Receptor Alpha as a Marker of Mesenchymal Stem Cells in Development and Stem Cell Biology. *Stem Cells Int* **2015**:362753. doi:10.1155/2015/362753

Fithian D, Kelly MA, Mow VC. 1990. Material properties and structure-function relationships in the menisci. *Clin Orthop Relat Res* **252**:19–31.

Fitzgerald J. 2017. Enhanced cartilage repair in 'healer' mice—New leads in the search for better clinical options for cartilage repair. *Semin Cell Dev Biol* **62**:78–85. doi:10.1016/j.semcdb.2016.04.018

Fitzgerald J, Rich C, Burkhardt D, Allen J, Herzka A, Little C. 2008. Evidence for articular cartilage regeneration in MRL/MpJ mice. *Osteoarthr Cartil* **16**:1319–1326. doi:10.1016/j.joca.2008.03.014

Flannery CR, Hughes CE, Schumacher BL, Tudor D, Aydelotte MB, Kuettner KE, Caterson B. 1999. Articular Cartilage Superficial Zone Protein (SZP) Is Homologous to Megakaryocyte Stimulating Factor Precursor and Is a Multifunctional Proteoglycan with Potential Growth-Promoting, Cytoprotective, and Lubricating Properties in Cartilage Metabolism. *Biochem Biophys Res Commun* **254**:535–541. doi:10.1006/bbrc.1998.0104

Fleuriel C, Touka M, Boulay G, Guérardel C, Rood BR, Leprince D. 2009. HIC1 (Hypermethylated in Cancer 1) epigenetic silencing in tumors. *Int J Biochem Cell Biol* **41**:26–33. doi:10.1016/j.biocel.2008.05.028

Frenkel SR, Bradica G, Brekke JH, Goldman SM, Ieska K, Issack P, Bong MR, Tian H, Gokhale J, Coutts RD, Kronengold RT. 2005. Regeneration of articular cartilage – Evaluation of osteochondral defect repair in the rabbit using multiphasic implants. *Osteoarthr Cartil* **13**:798–807. doi:10.1016/j.joca.2005.04.018

Froimson MI, Ratcliffe A, Gardner TR, Mow VC. 1997. Differences in patellofemoral joint cartilage material properties and their significance to the etiology of cartilage surface fibrillation. *Osteoarthr Cartil* **5**:377–386. doi:10.1016/S1063-4584(97)80042-8

Furman BD, Strand J, Hembree WC, Ward BD, Guilak F, Olson SA. 2007. Joint degeneration following closed intraarticular fracture in the mouse knee: A model of posttraumatic arthritis. *J Orthop Res* **25**:578–592. doi:10.1002/jor.20331

Gahunia HK, Pritzker KPH. 2020. Structure and Function of Articular Cartilage In: Gahunia HK, Gross AE, Pritzker KPH, Babyn PS, Murnaghan L, editors. Articular Cartilage of the Knee. New York, NY: Springer New York. pp. 3–70. doi:10.1007/978-1-4939-7587-7_1

Galliot B, Crescenzi M, Jacinto A, Tajbakhsh S. 2017. Trends in tissue repair and regeneration. *Development* **144**:357–364. doi:10.1242/dev.144279

Gawriluk TR, Simkin J, Thompson KL, Biswas SK, Clare-Salzler Z, Kimani JM, Kiama SG, Smith JJ, Ezenwa VO, Seifert AW. 2016. Comparative analysis of ear-hole closure identifies epimorphic regeneration as a discrete trait in mammals. *Nat Commun* **7**:11164. doi:10.1038/ncomms11164

Gilbert SJ, Bonnet CS, Blain EJ. 2021. Mechanical cues: Bidirectional reciprocity in the extracellular matrix drives mechano-signalling in articular cartilage. *Int J Mol Sci* **22**. doi:10.3390/ijms222413595

Glasson SS, Askew R, Sheppard B, Carito B, Blanchet T, Ma H-L, Flannery CR, Peluso D, Kanki K, Yang Z, Majumdar MK, Morris EA. 2005. Deletion of active ADAMTS5 prevents cartilage degradation in a murine model of osteoarthritis. *Nature* **434**:644–648. doi:10.1038/nature03369

Glasson SS, Blanchet TJ, Morris EA. 2007. The surgical destabilization of the medial meniscus (DMM) model of osteoarthritis in the 129/SvEv mouse. *Osteoarthr Cartil* **15**:1061–1069. doi:10.1016/j.joca.2007.03.006

Glasson SS, Chambers MG, Berg WB Van Den, Little CB. 2010. The OARSI histopathology initiative e recommendations for histological assessments of osteoarthritis in the mouse. *Osteoarthr Cartil* **18**:S17–S23. doi:10.1016/j.joca.2010.05.025

Globus M, Vethamany-Globus S, Lee YC. 1980. Effect of apical epidermal cap on mitotic cycle and cartilage differentiation in regeneration blastemata in the newt, Notophthalmus viridescens. *Dev Biol* **75**:358–372. doi:10.1016/0012-1606(80)90169-4

Goldring SR, Goldring MB. 2016. Changes in the osteochondral unit during osteoarthritis: Structure, function and cartilage bone crosstalk. *Nat Rev Rheumatol* **12**:632–644.

doi:10.1038/nrrheum.2016.148

Goss RJ, Grimes LN. 1972. Tissue interactions in the regeneration of rabbit ear holes. *Integr Comp Biol* **12**:151–157. doi:10.1093/icb/12.1.151

Gower JC. 1975. Generalized procrustes analysis. *Psychometrika* **40**:33–51. doi:10.1007/BF02291478

Griffin TM, Fermor B, Huebner JL, Kraus VB, Rodriguiz RM, Wetsel WC, Cao L, Setton LA, Guilak F. 2010. Diet-induced obesity differentially regulates behavioral , biomechanical , and molecular risk factors for osteoarthritis in mice.

Grimm C, Spörle R, Schmid TE, Adler I, Adamski J, Schughart K, Graw J. 1999. Isolation and embryonic expression of the novel mouse gene Hic1 , the homologue of HIC1 , a candidate gene for the Miller – Dieker syndrome **8**:697–710.

Grodzinsky AJ, Levenston ME, Jin M, Frank EH. 2000. Cartilage Tissue Remodeling in Response to Mechanical Forces. *Annu Rev Biomed Eng* **2**:691–713. doi:10.1146/annurev.bioeng.2.1.691

Guingamp C, Gegout-Pottie P, Philippe L, Terlain B, Netter P, Gillet P. 1997. Mono-iodoacetate-induced experimental osteoarthritis: A dose-response study of loss of mobility, morphology, and biochemistry. *Arthritis Rheum* **40**:1670–1679. doi:10.1002/art.1780400917

Guo T, Noshin M, Baker HB, Taskoy E, Meredith SJ, Tang Q, Ringel JP, Lerman MJ, Chen Y, Packer JD, Fisher JP. 2018. 3D printed biofunctionalized scaffolds for microfracture repair of cartilage defects. *Biomaterials* **185**:219–231. doi:10.1016/j.biomaterials.2018.09.022

Guzman RE, Evans MG, Bove S, Morenko B, Kilgore K. 2003. Mono-Iodoacetate-Induced Histologic Changes in Subchondral Bone and Articular Cartilage of Rat Femorotibial Joints: AN Animal Model of Osteoarthritis. *Toxicol Pathol* **31**:619–624. doi:10.1080/01926230390241800

Haase T, Sunkara V, Kohl B, Meier C, Bußmann P, Becker J, Jagielski M, von Kleist M, Ertel W. 2019. Discerning the spatio-temporal disease patterns of surgically induced OA mouse models. *PLoS One* **14**:e0213734. doi:10.1371/journal.pone.0213734

Hallgrímsson B, Katz DC, Aponte JD, Larson JR, Devine J, Gonzalez PN, Young NM, Roseman CC, Marcucio RS. 2019. Integration and the Developmental Genetics of Allometry. *Integr Comp Biol* **59**:1369–1381. doi:10.1093/icb/icz105

Hardingham TE, Fosang AJ. 1995. The structure of aggrecan and its turnover in cartilage. *J Rheumatol Suppl* **43**:86–90.

Haseeb A, Haqqi TM. 2013. Immunopathogenesis of osteoarthritis. *Clin Immunol* **146**:185–196. doi:10.1016/j.clim.2012.12.011

Hashimoto S, Ochs RL, Komiya S, Lotz M. 1998. Linkage of chondrocyte apoptosis and cartilage degradation in human osteoarthritis. *Arthritis Rheum* **41**:1632–1638. doi:10.1002/1529-0131(199809)41:9<1632::AID-ART14>3.0.CO;2-A

Hayami T, Pickarski M, Zhuo Y, Wesolowski GA, Rodan GA, Duong LT. 2006. Characterization of articular cartilage and subchondral bone changes in the rat anterior cruciate ligament transection and meniscectomized models of osteoarthritis. *Bone* **38**:234–243. doi:10.1016/j.bone.2005.08.007

Hayashi S, Fujishiro T, Hashimoto S, Kanzaki N, Chinzei N, Kihara S, Takayama K, Matsumoto T, Nishida K, Kurosaka M, Kuroda R. 2015. p21 deficiency is susceptible to osteoarthritis through STAT3 phosphorylation. *Arthritis Res Ther* **17**:1–11. doi:10.1186/s13075-015-0828-6

Hayes WC, Keer LM, Herrmann G, Mockros LF. 1972. A mathematical analysis for indentation of articular cartilage. *J Biomech* **5**:541–551. doi:doi.org/10.1016/0021-9290(72)90010-3

He Y, Zhang M, Song J, Warman ML. 2021. Cell depleted areas do not repopulate after diphtheria toxin-induced killing of mandibular cartilage chondrocytes. *Osteoarthr Cartil* **29**:1474–1484. doi:10.1016/j.joca.2021.06.003

Heinemeier KM, Schjerling P, Heinemeier J, Møller MB, Krogsgaard MR, Grum-Schwensen T, Petersen MM, Kjaer M. 2016. Radiocarbon dating reveals minimal collagen turnover in both healthy and osteoarthritic human cartilage. *Sci Transl Med* **8**:346ra90. doi:10.1126/scitranslmed.aad8335

Helminen HJ, Säämänen AM, Salminen H, Hyttinen MM. 2002. Transgenic mouse models for studying the role of cartilage macromolecules in osteoarthritis. *Rheumatology* **41**:848–856. doi:10.1093/rheumatology/41.8.848

Henry SP, Jang CW, Deng JM, Zhang Z, Behringer RR, De Crombrugghe B. 2009. Generation of aggrecan-CreERT2 knockin mice for inducible Cre activity in adult cartilage. *Genesis* **47**:805–814. doi:10.1002/dvg.20564

Hildebrand T, Rüegsegger P. 1997. A new method for the model-independent assessment of thickness in three-dimensional images. *J Microsc* **185**:67–75. doi:10.1046/j.1365-2818.1997.1340694.x

Hoch DH, Grodzinsky AJ, Koob TJ, Albert ML, Eyre DR. 1983. Early changes in material properties of rabbit articular cartilage after meniscectomy. *J Orthop Res* **1**:4–12. doi:10.1002/jor.1100010102

Hochberg MC, Martel-Pelletier J, Monfort J, Möller I, Castillo JR, Arden N, Berenbaum F, Blanco FJ, Conaghan PG, Doménech G, Henrotin Y, Pap T, Richette P, Sawitzke A, Souich P Du, Pelletier JP. 2016. Combined chondroitin sulfate and glucosamine for painful knee osteoarthritis: A multicentre, randomised, double-blind, non-inferiority trial versus celecoxib. *Ann Rheum Dis* **75**:37–44. doi:10.1136/annrheumdis-2014-206792

Holmes C, Stanford WL. 2007. Concise Review: Stem Cell Antigen-1: Expression, Function, and Enigma. *Stem Cells* **25**:1339–1347. doi:10.1634/stemcells.2006-0644

Hoshi H, Akagi R, Yamaguchi S, Muramatsu Y, Akatsu Y, Yamamoto Y, Sasaki T, Takahashi K, Sasho T. 2017. Effect of inhibiting MMP13 and ADAMTS5 by intra-articular injection of small interfering RNA in a surgically induced osteoarthritis model of mice. *Cell Tissue Res* **368**:379–387. doi:10.1007/s00441-016-2563-y

Hsueh M-F, Önnerfjord P, Bolognesi MP, Easley ME, Kraus VB. 2019. Analysis of "old" proteins unmasks dynamic gradient of cartilage turnover in human limbs. *Sci Adv* **5**:eaax3203. doi:10.1126/sciadv.aax3203

Hu X, Charles JP, Akay T, Hutchinson JR, Blemker SS. 2017. Are mice good models for human neuromuscular disease? Comparing muscle excursions in walking between mice and humans. *Skelet Muscle* **7**:1–15. doi:10.1186/s13395-017-0143-9

Huang H, Skelly JD, Ayers DC, Song J. 2017. Age-dependent Changes in the Articular Cartilage and Subchondral Bone of C57BL/6 Mice after Surgical Destabilization of Medial Meniscus. *Sci Rep* **7**:1–9. doi:10.1038/srep42294

Huey DJ, Hu JC, Athanasiou K a. 2012. Remains Elusive. *Science (80-)* **6933**:917–921. doi:10.1126/science.1222454

Hulin-Curtis SL, Bidwell JL, Perry MJ. 2013. Association between CCL2 haplotypes and knee osteoarthritis. *Int J Immunogenet* **40**:280–283. doi:10.1111/iji.12015

Hunter DJ, Bierma-Zeinstra S. 2019. Osteoarthritis. *Lancet* **393**:1745–1759. doi:10.1016/S0140-6736(19)30417-9

Hunter DJ, Schofield D, Callander E. 2014. The individual and socioeconomic impact of osteoarthritis. *Nat Rev Rheumatol* **10**:437–441. doi:10.1038/nrrheum.2014.44

Hunter DJ, Zhang YQ, Niu JB, Tu X, Amin S, Clancy M, Guermazi A, Grigorian M, Gale D, Felson DT. 2006. The association of meniscal pathologic changes with cartilage loss in symptomatic knee osteoarthritis. *Arthritis Rheum* **54**:795–801. doi:10.1002/art.21724

Hunziker EB, Quinn TM, Häuselmann HJ. 2002. Quantitative structural organization of normal adult human articular cartilage. *Osteoarthr Cartil* **10**:564–572. doi:10.1053/joca.2002.0814

Hunziker EB, Rosenberg LC. 1996. Repair of partial-thickness defects in articular cartilage: cell recruitment from the synovial membrane. *J Bone Joint Surg Am* **78**:721–733. doi:10.2106/00004623-199605000-00012

Hwang HS, Kim HA. 2015. Chondrocyte apoptosis in the pathogenesis of osteoarthritis. *Int J Mol Sci* **16**:26035–26054. doi:10.3390/ijms161125943

Ikegawa S, Sano M, Koshizuka Y, Nakamura Y. 2000. Isolation, characterization and mapping of the mouse and human PRG4 (proteoglycan 4) genes. *Cytogenet Genome Res* **90**:291–297. doi:10.1159/000056791

Illingworth CM. 1974. Trapped fingers and amputated finger tips in children. *J Pediatr Surg* **9**:853–858. doi:10.1016/S0022-3468(74)80220-4

Iqbal SM, Leonard C, C. Regmi S, De Rantere D, Tailor P, Ren G, Ishida H, Hsu CY, Abubacker S, Pang DSJ, T. Salo P, Vogel HJ, Hart DA, Waterhouse CC, Jay GD, Schmidt TA, Krawetz RJ. 2016. Lubricin/Proteoglycan 4 binds to and regulates the activity of Toll-Like Receptors In Vitro. *Sci Rep* **6**:18910. doi:10.1038/srep18910

Jablonski CL, Besler BA, Ali J, Krawetz RJ. 2021. p21 −/− Mice Exhibit Spontaneous Articular Cartilage Regeneration Post-Injury. *Cartilage* **13**:1608S-1617S. doi:10.1177/1947603519876348

Jablonski CL, Leonard C, Salo P, Krawetz RJ. 2019. CCL2 But Not CCR2 Is Required for Spontaneous Articular Cartilage Regeneration Post-Injury. *J Orthop Res* **37**:2561–2574. doi:10.1002/jor.24444

Jaisser F. 2000. Inducible gene expression and gene modification in transgenic mice. *J Am Soc Nephrol* **11 Suppl 1**:S95–S100.

Jay GD, Tantravahi U, Britt DE, Barrach HJ, Cha CJ. 2001. Homology of lubricin and superficial zone protein (SZP): Products of megakaryocyte stimulating factor (MSF) gene expression by human synovial fibroblasts and articular chondrocytes localized to chromosome 1q25. *J Orthop Res* **19**:677–687. doi:10.1016/S0736-0266(00)00040-1

Jay GD, Torres JR, Rhee DK, Helminen HJ, Hytinnen MM, Cha CJ, Elsaid K, Kim KS, Cui Y, Warman ML. 2007. Association between friction and wear in diarthrodial joints lacking lubricin. *Arthritis Rheum* **56**:3662–3669. doi:10.1002/art.22974

Jenal M, Trinh E, Britschgi C, Britschgi A, Roh V, Vorburger S a, Tobler A, Leprince D, Fey MF, Helin K, Tschan MP. 2009. The tumor suppressor gene hypermethylated in cancer 1 is transcriptionally regulated by E2F1. *Mol Cancer Res* **7**:916–22. doi:10.1158/1541-7786.MCR-08-0359

Jeon OH, Kim C, Laberge RM, Demaria M, Rathod S, Vasserot AP, Chung JW, Kim DH, Poon Y, David N, Baker DJ, Van Deursen JM, Campisi J, Elisseeff JH. 2017. Local clearance of senescent cells attenuates the development of post-traumatic osteoarthritis and creates a pro-regenerative environment. *Nat Med* **23**:775–781. doi:10.1038/nm.4324

Jia H, Ma X, Wei Y, Tong W, Tower RJ, Chandra A, Wang L, Sun Z, Yang Z, Badar F, Zhang K, Tseng W, Kramer I, Kneissel M, Xia Y, Liu XS, Wang JHC, Han L. 2018. Loading-Induced Reduction in Sclerostin as a Mechanism of Subchondral Bone Plate Sclerosis in Mouse Knee Joints During Late-Stage Osteoarthritis **70**:230–241. doi:10.1002/art.40351

Jimenez PA, Glasson SS, Trubetskoy O V., Haimes HB. 1997. Spontaneous Osteoarthritis in Dunkin Hartley Guinea Pigs: Histologic, Radiologic, and Biochemical Changes. *Lab Anim Sci* **47**:598–601.

Johnson K, Zhu S, Tremblay MS, Payette JN, Wang J, Bouchez LC, Meeusen S, Althage A, Cho CY, Wu X, Schultz PG. 2012. A Stem Cell-Based Approach to Cartilage Repair. *Science (80-)* **336**:717–721. doi:10.1126/science.1215157

Joutoku Z, Onodera T, Matsuoka M, Homan K, Momma D, Baba R, Hontani K, Hamasaki M, Matsubara S, Hishimura R, Iwasaki N. 2019. CCL21/CCR7 axis regulating juvenile cartilage repair can enhance cartilage healing in adults. *Sci Rep* **9**:1–12. doi:10.1038/s41598-019-41621-3

Julkunen P., Harjula T, Iivarinen J, Marjanen J, Seppänen K, Närhi T, Arokoski J, Lammi MJ, Brama PA, Jurvelin JS, Helminen HJ. 2009. Biomechanical, biochemical and structural correlations in immature and mature rabbit articular cartilage. *Osteoarthr Cartil* **17**:1628–1638. doi:10.1016/j.joca.2009.07.002

Julkunen Petro, Harjula T, Marjanen J, Helminen HJ, Jurvelin JS. 2009. Comparison of single-phase isotropic elastic and fibril-reinforced poroelastic models for indentation of rabbit articular cartilage. *J Biomech* **42**:652–656. doi:10.1016/j.jbiomech.2008.12.010

Julkunen P, Korhonen RK, Herzog W, Jurvelin JS. 2008. Uncertainties in indentation testing of articular cartilage: A fibril-reinforced poroviscoelastic study. *Med Eng Phys* **30**:506–515. doi:10.1016/j.medengphy.2007.05.012

Jurvelin JS, Räsänen T, Kolmonens P, Lyyra T. 1995. Comparison of optical, needle probe and ultrasonic techniques for the measurement of articular cartilage thickness. *J Biomech* **28**:231–235. doi:10.1016/0021-9290(94)00060-H

Kamekura S, Hoshi K, Shimoaka T, Chung U, Chikuda H, Yamada T, Uchida M, Ogata N, Seichi A, Nakamura K, Kawaguchi H. 2005. Osteoarthritis development in novel experimental mouse models induced by knee joint instability. *Osteoarthr Cartil* **13**:632–641. doi:10.1016/j.joca.2005.03.004

Karamchedu NP, Tofte JN, Waller KA, Zhang LX, Patel TK, Jay GD. 2016. Superficial zone cellularity is deficient in mice lacking lubricin: A stereoscopic analysis. *Arthritis Res Ther* **18**:1–12. doi:10.1186/s13075-016-0967-4

Karimian A, Ahmadi Y, Yousefi B. 2016. Multiple functions of p21 in cell cycle, apoptosis and transcriptional regulation after DNA damage. *DNA Repair (Amst)* **42**:63–71. doi:10.1016/j.dnarep.2016.04.008

Karsdal MA, Madsen SH, Christiansen C, Henriksen K, Fosang AJ, Sondergaard BC. 2008. Cartilage degradation is fully reversible in the presence of aggrecanase but not matrix metalloproteinase activity. *Arthritis Res Ther* **10**:1–12. doi:10.1186/ar2434

Kfoury Y, Scadden DT. 2015. Mesenchymal cell contributions to the stem cell niche. *Cell Stem Cell* **16**:239–253. doi:10.1016/j.stem.2015.02.019

Kiani C, Chen L, Wu YJ, Yee AJ, Yang BB. 2002. Structure and function of aggrecan. *Cell Res* **12**:19–

32. doi:10.1038/sj.cr.7290106

Kikinis R, Pieper SD, Vosburgh KG. 2014. 3D Slicer: A Platform for Subject-Specific Image Analysis, Visualization, and Clinical SupportIntraoperative Imaging and Image-Guided Therapy. New York, NY: Springer New York. pp. 277–289. doi:10.1007/978-1-4614-7657-3_19

Kim J, Braun T. 2020. Keeping Fibrotic Responses in Contractile Tissues at Bay: The Plot t(Hic1)ens. *Cell Stem Cell* **26**:129–130. doi:10.1016/j.stem.2019.12.010

Kinner B, Capito RM, Spector M. 2005. Regeneration of articular cartilage. *Adv Biochem Eng Biotechnol* **94**:91–123. doi:10.1007/b100001

Kleeman RU, Krocker D, Cedrano A, Tuischer J, Duda GN. 2005. Altered cartilage mechanics and histology in knee osteoarthritis: Relation to clinical assessment (ICRS Grade). *Osteoarthr Cartil* **13**:958–963. doi:10.1016/j.joca.2005.06.008

Klingenberg CP. 2016. Size, shape, and form: concepts of allometry in geometric morphometrics. *Dev Genes Evol* **226**:113–137. doi:10.1007/s00427-016-0539-2

Ko FC, Dragomir C, Plumb DA, Goldring SR, Wright TM, Goldring MB, Meulen MCH Van Der. 2013. In Vivo Cyclic Compression Causes Cartilage Degeneration and Subchondral Bone Changes in Mouse Tibiae. *Arthritis Rheum* **65**:1569–1578. doi:10.1002/art.37906

Koo TK, Li MY. 2016. A Guideline of Selecting and Reporting Intraclass Correlation Coefficients for Reliability Research. *J Chiropr Med* **15**:155–163. doi:10.1016/j.jcm.2016.02.012

Korhonen R., Wong M, Arokoski J, Lindgren R, Helminen H., Hunziker E., Jurvelin J. 2002. Importance of the superficial tissue layer for the indentation stiffness of articular cartilage. *Med Eng Phys* **24**:99–108. doi:10.1016/S1350-4533(01)00123-0

Kos CH. 2004. Cre/loxP system for generating tissue-specific knockout mouse models. *Nutr Rev* **62**:243–6. doi:10.1301/nr.2004.jun.243–246

Kosinska MK, Ludwig TE, Liebisch G, Zhang R, Siebert HC, Wilhelm J, Kaesser U, Dettmeyer RB, Klein H, Ishaque B, Rickert M, Schmitz G, Schmidt TA, Steinmeyer J. 2015. Articular joint lubricants during osteoarthritis and rheumatoid arthritis display altered levels and molecular species. *PLoS One* **10**:1–18. doi:10.1371/journal.pone.0125192

Kotwal N, Li J, Sandy J, Plaas A, Sumner DR. 2012. Initial application of EPIC-μCT to assess mouse articular cartilage morphology and composition: Effects of aging and treadmill running. *Osteoarthr Cartil* **20**:887–895. doi:10.1016/j.joca.2012.04.012

Koyama E, Shibukawa Y, Nagayama M, Sugito H, Young B, Yuasa T, Okabe T, Ochiai T, Kamiya N, Rountree RB, Kingsley DM, Iwamoto M, Enomoto-Iwamoto M, Pacifici M. 2008. A distinct cohort of progenitor cells participates in synovial joint and articular cartilage formation during mouse limb skeletogenesis. *Dev Biol* **316**:62–73. doi:10.1016/j.ydbio.2008.01.012

Kozhemyakina E, Zhang M, Ionescu A, Ayturk UM, Ono N, Kobayashi A, Kronenberg H, Warman ML, Lassar AB. 2015. Identification of a Prg4-expressing articular cartilage progenitor cell population in mice. *Arthritis Rheumatol* **67**:1261–1273. doi:10.1002/art.39030

Krawetz RJ, Abubacker S, Leonard C, Masson AO, Shah S, Narendran N, Tailor P, Regmi SC, Labit E, Ninkovic N, Corpuz JM, Ito K, Underhill TM, Salo PT, Schmidt TA, Biernaskie JA. 2022. Proteoglycan 4 (PRG4) treatment enhances wound closure and tissue regeneration. *npj Regen Med* **7**:32. doi:10.1038/s41536-022-00228-5

Kuyinu EL, Narayanan G, Nair LS, Laurencin CT. 2016. Animal models of osteoarthritis: classification, update, and measurement of outcomes. *J Orthop Surg Res* **11**:19. doi:10.1186/s13018-016-0346-5

Kyostio-Moore S, Nambiar B, Hutto E, Ewing PJ, Piraino S, Berthelette P, Sookdeo C, Matthews G, Armentano D. 2011. STR/ort mice, a model for spontaneous osteoarthritis, exhibit elevated levels of both local and systemic inflammatory markers. *Comp Med* **61**:346–355.

Laasanen MS, Töyräs J, Korhonen RK, Rieppo J, Saarakkala S, Nieminen MT, Hirvonen J, Jurvelin JS. 2003. Biomechanical properties of knee articular cartilage. *Biorheology* **40**:133–40.

Lakin BA, Snyder BD, Grinstaff MW. 2017. Assessing Cartilage Biomechanical Properties: Techniques for Evaluating the Functional Performance of Cartilage in Health and Disease. *Annu Rev Biomed Eng* **19**:27–55. doi:10.1146/annurev-bioeng-071516-044525

Lavoie J, Sim S, Quenneville E, Garon M, Moreau A, Bushmann MD, Aubin C-É. 2015. Mapping articular cartilage biomechanical properties of normal and osteoarthritis mice using indentation. *Osteoarthr Cartil* **23**:A254. doi:10.1016/j.joca.2015.02.463

Leonard CA, Lee WY, Tailor P, Salo PT, Kubes P, Krawetz RJ. 2015. Allogeneic bone marrow transplant from MRL/MpJ super-healer mice does not improve articular cartilage repair in the C57Bl/6 strain. *PLoS One* **10**. doi:10.1371/journal.pone.0131661

Lerch JP, Sled JG, Henkelman RM. 2011. MRI Phenotyping of Genetically Altered MiceMethods in Molecular Biology. pp. 349–361. doi:10.1007/978-1-61737-992-5_17

Levick JR, McDonald JN. 1995. Fluid movement across synovium in healthy joints: Role of synovial fluid macromolecules. *Ann Rheum Dis* **54**:417–423. doi:10.1136/ard.54.5.417

Li G, Sang EP, DeFrate LE, Schutzer ME, Ji L, Gill TJ, Rubash HE. 2005. The cartilage thickness distribution in the tibiofemoral joint and its correlation with cartilage-to-cartilage contact. *Clin Biomech* **20**:736–744. doi:10.1016/j.clinbiomech.2005.04.001

Li L, Jiang BE. 2015. Serum and synovial fluid chemokine ligand 2/monocyte chemoattractant protein 1 concentrations correlates with symptomatic severity in patients with knee osteoarthritis. *Ann Clin Biochem* **52**:276–282. doi:10.1177/0004563214545117

Li L, Newton PT, Bouderlique T, Sejnohova M, Zikmund T, Kozhemyakina E, Xie M, Krivanek J, Kaiser J, Qian H, Dyachuk V, Lassar AB, Warman ML, Barenius B, Adameyko I, Chagin AS. 2017. Superficial cells are self-renewing chondrocyte progenitors, which form the articular cartilage in juvenile mice. *FASEB J* **31**:1067–1084. doi:10.1096/fj.201600918R

Li MH, Xiao R, Li JB, Zhu Q. 2017. Regenerative approaches for cartilage repair in the treatment of osteoarthritis. *Osteoarthr Cartil* **25**:1577–1587. doi:10.1016/j.joca.2017.07.004

Li Y, Xu L. 2015. Advances in understanding cartilage remodeling. *F1000Research* **4**. doi:10.12688/f1000research.6514.1

Liao L, Zhang S, Gu J, Takarada T, Yoneda Y, Huang J, Zhao L, Oh C Do, Li J, Wang B, Wang M, Chen D. 2017. Deletion of Runx2 in Articular Chondrocytes Decelerates the Progression of DMM-Induced Osteoarthritis in Adult Mice. *Sci Rep* **7**:1–12. doi:10.1038/s41598-017-02490-w

Little CB, Barai A, Burkhardt D, Smith SM, Fosang AJ, Werb Z, Shah M, Thompson EW. 2009. Matrix metalloproteinase 13-deficient mice are resistant to osteoarthritic cartilage erosion but not chondrocyte hypertrophy or osteophyte development. *Arthritis Rheum* **60**:3723–3733. doi:10.1002/art.25002

Lockwood KA, Chu BT, Anderson MJ, Haudenschild DR, Christiansen BA. 2014. Comparison of loading rate-dependent injury modes in a murine model of post-traumatic osteoarthritis. *J Orthop Res* **32**:79–88. doi:10.1002/jor.22480

Loder S, Patel N, Morgani S, Sambon M, Leucht P, Levi B. 2023. Genetic models for lineage tracing in musculoskeletal development, injury, and healing. *Bone* **173**:116777. doi:10.1016/j.bone.2023.116777

Loebel C, Burdick JA. 2018. Engineering Stem and Stromal Cell Therapies for Musculoskeletal Tissue Repair. *Cell Stem Cell* 1–15. doi:10.1016/j.stem.2018.01.014

Loeser RF. 2009. Aging and osteoarthritis: the role of chondrocyte senescence and aging changes in the cartilage matrix. *Osteoarthr Cartil* **17**:971–979. doi:10.1016/j.joca.2009.03.002

Loeser RF, Olex AL, McNulty MA, Carlson CS, Callahan MF, Ferguson CM, Chou J, Leng X, Fetrow JS. 2012. Microarray analysis reveals age-related differences in gene expression during the development of osteoarthritis in mice. *Arthritis Rheum* **64**:705–717. doi:10.1002/art.33388

Logan M, Martin JF, Nagy A, Lobe C, Olson EN, Tabin CJ. 2002. Expression of Cre Recombinase in the developing mouse limb bud driven by a Prxl enhancer. *Genesis* **33**:77–80. doi:10.1002/gene.10092

Lohmander LS, Atley LM, Pietka TA, Eyre DR. 2003. The Release of Crosslinked Peptides From Type II Collagen Into Human Synovial Fluid Is Increased Soon After Joint Injury and in Osteoarthritis. *Arthritis Rheum* **48**:3130–3139. doi:10.1002/art.11326

Lohmander LS, Englund PM, Dahl LL, Roos EM. 2007. The long-term consequence of anterior cruciate ligament and meniscus injuries: Osteoarthritis. *Am J Sports Med* **35**:1756–1769. doi:10.1177/0363546507307396

Lowekamp BC, Chen DT, Ibáñez L, Blezek D. 2013. The design of simpleITK. *Front Neuroinform* **7**:1–14. doi:10.3389/fninf.2013.00045

Lu XL, Mow VC. 2008. Biomechanics of Articular Cartilage and Determination of Material Properties. *Med Sci Sport Exerc* **40**:193–199. doi:10.1249/mss.0b013e31815cb1fc

Maden M, Varholick JA. 2020. Model systems for regeneration: The spiny mouse, Acomys cahirinus. *Dev* **147**. doi:10.1242/dev.167718

Maenohara Y, Chijimatsu R, Tachibana N, Uehara K, Xuan F, Mori D, Murahashi Y, Nakamoto H, Oichi T, Chang SH, Matsumoto T, Omata Y, Yano F, Tanaka S, Saito T. 2021. Lubricin Contributes to Homeostasis of Articular Cartilage by Modulating Differentiation of Superficial Zone Cells. *J Bone Miner Res* **36**:792–802. doi:10.1002/jbmr.4226

Mahmoudian A, Lohmander LS, Mobasheri A, Englund M, Luyten FP. 2021. Early-stage symptomatic osteoarthritis of the knee — time for action. *Nat Rev Rheumatol* **17**:621–632. doi:10.1038/s41584-021-00673-4

Mak J, Jablonski CL, Leonard CA, Dunn JF, Raharjo E, Matyas JR, Biernaskie J, Krawetz RJ. 2016. Intra-articular injection of synovial mesenchymal stem cells improves cartilage repair in a mouse injury model. *Sci Rep* **6**:23076. doi:10.1038/srep23076

Mak J, Leonard C, Foniok T, Rushforth D, Dunn JF, Krawetz R. 2015. Evaluating endogenous repair of focal cartilage defects in C57BL/6 and MRL/MpJ mice using 9.4T magnetic resonance imaging: A pilot study. *Magn Reson Imaging* **33**:690–694. doi:10.1016/j.mri.2015.01.001

Malda J, de Grauw JC, Benders KEM, Kik MJL, van de Lest CHA, Creemers LB, Dhert WJA, van

Weeren PR. 2013. Of Mice, Men and Elephants: The Relation between Articular Cartilage Thickness and Body Mass. *PLoS One* **8**:1–8. doi:10.1371/journal.pone.0057683

Mankin HJ. 1968. The effect of aging on articular cartilage. *Bull N Y Acad Med* **44**:545–52.

Mannurita SC, Vignoli M, Bianchi L, Kondi A, Gerloni V, Breda L, Ten Cate R, Alessio M, Ravelli A, Falcini F, Gambineri E. 2014. CACP syndrome: Identification of five novel mutations and of the first case of UPD in the largest European cohort. *Eur J Hum Genet* **22**:197–201. doi:10.1038/ejhg.2013.123

Mansour JM. 2013. Biomechanics of cartilage. *Kinesiol Mech Pathomechanics Hum Mov Second Ed* 69–83.

Marcelino J, Carpten JD, Suwairi WM, Gutierrez OM, Schwartz S, Robbins C, Sood R, Makalowska I, Baxevanis A, Johnstone B, Laxer RM, Zemel L, Kim CA, Herd JK, Ihle J, Williams C, Johnson M, Raman V, Alonso LG, Brunoni D, Gerstein A, Papadopoulos N, Bahabri SA, Trent JM, Warman ML. 1999. CACP , encoding a secreted proteoglycan , is mutated in camptodactyly-arthropathy-coxa vara-pericarditis syndrome. *Nat Genet* **23**:319–322.

Maroudas A, Bayliss MT, Uchitel-Kaushansky N, Schneiderman R, Gilav E. 1998. Aggrecan turnover in human articular cartilage: Use of aspartic acid racemization as a marker of molecular age. *Arch Biochem Biophys* **350**:61–71. doi:10.1006/abbi.1997.0492

Martel-Pelletier J, Barr AJ, Cicuttini FM, Conaghan PG, Cooper C, Goldring MB, Goldring SR, Jones G, Teichtahl AJ, Pelletier JP. 2016. Osteoarthritis. *Nat Rev Dis Prim* **2**. doi:10.1038/nrdp.2016.72

Martel-Pelletier J, Boileau C, Pelletier JP, Roughley PJ. 2008. Cartilage in normal and osteoarthritis conditions. *Best Pract Res Clin Rheumatol* **22**:351–384. doi:10.1016/j.berh.2008.02.001

Mason RM, Chambers MG, Flannelly J, Gaffen JD, Dudhia J, Bayliss MT. 2001. The STR / ort mouse and its use as a model of osteoarthritis 85–91. doi:10.1053/joca.2000.0363

Masouros SD, Bull AMJ, Amis AA. 2010. (i) Biomechanics of the knee joint. *Orthop Trauma* **24**:84–91. doi:10.1016/j.mporth.2010.03.005

Masson AO, Besler B, Edwards WB, Krawetz RJ. 2022. High spatial resolution analysis using automated indentation mapping differentiates biomechanical properties of normal vs. degenerated articular cartilage in mice. *Elife* **11**:2021.10.26.465857. doi:10.7554/eLife.74664

Matsuoka M, Onodera T, Sasazawa F, Momma D, Baba R, Hontani K, Iwasaki N. 2015. An Articular Cartilage Repair Model in Common C57Bl/6 Mice. *Tissue Eng - Part C Methods* **21**:767–772. doi:10.1089/ten.tec.2014.0440

Matyas JR, Atley L, Ionescu M, Eyre DR, Poole AR. 2004. Analysis of Cartilage Biomarkers in the Early Phases of Canine Experimental Osteoarthritis. *Arthritis Rheum* **50**:543–552. doi:10.1002/art.20027

Mavers M, Cuda CM, Misharin A V., Gierut AK, Agrawal H, Weber E, Novack DV, Haines GK, Balomenos D, Perlman H. 2012. Cyclin-dependent kinase inhibitor p21, via its C-terminal domain, is essential for resolution of murine inflammatory arthritis. *Arthritis Rheum* **64**:141–152. doi:10.1002/art.33311

McCoy AM. 2015. Animal Models of Osteoarthritis. *Vet Pathol* **52**:803–818. doi:10.1177/0300985815588611

McGonagle D, Baboolal TG, Jones E. 2017. Native joint-resident mesenchymal stem cells for cartilage repair in osteoarthritis. *Nat Rev Rheumatol* **13**:719–730. doi:10.1038/nrrheum.2017.182

Merrild NG, Holzmann V, Ariosa-Morejon Y, Faull PA, Coleman J, Barrell WB, Young G, Fischer R, Kelly DJ, Addison O, Vincent TL, Grigoriadis AE, Gentleman E. 2022. Local depletion of proteoglycans mediates cartilage tissue repair in an ex vivo integration model. *Acta Biomater* **149**:179–188. doi:10.1016/j.actbio.2022.06.032

Miller RE, Lu Y, Tortorella MD, Malfait AM. 2013. Genetically engineered mouse models reveal the importance of proteases as osteoarthritis drug targets. *Curr Rheumatol Rep* **15**. doi:10.1007/s11926-013-0350-2

Miller RE, Tran PB, Das R, Ghoreishi-Haack N, Ren D, Miller RJ, Malfait AM. 2012. CCR2 chemokine receptor signaling mediates pain in experimental osteoarthritis. *Proc Natl Acad Sci U S A* **109**:20602–20607. doi:10.1073/pnas.1209294110

Miller TJ, Deptula PL, Buncke GM, Maan ZN. 2019. Digit tip injuries: Current treatment and future regenerative paradigms. *Stem Cells Int*. doi:10.1155/2019/9619080

Mimpen JY, Snelling SJB. 2019. Chondroprotective Factors in Osteoarthritis: a Joint Affair. *Curr Rheumatol Rep* **21**:41. doi:10.1007/s11926-019-0840-y

Miotla Zarebska J, Chanalaris A, Driscoll C, Burleigh A, Miller RE, Malfait AM, Stott B, Vincent TL. 2017. CCL2 and CCR2 regulate pain-related behaviour and early gene expression in post-traumatic murine osteoarthritis but contribute little to chondropathy. *Osteoarthr Cartil* **25**:406–412. doi:10.1016/j.joca.2016.10.008

Mohan G, Perilli E, Kuliwaba JS, Humphries JM, Parkinson IH, Fazzalari NL. 2011. Application of in vivo micro-computed tomography in the temporal characterisation of subchondral bone architecture in a rat model of low-dose monosodium iodoacetate-induced osteoarthritis. *Arthritis Res Ther* **13**:1–14. doi:10.1186/ar3543

Morais GP, Chemerka C, Masson A, Seerattan RA, da Rocha AL, Krawetz R, da Silva ASR, Herzog W. 2021. Excessive downhill training leads to early onset of knee osteoarthritis. *Osteoarthr Cartil* **29**:870–881. doi:10.1016/j.joca.2021.03.016

Moshtagh PR, Pouran B, Korthagen NM, Zadpoor AA, Weinans H. 2016. Guidelines for an optimized indentation protocol for measurement of cartilage stiffness : The effects of spatial variation and indentation parameters. *J Biomech* **49**:3602–3607. doi:10.1016/j.jbiomech.2016.09.020

Mow VC, Kuei SC, Lai WM, Armstrong CG. 1980. Biphasic creep and stress relaxation of articular cartilage in compression: Theory and experiments. *J Biomech Eng* **102**:73–84. doi:10.1115/1.3138202

Müller R, Büttner P. 1994. A critical discussion of intraclass correlation coefficients. *Stat Med* **13**:2465–2476. doi:10.1002/sim.4780132310

Murphy MP, Koepke LS, Lopez MT, Tong X, Ambrosi TH, Gulati GS, Marecic O, Wang Y, Ransom RC, Hoover MY, Steininger H, Zhao L, Walkiewicz MP, Quarto N, Levi B, Wan DC, Weissman IL, Goodman SB, Yang F, Longaker MT, Chan CKF. 2020. Articular cartilage regeneration by activated skeletal stem cells. *Nat Med* **26**:1583–1592. doi:10.1038/s41591-020-1013-2

Muthu S, Korpershoek J V., Novais EJ, Tawy GF, Hollander AP, Martin I. 2023. Failure of cartilage regeneration: emerging hypotheses and related therapeutic strategies. *Nat Rev Rheumatol* **19**:403–416. doi:10.1038/s41584-023-00979-5

Natoli RM, Scott CC, Athanasiou KA. 2008. Temporal effects of impact on articular cartilage cell death, gene expression, matrix biochemistry, and biomechanics. *Ann Biomed Eng* **36**:780–792. doi:10.1007/s10439-008-9472-5

Nguyen PHA, Submitted AD, Partial IN, Of F, Requirements THE, The FOR, Of D, Philosophy DOF, Studies P. 2020. Hic1 is a quiescence regulator of mesenchymal stromal cells in bone marrow and responsible for controlling the size of hematopoietic stem cell niche.

Norkin CC, Levangie PK. 2011. Joint structure and function : a comprehensive analysis , 5th ed. ed. Philadelphia: F.A. Davis Co.

Novince CM, Entezami P, Wilson CG, Wang J, Oh S, Koh AJ, Michalski MN, Sinder BP, Kozloff KM, Taichman RS, McCauley LK. 2013. Impact of proteoglycan-4 and parathyroid hormone on articular cartilage. *J Orthop Res* **31**:183–190. doi:10.1002/jor.22207

Novince CM, Michalski MN, Koh AJ, Sinder BP, Entezami P, Eber MR, Pettway GJ, Rosol TJ, Wronski TJ, Kozloff KM, McCauley LK. 2012. Proteoglycan 4: A dynamic regulator of skeletogenesis and parathyroid hormone skeletal anabolism. *J Bone Miner Res* **27**:11–25. doi:10.1002/jbmr.508

Oláh T, Michaelis JC, Cai X, Cucchiarini M, Madry H. 2021. Comparative anatomy and morphology of the knee in translational models for articular cartilage disorders. Part II: Small animals. *Ann Anat - Anat Anzeiger* **234**:151630. doi:10.1016/j.aanat.2020.151630

Orozco GA, Karjalainen K, Moo EK, Stenroth L, Tanska P, Rios JL, Tuomainen T V., Nissi MJ, Isaksson H, Herzog W, Korhonen RK. 2022. A musculoskeletal finite element model of rat knee joint for evaluating cartilage biomechanics during gait. *PLoS Comput Biol* **18**:1–23. doi:10.1371/journal.pcbi.1009398

Ovchinnikov DA, Deng JM, Ogunrinu G, Behringer RR. 2000. Col2a1-directed expression of Cre recombinase in differentiating chondrocytes in transgenic mice. *Genesis* **26**:145–146. doi:10.1002/(SICI)1526-968X(200002)26:2<145::AID-GENE14>3.0.CO;2-C

Pellettieri J, Alvarado AŚ. 2007. Cell turnover and adult tissue homeostasis: From humans to planarians. *Annu Rev Genet* **41**:83–105. doi:10.1146/annurev.genet.41.110306.130244

Percival CJ, Devine J, Darwin BC, Liu W, van Eede M, Henkelman RM, Hallgrimsson B. 2019. The effect of automated landmark identification on morphometric analyses. *J Anat* **234**:917–935. doi:10.1111/joa.12973

Poole AR, Kojima T, Yasuda T, Mwale F, Kobayashi M, Laverty S, Acvs D. 2001. Composition and Structure of Articular Cartilage A Template for Tissue RepairCLINICAL ORTHOPAEDICS AND RELATED RESEARCH. pp. 26–33.

Poulet B. 2017. Models to define the stages of articular cartilage degradation in osteoarthritis development. *Int J Exp Pathol* **98**:120–126. doi:10.1111/iep.12230

Poulet B, Westerhof TAT, Hamilton RW, Shefelbine SJ, Pitsillides AA. 2013. Spontaneous osteoarthritis in Str/ort mice is unlikely due to greater vulnerability to mechanical trauma. *Osteoarthr Cartil* **21**:756–763. doi:10.1016/j.joca.2013.02.652

Price J, Allen S. 2004. Exploring the mechanisms regulating regeneration of deer antlers. *Philos Trans R Soc B Biol Sci* **359**:809–822. doi:10.1098/rstb.2004.1471

Qadri M, Jay GD, Zhang LX, Richendrfer H, Schmidt TA, Elsaid KA. 2020. Proteoglycan-4 regulates fibroblast to myofibroblast transition and expression of fibrotic genes in the synovium. *Arthritis Res Ther* **22**:113. doi:10.1186/s13075-020-02207-x

Raghu H, Lepus CM, Wang Q, Wong HH, Lingampalli N, Oliviero F, Punzi L, Giori NJ, Goodman SB, Chu CR, Sokolove JB, Robinson WH. 2017. CCL2/CCR2, but not CCL5/CCR5, mediates monocyte recruitment, inflammation and cartilage destruction in osteoarthritis. *Ann Rheum Dis* **76**:914–922.

doi:10.1136/annrheumdis-2016-210426

Rahmati M, Nalesso G, Mobasheri A, Mozafari M. 2017. Aging and osteoarthritis: Central role of the extracellular matrix. *Ageing Res Rev* **40**:20–30. doi:10.1016/j.arr.2017.07.004

Rai MF, Hashimoto S, Johnson EE, Janiszak KL, Fitzgerald J, Heber-Katz E, Cheverud JM, Sandell LJ. 2012. Heritability of articular cartilage regeneration and its association with ear wound healing in mice. *Arthritis Rheum* **64**:2300–2310. doi:10.1002/art.34396

Rai MF, Sandell LJ. 2014. Regeneration of articular cartilage in healer and non-healer mice. *Matrix Biol* **39**:50–55. doi:10.1016/j.matbio.2014.08.011

Rajnoch C, Ferguson S, Metcalfe AD, Herrick SE, Willis HS, Ferguson MWJ. 2003. Regeneration of the ear after wounding in different mouse strains is dependent on the severity of wound trauma. *Dev Dyn* **226**:388–397. doi:10.1002/dvdy.10242

Ray H, Chang C. 2020. The transcription factor Hypermethylated in Cancer 1 (Hic1) regulates neural crest migration via interaction with Wnt signaling. *Dev Biol* **463**:169–181. doi:10.1016/j.ydbio.2020.05.012

Rees SG, Davies JR, Tudor D, Flannery CR, Hughes CE, Dent CM, Caterson B. 2002. Immunolocalisation and expression of proteoglycan 4 (cartilage superficial zone proteoglycan) in tendon. *Matrix Biol* **21**:593–602. doi:10.1016/S0945-053X(02)00056-2

Rennert RC, Sorkin M, Garg RK, Gurtner GC. 2012. Stem cell recruitment after injury: lessons for regenerative medicine. *Regen Med* **7**:833–50. doi:10.2217/rme.12.82

Rhee DK, Marcelino J, Baker M, Gong Y, Smits P, Lefebvre V, Jay GD, Stewart M, Wang H, Warman ML, Carpten JD. 2005. The secreted glycoprotein lubricin protects cartilage surfaces and inhibits synovial cell overgrowth. *J Clin Invest* **115**:622–631. doi:10.1172/JCI200522263

Richard D, Liu Z, Cao J, Kiapour AM, Willen J, Yarlagadda S, Jagoda E, Kolachalama VB, Sieker JT, Chang GH, Muthuirulan P, Young M, Masson A, Konrad J, Hosseinzadeh S, Maridas DE, Rosen V, Krawetz R, Roach N, Capellini TD. 2020. Evolutionary Selection and Constraint on Human Knee Chondrocyte Regulation Impacts Osteoarthritis Risk. *Cell* **181**:362-381.e28. doi:10.1016/j.cell.2020.02.057

Richardson SM, Kalamegam G, Pushparaj PN, Matta C, Memic A, Khademhosseini A, Mobasheri R, Poletti FL, Hoyland JA, Mobasheri A. 2016. Mesenchymal stem cells in regenerative medicine: Focus on articular cartilage and intervertebral disc regeneration. *Methods* **99**:69–80. doi:10.1016/j.ymeth.2015.09.015

Risch M, Easley JT, McCready EG, Troyer KL, Johnson JW, Gadomski BC, McGilvray KC, Kisiday JD, Nelson BB. 2021. Mechanical, biochemical, and morphological topography of ovine knee cartilage. *J Orthop Res* **39**:780–787. doi:10.1002/jor.24835

Robinson WH, Lepus CM, Wang Q, Raghu H, Mao R, Lindstrom TM, Sokolove J. 2016. Low-grade inflammation as a key mediator of the pathogenesis of osteoarthritis. *Nat Rev Rheumatol* **12**:580–592. doi:10.1038/nrrheum.2016.136

Roelofs AJ, Zupan J, Riemen AHK, Kania K, Ansboro S, White N, Clark SM, De Bari C. 2017. Joint morphogenetic cells in the adult mammalian synovium. *Nat Commun* **8**:1–14. doi:10.1038/ncomms15040

Rohlf FJ, Slice DE. 1990. Extensions of the Procrustes Method for the Optimal Superimposition of Landmarks. *Syst Biol* **39**:40–59.

Rood BR, Leprince D. 2013. Deciphering HIC1 control pathways to reveal new avenues in cancer therapeutics. *Expert Opin Ther Targets* **17**:811–827. doi:10.1517/14728222.2013.788152

Roos EM, Arden NK. 2016. Strategies for the prevention of knee osteoarthritis. *Nat Rev Rheumatol* **12**:92–101. doi:10.1038/nrrheum.2015.135

Rux D, Helbig K, Han B, Cortese C, Koyama E, Han L, Pacifici M. 2022. Primary Cilia Direct Murine Articular Cartilage Tidemark Patterning Through Hedgehog Signaling and Ambulatory Load. *J Bone Miner Res* **37**:1097–1116. doi:10.1002/jbmr.4506

Säämänen A -M, Tammi M, Jurvelin J, Kiviranta I, Helminen HJ. 1990. Proteoglycan alterations following immobilization and remobilization in the articular cartilage of young canine knee (stifle) joint. *J Orthop Res* **8**:863–873. doi:10.1002/jor.1100080612

Samosky JT, Burstein D, Grimson WE, Howe R, Martin S, Gray ML. 2005. Spatially-localized correlation of dGEMRIC-measured GAG distribution and mechanical stiffness in the human tibial plateau. *J Orthop Res* **23**:93–101. doi:10.1016/j.orthres.2004.05.008

Sanchez-Lopez E, Coras R, Torres A, Lane NE, Guma M. 2022. Synovial inflammation in osteoarthritis progression. *Nat Rev Rheumatol* **18**:258–275. doi:10.1038/s41584-022-00749-9

Sandell L, Aigner T. 2001. Articular cartilage and changes in artritis An introduction: Cell biology of osteoarthritis. *Arthritis Res* **3**:107–113.

Saunders TL. 2011. Transgenic Mouse Methods and Protocols. *Methods*. doi:10.1007/978-1-60761-974-1

Schlager S. 2017. Morpho and Rvcg – Shape Analysis in R In: Zheng G, Li S, Székely GBT-SS and DA, editors. Statistical Shape and Deformation Analysis. Elsevier. pp. 217–256. doi:10.1016/B978-0-12-810493-4.00011-0

Schmidt TA, Gastelum NS, Nguyen QT, Schumacher BL, Sah RL. 2007. Boundary lubrication of articular cartilage: Role of synovial fluid constituents. *Arthritis Rheum* **56**:882–891. doi:10.1002/art.22446

Schmidt TA, Plaas AHK, Sandy JD. 2009. Disulfide-bonded multimers of proteoglycan 4 (PRG4) are present in normal synovial fluids. *Biochim Biophys Acta - Gen Subj* **1790**:375–384. doi:10.1016/j.bbagen.2009.03.016

Schreiner P. 2010. Analysis of Hic1-expressing cells in the murine pancreas and their role in tissue regulation and regeneration. The University of British Columbia.

Scott RW, Arostegui M, Schweitzer R, Rossi FMV, Underhill TM. 2019. Hic1 Defines Quiescent Mesenchymal Progenitor Subpopulations with Distinct Functions and Fates in Skeletal Muscle Regeneration. *Cell Stem Cell* **25**:797-813.e9. doi:10.1016/j.stem.2019.11.004

Seidenstuecker M, Watrinet J, Bernstein A, Suedkamp NP, Latorre SH, Maks A, Mayr HO. 2019. Viscoelasticity and histology of the human cartilage in healthy and degenerated conditions of the knee. *J Orthop Surg Res* **14**:1–10. doi:10.1186/s13018-019-1308-5

Seifert AW, Kiama SG, Seifert MG, Goheen JR, Palmer TM, Maden M. 2012. Skin shedding and tissue regeneration in African spiny mice (Acomys). *Nature* **489**:561–565. doi:10.1038/nature11499

Sellam J, Berenbaum F. 2010. The role of synovitis in pathophysiology and clinical symptoms of osteoarthritis. *Nat Rev Rheumatol* **6**:625–35. doi:10.1038/nrrheum.2010.159

Setton LA, Mow VC, Müller FJ, Pita JC, Howell DS. 1994. Mechanical Properties of Canine Articular Cartilage Are Significantly Altered Following Transection of the Anterior Cruciate Ligament. *J*

Orthop Res **12**:451–463. doi:10.1002/jor.1100120402

Shah S, Mudigonda S, Underhill TM, Salo PT, Mitha AP, Krawetz RJ. 2022. Prx1 + and Hic1+ Mesenchymal Progenitors Are Present Within the Epidural Fat and Dura Mater and Participate in Dural Injury Repair. *Stem Cells Transl Med* **11**:200–212. doi:10.1093/stcltm/szab014

Shapiro F, Koide S, Glimcher MJ. 1993. Cell origin and differentiation in the repair of full-thickness defects of articular cartilage. *J Bone Jt Surg* **75**:532–553. doi:10.2106/00004623-199304000-00009

Sharif B, Garner R, Hennessy D, Sanmartin C, Flanagan WM, Marshall DA. 2016. Productivity costs of work loss associated with osteoarthritis in Canada from 2010 to 2031. *Osteoarthr Cartil* 1–10. doi:10.1016/j.joca.2016.09.011

Shats I, Deng M, Davidovich A, Zhang C, Kwon JS, Manandhar D, Gordân R, Yao G, You L. 2017. Expression level is a key determinant of E2F1-mediated cell fate. *Cell Death Differ* **24**:626–637. doi:10.1038/cdd.2017.12

Shepherd DET, Seedhom BB. 1999. Thickness of human articular cartilage in joints of the lower limb. *Ann Rheum Dis* **58**:27–34. doi:10.1136/ard.58.1.27

Sim S, Chevrier A, Garon M, Quenneville E, Lavigne P, Yaroshinsky A, Hoemann CD, Buschmann MD. 2017. Electromechanical probe and automated indentation maps are sensitive techniques in assessing early degenerated human articular cartilage. *J Orthop Res* **35**:858–867. doi:10.1002/jor.23330

Simha NK, Jin H, Hall ML, Chiravarambath S, Lewis JL. 2007. Effect of indenter size on elastic modulus of cartilage measured by indentation. *J Biomech Eng* **129**:767–775. doi:10.1115/1.2768110

Simon WH, Green WT. 1971. Experimental production of cartilage necrosis by cold injury: failure to cause degenerative joint disease. *Am J Pathol* **64**:145–154.

Smith MD. 2011. The normal synovium. *Open Rheumatol J* **5**:100–106. doi:10.2174/1874312901105010100

Soliman H, Paylor B, Scott RW, Lemos DR, Chang CK, Arostegui M, Low M, Lee C, Fiore D, Braghetta P, Pospichalova V, Barkauskas CE, Korinek V, Rampazzo A, MacLeod K, Underhill TM, Rossi FMV. 2020. Pathogenic Potential of Hic1-Expressing Cardiac Stromal Progenitors. *Cell Stem Cell* **26**:205-220.e8. doi:10.1016/j.stem.2019.12.008

Sonnery-Cottet B, Archbold P, Cucurulo T, Fayard JM, Bortolletto J, Thaunat M, Prost T, Chambat P. 2011. The influence of the tibial slope and the size of the intercondylar notch on rupture of the anterior cruciate ligament. *J Bone Jt Surg - Ser B* **93 B**:1475–1478. doi:10.1302/0301-620X.93B11.26905

Sophia Fox AJ, Bedi A, Rodeo SA. 2009. The Basic Science of Articular Cartilage: Structure, Composition, and Function. *Sport Heal A Multidiscip Approach* **1**:461–468. doi:10.1177/1941738109350438

Stockwell RA. 1967. The cell density of human articular and costal cartilage. *J Anat* **101**:753–63.

Stolz M, Gottardi R, Raiteri R, Miot S, Martin I, Imer R, Staufer U, Raducanu A, Düggelin M, Baschong W, Daniels AU, Friederich NF, Aszodi A, Aebi U. 2009. Early detection of aging cartilage and osteoarthritis in mice and patient samples using atomic force microscopy. *Nat Nanotechnol* **4**:186–192. doi:10.1038/nnano.2008.410

Strauss N, Hendee ED. 1959. THE EFFECT OF DIPHTHERIA TOXIN ON THE METABOLISM OF

HELA CELLS. *J Exp Med* **109**:145–163. doi:10.1084/jem.109.2.145

Swann AC, Seedhom BB. 1989. Improved Techniques for Measuring the Indentation and Thickness of Articular Cartilage. *Proc Inst Mech Eng Part H J Eng Med* **203**:143–150. doi:10.1243/PIME_PROC_1989_203_026_01

Tchorz JS, Suply T, Ksiazek I, Giachino C, Cloëtta D, Danzer CP, Doll T, Isken A, Lemaistre M, Taylor V, Bettler B, Kinzel B, Mueller M. 2012. A modified RMCE-compatible Rosa26 locus for the expression of transgenes from exogenous promoters. *PLoS One* **7**. doi:10.1371/journal.pone.0030011

Teeple E, Jay GD, Elsaid KA, Fleming BC. 2013. Animal Models of Osteoarthritis: Challenges of Model Selection and Analysis. *AAPS J* **15**:438–446. doi:10.1208/s12248-013-9454-x

Thomas CM, Fuller CJ, Whittles CE, Sharif M. 2007. Chondrocyte death by apoptosis is associated with cartilage matrix degradation. *Osteoarthr Cartil* **15**:27–34. doi:10.1016/j.joca.2006.06.012

Tustison NJ, Avants BB, Cook PA, Zheng Y, Egan A, Yushkevich PA, Gee JC. 2010. N4ITK: Improved N3 bias correction. *IEEE Trans Med Imaging* **29**:1310–1320. doi:10.1109/TMI.2010.2046908

Udo M, Muneta T, Tsuji K, Ozeki N, Nakagawa Y, Ohara T, Saito R, Yanagisawa K, Koga H, Sekiya I. 2016. Monoiodoacetic acid induces arthritis and synovitis in rats in a dose- and time-dependent manner: Proposed model-specific scoring systems. *Osteoarthr Cartil* **24**:1284–1291. doi:10.1016/j.joca.2016.02.005

Ueno M, Lyons BL, Burzenski LM, Gott B, Shaffer DJ, Roopenian DC, Shultz LD. 2005. Accelerated wound healing of alkali-burned corneas in MRL mice is associated with a reduced inflammatory signature. *Investig Ophthalmol Vis Sci* **46**:4097–4106. doi:10.1167/iovs.05-0548

Usmani SE, Ulici V, Pest MA, Hill TL, Welch ID, Beier F. 2016. Context-specific protection of TGFα null mice from osteoarthritis. *Sci Rep* **6**:1–11. doi:10.1038/srep30434

Van Helvert S, Storm C, Friedl P. 2018. Mechanoreciprocity in cell migration. *Nat Cell Biol* **20**:8–20. doi:10.1038/s41556-017-0012-0

Van Rechem C, Boulay G, Pinte S, Stankovic-Valentin N, Guerardel C, Leprince D. 2010. Differential Regulation of HIC1 Target Genes by CtBP and NuRD, via an Acetylation/SUMOylation Switch, in Quiescent versus Proliferating Cells. *Mol Cell Biol* **30**:4045–4059. doi:10.1128/MCB.00582-09

Vanwanseele B, Lucchinetti E, Stüssi E. 2002. The effects of immobilization on the characteristics of articular cartilage: Current concepts and future directions. *Osteoarthr Cartil* **10**:408–419. doi:10.1053/joca.2002.0529

Vidal P, Dickson MG. 1993. Regeneration of the distal phalanx: A case report. *J Hand Surg (British Eur Vol* **18**:230–233. doi:10.1016/0266-7681(93)90116-W

Vincent TL, McClurg O, Troeberg L. 2022. The Extracellular Matrix of Articular Cartilage Controls the Bioavailability of Pericellular Matrix-Bound Growth Factors to Drive Tissue Homeostasis and Repair. *Int J Mol Sci* **23**. doi:10.3390/ijms23116003

Vincent TL, Wann AKT. 2019. Mechanoadaptation: articular cartilage through thick and thin. *J Physiol* **597**:1271–1281. doi:10.1113/JP275451

Voehringer D, Liang H, Locksley RM. 2008. Homeostasis and Effector Function of Lymphopenia-Induced “Memory-Like” T Cells in Constitutively T Cell-Depleted Mice. *J Immunol* **180**:4742–4753. doi:10.4049/jimmunol.180.7.4742

Waller KA, Zhang LX, Elsaid KA, Fleming BC, Warman ML, Jay GD. 2013. Role of lubricin and boundary lubrication in the prevention of chondrocyte apoptosis. *Proc Natl Acad Sci U S A* **110**:5852–5857. doi:10.1073/pnas.1219289110

Wang M, Sampson ER, Jin H, Li J, Ke QH, Im HJ, Chen D. 2013. MMP13 is a critical target gene during the progression of osteoarthritis. *Arthritis Res Ther* **15**:1–11. doi:10.1186/ar4133

Wang Y, Chen X, Cao W, Shi Y. 2014. Plasticity of mesenchymal stem cells in immunomodulation: Pathological and therapeutic implications. *Nat Immunol* **15**:1009–1016. doi:10.1038/ni.3002

Ward BD, Furman BD, Huebner JL, Kraus VB, Guilak F, Olson SA. 2008. Absence of posttraumatic arthritis following intraarticular fracture in the MRL/MpJ mouse. *Arthritis Rheum* **58**:744–753. doi:10.1002/art.23288

Wayne Mcilwraith C, Fortier LA, Frisbie DD, Nixon AJ. 2011. Equine models of articular cartilage repair. *Cartilage* **2**:317–326. doi:10.1177/1947603511406531

Wei X, Gao J, Messner K. 1997. Maturation-dependent repair of untreated osteochondral defects in the rabbit knee joint. *J Biomed Mater Res* **34**:63–72. doi:10.1002/(SICI)1097-4636(199701)34:1<63::AID-JBM9>3.0.CO;2-L

Weissman IL. 2000. Stem cells: Units of development, units of regeneration, and units in evolution. *Cell* **100**:157–168. doi:10.1016/S0092-8674(00)81692-X

Wilhelmi G, Faust R. 1976. Suitability of the C 57 Black Mouse as an Experimental Animal for the Study of Skeletal Changes Due to Ageing , with Special Reference to Osteo-Arthrosis and Its Response to Tribenoside **296**:289–296.

Wilk K, Yeh SA, Mortensen LJ, Ghaffarigarakani S, Lombardo CM, Bassir SH, Aldawood ZA, Lin CP, Intini G. 2017. Postnatal Calvarial Skeletal Stem Cells Expressing PRX1 Reside Exclusively in the Calvarial Sutures and Are Required for Bone Regeneration. *Stem Cell Reports* **8**:933–946. doi:10.1016/j.stemcr.2017.03.002

Woods PS, Morin AA, Chen P, Mahonski S, Xiao L, Hurley M, Yadav S, Schmidt TA. 2021. Automated Indentation Demonstrates Structural Stiffness of Femoral Articular Cartilage and Temporomandibular Joint Mandibular Condylar Cartilage Is Altered in FgF2KO Mice. *Cartilage* **13**:1513S-1521S. doi:10.1177/1947603520962565

Wu L, Leijten JCH, Georgi N, Post JN, van Blitterswijk CA, Karperien M. 2011. Trophic Effects of Mesenchymal Stem Cells Increase Chondrocyte Proliferation and Matrix Formation. *Tissue Eng Part A* **17**:1425–1436. doi:10.1089/ten.tea.2010.0517

Young M, Richard D, Grabowski M, Auerbach BM, de Bakker BS, Hagoort J, Muthuirulan P, Kharkar V, Kurki HK, Betti L, Birkenstock L, Lewton KL, Capellini TD. 2022. The developmental impacts of natural selection on human pelvic morphology. *Sci Adv* **8**:1–23. doi:10.1126/sciadv.abq4884

Zelditch ML, Swiderski DL, Sheets HD. 2012. Geometric morphometrics for biologists: a primer. academic press.

Zhang L, Hu J, Athanasiou KA. 2009. The Role of Tissue Engineering in Articular Cartilage Repair and Regeneration. *Crit Rev Biomed Eng* **37**:1–57.

Zhang M, Mani SB, He Y, Hall AM, Xu L, Li Y, Zurakowski D, Jay GD, Warman ML. 2016. Induced superficial chondrocyte death reduces catabolic cartilage damage in murine posttraumatic osteoarthritis. *J Clin Invest* **126**:2893–2902. doi:10.1172/JCI83676

Zhang Y, Strehin I, Bedelbaeva K, Gourevitch D, Clark L, Leferovich J, Messersmith PB, Heber-Katz E. 2015. Drug-induced regeneration in adult mice. *Sci Transl Med* **7**:290ra92. doi:10.1126/scitranslmed.3010228

Zhao RC. 2013. Essentials of Mesenchymal Stem Cell Biology and Its Clinical Translation. doi:10.1007/978-94-007-6716-4

Zheng J, Xiong D, Sun X, Wang Jinglong, Hao M, Ding T, Xiao G, Wang X, Mao Y, Fu Y, Shen K, Wang Jianhua. 2012. Signification of Hypermethylated in Cancer 1 (HIC1) as Tumor Suppressor Gene in Tumor Progression. *Cancer Microenviron Off J Int Cancer Microenviron Soc* **5**:285–293. doi:10.1007/s12307-012-0103-1

Zheng L, Zhang Z, Sheng P, Mobasheri A. 2021. The role of metabolism in chondrocyte dysfunction and the progression of osteoarthritis. *Ageing Res Rev* **66**:101249. doi:10.1016/j.arr.2020.101249

Zhou BO, Yue R, Murphy MM, Peyer JG, Morrison SJ. 2014. Leptin-receptor-expressing mesenchymal stromal cells represent the main source of bone formed by adult bone marrow. *Cell Stem Cell* **15**:154–168. doi:10.1016/j.stem.2014.06.008

Zhou HW, Lou SQ, Zhang K. 2004. Recovery of function in osteoarthritis chondrocytes induced by p16INK4a-specific siRNA in vitro. *Rheumatology* **43**:555–568. doi:10.1093/rheumatology/keh127

Zhou Y, Qiu J, Wan L, Li J. 2022. The effect of matrix stiffness on the chondrogenic differentiation of mesenchymal stem cells. *J Mol Histol* **53**:805–816. doi:10.1007/s10735-022-10094-6